Modelling Studies of Solid Oxide Fuel Cells with Internal Methane Steam Reforming

Patrícia Antunes Pimentel de Aguiar

September 2002

A Thesis Submitted for the Degree of Doctor of Philosophy of the University of London and for the Diploma of Imperial College

Department of Chemical Engineering and Chemical Technology,
Imperial College of Science, Technology and Medicine,
Prince Consort Road, London SW7 2BY, United Kingdom.

Abstract

Thermal coupling of endothermic and exothermic reactions, where the first reaction often leads to the desired product and the second one serves as the process heat source, is seen as a promising application for autothermal reactors. Autothermal operation is applied here to a solid oxide fuel cell with internal methane steam reforming (IR-SOFC). A SOFC is an energy conversion device that produces electricity and heat directly from the electrochemical combination of a fuel with an oxidant. Thus, in an IR-SOFC, the heat necessary to sustain the endothermic reforming reactions, which produce the hydrogen and carbon monoxide required for the fuel cell operation, can be provided by the excess heat generated. The present work investigates an indirect internal reforming SOFC configuration (IIR-SOFC), where the reformer section is separate but adjacent to the cell anode and in close thermal contact with it.

Two steady-state models, for a fixed-bed and a coated-wall reforming reactor, have been developed to study the coupling between the thermal load associated with the rate of steam reforming at typical SOFC temperatures and the local amount of heat available from the fuel cell reactions. Simulations performed for the fixed-bed IIR-SOFC show that use of typical metal-based reforming catalysts leads to full methane consumption but undesirable local cooling at the reformer entrance. It is demonstrated that this local cooling can be minimised by the use of lower IIR activity catalysts, such as oxide-based catalysts, or catalysts with a non-uniform distribution of active metal and a diffusion barrier placed in the outer regions of the pellet; however, these can result in incomplete methane reformer conversion and subsequent direct internal reforming (DIR) on the Ni cermet anode. Reforming on the SOFC anode is shown to also result in full methane conversion and steep temperature gradients at the SOFC fuel channel entrance. Simultaneous reduction of the indirect and direct internal reforming reaction rates is found to considerably improve performance. Different operating conditions and flow configurations (counter-flow vs. co-flow) are also investigated. Simulation results for the coated-wall IIR-SOFC demonstrate that both configurations studied have similar overall behaviour, that catalyst coating thickness and activity can be combined to fulfil a desired operation, and that the use of a non-uniform catalyst axial distribution along the reformer can lead to smoother temperature profiles along the reactor. The dynamic response of the coated-wall IIR-SOFC system to load changes is investigated. Overall, simulation results show that significant improvements can be made to the operation of solid oxide fuel cells with internal methane steam reforming.

To my parents

Acknowledgements

I would like to thank my supervisors, Professor Lester Kershenbaum and Professor David Chadwick, for the opportunity they gave me of working with them, and for the guidance and encouragement throughout the course of this PhD.

I express my gratitude to "Fundação para a Ciência e a Tecnologia" for their financial support through the scholarship PRAXIS XXI/BD/15972/98, without which this PhD would not have been possible.

I would also like to thank Professor Costas Pantelides for gPROMS advice and the Energy Sources and Conversion Group of Rolls Royce (Strategic Research Centre) for advice on solid oxide fuel cell systems.

I express my warmth thanks to my family, especially Pai, Mãe, and Mano, for their continuous support during my stay in London, and to my friends in Portugal for always being ready and available during my short visits home.

Even if it sounds strange, I thank London, for being such an amazing city, for all its diversity, and for never making me feel like a foreigner.

Finally, I am grateful to those who, in one way or another, made my life in London so much easier and interesting. To the Portuguese connection, Marta, Isabel, Henrique, Ricardo, Sofia, and Richard, for taking care of the "irmãzinha mais nova do Carlos" as well as Alexandre, Dalila, Fernando, Frederico, Teresa, Ruben, Cristina, João, Sónia, and Dário. To the past and present people of the Applied Catalysis Group and Department of Chemical Engineering. From those who have left, special thanks to Stephen, for all the support throughout these years, to Tomas, for that big smile, to Paul, for his humour, and to Vicky, for being Vicky. From the ones still around, Jesus, Ludo, Javier, Eduard, Elvia, Nina, and Nacho, thank you so much, for all the crazy and unexpected nights whenever and wherever, and for being my family in London. To the Bridge and Domino partners, for those relaxing moments, and to the Mexican/Spanish connection (no names mentioned, it would probably be longer than this thesis!) for all the energetic parties, and for giving me no choice but to learn Spanish. To Nacho, for all the cinema and dinner escapes. And to all those I haven't mentioned but with whom I shared such nice moments. A very special thank you to Marta, Nacho, and Nina, my dearest, dearest friends - I don't need to say why, you were always there for me.

Table of Contents

List of Figures

List of Tables

Chapter 1

Introduction

Summary

Creation of an autothermal system by coupling an endothermic to an exothermic reaction can be achieved by matching the thermal requirements of those two reactions. Such autothermal operation is here applied to the operation of a solid oxide fuel cell with internal methane steam reforming, where the endothermic steam reforming and exothermic electrochemical reactions are thermally coupled. This internal reforming within a high temperature fuel cell is expected to simplify the system design, increasing its efficiency. This first chapter introduces the main subject of the thesis, clarifying its relevance and associated problems. It begins with autothermal operation or reactors, briefly reviewing some of the work done in this area, and proceeds with an introduction to fuel cells, explaining their general operation, main advantages, and applications. Issues related to internal reforming or fuel processing in high temperature fuel cells as well as the particular internal reforming solid oxide fuel cell system under study are also discussed. Finally, the research objectives and full thesis outline are presented.

Outline

1.1 Introduction

Creation of an autothermal system by coupling an endothermic to an exothermic reaction demands matching the thermal requirements of those two reactions. Here, this matching is applied to the operation of a solid oxide fuel cell (SOFC) with internal methane steam reforming, where the endothermic steam reforming reactions and the exothermic electrochemical ones are thermally coupled in a single unit. Such is expected to simplify the system design and lead to an increase in efficiency. In this configuration, the gases leaving the steam reforming reactor are not allowed to leave the system but are, instead, fed back, in some form of modified shell-and-tube configuration, to undergo an oxidation on the fuel cell anode. The heat transfer between the two systems should be able to provide autothermal operation. However, such thermal coupling is not easy to achieve because of the potential mismatch between the thermal load associated with the rate of steam reforming at typical SOFC temperatures (700 - 1000°C) and the local amount of heat available for this purpose from the fuel cell reactions. How this can be accomplished and what modifications can be suggested to improve the overall performance of this coupled system are main research objectives and issues discussed in this thesis.

Mathematical modelling is the medium through which such objectives are here addressed. It allows the consideration and comparison of several configurations such that the more promising designs can later be optimised or used to simulate the effect of a number of disturbances.

The aim of this first chapter is to introduce the subject of this thesis in detail, explaining its relevance and the problems associated with it. It starts with a short review in autothermal operation or autothermal multifunctional reactors, where some of the reactor configurations so far proposed and studied are introduced. It covers mainly systems with weakly to moderately exothermic reactions as well as the thermal coupling of endothermic and exothermic reactions, of major importance for this project. The chapter proceeds with an introduction to fuel cells, explaining their general operation, main advantages, and main applications, and providing a short description of the current

types of fuel cell systems. Issues related to internal reforming in high temperature fuel cells, i.e. solid oxide fuel cells and molten carbonate fuel cells (MCFC), are then discussed. Next, the internal reforming solid oxide fuel cell system under study is described and potential problems and corresponding solutions discussed. Finally, the research objectives and full thesis outline are presented.

1.2 Autothermal Operation

Autothermal multifunctional reactors have been receiving considerable academic and industrial attention for the past decades, as it is necessary, for economic reasons, to recover as much as possible the heat produced by exothermic reactions. The concept of integrating reaction and heat exchange in one compact unit instead of in a complex network of reactors and heat exchangers has demonstrated several advantages, such as heat loss minimisation and lesser sensitivity to perturbations. However, optimisation and design of autothermal reactors is a nontrivial task as the intrinsic feedback of heat gives rise to a complex and sometimes unstable parametric and dynamic behaviour (operation is in the region of multiple steady-states), where the temperature profile has a decisive influence on the desired product yield and heat recovery efficiency (Kolios et al., 2000). Co-currently or counter-currently cooled reactors are the two simplest examples of autothermal reactors. Unlike non-autothermal co-current reactors, which are unconditionally stable, autothermal co-current reactors have been reported to exhibit multiple steady-states within a broad range of operating conditions (Pedernera et al., 1997). The most common examples of multifunctional reactors are, however, autothermal reactors for weakly to moderately exothermic reactions, where the cold reactor feed is heated up to the required reaction temperature by the hot reactor effluent. This can be done in a separate heat exchanger or by partial or total integration of the heat exchanger into the reactor. Examples of important industrial reactions that can be carried out making use of the separate heat exchanger concept include ammonia and methanol synthesis, SO_2 oxidation, phthalic anhydride synthesis, and the water-gas shift reaction (Froment and Bischoff, 1990). Advantageous concepts of such autothermal reactors, with integration of either regenerative or recuperative heat exchange into the catalyst packing of a fixed-bed reactor, are discussed next. A more

recent and promising application of autothermal multifunctional reactors includes thermal coupling between endothermic and exothermic reactions, briefly discussed in Section 1.2.2.

1.2.1 Weakly to Moderately Exothermic Reactions

Design options for autothermal reactors for weakly to moderately exothermic reactions include the reverse-flow reactor and the counter-current fixed-bed reactor.

Reverse-flow operation in a fixed-bed catalytic reactor can be seen as an engineering technique that successfully applies the concept of forced unsteady-state conditions in heterogeneous catalytic reactors. Important advantages of reverse-flow reactor technologies in comparison with traditional steady-sate processes include: the possibility of using the fixed catalyst bed as a heat and mass accumulator and as a regenerative counter-current heat exchanger which allows autothermal operation of exothermic processes at low and fluctuating inlet reactant concentrations. Furthermore, creation of thermodynamically favourable conditions for reversible reactions, such as declining temperature profiles for exothermic processes and increasing temperature profiles for endothermic ones; intensive energy trapping that allows an efficient heat recovery for an exothermic reaction or a substantially decrease in energy consumption for an endothermic one; the possibility of combining endothermic and exothermic reactions in one catalyst bed providing energy economy; and a smaller reactor size, simplification of the unit flow diagram, and reduction in the average reactor temperature with consequent decrease of pressure drop and heat losses. The application of the reverse-flow reactor concept for weakly exothermic reactions has been widely studied in the recent years. The main applications so far are in the field of waste gas purification and are discussed in a comprehensive review by Matros and Bunimovich (1996). Modelling works have aided in building a better understanding of fixed-bed reactors with periodic flow reversal, studying the dependence of the system behaviour on key parameters as well as system multiplicity and instability (Salinger and Eigenberger, 1996a, 1996b). Calculations have shown that when sections of the catalytic reactor are replaced with inert ones a design modification can force the reactor to a desired stable solution.

Autothermal counter-current reactors, where counter-current heat exchange can be integrated into a catalyst bed or a counter-current heat exchanger can be filled with catalyst, have also been the subject of several studies (Kolios et al., 2000). A counter-current reactor has been shown to exhibit three steady-states for the same operating conditions, thus three different catalyst bed inlet temperatures can be obtained for a given coolant inlet temperature. Nieken et al. (1995) showed the equivalence between the counter-current reactor and a reverse-flow reactor for short switching periods.

1.2.2 Coupling of Endothermic & Exothermic Reactions

The thermal coupling of endothermic and exothermic reactions, where the endothermic reaction leads to the desired product and the exothermic one (usually combustion) serves as a heat source for the process, is a promising new application of autothermal multifunctional reactors. Once more, two alternative designs exist which are based on different heat recovery mechanisms: the counter-current fixed-bed reactor using indirect or recuperative heat exchange (Frauhammer et al., 1999) and the reverse-flow fixed-bed reactor using direct or regenerative heat exchange. To achieve this goal, three different modes of operation have recently been proposed: simultaneous, asymmetric, and symmetric operation, respectively.

Under simultaneous operation (Blanks et al., 1990) the reactants for both endothermic and exothermic reactions are mixed and all reactions run more or less in parallel. However, in this operation mode, and as both reactions take place simultaneously, non-selective combustion of the reaction mixture can lead to low product selectivity. In the asymmetric or symmetric operation modes both reactions run separately. Under asymmetric conditions (Kulkarni and Dudukovic, 1996; Kolios and Eigenberger, 1999; Frauhammer et al., 1999), the feed for the endothermic reaction always comes from one side (in the regenerative mode during one portion of the whole period) and the feed for the exothermic reaction comes from the opposite side (during the rest of the period). Therefore in the counter-current operation mode the reactions are separate in space and for the reverse-flow case the reactions are separate in time. Under symmetric conditions, the feed for the endothermic reaction comes from both sides, as in the simultaneous operation, but the hot exhausts of the external exothermic

reaction are supplied directly or indirectly in the middle of the reactor (Snyder and Subramaniam, 1994; Kolios and Eigenberger, 1999). A review of such autothermal fixed-bed reactor concepts has been recently made by Kolios et al. (2000), where the coupling of methane steam reforming and methane combustion is used as an example.

Reverse-flow operation for the combination of endothermic and exothermic reactions has been experimentally tested by Blanks et al. (1990). Hydrogen production through the highly endothermic steam reforming of natural gas was combined with the exothermic methane combustion. Reverse-flow operation made it possible to achieve high temperatures in the catalyst bed at low average difference between the outlet and inlet gas temperature, and thus methane consumption during exothermic combustion was very low. Frauhammer et al. (1999) studied a monolithic counter-current reactor concept for the coupling of an endothermic high-temperature synthesis reaction and a combustion reaction. These authors have observed that, the introduction of inert reactor zones lead to a significant reduction of catalyst costs and to a decoupling of chemical conversion and local temperature, important for an optimisation of the temperature and conversion profiles.

A new example of autothermal operation is the electrochemical oxidation of hydrogen in solid oxide fuel cell monolithic arrangements operating under forced periodic reverse-flow. Neophytides (1999) and Neophytides and Tripakis (1996) have studied the dynamic operation of this combined system under different flow configurations reporting an improved and more efficient SOFC operation and simplified flow diagram. These authors have shown that this reverse-flow operation leads to the formation and propagation of temperature and concentration profiles along the reactor, which cannot be obtained in a steady-state regime, and that a high-temperature moving heat front is trapped in the reactor maintaining high temperatures while the feed gas remains at low temperature.

In the present work, autothermal operation is also applied to the operation of a solid oxide fuel cell. The system under study is one where the exothermic electrochemical SOFC reactions are thermally coupled with the hydrogen producing endothermic methane steam reforming reaction. This is achieved through either a counter-current or co-current design instead of a reverse-flow one. However, in order to accomplish this, knowledge concerning fuel cells is first required.

1.3 Fuel Cells

Fuel cells are energy conversion devices that produce electricity and heat directly from a gaseous fuel by electrochemical combination of that fuel with an oxidant.

The basic principle of fuel cells was first successfully demonstrated by Sir William Grove in 1839. However, it took 120 years until NASA proved some of their potential applications in providing power, heat, and potable water during space flights. This was not because fuel cells environmental attributes were not already known, but because several technical challenges still needed to be met to achieve a viable power system. In the 1960s, the industry began to recognise the commercial potential of fuel cells, but encountered technical barriers and high investment costs as fuel cells were not yet economically competitive with the existing energy producing technologies.

Factors that motivated great advances in fuel cell technology over the last few years were the increasing social awareness concerning the environmental consequences of burning fossil fuels, as their combustion releases harmful emissions (carbon dioxide, methane, nitrous oxide, water vapour, ozone, etc.) into the air, which influence the Greenhouse Effect, and the expectancy in oil price increase, as the excess production capacity begins to decline. The transportation sector, likely to be the most heavily affected, is putting great effort into fuel cells development (Carrette et al., 2000).

1.3.1 General Operation of a Fuel Cell

Similarly to internal combustion engines and batteries, fuel cells convert energy from one form to another. Internal combustion engines, as well as conventional utility power plants, change the chemical energy of a fuel into thermal energy that generates mechanical energy and, in case of a power plant, electrical energy. These engines are less efficient than fuel cells because of the conversion of thermal to mechanical energy, which is limited by the Carnot Cycle (see Chapter 2, Section 2.2.4.3). Batteries and fuel cells are similar in the sense they both efficiently convert chemical energy directly into electricity. The difference is that in batteries the chemical energy has to be stored prior to being consumed and, upon being used up, the battery must be either recharged or replaced, while fuel cells can operate continuously and as long as an external supply of

fuel is present. Fuels and oxidants applied in fuel cells can be any gases or liquids capable of being electrochemically oxidised and reduced. However, due to its high electrochemical activity, hydrogen is the most frequently utilised fuel. Air is commonly applied as an oxidant, since it is readily and economically available. The fundamental mechanism of the operation of a fuel cell is the inverse water electrolysis reaction. Electrocatalytic oxidation of hydrogen at the anode and reduction of oxygen at the cathode create a potential difference between those electrodes. This can be exploited in an external circuit if a gas-tight electrolyte placed between the electrodes allows for ionic mass and charge transfer. The main fuel cell reaction product, when hydrogen is the fuel, is pure water and the chemical energy of the reaction is liberated as electricity and heat (Joon, 1998).

1.3.2 Advantages of Fuel Cells

Fuel cells possess great potential as a more efficient and cleaner alternative method of electricity generation than conventional generators, hence fuel cells can be operated with a near-constant efficiency ranging from 40 to 60%, depending on type and design, compared with typical internal combustion engine efficiencies of 30%. Fuel cell systems are flexible regarding the primary fuel in use. In fact, any fuel from which a hydrogen-containing gas mixture can be produced is appropriate. However, the conversion to hydrogen causes some efficiency loss and clean-up of the fuel or product gas may be necessary. Due to this gas clean-up as well as to the fact that the electrochemical reactions in the cell are very clean, fuel cell plants exhibit extremely low emission levels. Emissions of CO_2 are, however, nearly always involved in the production of the hydrogen fuel needed. Added environmental benefits are due to the absence of moving parts. Noise and vibration levels are normally attributed to the auxiliary equipment and can be minimised, making fuel cells highly reliable and low in maintenance costs (Joon, 1998; Larminie and Dicks, 2000). In addition to high conversion efficiency and environmental acceptability, fuel cells also present siting flexibility and modularity (allowing for a wide range of power plant electrical outputs), and they do not suffer appreciably from problems of lubrication, wear, leakage and heat loss, which affect the reliability of traditional heat engines (Finnerty et al., 1998).

Another feature of fuel cells is that the exhaust heat is suitable for use in residential, commercial, and industrial co-generation applications. This simultaneous utilisation of electricity and heat is much more efficient than the single production of electricity as considerable waste heat is normally produced. This heat can be used to either produce more electricity (in a gas or steam turbine) or accommodate a plant with heat and warm water. This is especially true for the case of high temperature fuel cells where the possibility of integration with steam and gas turbines enables electrical efficiencies up to 70%. These high temperature fuel cells can also allow for plant simplification and cost saving as H_2/CO mixtures can be used as fuel or, alternatively, fuel processing can take place in the cell itself (Joon, 1998).

The most important disadvantage of fuel cells at present is their cost. It is predicted that the role fuel cells will play in the future will be determined by the economical efficiency achieved and by the emission regulations with time set.

1.3.3 Different Types of Fuel Cells & Their Applications

Despite the simple working principle of fuel cells, electrochemical reactions do not readily take place and, unless special materials are used as electrodes and electrolytes, the current density is extremely low and electrical power losses are considerable. One of the limitations of the Grove cell was the limited current produced as a result of the Pt electrodes small effective area. Increasing this area, and hence the power density was one of the first challenges. Optimisation of electrode catalysts and structures, combined with effective electrolyte and electrode–electrolyte contact continue to be factors where improvements in power density are still sought. In addition, Grove used hydrogen produced by water electrolysis as fuel in his cells. Today, hydrogen or hydrogen rich gas from hydrocarbon or bio-mass sources are the preferred fuels. The means for using methanol, methane or higher hydrocarbons directly are then significant technical challenges, as well as limitations to the wide scale exploitation of fuel cells.

The Alkali Fuel Cell (AFC) system provided the on-board power system for the Apollo lunar programme, stimulating the restart of the interest in fuel cell technology. Furthermore, it was also during the 1960s that the other five fuel cell systems, that are the subject of extensive development today, were originally conceived. All of them with

the common features of separate reactions occurring at the electrodes and ions moving through the electrolyte while electrons move round an external circuit. These are the Solid Polymer Fuel Cell or Proton Exchange Membrane Fuel Cell (SPFC or PEMFC), Phosphoric Acid Fuel Cell (PAFC), Molten Carbonate Fuel Cell (MCFC), Solid Oxide Fuel Cell (SOFC), and Direct Methanol Fuel Cell (DMFC). These cells have different electrolytes and operating conditions, and, consequently, different anode and cathode reactions, electrocatalysts, and dominant migrating ion through the electrolyte. Table 1.1 presents the characteristic features of aforementioned fuel cells (Acres, 2001; Acres et al., 1997). With the exception of the direct methanol fuel cell, characterisation and nomenclature of fuel cells is usually by the electrolyte employed in the cell, their most important component. The electrolyte determines the operating temperature and with that the catalysts to be applied in the electrodes, as well as the process gas requirements. A second grouping is by the operating temperature. There are, thus, low and high temperature fuel cells. Low temperature fuel cells operate between 50 and 200°C and include the AFC, the PEMFC, the PAFC, and the DMFC. High temperature fuel cells operate between 600 and 1100°C and include the MCFC and the SOFC.

In the alkali fuel cell, a concentrated solution of potassium hydroxide acts as electrolyte and coolant. It conducts hydroxyl ions from the cathode to the anode and is sensitive to carbon dioxide poisoning. In the PEMFC, the electrolyte is a solid polymer, which when hydrated, conducts protons from the anode to the cathode. Both these types of fuel cell operate at a temperature level that requires the use of platinum as a catalyst in the electrodes. However, at these temperatures platinum is highly sensitive to poisoning by carbon monoxide. The same is true for the PAFC which operates around 200°C. In this cell the electrolyte also conducts protons from the anode to the cathode and is kept in place by an inert porous structure. Both the PAFC and PEMFC are, however, tolerant to CO_2 (Joon, 1998). The electrolyte of the MCFC is a molten mixture of alkali metal carbonates. This cell operates at high temperatures at which the alkali carbonates form a highly conductive carbonate salt, with carbonate ions providing ionic conduction. Unlike with all other fuel cells, CO_2 needs to be supplied to the MCFC cathode together with oxygen. This is converted to carbonate ions, which provide the mean of ion transport between the cathode and the anode, where they are converted back to CO_2. Due to the high operating temperatures of MCFCs, nickel catalysts can be

used in the electrodes (Larminie and Dicks, 2000; Joon, 1998). The same is true for SOFCs, which are considered in more detail in Section 1.3.3.1.

Table 1.1 Characteristics of the six main types of fuel cells.

Fuel cell	Electrolyte	Cathode catalyst	Anode catalyst	Temp., °C
AFC	Potassium hydroxide	Pt/Au, Pt, Ag	Pt/Au, Pt, Ag	50 – 90
PEMFC	Solid proton conducting polymer	Pt	Pt, Pt/Ru	50 – 125
PAFC	Orthophosphoric acid	Pt/Cr/Co, Pt/Ni	Pt	190 – 210
MCFC	Lithium/potassium carbonate mixture	Li/NiO	Ni, Ni/Cr	600 – 700
SOFC	Stabilised zirconia	$LaSrMnO_3$	Ni/ZrO_2	700 – 1100
DMFC	Sulphuric acid or solid polymer			50 – 120

Fuel cell	Anode reaction	Ion transport	Cathode reaction
AFC	$H_2 + 2OH^- \rightarrow 2H_2O + 2e^-$	$\leftarrow OH^-$	$1/2O_2 + H_2O + 2e^- \rightarrow 2OH^-$
PEMFC	$H_2 \rightarrow 2H^+ + 2e^-$	$H^+ \rightarrow$	$1/2O_2 + 2H^+ + 2e^- \rightarrow H_2O$
PAFC	$H_2 \rightarrow 2H^+ + 2e^-$	$H^+ \rightarrow$	$1/2O_2 + 2H^+ + 2e^- \rightarrow H_2O$
MCFC	$H_2 + CO_3^{2-} \rightarrow H_2O + CO_2 + 2e^-$ $CO + CO_3^{2-} \rightarrow 2CO_2 + 2e^-$	$\leftarrow CO_3^{2-}$	$1/2O_2 + CO_2 + 2e^- \rightarrow CO_3^{2-}$
SOFC	$H_2 + O^{2-} \rightarrow H_2O + 2e^-$ $CO + O^{2-} \rightarrow CO_2 + 2e^-$ $CH_4 + 4O^{2-} \rightarrow 2H_2O + CO_2 + 8e^-$	$\leftarrow O^{2-}$	$1/2O_2 + 2e^- \rightarrow O^{2-}$

Fuel cell systems

A complete fuel cell system consists, in general, of four main sections: fuel processing, fuel cell stack power generation, power conditioning, and heat recovery and/or power generation using integrated gas and steam turbines. Fuel processing is discussed in more detail in Section 1.3.4. The electrochemical power generation takes place in the individual stacks, which produce direct current. This is then converted to alternating current in the power conditioning section. The primary fuel energy not utilised for electric power production is available as waste heat and needs to be removed from the fuel cell. Heat removal from the stacks is generally accomplished by making use of the process gases, especially high oxidant flow (Joon, 1998).

To simplify the manufacture of single components and assembly of those components into a cell, fuel cells are generally constructed according to a flat plate design. An exception is the SOFC tubular design. Active areas can reach up to 1 m^2 for

PAFCs and MCFCs but are generally smaller for other fuel cell types. The combined thickness of electrodes and electrolytes rarely exceeds a few millimetres. The electrodes are electric conductors. These need to have high porosity to maximise the electrocatalytic surface area and enable the transport of process gases to and from the catalytic sites. As the electrochemical reactions take place at the interface between the electrode catalyst and the electrolyte, sufficient contact area has to be provided. The electrolyte, apart from being an electrical insulator and ionic conductor, acts as a gas barrier between the two electrodes. Operating fuel cells produce direct current with densities that can reach several A/cm^2. However, single cell voltages range only between 0.5 and 1 V, and so, for practical purposes, cells need to be connected in series. In a planar design, series connection can easily be accomplished by stacking individual cells with a bipolar plate in between. This plate provides the electrical contact between the anode of one cell and the cathode of the adjacent cell, while keeping their process gases separated. Dependent upon stack design, any flow configuration can be realised, i.e., co, counter, and cross flow in the anode and cathode compartments, respectively. However, they all have in common a lateral flow over the electrodes, resulting in depletion of reacting species and enrichment of reaction products towards the cell outlet. This creates a lateral current density, voltage, and temperature gradient. The latter may be as high as 100 °C in high temperature cells and needs to be kept within certain limits by adequate cooling (Joon, 1998).

Applications

Due to the various fuel cell advantages presented in Section 1.3.2, fuel cell applications include stationary, portable power, or transportation utilisation (Cacciola et al., 2001). Within the stationary electricity production market, possible fuel cell applications can be categorised as small power plants for residential or domestic use (less than 10 kW), medium/large power plants for electricity production and co-generation for buildings, and for industrial and commercial use (from 10 to 300 kW) and large power plants (up to 20 MW). The AFC has already been used extensively in space technology and for some special military applications like submarines. PEMFCs have recently attracted significant attention as a potential source of power in transportation applications and many of the major car manufacturers have embarked on

dedicated fuel cell car development programmes. PAFC stacks have been used in the initial commercialisation of stationary fuel cell systems. These have been under development for about 30 years and are considered the most mature type of fuel cells. However, a serious problem for their commercialisation is still their high cost.

1.3.3.1 Solid Oxide Fuel Cells

A solid oxide fuel cell consists of two porous ceramic electrodes, the anode and cathode, separated by a solid ceramic electrolyte. Typical SOFC materials are stabilised zirconia for the electrolyte, nickel/zirconia cermet for the anode, and doped lanthanum manganite for the cathode (Yamamoto, 2000; Badwal and Foger, 1996). It operates at high temperatures (700-1100 °C) and atmospheric or elevated pressures, and can use hydrogen, carbon monoxide, and hydrocarbons as fuel and air (or oxygen) as oxidant. In this cell, the oxygen ions formed at the cathode migrate through the ion-conducting solid ceramic electrolyte to the anode/electrolyte interface where they react with the hydrogen and carbon monoxide contained in (and/or produced by) the fuel, producing water and carbon dioxide while releasing electrons that flow back to the cathode/electrolyte interface via an external circuit (Ferguson et al., 1996). An oxygen concentration gradient is formed by burning oxygen with fuel on the anode side, while leaving the cathode side exposed to abundant atmospheric oxygen. The driving force of the operation is then the chemical potential gradient of oxygen across the electrolyte (Guo et al., 1999). Figure 1.1 illustrates a general scheme of a SOFC, where both the hydrogen and carbon monoxide electrochemical reactions are presented.

The attractiveness of a solid oxide fuel cell relates principally to its solid state nature and its high operating temperature. The solid electrolyte eliminates problems of electrolyte containment and migration, and allows for designs that utilise the electrolyte as part of the structural members of the cells. The solid state character of all SOFC components means that, in principle, there is no restriction on the cell configuration. The high operating temperature allows for internal reforming of gaseous fuel within the cells (see Section 1.3.4), promotes rapid kinetics with non-precious materials, and produces high quality heat for energy conversion or other uses. However, it also places rigorous requirements on its ceramic materials, such as stability in oxidising and/or

reducing environments, chemical compatibility with the various ceramics employed, thermal expansion compatibility of the various components over a large temperature range, and adequate electronic and ionic conductivity (Lee et al., 1990). The SOFC appears to be one of the most promising of the fuel cell systems and an ideal device for small-scale stationary application. Recently, energy and useful compounds cogeneration in SOFCs is getting increased attention (Badwal and Foger, 1996). This can be achieved, for example, by partial oxidation of methane to syngas (Ishihara et al., 1999) or selective oxidation of methane to ethene, ethane, and carbon monoxide (Tagawa et al., 1999).

SOFC stack designs

As previously mentioned, in order to achieve workable power outputs, single cells need to be combined in multi-cell units or stacks. Numerous SOFC designs have been developed throughout the years; Figure 1.2 illustrates some of them. These designs can be classified into self-supporting, where the electrolyte (80-250 μm in thickness) forms a structural element of the design, and supported concepts, where the electrolyte is deposited as a thin layer (<50 μm) on porous support structures. The Westinghouse tubular stack design is so far the most advanced SOFC concept. This belongs to the class of supported concepts as the cathode, electrolyte, and anode layers are successively deposited on the outside of a porous zirconia support tube (see Figure 1.2a). In this design the oxidant is injected through a co-axial ceramic injector tube near to the closed end of the cell and flows through the space between the cell and the injector tube to the open end of the cell. Fuel flows co-currently to the oxidant on the outside of that tube. The major advantages of tubular concepts are: no high temperature seals between the cathode and anode compartments are required and stage injection of feed and oxidant is possible. Disadvantages include lower power densities compared to other designs and expensive fabrication methods.

Currently, the most widely investigated concept and the cheapest SOFC unit is the planar or flat plate design. In this concept, the components are fabricated individually and then stacked together and sealed. As referred above, series connection can easily be accomplished by stacking individual cells with a bipolar plate in between. This plate provides the electrical contact between the anode of one cell and the cathode of the adjacent cell, while keeping the process gases separated, resulting in lower ohmic

losses than in tubular arrangements. External and internal co-flow, counter-flow, and cross-flow (see Figure 1.2b) arrangements are possible. One of the major disadvantages of this planar design is the need for gas-tight sealing around the edge of the cell.

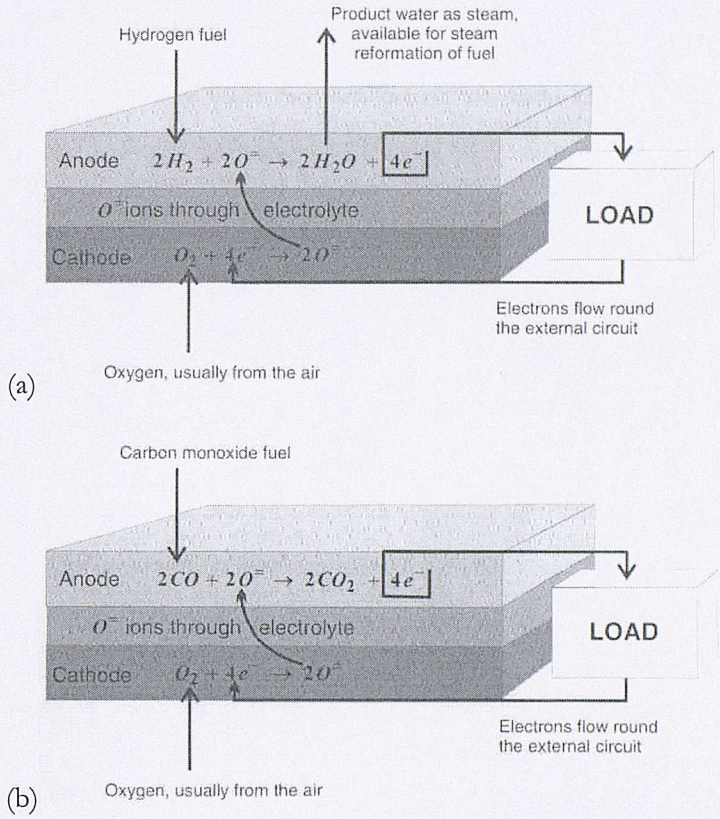

Figure 1.1 Generic representation of a solid oxide fuel cell illustrating the separate anode and cathode reactions when using hydrogen (a) and carbon monoxide (b) as fuel (Larminie and Dicks, 2000).

The monolithic design is the newest SOFC stack concept. This consists of many cells fabricated as a single unit and has the potential to achieve high power density because of its compact and lightweight structure. Counter-flow, co-flow, and cross-flow monolithic stack arrangements (see Figure 1.2c) are under consideration (Badwal and Foger, 1996).

One last possible design is the segmented-cell-in-series design, which consists of segmented cells connected in electrical and gas flow series. The cells are either arranged as a thin banded structure on a porous support (see Figure 1.2d) or fitted one into the other to form a tubular self-supporting structure. The interconnect provides sealing between the anode of one cell and the cathode of the next. In this design, the fuel flows

from one cell to the next inside the tubular stack of cells, and the oxidant flows outside. This stack design offers the advantage of improved stack efficiency.

More information on the science and technology of solid oxide fuel cells up to 1994 can be found in Minh and Takahashi (1995).

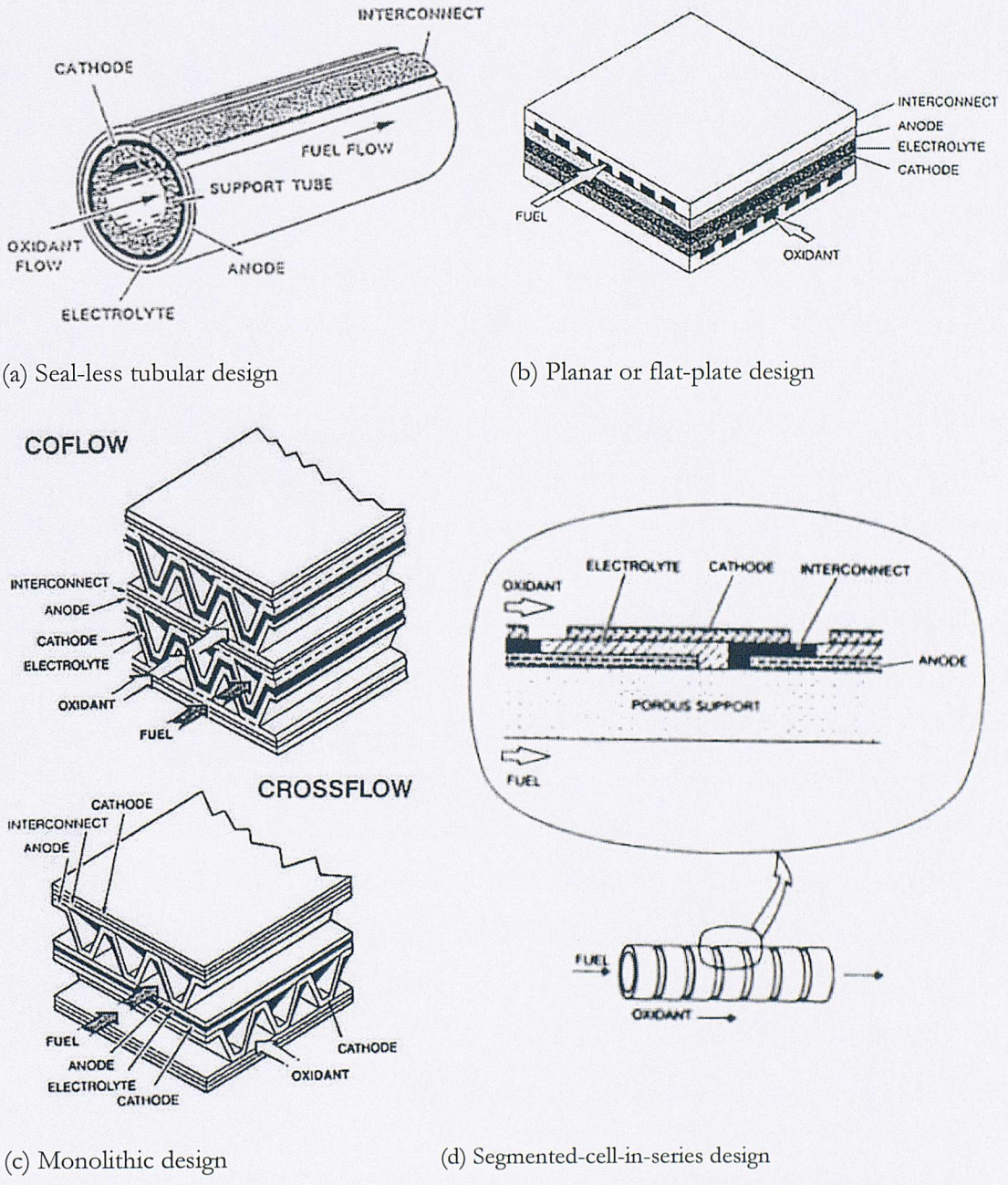

(a) Seal-less tubular design

(b) Planar or flat-plate design

(c) Monolithic design

(d) Segmented-cell-in-series design

Figure 1.2 Possible designs for solid oxide fuel cell stacks (Minh and Takahashi, 1995).

1.3.4 Fuel Processing & High Temperature Fuel Cells

The direct methanol fuel cell has a carbonaceous fuel (methanol) fed directly to the anode, while all other fuel cells need to convert the primary fuel into a hydrogen-rich gas required for the electrochemical reaction on the anode side. Hydrogen can be obtained from various sources, like natural gas, coal-gas, methanol, landfill gas, and other low-molecular-weight liquid fuels containing hydrocarbons. Therefore, power generation can always be assured. Of all the potential sources of hydrogen, natural gas offers many advantages as it is widely available, clean, and can be converted to hydrogen relatively easily (Dicks, 1996). One option is to convert the hydrocarbon feed indirectly in a fuel processing system, such as an external catalytic steam reformer or partial oxidation reactor (Dicks, 1996, 1998; Finnerty et al., 2000). In the case of a reformer, heat needs to be available to drive the steam reforming reaction (1.I). One method of achieving this is, for example, to feed the exhaust gases from the anode and cathode into a burner where the excess fuel from the anode is combusted. The heat generated in the burner can then be used to preheat both the steam and the fuel and provide the heat needed in the reformer. A more elegant and efficient method of providing heat for reforming in fuel cell systems is to carry out the reforming in the cell stack, as is discussed later (Clarke et al., 1997; Rostrup-Nielsen and Christiansen, 1995). In the case of a partial oxidation reactor, it should be noted that less hydrogen is produced per mole of methane through the partial oxidation reaction (1.II) than through the steam reforming reaction (1.I). Therefore, fuel cell systems employing partial oxidation generally have lower electrical generation efficiencies than those employing steam reforming. However, for certain applications, the lower efficiency may be offset by other advantages, such as compactness, rapid start-up and response to load change, and cost. The possibility of using methane or natural gas directly as the fuel to be electrochemically oxidised on the anode would be another option. The complete oxidation of methane to CO_2 and H_2O is a highly exothermic reaction with a very small entropy change. Thus, the efficiency of this process would be close to 100%. Several anode materials have been studied since the 1960s, however, none of them have so far proved to be effective enough to make such fuel cells viable power generators (Park et al., 2000; Finnerty et al., 2000; Clarke et al., 1997; Dicks, 1996).

$$CH_4 + H_2O \leftrightarrow 3H_2 + CO \quad (1.I)$$

$$CH_4 + 1/2\,O_2 \leftrightarrow CO + 2H_2 \quad (1.II)$$

Catalytic steam reforming of hydrocarbons is then an attractive method of producing the hydrogen required by fuel cells. This process is typically performed between 750 and 900 °C and is thus compatible with high temperature fuel cells such as molten carbonate and solid oxide fuel cells. These cells operate at high enough temperatures for the endothermic steam reforming reaction to be carried out within the stack, giving rise to an internal reforming fuel cell. The heat released in a fuel cell can provide the heat for the reforming reaction which, depending on the operating conditions, can vary from 40 to 70% of the total heat produced. Thus, internal reforming fuel cells eliminate the requirement for a separate fuel reformer and are then expected to simplify the overall system design, making the entire system a more attractive and efficient mean of producing electrical power. In addition, the requirement for cell cooling, which is usually achieved by flowing excess air through the cathode, is also significantly reduced (Nakagawa et al., 2001; Lee et al., 1990).

Various MCFC and SOFC internal reforming concepts have been developed (Dicks, 1998). There are two main approaches to internal reforming within a high temperature fuel cell: indirect or integrated (IIR) and direct (DIR) internal reforming. Figure 1.3 illustrates these two internal reforming approaches. In the first approach, the reformer section is separate but adjacent to the fuel cell anode and in close thermal contact with it. In the latter approach, methane is fed directly into the cell and the reforming takes place directly on the anode (Clarke et al., 1997). One advantage of IIR is that the reformer and cell environments do not have a direct physical effect on each other, however, the conversion of methane to hydrogen is not promoted to the same extent as with direct internal reforming. For a DIR configuration, part of the steam required for the reforming reaction can be obtained from the fuel cell electrochemical oxidation of hydrogen, and, because of the continuing consumption of hydrogen, the equilibrium of the reforming reaction may be further shifted to the right, increasing the conversion of methane (Ahmed and Foger, 2000; Joon, 1996) and leading to a more evenly distributed load of hydrogen. This may also result in a more uniform temperature

distribution. However, the DIR approach requires an anode material that possesses good catalytic properties for steam reforming as well as for effective generation of power (Lee et al., 1990). For the MCFC, the conventional anodes have insufficient activity to catalyse a reforming reaction, and so, reforming can only be achieved with the addition of a separate catalyst. However, degradation of the steam reforming catalyst caused by poisoning due to alkali from the electrolyte in a DIR-MCFC may severely limit catalyst lifetime. Dicks (1998) provides a review on the recent advances in catalyst formulation for DIR-MCFCs and on the development of porous shields to protect the catalyst. In the case of a SOFC, the reforming may occur internally. It has been shown that the state-of-the-art SOFC nickel cermet anodes can provide sufficient activity for the steam reforming and shift reactions without the need for any additional catalyst (Dicks, 1998; Clarke et al., 1997). Ni/ZrO_2 has been adopted by most SOFC groups since it is excellent for the oxidation of hydrogen and has a good match of properties with the ZrO_2 electrolyte. Ni provides its electronic conductivity and YSZ its ionic conductivity (Park et al., 2000).

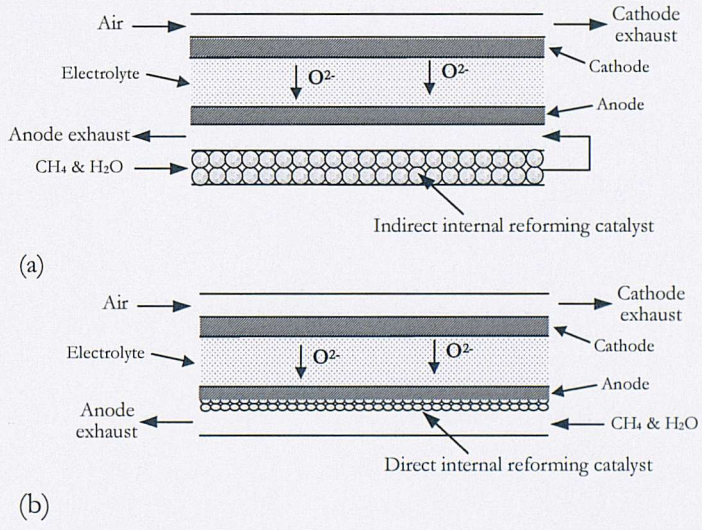

Figure 1.3 Schematic diagram of an indirect internal reforming (a) and a direct internal reforming (b) solid oxide fuel cell system.

A problem related to direct internal reforming is the carbon deposition on the anode, under such a carbon-rich reaction environment and high operating temperature, and the subsequent electrocatalyst deactivation leading to loss of cell performance and poor durability. Carbon formation on nickel-based electrodes can either encapsulate

active surfaces, reducing fuel conversion and hydrogen production, or form filaments, which force the Ni away from the YSZ support, destroying current pathways and limiting performance. The addition of molybdenum and cerium metal oxides to Ni-based catalysts has been observed to reduce carbon deposition, and in some cases, to increase fuel conversion (Finnerty et al., 1998, 2000; Park et al., 2000). The high steam/carbon ratios typically used in conventional steam reformers to suppress carbon formation is unattractive as it lowers the electrical efficiency of the fuel cell by steam dilution of the fuel (Park et al., 2000). Hence, advanced anode materials that allow for direct internal reforming at low steam/carbon ratios could offer significant benefits.

A second problem is the strong cooling effect caused by the highly endothermic reforming reaction that can generate large temperature gradients across the cell and limit the amount of internal reforming allowed in practice. In fact, it has been shown that in DIR cells, all the methane is usually completely reformed within a small distance from the anode entrance (Fellows, 1998; Meusinger et al., 1998; Achenbach and Riensche, 1994). To solve this, Cavallaro and Freni (1998) proposed an internal autothermal reforming (ATR) MCFC system, operating both as a direct or an indirect configuration. This ATR system consists of the combination of the exothermic methane partial oxidation reaction with the endothermic steam reforming so that the overall process becomes almost isothermal and suitable for combination with a MCFC. In the same line of thought, other recently studied possible MCFC designs, in the search for less endothermic reactions or combined reactions related to that of direct methane steam reforming, involve, for instance, methane, ethanol, and methanol indirect internal steam reforming (Maggio et al., 1998; Cavallaro et al., 2001). These studies are in agreement with the wide need for energy sources diversification, traditionally based on the use of fossil hydrocarbons, while alternative fuels like alcohols can be directly produced by biomass fermentation or synthesis processes. However, different raw fuels produce substantial differences. Maggio et al. (1998) performed a theoretical study on the use of ethanol, methanol, or methane as possible fuels, where the use of ethanol was more advantageous in terms of energy density, cell voltage, and electrical power density. The use of ethanol as an alternative fuel for SOFC systems has also been thermodynamically studied (Tsiakaras and Demin, 2001). Shinoki et al. (1995) presented a very interesting paper comparing two cross-flow stack configurations: the normally defined direct

internal reforming MCFC and an advanced internal reforming (AIR) one, which is nothing else but the combination of the direct and indirect IR concepts. This AIR configuration contains two reforming sections, one in the flow path before the anode and the other on the anode itself. They reported an improvement in the heat balance between the endothermic steam reforming and the exothermic electrochemical reactions that led to better temperature distribution and higher stack performance for the AIR configuration. In addition, and in order to achieve better cell cooling, the catalyst load distribution was adjusted in order to match the thermal requirements of the two reactions involved. As is seen later, this AIR has a lot of similarities with the system under study here.

For SOFCs, for instance, possible approaches to reduce the local cooling problems are partial external pre-reforming of natural gas (Meusinger et al., 1998) and reduction of the rate of reforming on the anode, usually achieved by partially poisoning the active sites. The pre-reforming is also desirable to remove high molecular weight hydrocarbons from the fuel gas, which would otherwise crack to produce carbon. However, with either one of the above approaches, some of the advantages of full internal reforming of methane are sacrificed. These, together with alternative anode materials, need to be optimised (Ahmed and Foger, 2000; Dicks, 1998; Clarke et al., 1997). Alternative configurations of DIR MCFC and SOFC stacks have been proposed in order to reduce the endothermic effect in DIR stacks (Fellows, 1998). Finally, it is worth noting that in an internal reforming fuel cell, although the reforming and electrochemical reactions may be synergistic, integration of the two processes may reduce the flexibility of operation of the fuel cell. This is likely to be more of a problem with DIR compared with IIR (Clarke et al., 1997).

1.3.4.1 Internal Reforming Fuel Cell System

An alternative to the DIR is then the indirect internal reforming configuration, where the catalysts for the reforming and electrochemical reactions can be designed separately. The main focus of this thesis is in an indirect internal steam reforming solid oxide fuel cell system (IIR-SOFC). Although this method can be regarded as a desirable way of processing methane or natural gas fuel for the fuel cell, several technical problems still

need to be faced in realising this SOFC concept in practice. A possible IIR-SOFC configuration and the one studied in the present work is schematically illustrated in Figure 1.4. In this tubular design the fuel cell is constructed around a steam reforming reactor. The fuel stream first flows along this central inner reformer before reversing at the closed end of the outer reactor to flow along the cell anodes. The endothermic steam reforming reaction occurs in the reformer, while the outlet stream is subjected to the exothermic electrochemical oxidation reactions in the anode. Heat transfer between the inner and outer reactors is then expected to provide the required autothermal operation. The electrolyte and cathode layers are deposited over the anode and, on the outer side, the air is fed to the cathode. The air flow can either be co- or counter-flow to the fuel flow in the anode, which implies that it will then be counter- or co-flow to the fuel flow in the inner reformer.

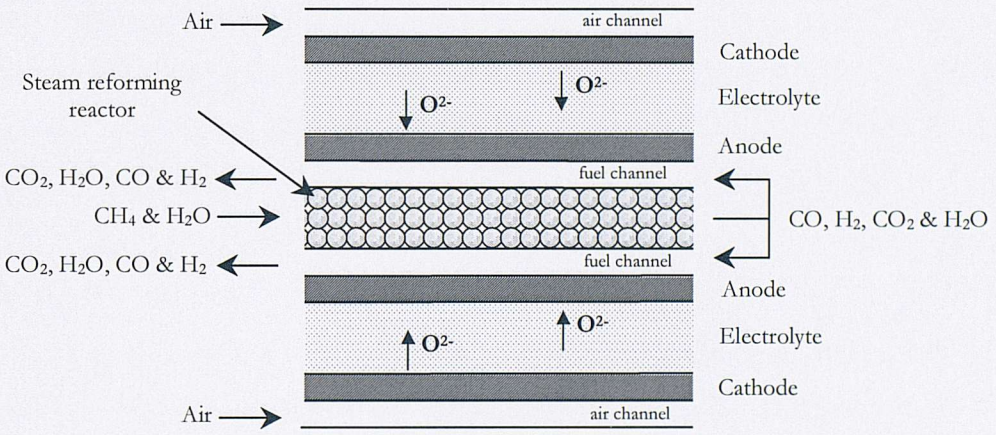

Figure 1.4 Schematic diagram of a solid oxide fuel cell with an indirect internal reformer.

Other possible IIR configurations have been proposed throughout the years either in combination with MCFC or SOFC systems. A possible IIR planar arrangement alternates the plate reformers with small cell packages, so that the reformate from each cell is fed to neighbouring cells. One other possibility is the one where the reforming catalyst is placed in the gas distribution path of each cell. Rostrup-Nielsen and Christiansen (1995) studied this phenomenon applied to the internal reforming in a molten carbonate fuel cell stack, stating that it can be carried out either as anode chamber reforming or as stack heat integrated reforming in the cooling channels of the

stack. Finally, another fuel cell concept, based on indirect internal reforming and developed by Rolls Royce (UK), is the integrated planar SOFC (Gardner et al., 2000). In this design, as in the system under study in this thesis, the fuel stream first flows along a central inner reactor before reversing at the closed end of the outer reactor to flow along the cell anodes.

1.4 Research Objectives

One of the main challenges associated with an indirect internal reforming fuel cell configuration is the mismatch between the thermal load associated with the rate of steam reforming at typical SOFC temperatures and the local amount of heat available from the fuel cell reactions. This is attributed to the specific reaction conditions, under which the inherent kinetics of the reforming reactions are extremely rapid and, although usually limited by mass and heat transfer considerations, are still orders of magnitude higher than the corresponding fuel cell electrochemical reactions (as will be seen later). Under these conditions, significant local cooling can occur, leading to thermally induced fractures of the ceramic components. To eliminate such effect it is required to reduce the rate of the reforming reactions and the corresponding local energy flux demand. However, the steam reforming catalyst needs to provide sufficient activity for the lifetime of the stack so that the rate of the reforming reaction is matched to the rate of the electrochemical reactions. On this basis, application of an appropriate reforming catalyst activity is essential to ensure that the temperature variations are kept to a minimum, to reduce thermal stresses and thereby contribute towards a long stack life.

Mathematical modelling is an integral and cost-effective tool for the design of solid oxide fuel cells. It can be utilised for performance prediction under specific operating conditions and for various cell configurations. It can also provide information on the effect and relative importance of the multiple variables and parameters and on their behaviour as functions of position and time. The information provided by such models is generally an initial step towards the optimisation of cell design and operating conditions. It has become evident that internal reforming of methane is also a crucial point to be considered when modelling such systems since the cooling effect of the endothermic reforming reaction strongly affects the operating conditions of the stack.

On this basis, the main objective of the present research project has been to model the indirect internal reforming solid oxide fuel cell configuration illustrated in Figure 1.4. The developed model enables the simultaneous occurrence and efficient thermal coupling of both the steam reforming and the fuel cell electrochemical oxidation reactions, for which a method must be devised that properly reduces the rate of the reforming reaction at SOFC operating conditions.

1.5 Thesis Outline

The next six chapters are intended to present the developed models, solutions proposed to achieve the research objectives, results obtained and main conclusions withdrawn. To model an IIR-SOFC system, two models are required: a solid oxide fuel cell model and a steam reforming reactor model. These are presented in two separate chapters. Chapter 2 commences with a review of the general fuel cell operation principles and relationship between the relevant electrochemical variables and proceeds with the development of the solid oxide fuel model. Chapter 3 gives a brief introduction to the steam reforming process, including common catalysts and rate kinetic expressions derived, and then continues with the development of the catalytic fixed-bed tubular reformer model. Chapter 4 presents the main results obtained with the developed coupled model, where the local cooling effect caused by the strongly endothermic reforming reactions is demonstrated, and the improved performance results, with the corresponding solution methods, are discussed. Chapters 5 and 6 address alternative solution methods. Chapter 5 discusses the determination of optimal catalyst particle distributions that are intended to reduce the rate of the reforming reactions (but still have them relatively insensitive to deactivation by coking) and Chapter 6 refers to a second steam reforming reactor configuration – a coated-wall reactor. In Chapter 6, a dynamic model of the coated-wall IIR-SOFC system is also developed and the obtained results presented. In chapter 7, the main conclusions are summarised and possible future research fronts are proposed.

Chapter 2

General Fuel Cell Principles & Solid Oxide Fuel Cell Modelling

Summary

Mathematical modelling is an essential tool for the design of solid oxide or any other type of fuel cell. This second chapter first explains the general electrochemical and thermodynamic principles common to all types of fuel cells, including the derivation of the Nernst equation for the open-circuit potential, the relation between cell potential and current withdrawn, and the phenomena that can lead to potential losses in an operating fuel cell. The terms fuel utilisation factor, air ratio, and fuel cell efficiency that determine the operating conditions and output performance of a fuel cell are also here introduced. A literature review on high temperature fuel cells is presented. In the third part of this chapter the above explained theory is applied to the solid oxide fuel cell system under study and the system model is derived. The developed model consists of mass and energy balances and of the electrochemical model that relates gas composition and temperature with potential, current density, power, and other cell variables.

Outline

2.1 Introduction

As with any chemical engineering system, mathematical modelling is an essential tool for the design of solid oxide or any other type of fuel cell, as it is important to know the response of a cell stack under normal or transient operating conditions. Such models can provide a picture of cell stress, potential, current density, and temperature as functions of position and time and for various cell configurations and operating conditions. These can also be used to examine the effects of changes on one or more variables or the relative system sensitivity to the most important design and uncertain parameters. In the design phase, a model can be useful in determining the required size of the stack and in making design decisions regarding structure-specific parameters, such as the anode, electrolyte, cathode, and interconnect layers thickness and the dimensions of the fuel and oxidant gas channels. In a later stage, a model can still be helpful to the fuel cell system operator in determining, for a particular stack, the most favourable operating conditions, by calculating a priori the effects of altering process variables, such as power demand, flow rates, and feed conditions, and in using the information provided by such models to optimise cell design and operating parameters (Ahmed et al., 1991; Minh and Takahashi, 1995).

However, in order to mathematically understand fuel cells, knowledge of the thermodynamic principles and ruling laws that relate the fuel and oxidant gas stream composition and temperature with the voltage or potential, current density, and other fuel cell variables, is first required. The aim of this chapter is first to explain those principles and then to derive the mathematical model of the particular fuel cell system under study. The information presented in this chapter and in Chapter 1, Sections 1.3 and 1.4, is intended to be complementary, although some repetition might sometimes occur. Section 2.2 is supposed to be general to all fuel cell devices, although all the examples given are for the particular case of a solid oxide fuel cell fuelled with hydrogen. Main references used when writing this section were Minh and Takahashi (1995), Kordesch and Simader (1996), and Larminie and Dicks (2000), unless otherwise stated. Section 2.3 presents a literature review in fuel cells modelling and Section 2.4 the developed SOFC model.

2.2 General Fuel Cell Principles

As described in Chapter 1, a fuel cell is an electrochemical device that converts the chemical energy of a fuel gas and an oxidant gas directly to electrical energy and heat without combustion as an intermediate step. The operating principles of a fuel cell are similar to those of a battery as both involve the electrochemical combination of reactants to generate electricity. In fuel cells, two separate electrochemical reactions occur, the overall reaction being the same as that of combustion. For example, for a hydrogen fuel and oxygen oxidant, the electrochemical reactions consist of the H_2 oxidation at the anode (2.I) and of the O_2 reduction at the cathode (2.II). The overall reaction in this case, like combustion, yields water as the reaction product (2.III).

Anode reaction	$H_2 + O^{2-} \rightarrow H_2O + 2e^-$	(2.I)
Cathode reaction	$1/2\,O_2 + 2e^- \rightarrow O^{2-}$	(2.II)
Overall reaction	$H_2 + 1/2\,O_2 \rightarrow H_2O$	(2.III)

In the specific operation of a SOFC, for example, fuel is fed to the anode, where it is oxidised and electrons are released to the external circuit. Oxidant is fed to the cathode, where it accepts the electrons from the external circuit and is then reduced. The electron flow through the external circuit produces direct current electricity.

2.2.1 Nernst Equation & Open-Circuit Potential

Because chemical engineers are, in general, not overly familiar with electrochemical systems, the relevant background will be presented here in some detail.

In a fuel cell, the electrical energy released results from the change in the Gibbs free energy, ΔG, caused by the above overall reaction (2.III). The free energy change of a certain chemical reaction is generally explained as a measure of the maximum work obtainable from that specific reaction*. In a fuel cell, the external work done involves

* Knowledge of the Gibbs free energy change is important. It indicates whether a reaction will occur or not. If ΔG is positive the forward reaction can not occur for the assumed composition of reactants and products. If ΔG is negative that reaction can occur.

moving the oxidation reaction released electrons round the external circuit. Thus, if there are no losses in the fuel cell (or if the process is reversible), all the Gibbs free energy is converted into electrical energy. This leads to the determination of the reversible or open-circuit potential of a fuel cell. For instance, in hydrogen fuelled fuel cells, two electrons pass round the external circuit for each water molecule produced and each hydrogen molecule used (see reaction 2.I in Section 2.2). Hence, for one mole of H_2 used, 2N electrons pass round the external circuit, where N stands for the Avagadro' number. If $-e$ is the electric charge of one electron, the charge that flows round the circuit is then $-2Ne = -2F$ Coulombs, where F is the Faraday's constant. On the other hand, if U is the potential of that fuel cell, then the electrical work done (or output power) moving this charge round the circuit is -2FU Joules*. If the system is reversible, the electrical work done is equal to the Gibbs free energy released and the fuel cell voltage is equal to the open-circuit voltage or potential. Thus,

$$\Delta G = -2FU^{OCP} \Leftrightarrow U^{OCP} = \frac{-\Delta G}{2F}. \tag{2.1}$$

This fundamental equation gives the theoretical reversible open-circuit voltage (OCV) or open-circuit potential (OCP) of a hydrogen fuel cell. The Gibbs free energy of a given reaction changes with pressure, temperature, gas composition, and state of the reactants. For the hydrogen oxidation reaction, and if the pressure of the reactants and products are in bar and the water product is in the form of steam, equation (2.2) expresses such relation.

$$\Delta G = \Delta G^0 + \Re T \ln\left(\frac{p_{H_2O,f}}{p_{H_2,f} p_{O_2,a}^{1/2}}\right)^{\dagger} \tag{2.2}$$

ΔG^0 in equation (2.2) stands for the Gibbs free energy change for standard temperature and pressure and pure reactants for the H_2 oxidation reaction. By combining equations (2.1) and (2.2), both the open-circuit potential Nernst equation

* In electrical applications, power is generally defined as the product between cell voltage and current.

† The subscripts f and a used stand for fuel channel or anode and air channel or cathode, respectively. This notation is meant to be compatible with the one to be used in Section 2.4.

(2.3) and the relation (2.4) for the open-circuit potential for standard temperature and pressure and pure reactants for the H_2 oxidation reaction, U^0, are obtained.

$$U^{OCP} = U^0 - \frac{\Re T}{2F} \ln\left(\frac{p_{H_2O,f}}{p_{H_2,f} p_{O_2,a}^{1/2}} \right) \tag{2.3}$$

$$U^0 = \frac{-\Delta G^0}{2F} * \tag{2.4}$$

Hence, in order to calculate the value of U^0, knowledge of ΔG^0 is required. This can be obtained from the thermodynamic relation

$$\Delta G = \Delta H - T\Delta S \Rightarrow \Delta G^0 = \Delta H^0 - T\Delta S^0, \tag{2.5}$$

where ΔH and ΔS represent, respectively, the enthalpy and entropy change of the overall reaction taking place.

As can be seen from equation (2.3), the open-circuit potential is a local quantity, as it depends on the gas composition and temperature at the cathode and anode. It can be seen that, if the partial pressure of hydrogen falls as the gas mixture passes through the cell, the OCP drops. Also contributing for the potential drop are the oxygen utilisation from the air and the fact that the hydrogen is essentially replaced by steam. From the Nernst equation (2.3) one can see that both the decrease on the oxygen partial pressure and the increase on the steam partial pressure as the hydrogen reacts, cause the OCP to decrease. An issue with high temperature fuel cells, as are SOFCs, is the RT term in the mentioned equation, which means that the OCP drop is greater for this type of cells, as will be seen in the next section.

2.2.2 Operating Fuel Cell Potential & Potential Losses

The theoretical open-circuit voltage given by equation (2.3) is the maximum voltage that can be achieved by a fuel cell under specific operating conditions. However, the voltage

---

* For a process in equilibrium and at constant temperature and pressure, $\Delta G = 0$. So, from eq. (2.2) $\Delta G^0 = -\Re T \ln K_{eq} \Rightarrow U^0 = \frac{\Re T}{2F} \ln K_{eq}$. Note that, initially, no water is normally present and, therefore, according to equation (2.3), the initial open-circuit is infinite, at least theoretically.

of an operating cell, U, equal to the voltage difference between the cathode and the anode, is generally lower than this, often considerably lower. As the current is drawn from a fuel cell, the cell voltage falls due to various losses. This reduction in a cell voltage depends on the current density and on several other factors such as temperature, pressure, gas flow rate and composition, and cell material. This is a common characteristic of all types of fuel cells. Figure 2.1 illustrates the regions in which various types of voltage losses predominate.

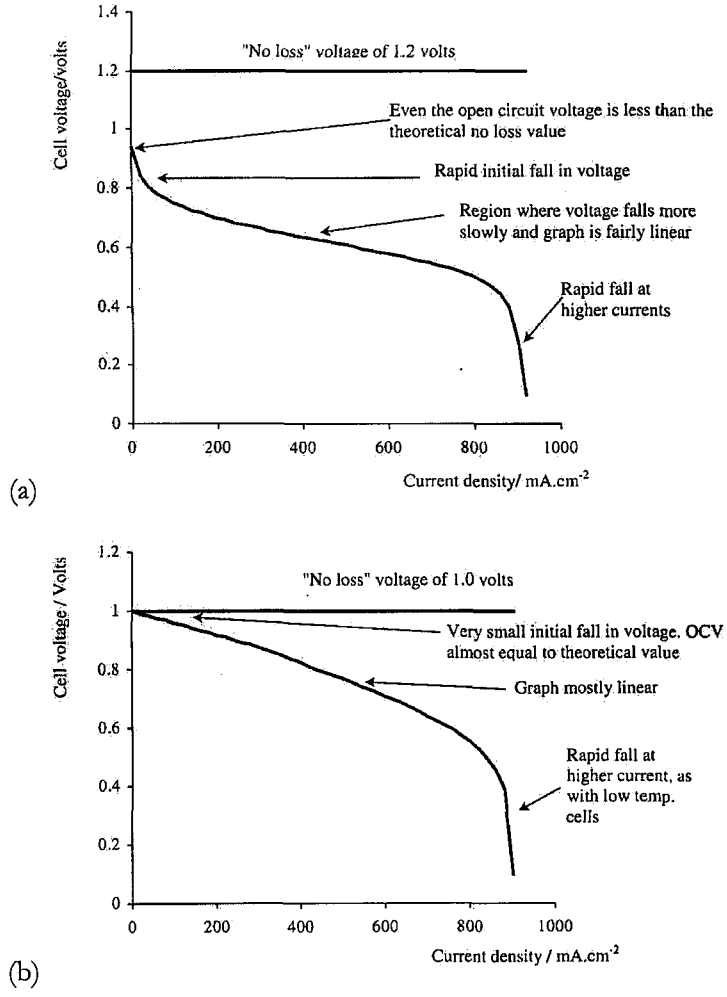

Figure 2.1 Voltage/current density graph for a typical air pressure (a) low temperature (about 40°C) and (b) high temperature (about 800°C) fuel cell (Larminie and Dicks, 2000).

Figure 2.1a shows a typical voltage/current density graph for a single fuel cell operating at about 40°C and normal pressure. The graph shows that, in practice, even the OCP (voltage value when there is no current being drawn) is lower than the

theoretical reversible voltage value. The shape of the graph indicates that: initially, and for low current density values, the voltage drops significantly; the voltage then falls more slowly and linearly; and finally, for higher current density values, the voltage drops again very rapidly. These are the main observations from a low temperature fuel cell voltage/current density graph. However, if the fuel cell is operated at high temperature, the shape of such curve changes considerably, as seen in Figure 2.1b for a typical SOFC operating at about 800°C. As a first observation one can notice that the open-circuit potential is lower for a high temperature fuel cell, as this quantity decreases with temperature (see Section 2.2.1), and is very close to its theoretical value. Also, the initial voltage drop for low current density values is markedly lower than for low temperature fuel cells and the graph is much more linear. For higher current density values, the voltage drops very rapidly as with low temperature cells. Comparing both graphs it can be seen that, although the reversible voltage is lower for a high temperature fuel cell, the operating voltage of these cells is generally higher as the voltage losses are much smaller.

The characteristic shape of the voltage/current density graphs in Figure 2.1 shows that, as the current is drawn from a fuel cell, the voltage falls. This is due to internal resistances or ohmic losses and to anode and cathode polarisation losses. The voltage or potential of an operating cell is thus generically given by equation (2.6). This equation can be derived from Kirchoff's and Ohm's laws by considering a cell as many small elements in series, and each one of those elements as a local battery with its own internal resistance.

$$U = U^{OCP} - jR_{OHM} - (\eta_A + \eta_C)^* \tag{2.6}$$

In the above equation, jR_{OHM} stands for the internal resistance or ohmic loss (j is the current density and R_{OHM} the internal resistance of the fuel cell, which includes electronic, ionic, and contact resistance), and η_A and η_C for the anode and cathode polarisation or overpotential, respectively. In Section 2.2.3, it is seen that these internal and polarisation losses are in part responsible for the heat produced in an operating fuel cell.

---

* η_C is here taken as a positive quantity.

Ohmic losses are caused by resistance to conduction of ions (through the electrolyte) and electrons (through the electrodes and current collectors) and by contact resistance between cell components. This voltage drop is important in all types of cells and is essentially linear and proportional to current density. R_{OHM} can be obtained from measured cell resistances or be estimated from the effective distance between the components. Ways of reducing the internal resistance of a cell include: use of electrodes and electrolytes with the highest possible conductivity; use of appropriate materials for the bipolar plates or cell interconnects; and fabrication of electrolytes as thin as possible.

Anode and cathode polarisation or overpotential losses are associated with the electrochemical reactions taking place at the electrode/electrolyte interfaces and can be categorised in activation or charge transfer and concentration or mass transport overpotentials. These can not be eliminated, although temperature, pressure, electrolyte composition, electrode material, and cell design can naturally influence their magnitude.

Activation or charge transfer overpotentials can be explained in several ways. Some references state that these arise from charge transfer resistance of the electrochemical reactions at the anode and cathode, and others that these are caused by the slowness of the reactions taking place on the surface of the electrodes. An easier to understand explanation is that, as in any chemical reaction, in electrochemical reactions an energy barrier must be overcome by the reaction species. This energy barrier, called the activation energy, results in the activation polarisation. This may then be regarded as the extra potential necessary to reduce the energy barrier of the rate-determining step of the reaction to a value such that the electrode reaction proceeds at a desired rate. Activation polarisation is generally due to one or more slow rate-determining steps in the electrode reaction. The slow step can be related to adsorption of reactant onto the surface of the electrode, electron transfer, desorption of product, or any other step. The electrode reaction rate is a function of the temperature, pressure, and electrode material. At high temperatures, as in the case of SOFCs, reaction rate is rapid, and as a result, activation polarisation is usually small. For low and medium temperature fuel cells, activation overpotentials occur mainly at the cathode and are the most significant cause of voltage drop. Ways of reducing the activation overpotentials are: increasing

temperature and pressure; using more effective catalysts; and increasing reactant concentration, e.g. using pure oxygen instead of air. The last two points explain the discrepancy between theoretical OCV and actual OCV observed in Figure 2.1, since both of them affect the catalyst site occupancy not taken into account in the Nernst equation. Finally, this overpotential is often given by the non-linear Butler-Volmer equation. For high overpotentials this is often simplified and the Tafel equation, that gives the overpotential as a function of the current logarithm, is obtained (Minh and Takahashi, 1995). More information on the possible approximations of the Butler-Volmer equation for activation overpotentials can be found in Appendix A.1. In terms of the voltage/current density graphs, as the activation polarisation predominates under low current density values, it is responsible for the initial voltage fall.

Concentration, mass transport, or diffusion overpotentials appear when the electrode reaction is hindered by mass transport effects, i.e., when the feeding velocity of the reactant and/or the removing velocity of the product from the electrode is slower than that corresponding to the discharged current. Concentration polarisation is dependent on the mass transport properties of the system, that are in turn a function of the temperature, pressure, concentration, and physical properties. In SOFCs, for example, the reactants must diffuse through the porous anode and cathode and so the electrode structure is important. Since the electrode reaction rate is a function of concentration of the reactant gases, concentration polarisation becomes more severe as the degree of conversion increases. In terms of the voltage/current density graphs, the concentration polarisation is responsible for the voltage drop observed for high current density values.

Another type of voltage loss, not included in the above equation but worth mentioning, is due to fuel crossover and internal currents. This energy loss results from the wasted fuel that passes through the electrolyte and, to a lesser extent, electron conduction through the electrolyte. It is know that the electrolyte should only transport ions through the cell, however, a certain amount of fuel diffusion and electron flow is possible. These are small and their effect usually not very important, although it has a marked effect on the OCP of low temperature cells.

2.2.3 Faraday's Law, Power & Heat Produced in a Fuel Cell

In Section 2.2.1, it has been shown how the open-circuit potential is related to the Gibbs free energy change of the electrochemical reaction taking place in a cell, and how this quantity is related, through the Nernst equation, to the pressure, temperature, gas composition, and reactants state. In Section 2.2.2, the relation between operating potential, open-circuit potential, and the various potential losses in a cell has been derived. Thus, it is now known what is the dependence of the electrochemical variables on the gas streams properties. However, the dependence of the gas streams properties on the electrochemical variables has not been determined yet.

Faraday's law relates the flux of reactants and products to the electric current drawn by an electrochemical reaction. According to this law, and when only H_2 oxidation is present, the local amount of H_2 and O_2 consumed and H_2O produced, is related to the local electric current density, j or j_{H_2}, produced in the cell through

$$R_{elect} = \frac{j}{2F} = \frac{j_{H_2}}{2F}, \tag{2.7}$$

where R_{elect} stands for the hydrogen oxidation reaction rate (mol/m^{2}s). This relation relies on the fact that solid electrolytes such as YSZ are pure ionic conductors, and so only oxygen ions can permeate through the electrolyte to take part on the oxidation reaction at the anode/electrolyte interface (Guo et al., 1999), and is utilised when deriving the mass and energy balances that compose a certain cell model.

As mentioned before, in addition to electric power, heat is also produced in a fuel cell. This heat production results from the inefficiency of the cell to convert all the Gibbs free energy change into electricity. The local heat produced (W/m^2) is given by

$$\text{Local heat produced per area} = (-\Delta H)_{elect} R_{elect} - P_{SOFC}. \tag{2.8}$$

where P_{SOFC} (W/m^2) stands for the local power density (per electrode active surface area) from a cell and $(-\Delta H)_{elect}$ for the enthalpy change of the reaction taking place. The product between the operating cell voltage and the local current density expresses the local power density, as shown by equation (2.9).

$$P_{SOFC} = jU \tag{2.9}$$

Equation (2.8) is nothing else but the difference between the enthalpy released by the exothermic electrochemical reactions and the local power density withdrawn from the cell. Combining equations (2.1) and (2.5-2.9) the following relation results:

$$\text{Local heat produced per area} = \frac{j}{2F} T(-\Delta S)_{elect} + j^2 R_{OHM} + j(\eta_A + \eta_C), \tag{2.10}$$

where $(-\Delta S)_{elect}$ stands for the entropy change. Thus, in a fuel cell, the local heat production is due to the entropy change of the electrochemical reactions and to the resistance to current flow and polarisation losses discussed in Section 2.2.2. Expression (2.8) is used in Section 2.4 for the derivation of the cell energy balances.

2.2.4 Fuel Cell Performance Factors

When referring to the operation of fuel cells, in addition to all geometry and property data and inlet temperatures and compositions, it is usual to specify the average current density (or total current) being drawn by the fuel cell, the fuel utilisation factor, and the air ratio. These three parameters are given quantities from which the molar flux of fuel and air are then determined. Other parameters that are useful in accessing the overall performance of the cell include the cell power and the fuel cell efficiency. It is then important to define fuel utilisation factor, air ratio, and fuel cell efficiency. The next three sections present the definition of these parameters.

2.2.4.1 Fuel Utilisation Factor

Fuel utilisation can represent a problem in fuel cell operation, as the hydrogen concentration and, consequently, the open-circuit and operating potentials decrease with an increase of this quantity. Potential drop in a fuel cell is a very important issue to consider as it is directly related to the power output and cell efficiency. Generally, a fuel cell can not be designed to consume all the hydrogen, some of it must simply pass straight through, although this is nearly always later recycled back to the cell. Feeding the air and fuel through the cell in opposite directions (counter-flow) can reduce the

total potential drop in a cell. This means that the part of the cell with the exiting fuel has at least the highest oxygen partial pressure and, therefore, the OCP cell drop due to fuel and air utilisation is spread more evenly through the cell (see Section 2.2.1).

By setting the fuel utilisation factor, the fraction of the total inlet fuel that is consumed in the cell is a priori defined. This factor, also known as current efficiency (but different from the fuel cell efficiency), is said to reflect the loss in efficiency caused if all the reactants are not converted to reaction products and, consequently, not used to produce electric energy. Generically, the definition of the fuel utilisation factor is similar to the concept of conversion in chemical reaction systems, i.e.:

$$U_{fuel} = \frac{\text{inlet fuel (mol/s)} - \text{outlet fuel (mol/s)}}{\text{inlet fuel (mol/s)}}. \tag{2.11}$$

For pure hydrogen fuelled fuel cells and taking Faraday's law into account (as an integrated quantity and not as a local one), the relation between the fuel utilisation factor, the total current density, $\bar{j}$, and the hydrogen fuel flow rate, $F_{H_2}^{mol}$, is obtained.

$$U_{fuel} = \frac{\bar{j}A_{Act}}{2FF_{H_2}^{mol}} \tag{2.12}$$

2.2.4.2 Air Ratio

The heat in a SOFC is normally removed with the flowing fuel and oxidant gases. However, as the fuel gas cannot carry enough heat out of the cell chamber, excess air is normally used as a coolant (Hirano et al., 1992). The air ratio reflects the excess air (more precisely, oxygen), in relation to that which is stoichiometrically needed, that is supplied to the cell for the purpose of cooling, and can be defined as:

$$\lambda = \frac{\text{oxygen supplied (mol/s)}}{\text{oxygen stoichiometrically needed (mol/s)}}. \tag{2.13}$$

Similarly to what was done in the previous section, the relation between the air ratio, the total current density, and the air flow rate, F_{air}^{mol}, is given by:

$$\lambda = \frac{4Fy_{O_2}F_{air}^{mol}}{\bar{j}A_{Act}}, \tag{2.14}$$

where y_{O_2} is the molar fraction of oxygen in the air stream.

2.2.4.3 Fuel Cell Efficiency

Direct conversion of fuel energy to electricity is the key characteristic of fuel cell operation. In a conventional thermal power system, the chemical energy of the fuel is transformed first to thermal energy, then to mechanical energy, and finally to electrical energy. Other energy conversion systems involve the conversion of chemical energy to thermal energy and then to electricity. However, the efficiency of the thermal-to-mechanical and thermal-to-electrical energy conversions is subject to the Carnot limitation. The Carnot efficiency limit of a combustion-type system operated between high temperature (T_h) and low temperature (T_l) heat sources is given as

$$\varepsilon = 1 - \frac{T_l}{T_h}, \tag{2.15}$$

where ε is the efficiency and T the temperature in Kelvins. To obtain a high value of ε, a T_h as high as possible and a T_l as low as possible are desirable. However, there is a practical limit on this efficiency due to high limits on T_h (temperature of material stability) and low limits on T_l (room temperature). The operation of a fuel cell is not Carnot limited.

A fuel cell converts chemical energy directly to electricity, and thus, can yield a higher efficiency than a combustion-type conversion system. Indeed, it is commonly supposed that if there are no losses during operation, the efficiency could be 100% and, if efficiency is defined in a particular way, this can be true. As mentioned before, it is the Gibbs free energy that is converted into electrical energy. So, if none of the losses discussed in Section 2.2.2 occur, all the Gibbs free energy would be converted into electrical energy and the efficiency could be said to be 100%. However, since the overall reaction in a fuel cell is the same as in a combustion process, a more common definition

of efficiency is to compare the electrical energy produced or cell power output with the heat that would be released by burning the same quantity of fuel. Thus,

$$\eta_{SOFC} = \frac{\text{power (W)}}{\text{total enthalpy of the inlet fuel (W)}}. \tag{2.16}$$

As is defined, the fuel efficiency represents the percent of the total chemical energy in the inlet fuel stream that is converted into electrical energy. Once again, and for a hydrogen fuelled fuel cell, the fuel cell efficiency is given by:

$$\eta_{SOFC} = \frac{\overline{P_{SOFC}}}{F_{H_2}^{mol}(-\Delta H)_{elect}}, \tag{2.17}$$

where $\overline{P_{SOFC}}$ is the power output (W) given by

$$\overline{P_{SOFC}} = \bar{j} U A_{Act}. \tag{2.18}$$

As seen above, in a fuel cell, the net chemical energy consumed is either converted to electrical energy (power) or to heat generation due to the entropy change of the electrochemical reactions, to resistance to current flow, and to losses by polarisation. Therefore, the total heat generated in the cell is directly proportional to the fuel consumed and to $(1-\eta_{SOFC})$.

The upper limit to the fuel cell efficiency just defined is obtained when the power in equation (2.17) is replaced by the maximum electrical energy available, i.e., the total Gibbs free energy change of the inlet fuel.

All the main features and vocabulary associated with fuel cells have now been introduced. The next section presents a literature review in fuel cells modelling. It first starts with the specific case of solid oxide fuels cells, as these are the main focus of this thesis, but it also contains some examples of the work performed in modelling the also high temperature molten carbonate fuel cells.

2.3 Literature Review in Fuel Cells Modelling

As is shown in this section, there have been in the past years several publications, at various levels of sophistication, focusing on modelling SOFC systems. Such models can

be for different geometries – tubular, planar, cylindrical, or monolithic; different flow configurations – cross-flow, co-flow, counter-flow, or forced periodic reversal of flow; can range from one-dimensional to three-dimensional; and can consider or neglect time-dependent effects, or a fuel recycling system. They can also differ in the several assumptions made as the mass and heat balances and the electrochemical model are put together. The possibility of methane or natural gas internal reforming, either direct or indirect, is also often considered, given the importance the reforming reaction cooling effect has in terms of fuel cell stack operating conditions. The aim of this section is to present the main achievements of some of those publications, such as assumptions made when developing the models, particular features that each model might have, and main conclusions drawn. The solution of such models normally allows for the spatial or transient (if the model is not a steady-state one) computation of the main variables of the model. These can be temperature, composition or components partial pressure of the air and fuel streams, flow rates, electrical potential, current or current density, power or power density, Nernst potential, and efficiency, among others.

Debenedetti and Vayenas (1983) examined the steady-state behaviour of solid oxide fuel cells, including steady-state multiplicity, the importance of design and operating parameters in maintaining ignited steady-states, and scale-up criteria. In their algebraic model, Debenedetti and Vayenas considered the entire fuel cell reactor as an ensemble of well-mixed cells and neglected any activation and concentration polarisation. They state that, similar to chemical reactors, fuel cells exhibit steady-state multiplicity over a wide range of parameters.

Vayenas et al. (1985) studied the effect of inlet temperature and gas flow rate in the performance of a cross-flow monolithic type SOFC. In this cell the electrochemical reaction was carbon monoxide oxidation over Pt, instead of the more commonly studied hydrogen oxidation. They assumed that the top and bottom cell surfaces were insulated, so that there was no net heat flux in the vertical direction and thus developed a steady-state, two-dimensional mixing cell model, instead of the normally three-dimensional model associated with cross-flow cells.

Ahmed et al. (1991) have also developed a steady-state mathematical model of a cross-flow monolithic solid oxide fuel cell stack with a honeycomb structure of cells. By

dividing a single-cell layer into a number of nodes and, based on the average thermal and compositional conditions at each node, their model was represented by a set of heat and mass-transfer algebraic equations for each node in a cell layer. Ahmed et al. (1991) assumed a linear relationship between current density and voltage in their model.

Hirano et al. (1992) have developed a simple computer programme for a tubular SOFC incorporating an inner reforming process and a fuel recycling system. Their programme was applied to the conventional SOFC power generation system proposed by Westinghouse Electric Corporation. The main assumptions for such model included one-dimensional temperature distribution with no heat transfer by radiation, constant mass transfer polarisation, and no activation polarisation.

Achenbach (1994) presented a very complete although not fully explained mathematical simulation of a planar SOFC. This model accounts for three-dimensional and time-dependent effects as well as direct internal methane steam reforming on the anode, and was used to discuss the effects of different flow manifolding, i.e., cross-, co-, or counter-flow. The counter-flow configuration was reported as the most efficient option. The effects of radiation from the outer stack surface to the surroundings and of anode gas recycling on the operating conditions of the stack were also analysed. Main conclusions withdrawn were that: in such DIR fuel cell systems, recycling of the anode gas is important since it allows for the utilisation of the electrochemically produced steam by the reforming reaction; an increase in the recycling ratio provides a more uniform current density distribution and a lower fuel utilisation, voltage, and efficiency. Finally, the response of this planar SOFC to load change was also discussed. In Achenbach (1994, 1995), a positive current density step function is set to the cell and the response of the cell voltage is calculated. The results have shown that the intermediate period, between the disturbance imposed and the new calculated steady-state, is characterised by an undershooting of the cell voltage. The reason given for the voltage undershooting was that, immediately after the positive jump in the current density, the cell temperature is still low and related to the initial current density. After that, the higher amount of waste heat produced with a higher current density causes an increase in cell temperature, which results in a cell voltage increase due to the decreasing internal cell resistance.

Bessette II et al. (1995) developed a steady-state, three-dimensional model of a single tubular SOFC. In this model, all heat-transfer terms were explicitly included and temperature dependent transport properties were used, being all the parameters obtained from independent sources. Both concentration and activation polarisation are accounted for. The developed model was used to study the effect of different oxidants (pure oxygen or air) and electrochemically oxidised fuels (pure H_2 or H_2 and CO), and of DIR of methane on the cell temperature profiles. The results showed that the methane gets all converted in the first one fifth of the cell length and that there is a thermal sink associated with the endothermic DIR.

Ferguson et al. (1996) have also presented a steady-state, three-dimensional model of a SOFC. They studied the behaviour of the system to changes in the fuel fed, cell geometry, and anode thickness. As the fuels considered were hydrogen or natural gas, direct internal reforming was included in their model. The studied geometries were planar (co, counter, and cross-flow), tubular, and cylindrical. The planar counter-flow geometry was found to be the most efficient.

Costamagna et al. (1996) studied a tubular SOFC system, where methane is first partially oxidised or combusted and then reformed by water and carbon dioxide. A steady-state simulation of the electrochemical reactor, taken as an ideal plug flow one, and including mass, heat, and charge balances is presented.

Guo et al. (1997, 1999) studied the behaviour of SOFC reactors by developing two simple mathematical models, where the gas channels were either considered as having well-mixed flow or plug flow. The main focus of these papers was to study the oxidative coupling of methane to ethane and ethene in a SOFC.

Hall and Colclaser (1999) have simulated the transient operation of a tubular SOFC. The results reported show the same general response and trends published by Achenbach (1994, 1995) for a planar SOFC.

Palsson et al. (2000) developed a steady-state, two-dimensional model of a DIR cross-flow planar SOFC stack, for which some assumptions, i.e., cell dimensions, material characteristics, and DIR kinetics are based in Achenbach (1994). The influence of cell voltage, pressure, air and fuel inlet temperatures and flow rates on fuel efficiency, fuel utilisation, and mean outlet temperature was studied in this paper.

Iwata et al. (2000) developed a two-dimensional (for co-flow and counter-flow configurations) and a three-dimensional (for a cross-flow configuration) simulation programme for a planar-type SOFC. The programme considered mass, heat, and charge balances along the flow directions and perpendicular to the electrolyte membrane. The simulation results showed that, under adiabatic boundary conditions, a temperature increase along the flow direction for the co-flow case and a maximum in the temperature profile near the fuel inlet for the counter-flow one. The effects of gas re-circulation ratio, operating pressure, physical properties, and radiation on current and temperature distributions were also studied by these authors.

Unlike most of the publications above presented and during the work presented in this thesis, Nagata et al. (2001) reported a numerical study of an indirect internal reforming SOFC system. They also believe that fuel internal reforming can act as an efficient cooling system. These authors presented an internal reforming design where a tubular internal reformer with adjusted catalyst density is inserted into a tubular SOFC stack. In such design, the fuel flows along the axis of the internal reformer where it is partially reformed before reversing to flow along the cell anode. These authors have developed a one-dimensional model of temperature and composition along the flow direction and studied the effect of catalyst density (uniform and non-uniform), fuel recirculation, fuel and air inlet temperature, and air recirculation. The main conclusions presented by Nagata et al. (2001) were that: by setting an appropriate uniform catalyst density, a moderate temperature distribution in the cell stack and a higher temperature of the exhaust gas is obtained; by setting a graded catalyst density, the temperature distribution is flatter and the exhaust temperature increases slightly; by increasing the inlet gas temperature, a slight increase in the cell efficiency is observed; and the effect of changing the air inlet temperature is stronger than changing the fuel inlet temperature. These results are compatible with the ones to be presented in this thesis.

Campanari (2001) developed a simplified model based on a semi-empirical cell voltage of a tubular SOFC stack with natural gas direct internal reforming and internal air preheating. The aim of this work was to carry out a parametric analysis of the stack working conditions, such as the cell efficiency and the power output. The varied operating parameters were the current, the fuel utilisation, the air utilisation, and the composition of fuel feed.

Haynes and Wepfer (2001) developed a thermal transport model to analyse the steady-state heat transfer within the tubular solid oxide fuel cell developed by SiemensWestinghouse. They observed that, mainly due to radiation heat transfer, the air stream is near thermal equilibrium with the fuel cell when it exits the supply pipe and contacts the cell and that the design point is the inlet air temperature, which has a linear increase and decrease with voltage and fuel utilisation, respectively.

As seen so far, the prevailing mode of operation of a fuel cell is under conditions being constant in space and in time, while in all instances thermal management and heat exchangers are needed to bring the feedstock up to the operating temperature of the SOFC stack. However, as already referred to in Chapter 1, Neophytides and Tripakis (1996) and Neophytides (1999) showed that the operation of a SOFC under forced periodic reversal flow can lead to significantly improved operation and a simplified flow diagram, allowing for the combination of regenerative heat preheater and electrocatalytic converter concepts. Neophytides and Tripakis (1996) proposed the forced periodic reversal of flow for the case of a co-current flow solid oxide monolithic fuel cell, applying a one-dimensional non-steady-state heterogeneous model. In this model, they have neglected activation and concentration overpotentials. The effect of variables such as the inlet temperature, the semi-cycle operation, external load, and maximum temperature on equilibrium conversion was studied. Main conclusions from this study were that very low inlet temperature gas mixtures can be processed autothermally, even at ambient temperature, leading to a highly efficient reactor operation, which is favourably compared to the maximum reactor efficiency achieved under steady-state operation and an inlet temperature of 1000 K. Neophytides (1999) studied the same forced periodic reversal of flow for the case of a planar cross-flow SOFC monolith, applying a two-dimensional model. The operation of both the cross-flow and co-current flow SOFC arrangements was found similar.

Although special attention has been given to the cases where hydrogen or carbon monoxide are either directly fed to the SOFC to be electrochemically oxidised or are produced through direct or indirect internal reforming, other reactions are also possible and have been studied to produce electricity within a fuel cell system. Guo et al. (1997, 1999) presented the example of the oxidative coupling of methane to ethane and ethane. Other possible oxidation reactions within SOFCs are the conversion of

ammonia to nitric oxide over Pt, the conversion of sulphur to SO_2 and SO_3, and the ethylene epoxidation. References for studies on these reactions can be found in Vayenas et al. (1985).

As mentioned before, a few examples of the work performed when modelling molten carbonate fuel cell systems are also presented. These are also categorised as high temperature fuel cells and contain some common features with SOFCs, such as the possibility of performing direct or indirect internal reforming.

Mori et al. (1989) presented a paper where the steam reforming reaction of methane in an internally reformed MCFC was studied employing an equilibrium calculation. In this paper the effect of fuel utilisation, steam to carbon ratio, and temperature on methane conversion and anode gas composition was studied.

He and Chen presented a set of papers concerning the operation of molten carbonate fuel cells. In 1995 (He and Chen, 1995), they derived a numerical three-dimensional simulation, composed of mass, energy, and momentum balances, to analyse the steady-state performance of a MCFC stack with regard to safe and efficient electricity generation. The model was then used to determine the three-dimensional distributions of temperature, pressure, gas composition, and density for three different manifolds (co, counter, and cross-flow) in a stack. Later on, He (1998) studied the response of a MCFC system to load and gas flow rate changes. The cases to which the model was applied indicate that the system output power has a fast response to a current step change and a slow response to a gas flow rate change. He and Chen (1998) have also analysed the performance of a MCFC stack under transient conditions. The simulation-derived current and temperature distributions under a step voltage change showed that the current density profile changes rapidly in the beginning and slowly in the following stages and that the temperature response is slow.

Yoshiba et al. (1998) developed a three-dimensional numerical model of a MCFC stack. They compared the performance of five gas flow geometries based on cell voltage, current density, and temperature profiles and on the net output power. The five gas flow geometries considered were the conventional co, counter, and cross-flow geometries plus the cathode exchange parallel flow (combination of co and counter-flow) and the cathode exchange cross flow (cathode gas flow alternates in direction

although always cross-currently to the anode gas flow). From the point of view of stack performance, cooling power, and maximum temperature control, the co-flow type stack was reported as the most advantageous.

Cavallaro and Freni (1998) proposed the integrated autothermal reforming (ATR) MCFC system already referred to in Section 1.3.4, Chapter 1. This system has been modelled and its performance evaluated as a function of some parameters, such as pressure, inlet flow rates of oxygen and steam, current density, and cell configuration (direct or indirect), and their influence on the overall process economy in terms of gas outlet composition and thermal balance.

Koh et al. (2000) developed a mathematical model to predict the temperature profiles for external reforming co-flow MCFC stacks under constant-load operation and to analyse the effect of various stack parameters on cell temperature. The validity of the model was proved by comparison with measured temperature data obtained from the operation of a 5 kW test stack. The simulation results corroborated the fact that the cathode gas is an efficient cooling medium and that control of the stack temperature can be achieved by changing the cathode gas flow rate.

During the course of this work, Park et al. (2002) presented a mathematical model of a cross-flow type indirect internal reforming MCFC. In this paper, temperature and gas composition distributions are analysed both in the reformer and in the fuel cell. In the reformer, the conversion of methane reaches 99% and the endothermic reforming reaction is found to lead to a non-uniform temperature distribution.

2.4 Solid Oxide Fuel Cell Model

Several configurations are possible for indirect internal reforming solid oxide fuel cells. As described in Chapter 1, the configuration reported here is based on a simple, generic annular design where the fuel cell anode, electrolyte, and cathode layers are constructed around a tubular steam reforming reactor (see Chapter 3). In this design, the fuel is first fed to the inner reformer, whose exit gases are then fed to the fuel cell anode. On the outer side, air is fed to the cathode, either counter-currently or co-currently to the fuel

flow in the fuel channel. Figure 2.2 schematically illustrates the described IIR-SOFC configuration.

As seen above, SOFC models are typically based on solving simultaneous mass, energy, and potential balance equations. To produce a useful voltage, a complete SOFC system can not be made up of a single solid oxide fuel cell, as its voltage is quite small (about 0.7 volts when drawing a useful current), but of several repeating electrochemical cells in a module, connected both in series and/or in parallel and assembled to compose a stack. However, when modelling a SOFC this is usually done for the smallest unit cell or module. Such model can then be used to compute the operating conditions of the whole stack provided the boundary conditions for each unit cell are independent and that adequate ones are established for the stack exterior.

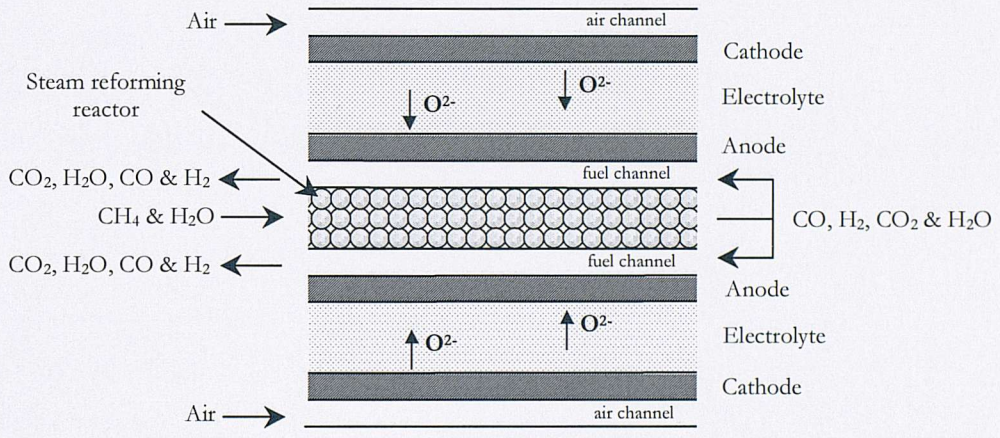

Figure 2.2 Indirect internal reforming solid oxide fuel cell under study (not to scale).

The SOFC model here derived and explained in detail in the following sections, is a steady-state, one-dimensional one. Pressure drop along the channels is neglected. For the purpose of modelling, it is considered that the SOFC is composed of the fuel and air channels and of the electrochemically active tri-layer region represented by the anode, electrolyte, and cathode and from now on referred to as solid structure. The developed model consists of: two mass balances, to the fuel and air channels; three energy balances, to the fuel and air channels and to the solid structure; and an electrochemical model that relates the fuel and air gas composition and temperature to the voltage, current density, and other cell variables. The following three sections are then related to the development of those mass and energy balances as well as of the

electrochemical model. It should be remembered that this SOFC model is meant to be coupled with the steam reforming reactor presented in Chapter 3, and therefore, appropriate boundary conditions reflecting the heat transfer from the SOFC to the reformer are already accounted for in this chapter.

2.4.1 Solid Oxide Fuel Cell Mass Balances

The developed fuel and air channels mass balances are shown in Table 2.2. For the mass balance in the fuel channel, the chemical species considered are CH_4 (as this might flow through from the reformer), H_2O, CO, H_2, and CO_2 while for the air channel are O_2 and N_2 (as the oxidant is considered to be air and not pure oxygen). The molar flux in these gas channels is considered to be convective in the flow direction. The gas flow in the air channel is considered to be counter-flow to the one in the fuel channel, as can be seen through both the boundary conditions and the positive sign of the convective term in the fuel channel mass balance (2.20). In Chapter 4, a co-flow case is also considered.

Table 2.1 Electrochemical reactions considered.

Anode reaction	$H_2 + O^{2-} \rightarrow H_2O + 2e^-$	(2.I)	$CO + O^{2-} \rightarrow CO_2 + 2e^-$	(2.IV)
Cathode reaction	$1/2O_2 + 2e^- \rightarrow O^{2-}$	(2.II)		
Overall reaction	$H_2 + 1/2O_2 \rightarrow H_2O$	(2.III)	$CO + 1/2O_2 \rightarrow CO_2$	(2.V)

As referred to in Chapter 1, in practical applications, SOFCs may use gaseous mixtures that contain, in addition to hydrogen, carbon monoxide, carbon dioxide, water, and methane or other hydrocarbons. Because of their high operating temperature, the presence of CO and CO_2 in the fuel does not poison the anode reaction and, in YSZ-based SOFCs, CO normally functions as a fuel. Here, simultaneous electrochemical conversion of H_2 and CO to H_2O and CO_2 and equilibrium of the shift reaction (Park et al., 2002; Ahmed and Foger, 2001) are assumed to take place in the fuel channel. This is in opposition to the usual assumption that only H_2 is electrochemically oxidised and that all CO is converted through the shift reaction (2.VI). Table 2.1 presents the electrochemical reactions considered – hydrogen oxidation reactions (2.I-2.III), already presented in Section 2.2, and carbon monoxide oxidation reactions. It is assumed that

any methane present in the fuel channel would be reformed to H_2, CO, and CO_2 and, hence, not electrochemically oxidised at the anode.

$$CO + H_2O \Leftrightarrow CO_2 + H_2 \tag{2.VI}$$

The electrochemical reactions in Table 2.1 are assumed to occur only at the anode/electrolyte and cathode/electrolyte interfaces although, for the purpose of modelling, these need to be considered in the mass balances of the fuel and air channels. Furthermore, and as only heterogeneous indirect steam reforming is so far present, no reforming reactions are considered in the fuel channel mass balance (although this will be later considered in Chapter 4, where a combined indirect and direct SOFC model is used). Any methane that might eventually not be fully converted in the reformer will simply flow through the channel. In the air channel, only the reduction reaction of O_2 to O^{2-} ions is considered (this determines the flux of O^{2-} ions through the electrolyte to the anode/electrolyte interface where the oxidation reactions take place). As explained in Section 2.2.3, the rate of the hydrogen and carbon monoxide oxidation reactions, here represented as $R_{elect,1}$ and $R_{elect,2}$, respectively, is related to the electric current drawn by each reaction, j_{H_2} and j_{CO}, by Faraday's law. Thus,

$$R_{elect,1} = \frac{j_{H_2}}{2F}, \quad R_{elect,2} = \frac{j_{CO}}{2F}. \tag{2.19}$$

Table 2.2 Mass balances for the SOFC steady-state model.

Fuel channel

$$u_f \frac{dC_{i,f}}{dz} + \sum_k \nu_{ik} R_{elect,k} A_{Act}/V_f = 0 \tag{2.20}$$

Boundary conditions: $z = L: \; C_{i,f}\big|_{z=L} = C_{i,b}\big|_{\forall r, z=L}$

Air channel

$$-u_a \frac{dC_{i,a}}{dz} + \sum_k \nu_{ik} R_{elect,k} A_{Act}/V_a = 0 \tag{2.21}$$

Boundary conditions: $z = 0: \; C_{i,a} = C_{i,a}^0$

In equations (2.20-2.21) in Table 2.2, $R_{elect,k}$ represents equations (2.19) and ν_{ik} represents the stoichiometric coefficients of each component in reactions (2.III) and (2.V) in Table 2.1.

In the system under study, the SOFC and the reformer systems are coupled, and thus, the SOFC fuel channel feed corresponds to the exit stream from the reformer. This situation is accounted for in the boundary condition of the fuel channel mass balance.

2.4.2 Solid Oxide Fuel Cell Energy Balances

In a fuel cell, current and temperature distributions are strongly coupled. Therefore, knowledge of the predominant heat transfer processes is required. Such processes can be: heat release arising from the electrochemical reactions, electrical resistances, and anode fuel chemistry; convective heat transfer between the cell components and the fuel and air gas streams; and heat conduction through the cell components.

Many authors have made different assumptions when modelling heat transfer within a SOFC. Ferguson et al. (1996), for instance, considered that, for the solid parts of the FC, the thermal flux is mainly conductive and modelled by Fourier's law of heat conduction and that, in the gas channels, the thermal flux is mainly convective in the gas flow direction and conductive from the channels to the solid parts. Bessette II et al. (1995) assumed that all three modes of heat transfer, convection, radiation between the support and injection tubes, and three-dimensional conduction in the solid material, were present. At the axial ends, they have considered that either a convective, adiabatic, or constant heat flux boundary condition could be established. Costamagna et al. (1996), considered the radiation effects between cells and shell negligible and, as an approximate calculation, they have increased the axial heat conductivity of the solid by one order of magnitude to take into account the radiation phenomena between different axial points of different cells. Achenbach (1994) and Hall and Colclaser (1999) considered heat transfer by conduction, convection, and radiation. Achenbach (1994) has assumed the solid to be a quasi-homogeneous material with respect to conduction of heat, defining a separate effective conductivity for each coordinate that accounts for radiation and conduction through the solid and gas phase. Achenbach (1994) also

believed that heat transfer through the stack surface to the surroundings influences significantly the temperature field, so that a three-dimensional simulation is necessary, and that an effective thermal insulation should be provided to prevent the stack from cooling down. In his model, Achenbach allowed for heat convection and radiation from each of the stack surfaces to a wall of arbitrary temperature. Palsson et al. (2000) developed a model of a planar SOFC stack, where some of the assumptions were based in Achenbach (1994). However, these authors considered all the exterior walls as adiabatic. Iwata et al. (2000) used different view factors to study the effect on the temperature profiles of radiation between the outer interconnector and an electric furnace surface. Both Vayenas et al. (1985) and Hirano et al. (1992) neglected, in their studies, the radiative heat transfer despite the typically high operating temperatures of solid oxide fuel cells.

All these issues were taken into account when developing the SOFC model presented in Table 2.3. This considers energy balances to the fuel channel, air channel, and solid structure.

The thermal flux in the solid structure is conductive and modelled by Fourier's law of heat conduction and in the gas channels is convective in the gas flow direction and conductive from the channels to the solid parts. It is assumed that all reaction enthalpies are released at the tri-layer solid structure (Ahmed et al., 1991; Achenbach, 1994). As there is close thermal contact between the two coupled systems, heat transfer between the fuel gas streams in the SOFC and adjacent reformer needs to be considered. This is accounted for in the fuel channel energy balance (2.22). Due to the high temperatures involved, radiation between the SOFC solid structure and the reformer wall is also accounted for. For this purpose, the general expression for radiation between two long concentric cylinders is considered (Incropera and De Witt, 1990), as can be seen in the solid structure balance (2.24). As for the air channel external surface, this could be an adiabatic surface, one having a constant heat flux, or one with a heat transfer, either by convection or radiation, to a constant temperature wall. Here it is assumed that the cell module being modelled is placed on the central region of a stack and so there is no heat flux through its external walls. Once again, as the SOFC and the reformer are coupled, the boundary condition of the fuel channel energy balance states that the inlet gas temperature is the same as the reformer outlet stream.

Table 2.3 Energy balances for the SOFC steady-state model.

Fuel channel

$$u_f\left(\rho_f c_{p,f}\right)\frac{dT_f}{dz} + h_f\, A_f/V_f\left(T_{ss} - T_f\right) + \alpha_R\, A_R/V_f\left(T_b\big|_{r=r_R} - T_f\right) = 0 \tag{2.22}$$

Boundary conditions: $z = L:\ T_f\big|_{z=L} = T_b\big|_{\forall r,\, z=L}$

Air channel

$$-u_a\left(\rho_a c_{p,a}\right)\frac{dT_a}{dz} + h_a\, A_{ss}/V_a\left(T_{ss} - T_a\right) = 0 \tag{2.23}$$

Boundary conditions: $z = 0:\ T_a = T_a^0$

Solid structure

$$\lambda_{ss}\frac{d^2T_{ss}}{dz^2} - h_f\, A_f/V_{ss}\left(T_{ss} - T_f\right) - h_a\, A_{ss}/V_{ss}\left(T_{ss} - T_a\right) + \\ + \left[\sum_k \left(-\Delta H\right)_{elect,k} R_{elect,k} - jU\right] A_{Act}/V_{ss} + \frac{\sigma A_R/V_{ss}\left(T_b^4\big|_{r=r_R} - T_{ss}^4\right)}{\frac{1}{\epsilon_1} + \frac{A_R}{A_f}\left(\frac{1}{\epsilon_2} - 1\right)} = 0 \tag{2.24}$$

Boundary conditions $z = 0:\ \left.\frac{dT_{ss}}{dz}\right|_{z=0} = 0;\ z = L:\ \left.\frac{dT_{ss}}{dz}\right|_{z=L} = 0$

2.4.3 Solid Oxide Fuel Cell Electrochemical Model

In this section, the electrochemical theory previously explained, and presented in Section 2.2, is used for the derivation of the electrochemical SOFC model. Note that in Section 2.2 all the expressions and performance factors presented were for the specific case of a hydrogen-fuelled fuel cell. However, the system under study here is an indirect internal stem reforming SOFC for which two points are important to consider. First, both the H_2 and CO electrochemical oxidation reactions are taken into consideration, and second, the system inlet fuel is no longer pure hydrogen being fed to the fuel cell anode, but a mixture of methane, water, carbon monoxide, hydrogen, and carbon dioxide being fed to the inner reformer. For these reasons, the expressions derived in Section 2.2 need to be redefined.

The first electrochemical variable normally defined is the open-circuit potential given by the Nernst equation. However, unlike what was presented in Section 2.2, two possible open-circuit potentials, for both the H_2 and CO oxidation reactions occurring at the cell, can now be derived. Thus, the open-circuit potential for the H_2 and CO oxidation are given by equations (2.25) and (2.26), respectively.

$$U_{H_2}^{OCP} = U_{H_2}^{0} - \frac{\Re T_f}{2F} \ln\left(\frac{p_{H_2O,f}}{p_{H_2,f} p_{O_2,a}^{1/2}} \right) \tag{2.25}$$

$$U_{CO}^{OCP} = U_{CO}^{0} - \frac{\Re T_f}{2F} \ln\left(\frac{p_{CO_2,f}}{p_{CO,f} p_{O_2,a}^{1/2}} \right) \tag{2.26}$$

However, as referred to in Section 2.4.1, one of the assumptions in deriving the fuel channel balances is that the water-gas shift reaction (2.VI) is in equilibrium, for which the following equilibrium constant (2.27) holds.

$$K_{eq,WGSR} = \frac{p_{CO_2,f} p_{H_2,f}}{p_{CO,f} p_{H_2O,f}} = \frac{K_{eq,elect,2}}{K_{eq,elect,1}}. \tag{2.27}$$

$K_{eq,elect,1}$ and $K_{eq,elect,2}$ stand for the equilibrium constants of the overall reactions (2.III) and (2.V), respectively. By replacing equation (2.27) into equation (2.26) and taking into account that, as seen in Section 2.2,

$$U_{CO}^{0} = \frac{\Re T_f}{2F} \ln\left(K_{eq,elect,2}\right), \tag{2.28}$$

the following relation can be obtained,

$$\begin{aligned} U_{CO}^{OCP} &= \frac{\Re T_f}{2F} \ln\left(K_{eq,elect,2}\right) - \frac{\Re T_f}{2F} \ln\left(\frac{p_{CO_2,f}}{p_{CO,f} p_{O_2,a}^{1/2}} \right) \\ &= \frac{\Re T_f}{2F} \ln\left(K_{eq,elect,1} K_{eq,WGSR}\right) - \frac{\Re T_f}{2F} \ln\left(\frac{p_{CO_2,f}}{p_{CO,f} p_{O_2,a}^{1/2}} \right) \\ &= \frac{\Re T_f}{2F} \ln\left(K_{eq,elect,1}\right) + \frac{\Re T_f}{2F} \ln\left(\frac{p_{CO_2,f} p_{H_2,f}}{p_{CO,f} p_{H_2O,f}} \right) - \frac{\Re T_f}{2F} \ln\left(\frac{p_{CO_2,f}}{p_{CO,f} p_{O_2,a}^{1/2}} \right) \end{aligned}$$

$$= U_{H_2}^0 - \frac{\Re T_f}{2F} \ln\left(\frac{p_{H_2O,f}}{p_{H_2,f} p_{O_2,a}^{1/2}}\right) = U_{H_2}^{OCP}$$

demonstrating that the open-circuit potential is, in such a case, the same for both the electrochemical reactions considered. Hence, for the open-circuit potential, only $U_{H_2}^{OCP}$ is from now on used.

As seen before, the OCP is the maximum potential that can be achieved by a SOFC under specific operating conditions. However, due to potential losses that occur as the current is drawn from the cell (see Section 2.2.2), the potential of an operating cell, U, is always lower than this. In the present model, the principal electrochemical reactions are considered to be kinetically controlled, i.e., only activation overpotentials are taken into account. The anode and cathode overpotentials here considered are given by equations (2.29-2.31), written in terms of electrical resistances (Achenbach, 1994)*. These simplified equations are based on the Butler-Volmer equation for activation overpotentials and on the assumption that these overpotentials are small. In Appendix A.1, the Butler-Volmer equation and corresponding approximations are presented and discussed.

Table 2.4 Anode and cathode overpotentials for the SOFC steady-state model.

Anode overpotential	$\frac{1}{R_{A,H_2}} = \frac{2F}{\Re T_f} K_{A,H_2} \left(\frac{p_{H_2,f}}{p^0}\right)^m \exp\left(-\frac{E_A}{\Re T_f}\right)$	(2.29)
Anode overpotential	$\frac{1}{R_{A,CO}} = \frac{2F}{\Re T_f} K_{A,CO} \left(\frac{p_{CO,f}}{p^0}\right)^m \exp\left(-\frac{E_A}{\Re T_f}\right)$	(2.30)
Cathode overpotential	$\frac{1}{R_C} = \frac{4F}{\Re T_a} K_C \left(\frac{p_{O_2,a}}{p^0}\right)^m \exp\left(-\frac{E_C}{\Re T_a}\right)$	(2.31)

* Overpotentials are usually represented as a voltage loss. Thus, and as these overpotentials are written in terms of electrical resistances instead, they need to be multiplied by the corresponding current density, as is done in equations (2.32) and (2.34).

Finally, equations (2.32-2.34) yield the relationship between the cell voltage and the local current densities (both the total and the partial current densities produced by the two oxidation reactions). For the derivation of such equations, it is assumed that the total cell current passes through the cathode and ohmic resistances and that the anodic current divides according to the particular H_2 and CO conversion rates. The relationship between the two anodic current densities and the total current in the cell is given by equations (2.33) and (2.34). One last point related to the cell voltage is that, as this is equal to the voltage difference between the cathode and the anode and as both these electrodes are normally good conductors, a constant cell voltage throughout the cell is considered. This is a commonly used assumption, even though in practice the system modelled consists of several cells connected in series and not of a single long cell (Haynes and Wepfer, 2000).

$$U = U_{H_2}^{OCP} - \left(R_{OHM} j + R_{A,H_2} j_{H_2} + R_C j\right) \tag{2.32}$$

$$j = j_{H_2} + j_{CO} \tag{2.33}$$

$$R_{A,H_2} j_{H_2} = R_{A,CO} j_{CO} \tag{2.34}$$

For the complete definition of the problem and similarly to what was done in Section 2.2.4, the performance factors for the system under study are here presented. Table 2.5 presents the utilisation factor, air ratio, fuel cell efficiency, and overall power output as a function of the system variables. Note that the inlet fuel in the definition of the fuel utilisation factor, equation (2.35), and of the fuel cell efficiency, equation (2.37), is referred to methane and to the reformer entrance. LHV in equation (2.37) stands for lower heating value, i.e., enthalpy of combustion assuming that the product water is in the form of steam.

In the next chapter, Chapter 3, the tubular steam reforming fixed-bed catalytic reactor model, to be coupled with this solid oxide fuel cell model, is developed.

---

* This relation is easily understood if one considers that the cell voltage could also be written considering the carbon monoxide electrochemical reaction $U = U_{CO}^{OCP} - \left(R_{OHM} j + R_{A,CO} j_{CO} + R_C j\right)$.

Table 2.5 SOFC model performance factors.

Fuel utilisation factor	$U_{fuel} = \frac{\bar{j}A_{Act}}{8Fy^{0}_{CH_4,R}F_R^{mol,0}}$	(2.35)
Air ratio	$\lambda = \frac{4Fy^{0}_{O_2,a}F_a^{mol,0}}{\bar{j}A_{Act}}$	(2.36)
Fuel cell efficiency	$\eta_{SOFC} = \frac{\overline{P_{SOFC}}}{y^{0}_{CH_4,R}F_R^{mol,0}LHV^{0}_R}$	(2.37)
Power	$\overline{P_{SOFC}} = \bar{j}A_{Act}U$	(2.38)

Notation

A_{Act}	active surface area for the electrochemical reactions, m^2
A_f	fuel channel outer surface area ($2\pi r_f L$), m^2
A_R	reformer outer surface area ($2\pi r_R L$), m^2
A_{ss}	solid structure outer surface area ($2\pi r_{ss} L$), m^2
C_i	molar concentration of component i, mol/m^3
c_p	specific heat of the gas streams, kJ/kgK
E_A, E_C	activation energy (equations (2.29-2.31)), kJ/mol
$-e$	electric charge of one electron, C
F	Faraday's constant (F = Ne), C/mol
F^{mol}	molar flow rate, mol/s
h	heat transfer coefficient, kJ/m^2sK
K_{A,H_2}	pre-exponential factor (equations (2.29)), A/m^2
$K_{A,CO}$	pre-exponential factor (equations (2.30)), A/m^2
K_C	pre-exponential factor (equations (2.31)), A/m^2
$\bar{j}, j, j_{H_2}, j_{CO}$	average, total, and partial current densities, A/m^2
K_{eq}	equilibrium constant
L	system length, m
LHV	lower heating value
m	exponent (equations (2.29-2.31))
n	number of electrons participating in the electrochemical reaction
N	Avagadro's number
OCP	open-circuit potential
OCV	open-circuit voltage
p^0	standard partial pressure, bar
p_i	partial pressure of component i, bar
P_{SOFC}	local power density, W/m^2

$\overline{P_{SOFC}}$	power, W
R_{A,H_2}	anode overpotential (polarisation resistance) for H_2 oxidation, Ωm^2
$R_{A,CO}$	anode overpotential (polarisation resistance) for CO oxidation, Ωm^2
R_C	cathode overpotential (polarisation resistance), Ωm^2
$R_{elect,k}$	rate of the electrochemical reaction k, mol/m^2s
R_{OHM}	total cell resistance, including both ionic and electronic resistances, Ωm^2
r_R	reactor outer radius, m
r_f	fuel channel outer radius, m
r_{ss}	solid structure outer radius, m
r_a	air channel outer radius, m
$\Re$	gas constant, kJ/molK
SOFC	solid oxide fuel cell
T	temperature, K
u	velocity, m/s
U	potential, V
U^{OCP}	open-circuit potential (OCP), V
U^0	OCP for standard temperature and pressure and pure reactants, V
U_{fuel}	fuel utilisation factor
V_a	air channel volume $\left(\pi(r_a^2 - r_{ss}^2)L\right)$, m^3
V_f	fuel channel volume $\left(\pi(r_f^2 - r_R^2)L\right)$, m^3
V_{ss}	solid structure volume $\left(\pi(r_{ss}^2 - r_f^2)L\right)$, m^3
y_i	molar fraction of component i
z	system axial coordinate, m

Greek letters

α_R	overall heat transfer coefficient, kJ/m^2sK
$(-\Delta G)$	Gibbs free energy change of a reaction, kJ/mol
$(-\Delta G)^0$	Gibbs free energy change for standard temperature and pressure and pure reactants, kJ/mol
$(-\Delta H)$	enthalpy change of a reaction, kJ/mol
$(-\Delta H)^0$	enthalpy change for standard temperature and pressure and pure reactants, kJ/mol
$(-\Delta S)$	entropy change of a reaction, kJ/molK
$(-\Delta S)^0$	entropy change for standard temperature and pressure and pure reactants, kJ/molK
ϵ_1, ϵ_2	emissivity
σ	Stefan-Boltzmann constant, W/m^2K^4
λ	air ratio
λ_{ss}	thermal conductivity of the solid structure, kJ/msK

ν_{ik}	stoichiometric coefficient of component i in electrochemical reaction k
ρ	gas streams density, kg/m^3
η_A, η_C	anode and cathode overpotentials, V
η_{SOFC}	fuel cell efficiency

Superscripts

0	feed conditions (reformer and air channel inlet) or standard state

Subscripts

a	air channel
A	anode
b	bulk phase in the reformer
C	cathode
elect	electrochemical reactions
f	fuel channel
i	component
k	reaction
R	reformer
ss	solid structure
WGSR	water gas shift reaction

Chapter 3

Steam Reforming Process & Fixed-Bed Reactor Modelling

Summary

Catalytic steam reforming of natural gas or other hydrocarbons has been widely studied and is a well-established industrial process of producing the hydrogen or synthesis fuel gas required by solid oxide fuel cells. This third chapter is related to the development of the steam reforming fixed-bed reactor model that is later coupled with the solid oxide fuel cell model just presented in Chapter 2. It first gives a brief description of the industrial steam reforming process and most used catalysts and introduces the kinetic expressions here adopted. General mathematical modelling of fixed-bed catalytic reactors and associated parameters is discussed and, finally, the developed reactor model is presented. This is a steady-state, heterogeneous, two-dimensional model, accounting for intraparticle and interparticle mass gradients but only interparticle thermal gradients.

Outline

3.1 Introduction

Steam reforming is an essential process for the manufacture of hydrogen or synthesis gas from hydrocarbons. Its applications are widespread both in the petrochemical and, as this work demonstrates, in the energy industry. In the past years, numerous reviews have been published concerning this process, its kinetics, and related catalytic aspects (Twigg, 1996; Dicks, 1996; Rostrup-Nielsen, 1984).

The aim of this chapter is to develop the model for the inner steam reforming reactor illustrated in Figure 2.2 (Chapter 2). For that purpose, it first starts by briefly explaining the generic steam reforming process, including main reactions and operating conditions involved. The kinetic expressions used in the model and the correspondent reaction mechanism is also presented. Section 3.3 discusses issues related to fixed-bed reactors modelling and Section 3.4 presents the developed reformer model.

3.2 Steam Reforming Process

In recent years, hydrogen has become a widely used feedstock in the chemical, petroleum refining, and petrochemical industries. Areas in which hydrogen is employed include: fuel cells; hydrogenation reactions, such as hydrotreating and hydrocracking processes; synthesis gas applications, such as production of ammonia and methanol; oxo-alcohols and Fischer-Tropsch synthesis; and the manufacture of chemicals with specific end uses, such as for pharmaceuticals. Hydrogen is expected to be an important energy source in the future, as it offers several environmental and economic advantages when compared to other fuels.

Steam reforming of light hydrocarbons, run on nickel catalysts, is the most widely employed route for hydrogen or synthesis gas industrial production due to its simple construction, operation, and well-established technology. The aim of a steam reforming process is to extract the maximum quantity of hydrogen held both in the steam and in the hydrocarbon feedstock, thus converting hydrocarbons into mixtures of hydrogen, carbon monoxide, carbon dioxide, and methane. Main feedstocks to this process include natural gas, other hydrocarbon fuels, or alcohols. The chemical composition of natural gas varies according to the source. However, its principal

component is always methane, the remainder being small amounts of low molecular weight hydrocarbons and often nitrogen and CO_2. Small amounts of sulphur, that need to be removed, are also usually present as simple compounds, i.e., hydrogen sulphide, carbonyl sulphide, or mercaptans. Nevertheless, natural gas is the cleanest of all primary fossil fuels and the most environmentally acceptable in terms of its products of combustion. Steam reforming of methane is highly endothermic and for large-scale industrial production is usually carried out in rows of fixed-bed tubular reactors inserted into a gas-fired furnace, where fuel combustion promotes the heating of the reformer tubes. The temperature in each tube ranges from 675 to 1000 K, to ensure an adequate reaction rate and maximise the H_2 production, and the pressure is generally around 30 bar (Xu and Froment, 1989a). Thus, it is the demand for considerable energy input, resulting from the high endothermicity of the reforming reactions, and the existence of catalyst deactivation that turn out to be the major drawbacks of catalytic steam reforming (Rostrup-Nielsen, 1984). Catalytic partial oxidation of methane, which is mildly exothermic, could be another alternative. However, this gives a lower synthesis gas ratio, as referred to in Chapter 1. Therefore, this process is more suitable for use in processes such as Fischer-Tropsch synthesis and methanol production. Direct methane cracking, carbon dioxide reforming of methane, use of membrane or fixed-bed reactors with reversal of flow, and thermochemical or photocatalytic water splitting are some of the alternative techniques for hydrogen production (Avci et al., 2001).

Steam reforming of natural gas utilises two main reversible reactions (3.I-3.II), known as the reforming reaction and the water-gas shift reaction.

$$CH_4 + H_2O \leftrightarrow 3H_2 + CO \tag{3.I}$$

$$CO + H_2O \leftrightarrow H_2 + CO_2 \tag{3.II}$$

The reforming reaction is strongly endothermic and favoured by high temperature as well as by low pressure, and the water-gas shift reaction is mildly exothermic and favoured by low temperature although largely unaffected by changes in pressure. It is evident from the principle of Le Chatelier that at higher temperatures less methane and more carbon monoxide are present in the equilibrium gas, and that the methane content increases with pressure and decreases with increasing steam to carbon ratio. However, to maximise the overall efficiency of the hydrogen production,

reformers are normally operated at high temperature and pressure. These reformers are generally followed by a shift process, which by using two different catalysts permits the shift reaction to be brought to equilibrium at as low a temperature as possible, further producing hydrogen.

From reaction (3.I), it can be seen that the stoichiometric requirement for the steam to carbon ratio, when methane is the hydrocarbon feed, is 1.0. However, it has been demonstrated that this is not practicable, as all catalysts so far developed tend to promote carbon-forming reactions under reforming conditions. Such carbon-forming reactions can only be suppressed by using an excess of steam, with the result that the minimum ratio is in the region of 1.7. However, and as the reforming reaction itself is also promoted by an excess of steam, ratios of 3.0-3.5 are commonly used.

The reforming of saturated naphthas of general formula C_nH_{2n+2} is based on reaction (3.III) and (3.I-3.II).

$$C_nH_{2n+2} + nH_2O \rightarrow (2n+1)H_2 + nCO \qquad (3.III)$$

Reaction (3.III) is also strongly endothermic and, depending on the process conditions, the overall heat of reaction could be either positive, zero, or negative. However, at the high temperatures of interest in reforming reactions, reaction (3.III) can be considered as irreversible if the hydrocarbon is not methane (Rostrup-Nielsen, 1984). Also at these temperatures, the hydrocarbons may react, in parallel to reaction (3.III), by thermal cracking into olefins that can easily form coke via reaction (3.IV). Reactions (3.V) and (3.VI) are two other possible carbon-forming reactions. These are reversible, whereas reaction (3.IV) is irreversible for $n > 1$. As referred to above, steam is normally added well in excess of the stoichiometric requirement of reaction (3.I). This is done so that the equilibrium of reaction (3.II) moves towards more CO_2 production rather that more CO. This way carbon deposition via the Boudouard reaction (3.VI) is also avoided.

$$C_nH_{2n+2} \rightarrow \text{"carbonaceous deposits"} + (n+1)H_2 \qquad (3.IV)$$

$$CH_4 \leftrightarrow C + 2H_2 \qquad (3.V)$$

$$2CO \leftrightarrow C + CO_2 \qquad (3.VI)$$

Steam can also be completely (or in part) replaced by carbon dioxide that, for some applications, gives a more favourable H_2/CO ratio, through reaction (3.VII).

$$CH_4 + CO_2 \leftrightarrow 2H_2 + 2CO \qquad (3.VII)$$

Alcohols may also be steam reformed. These are in general more reactive than hydrocarbons and the reaction can be carried out at lower temperatures. For the case of methanol, it can be steam reformed through reaction (3.VIII) at around 250°C over a Cu/ZnO catalyst (Dicks, 1998).

$$CH_3OH + H_2O \leftrightarrow 3H_2 + CO_2 \qquad (3.VIII)$$

3.2.1 Steam Reforming Catalysts

Nickel, has been, for many years, recognised as the most suitable and the preferred active metal for industrial steam reforming catalysts. Other possible metals would be cobalt, platinum, palladium, iridium, ruthenium, and rhodium. Although some of these precious metals are considerably more active per unit weight than nickel, nickel is much cheaper and sufficiently active to enable suitable catalysts to be produced economically.

On nickel it has been fairly well established that the key reactions occur over a surface layer of nickel atoms. However, if carbon layers are allowed to build up, a filament or whisker of carbon can start to grow attached to a nickel crystallite. Such carbon filaments can generate massive forces within the catalyst pellet and, once started, can lead to rapid catalyst breakdown, and blocking of the reactor tubes. Reactions (3.IV) and (3.V) tend to lead to a surface pyrolytic carbon, which can encapsulate the nickel particles. Such reactions have the greatest risk of occurring at the inlet of a reformer where there is almost no hydrogen present. At this point the likelihood of carbon formation is governed not so much by equilibrium considerations but by the relative kinetics of the carbon forming and carbon removal reactions. Fortunately, carbon filaments do not appear to form on precious metals such as ruthenium or rhodium, which are also active for steam reforming. Thus, if cost is not an issue, the use of precious metal catalysts can significantly reduce the risk of carbon deposition (Dicks, 1996; Clarke et al., 1997).

Commercial steam reforming catalysts must be manufactured in such a way that the maximum stable nickel surface area is available to the reactants. This is usually done, either through precipitation or impregnation, by dispersing the nickel as small crystallites on a refractory oxide support, which must be sufficiently porous to facilitate the access of the gas to the nickel surface. The choice of support is then governed by the surface area required, as well as the need for stability in the operating environment. Typical ceramic supports are α-alumina, the most stable alumina, magnesia, magnesium aluminium spinel, zirconia, and other ceramic oxides (Rostrup-Nielsen, 1984). The physical form of these catalysts has been developed for many years to maximise activity and rate of heat transfer within the reformer reactor. Usually ring-shaped pellets are used in steam reforming. Catalyst pellet sizes are generally a compromise between ensuring good packing, mechanical stability, and low pressure drop (Clarke et al., 1997). One curiosity with these Ni catalysts is that it has been demonstrated that both with impregnated and precipitated catalysts there is an optimum beyond which an increase in the nickel content does not produce any further significant increase in activity. Typically these optima are approximately 20% for precipitated catalysts and up to about 15% for impregnated catalysts, although these values depend on the nature and physical properties of the actual support (Twigg, 1996; Rostrup-Nielsen, 1984).

3.2.2 Steam Reforming Kinetics & Mechanisms

Several studies have been published on the kinetics of methane steam reforming. There is a general agreement that the reaction is first order in methane, but there is less agreement with the other kinetic parameters. This is due, in part, to the use of different catalysts or experimental conditions, but also to the lack of appreciation of diffusion and heat transfer limitations. References where some of these kinetic expressions can be found include Rostrup-Nielsen (1984), Xu and Froment (1989a), Twigg (1996), Clarke et al. (1997), etc.

Here, and since the focus of this work is the coupling of the system, well-documented kinetics and catalyst properties, such as the work of Xu and Froment (1989a, 1989b), are used. These rate models are considered to be the most general and have been extensively used in the literature (Avci et al., 2001; Grevskott et al., 2001;

Ding and Alpay, 2000; Kvamsdal et al., 1999; Levent et al., 1998; De Groote and Froment, 1996). Xu and Froment (1989a) derived the intrinsic rate equations for the steam reforming of methane on a $Ni/MgAl_2O_4$ catalyst. For this purpose, they considered a large number of detailed reaction mechanisms. After analysis of the system behaviour and from a set of eleven reactions that may occur among CH_4, CO_2, CO, H_2, H_2O, and carbon, they considered that the process in study is described by the steam reforming (3.IX and 3.XI) and the water-gas shift (3.X) reactions. However, since the shift reaction has been assumed in equilibrium in the SOFC model (see Chapter 2), the same is done in the reformer model. This assumption reflects the real situation as it is known that the ceramic materials used in solid oxide fuel cells are active for the shift reaction at SOFC temperatures and that this reaction is generally in equilibrium (Laosiripojana, 2003; Nagata et al., 2001).

$$CH_4 + H_2O \leftrightarrow 3H_2 + CO \quad (3.IX)$$

$$CO + H_2O \leftrightarrow H_2 + CO_2 \quad (3.X)$$

$$CH_4 + 2H_2O \leftrightarrow 4H_2 + CO_2 \quad (3.XI)$$

Among the large number of reaction schemes developed, two were proposed to represent the steam reforming system kinetics. The two schemes proposed differ in the appearance of CO and CO_2, and followed these assumptions:

i. H_2O reacts with surface Ni atoms, yielding adsorbed oxygen and gaseous H_2.

ii. Methane is adsorbed on surface nickel atoms. The adsorbed CH_4 either reacts with the adsorbed oxygen or is dissociated to form chemisorbed radicals, such as CH_3-*l*, CH_2-*l*, CH-*l*, and C-*l*.

iii. The concentrations of the carbon-containing radicals, CH_3-*l*, CH_2-*l*, CH-*l*, and C-*l*, are much lower than the total concentration of the active sites.

iv. The adsorbed oxygen and the carbon containing radicals react to form CH_2O-*l*, CHO-*l*, CO-*l*, or CO_2-*l*.

v. The hydrogen formed is directly released into the gas phase and/or the gaseous hydrogen is in equilibrium with H-*l* or H_2-*l*.

vi. All the reaction schemes are thought to have a step for reactions (3.IX), (3.X), and (3.XI) with a rate potentially much slower than that of the other steps, so that it controls the overall reaction rate. It is the rate-determining step (r.d.s.).

The reaction scheme leading to the retained set of rate equations is shown in Table 3.1. The rate equations were written for the rate-determining step of each of the three global reactions (3.IX), (3.X), and (3.XI) in terms of concentration of adsorbed species, which were then eliminated by means of the Langmuir equilibrium relations and a balance to the active sites. The resulting rate equations are presented in Table 3.2 in terms of gas-phase partial pressures and contain a denominator that represents the adsorption of reacting species.

Table 3.1 Steam reforming reactions scheme.

H_2O	+	l	=	O-l	+ H_2	
CH_4	+	l	=	CH_4-l		
CH_4-l	+	l	=	CH_3-l	+ H-l	
CH_3-l	+	l	=	CH_2-l	+ H-l	
CH_2-l	+	O-l	=	CH_2O-l	+ l	
CH_2O-l	+	l	=	CHO-l	+ H-l	
CHO-l	+	l	=	CO-l	+ H-l	r.d.s. R_1
CO-l	+	O-l	=	CO_2-l	+ l	r.d.s. R_2
CHO-l	+	O-l	=	CO_2-l	+ H-l	r.d.s. R_3
CO-l			=	CO	+ l	
CO_2-l			=	CO_2	+ l	
2H-l			=	l	+ H_2-l	
H_2-l			=	H_2	+ l	

Table 3.2 Rate equations for reactions (3.IX-3.XI).

$$R_1 = \frac{k_1}{p_{H_2}^{2.5}}\left(p_{CH_4}p_{H_2O} - \frac{p_{H_2}^3 p_{CO}}{K_1}\right)DEN^{-2} \tag{3.1}$$

$$R_2 = \frac{k_2}{p_{H_2}}\left(p_{CO}p_{H_2O} - \frac{p_{H_2}p_{CO_2}}{K_2}\right)DEN^{-2} \tag{3.2}$$

$$R_3 = \frac{k_3}{p_{H_2}^{3.5}}\left(p_{CH_4}p_{H_2O}^2 - \frac{p_{H_2}^4 p_{CO_2}}{K_3}\right)DEN^{-2} \tag{3.3}$$

$$\text{where } DEN = 1 + K_{CO}p_{CO} + K_{H_2}p_{H_2} + K_{CH_4}p_{CH_4} + \frac{K_{H_2O}p_{H_2O}}{p_{H_2}} \tag{3.4}$$

The rate coefficients, k_j, and the adsorption constants, K_i, were parameterised according to the Arrhenius and van't Hoff equations (3.5) and (3.6), respectively. Table 3.3 presents the resultant parameters.

$$k_j = A(k_j)\exp\left[-\frac{E_j}{RT}\right] \tag{3.5}$$

$$K_i = A(K_i)\exp\left[-\frac{\Delta H_i}{RT}\right] \tag{3.6}$$

Table 3.3 Estimated parameters for equations (3.5) and (3.6).

Pre-exponential factors for Arrhenius equation (3.5) and van't Hoff equation (3.6)						
$A(k_1)^*$	$A(k_2)^{**}$	$A(k_3)^*$	$A(K_{CO})^{***}$	$A(K_{H_2})^{***}$	$A(K_{CH_4})^{***}$	$A(K_{H_2O})$
$4.225\ 10^{15}$	$1.955\ 10^{6}$	$1.020\ 10^{15}$	$8.23\ 10^{-5}$	$6.12\ 10^{-9}$	$6.65\ 10^{-4}$	$1.77\ 10^{5}$

Activation energy (kJ/mol)			Enthalpy change of adsorption (kJ/mol)			
E_1	E_2	E_3	ΔH_{CO}	ΔH_{H_2}	ΔH_{CH_4}	ΔH_{H_2O}
240.1	67.13	243.9	-70.65	-82.90	-38.28	88.68

* ($kmolbar^{0.5}/kg_{cat}h$). ** ($kmol/barkg_{cat}h$). *** (bar^{-1}).

Table 3.4 presents the temperature dependent expressions for the equilibrium constants, K_j, of reactions (3.IX-3.XI) (Twigg, 1996).

Table 3.4 Equilibrium constants of reactions (3.IX-3.XI).

$$\ln(K_1) = -[z(z(z(0.2513\times z - 0.3665) - 0.58101) + 27.1337) - 3.2770]^* \tag{3.7}$$

$$\ln(K_2) = [z(z(0.63508 - 0.29353\times z) + 4.1778) + 0.31688] \tag{3.8}$$

$$\ln(K_3) = [z(z(z(0.13432\times z + 0.02857) - 1.23864) + 22.9354) - 3.58003]^* \tag{3.9}$$

where $z = 1000/T - 1$

* (bar^2).

3.3 Modelling of Fixed-Bed Reactors

As is well known, most catalytic processes are carried out in fixed-bed reactors. Many considerations go into the design of these types of reactors, including mode of heat exchange, pressure drop, safe operating temperature range, mode of catalyst packing,

etc. Rapid temperature rises in the bed, caused by highly exothermic reactions, may have, for example, an unfavourable effect in selectivity, equilibrium conversion, and/or catalyst stability, or it may even lead to an unsafe reactor operation under certain feed conditions. In the case of a highly endothermic reaction, the temperature drop may be such as to extinguish the reaction before the desired conversion is attained. Therefore, these and several other issues must be considered. Reactor modelling is becoming more and more important in the design of fixed-bed reactors. Such models can have a wide range of applications, such as: scaling-up laboratory or pilot-plant reactors; improving performance of existing reactors; optimising configurations and operating conditions; determining control and start-up policies; and analysing the effect of different feedstocks, catalysts, and reaction conditions on product distribution (Martinez et al., 1985). The required degree of sophistication of a certain model depends on the required level of prediction accuracy, on the economic incentive for that prediction, and on the availability of accurate design information and adequate computing facilities.

Several assumptions need to be made to write realistic but useful models for fixed-bed catalytic reactors. In the past 50 years, numerous studies have been made on this subject, resulting in the development of various mathematical models that can now be found in a number of textbooks, such as Froment and Bischoff (1990), Rase (1990), Lee (1985), Smith (1981), among others. Fixed-bed reactor models can be categorised in many ways, each category having different levels of complexity. These can be, for instance, pseudo-homogeneous or heterogeneous models, and/or one-dimensional or two-dimensional models. Models can also be distinguished by considering or not axial mixing or dispersion in the reactor, by the intra/interparticle composition and temperature gradients assumed, or by the different boundary conditions taken into account. Each one of these models can still be dynamic or steady-state, depending on whether or not time-dependent effects are considered. The variety of models so far established results from different combinations of the above mentioned categories. Thus, these models are all interrelated and, under simplifying assumptions, can all be derived from the more complex ones.

Additional phenomena that might have to be considered in establishing a reactor model include pressure drop through the fixed-bed, nonuniform velocity profile, variable porosity, dependence of certain properties in temperature and composition,

catalyst deactivation for dynamic models, etc (Martinez et al., 1985). The following sections explain the main differences within some of the above categories.

3.3.1 Pseudo-Homogeneous & Heterogeneous Models

A pseudo-homogeneous model does not account explicitly for the presence of the catalyst but instead it brings together the fluid and solid phases into a single continuous phase. A heterogeneous model considers both the fluid and the solid phases separately, having mass and heat balances for both of them (Avci et al., 2001; Quinta Ferreira et al., 1992a, 1992b, 1996; Rodrigues and Quinta Ferreira, 1990; Martinez et al., 1985). These kinds of models are further explained in Section 3.3.3.

3.3.2 One-Dimensional & Two-Dimensional Models

A one-dimensional model considers only variations along the axial direction of the reactor, in opposition with the two-dimensional one that can consider mass and/or heat variations both in the axial and radial directions. In a one-dimensional model, the only transport mechanism operating is the overall flow itself, and this can be considered of the plug flow type. Two-dimensional models are better for non-adiabatic reaction systems with a pronounced heat effect. The radial effects, represented by the first and second order derivative terms with relation to the radial reactor co-ordinate, are then important for highly endothermic or exothermic reactions which tend to be heated or cooled from the reactor wall (Quinta Ferreira et al., 1992a, 1992b, 1996; Rodrigues and Quinta Ferreira, 1990; Martinez et al., 1985). Rostrup-Nielsen (1984) refers the importance of using two-dimensional models for a more thorough analysis of the local parameters in a catalyst bed, such as the knowledge of the radial temperature gradients, which are important, for instance, in identifying the risk of carbon formation.

3.3.3 Axial & Radial Dispersion Terms

The most basic combination of the above categories leads to a pseudo-homogeneous one-dimensional model. This model is the most used until now, since it has been

considered sufficiently representative, but more so because it is the more convenient and simpler to use. However, it is argued that the flow in a fixed-bed deviates considerably from the ideal pattern because of flow velocity and temperature radial variations and of mixing effects due to turbulence and presence of the packing.

Mixing in the axial direction is accounted for by superimposing an effective transport mechanism on the overall transport by plug flow. The flux due to this mechanism is described by a formula analogous to Fick's law for mass transfer or Fourier's law for conduction heat transfer. Axial mixing smoothes axial gradients of concentration and temperature so that it decreases the conversion obtained in a given reactor. Mass and heat axial dispersion effects for a gas flowing through a packed bed are commonly characterised by the axial mass and heat Peclet numbers, Pe_{am} and Pe_{ah}*. It is normally considered that these effects are negligible compared to convection when either the axial Peclet numbers are large or the reactor length is more than fifty times the particle diameter (Odendaal et al., 1987; Froment and Bischoff, 1990). This is based on the mixing cell dispersion analogy, in which the bed is considered to consist of L/d_p CSTRs in series (Lee, 1985). Some more accurate criteria have been derived and can be found in Froment and Bischoff (1990). If axial dispersion is not negligible Pe_{am} and Pe_{ah} need to be determined. These are a function of the axial effective diffusivity coefficient, D_{ea}, and of the axial thermal conductivity coefficient, λ_{ea}, respectively (see notation). From an extensive review of experimental and theoretical results, Gunn (1987) derived correlations for D_{ea} in fixed beds of spheres and cylinders. However, for design purposes the axial mass Peclet number, Pe_{am}, based on the particle diameter, is generally considered to lie between 1 and 2, for Reynolds numbers based on the particle diameter higher than 1 (Odendaal et al., 1987). As for λ_{ea} little information is available. Votruba et al. (1972) evaluated the axial thermal conductivity in packed beds from steady-state axial temperature profiles. These authors used solid particles of different sizes and shapes covering a large interval of Reynolds numbers (Re between 0.1 and 10^3) and establishing an empirical relation for the estimation of the Peclet number for axial heat transport.

---

* From a certain model, several dimensionless parameters can be derived. These depend upon the system characteristics and operating conditions as well as upon the reaction kinetics. All the parameters have a physical meaning associated with them. The Peclet numbers are, for example, a measure of the relative magnitude of convection and diffusion transport on the reactor, both for mass or heat transport and on the axial or radial direction. See Notation for the mathematical definition of these parameters.

As mentioned above, when reactions with a pronounced heat effect are carried out in a fixed-bed reactor, there is a need for the model to predict temperature and conversion profiles in more detail. For this reason, use is often made of the effective transport concept for the flux of mass and heat in the radial direction, leading to the above-referred two-dimensional models. Mass and heat radial dispersion can also be characterised by the radial mass and heat Peclet numbers, Pe_{rm} and Pe_{rh}. However, while a large value of the Peclet number for axial dispersion results in negligible dispersion effects compared with convection, the inverse is true for radial dispersion, since now the transfer mechanism is conduction and a larger value of the radial Peclet number means a higher resistance to conduction. Normally, radial dispersion terms can not be neglected unless the bed is adiabatic. Lee (1985) refers that radial terms can be neglected if R/d_p does not exceed 4. Typical mass radial Peclet numbers are discussed in Appendix B.1.

The effective heat transport in the radial direction can be represented by the radial effective thermal conductivity coefficient, λ_{er}. When this effect is determined from heat transfer experiments in packed beds, it is often observed that λ_{er} decreases strongly in the vicinity of the wall. It is as if a supplementary resistance is experienced near the wall, which is probably due to variations in the packing density and flow velocity. Two alternatives are possible in such a case: either to use a mean λ_{er} or to consider λ_{er} to be constant in the central core of the reactor and introduce a new coefficient accounting for the heat transfer near the wall, α_R (Froment and Bischoff, 1990). When the prediction of the temperature profile is important, the second approach is normally preferred. This is the approach followed in this work. Froment and Bischoff (1990) states that the computed results are not very sensitive with respect to Pe_{mr} but are very sensitive with respect to λ_{er} and α_R. Kvamsdal et al. (1999) corroborated this view. These authors have used a dynamic two-dimensional pseudo-homogeneous dispersion model to simulate the performance of a fixed bed catalytic reformer. They have found that the choice of correlation for the wall heat transfer coefficient and the effective bed conductivity had a limited impact on the predicted conversions, but had a significant effect on the wall temperature predictions. They have also concluded that, although the existing correlations to calculate the above parameters should be improved, the correlations derived by De Wash and Froment (1972) were the best option. The calculation of these two parameters is also presented in Appendix B.1.

The approach just described is such that some of the equation parameters are effective as they lump fluid and solid phase phenomena that would otherwise have to be expressed by means of additional equations, to be solved simultaneously in the reactor simulation. This is the case for pseudo-homogeneous models, where lumped parameters, which represent the contribution of both phases, are normally used. However, for heterogeneous models, the radial heat transfer in the solid and fluid phases has sometimes been considered separately (Quinta Ferreira et al., 1992b; Martinez et al., 1985; De Wasch and Froment, 1971). Using a two-phase heterogeneous model for a fixed-bed reactor, Odendaal et al. (1987) studied the sensitivity of thermal transport in the axial and radial directions, in the highly exothermic solid catalysed oxidation of naphthalene. Such model considers a separate continuity equation for axial and radial dispersion of heat in the solid phase and also heat transfer between the fluid and the reactor wall as well as between the solid catalyst and the wall. Odendaal et al. (1987) also reported that axial dispersion of heat and mass in both the fluid and solid phases are of little consequence in both steady-state and transient operation modes for $L/d_p > 50$. However, they state that the radial temperature distribution is sensitive to the choice of both the bed solid phase effective conductivity and the fluid thermal Peclet number as well as to the wall coefficients governing fluid-wall and solid-wall heat transport at the boundary.

3.3.4 Intraparticle & Interparticle Resistances

Finally, heterogeneous models can also be distinguished by the different intraparticle and interparticle mass and heat gradients considered. In a fixed-bed reactor, the reaction generally takes place within the catalyst particles and the fluid phase is simply a medium that supplies the reactants and carries out the products. For very rapid reactions with an important heat effect, where the rate of reaction is not uniform throughout the particle, it may be necessary to distinguish between conditions in the fluid, on the catalyst surface, and/or inside the catalyst. Hence, in such cases, equations describing the concentration and temperature inside the particle are normally added to the fluid phase set of equations. Nevertheless, it is generally accepted that the main resistance to mass transfer is inside the pellet and that the main resistance to heat transfer is in the film

surrounding the particle. This way, the most common models consider isothermal particles with thermal gradients on the film surrounding the particle (Quinta Ferreira et al., 1992a, 1992b, 1996; Odendaal et al., 1987). The influence of the pellet phase variables is, in some cases, expressed in terms of an effectiveness factor, η. In its classical sense, the effectiveness factor is a factor that multiplies the reaction rate at the particle surface conditions to yield the rate that is actually experienced when the conditions inside the particle are different. This factor then measures the influence of transport resistances on the overall reaction rate and is defined as the ratio between the actual rate of reaction and the rate of reaction at the catalyst surface (equation (3.17) in Table 3.5). For isothermal pellets, for example, a unity value of η indicates that intraphase diffusion is not a significant limitation, whereas lower values of η indicate that only some catalyst percentage is being used in an effective manner. For non-isothermal pellets, and if the reaction taking place is exothermic, η can even be higher than unity. The calculation of this effectiveness factor may be more or less complicated, ranging from the solution of simple algebraic equations (that result from the analytical solution of the catalyst particle mass balances, usually possible for isothermal first order reactions) to the solution of coupled (mass and heat balances) nonlinear boundary value problems. Quinta Ferreira et al. (1992a, 1992b, 1996) and Rodrigues and Quinta Ferreira (1990) considered the case where the catalysts have large-pores and developed a two-dimensional heterogeneous model which includes both diffusion and intraparticle convection as a mechanism of transport inside the solid catalyst particle. This model was compared with two other two-dimensional models, a pseudo-homogeneous and conventional heterogeneous, and an increase in the effectiveness factors was reported. De Groote and Froment (1996) on the other hand, developed a one-dimensional heterogeneous model where the effectiveness factors were set to certain constant values.

Heterogeneous models can also differ on the geometry assumed to model the catalyst pellets that compose the fixed-bed. These pellets can have different shapes or geometries, which may not always be considered uniform. The most common geometries assumed when modelling catalyst pellets are the slab, the cylindrical, and the spherical geometries.

3.3.5 Boundary Conditions

One last point in modelling is related to the boundary conditions. As can be seen from the models described, these can be composed of ordinary or differential equations that can be first or second-order. For a steady-state pseudo-homogeneous one-dimensional model, the resultant model is composed of a set of ordinary differential equations that normally only require the initial (normally at the entrance of the reactor) composition and temperature to be set. In the extreme case of model complexity, is the dynamic heterogeneous, two-dimensional model, accounting for axial dispersion and intra and interparticle mass and temperature gradients. In such a case, a complex two-point boundary-value problem composed of a set of ordinary and partial differential equations is obtained. Such a model requires initial conditions for the composition and temperature profiles, as well as two boundary conditions for the axial reactor coordinate, the radial reactor coordinate, and the radial catalyst particle coordinate. Each one of these boundary conditions depends on the system under study.

3.3.6 Parameters in Modelling of Fixed-Bed Reactors

Just as important as the model selection is the existence of reliable values for the parameters involved. The difference that exists between elaborated and simple models is, in many cases, of the same order of magnitude as the difference generated by the uncertainty on those parameters. Of special relevance is the determination of heat transfer parameters, whose uncertainties can, for instance, significantly influence the prediction of the hot-spot value in nonadiabatic reactors, important in preventing from catalyst sintering or reactor runaway (Martinez et al., 1985).

Heat and mass transfer parameter can either be evaluated from correlations or experimental measurements. Correlations are the simplest and cheapest way of doing so and are, in most cases, available in the literature. However, the dispersion of data is so large that care must be taken when selecting a particular correlation. When both transfer and kinetic parameters are simultaneously obtained from experimental data, a good fitting is expected. However, a large interdependence of those parameters can exist and extrapolation of any of the values can be dangerous (Martinez et al., 1985).

In this thesis, all parameter values are based either in values found or calculated using correlations in the literature (Appendix B.1). Based on the issues discussed above, the fixed-bed steam reforming reactor model developed can now be presented.

3.4 Fixed-Bed Steam Reforming Reactor Model

This section is concerned with the fixed-bed steam reforming reactor model. As seen above, steam reforming is a highly endothermic reaction that is normally characterised as having diffusional limitations inside the catalyst particle (Xu and Froment, 1989b). In addition, the system dimensions (that are only presented in the next chapter) are such that $L/d_p >> 50$ and $D_R/d_p > 10$. Based on these and on the issues discussed on Sections 3.3.1-3.3.4, it was considered that the best model to describe the reformer behaviour would be a heterogeneous, two-dimensional one, that accounts both for intraparticle and interparticle mass gradients and for interparticle thermal gradients. The described steady-state reactor model is presented in Table 3.5.

As a heterogeneous model is being considered, both the fluid and the solid phases are modelled. The model is composed of the fluid phase mass and energy balances (3.10-3.11), of the solid phase or catalyst particle mass balance (3.16), and of the fluid/particle interface or catalyst particle energy balance (3.17). The chemical species considered are CH_4, H_2O, CO, H_2, and CO_2. The mass and energy balances to the fluid phase are derived assuming constant velocity, constant density and heat capacity of the fluid phase, and constant dispersion coefficients. Tests have been made to check whether constant velocity and density were sensible assumptions to take. Differences encountered were found negligible. The boundary conditions (3.12) and (3.13) imply that there is symmetry of composition and temperature around the centreline of the reformer and that there is no reactant transport across the reformer wall. Equation (3.14) is not the commonly used energy balance boundary condition. If just the first term of the right hand side were used, it would mean that the heat transfer to the heating fluid (as an endothermic reaction is taking place), whose temperature is T_f is equal to the heat conducted at the interior wall. However, there are two terms in equation (3.14). In the particular case under study here, and as the reformer and SOFC models need to be coupled (Chapter 2), T_f is the temperature of the gas stream flowing

through the fuel channel in the solid oxide fuel cell, and hence, that first term accounts for the overall conduction heat transfer from the SOFC to the reformer. An equivalent relation on the solid oxide fuel cell side has been presented in Chapter 2. The second term on the right hand side of equation (3.14) accounts for radiation between the SOFC solid structure (see Chapter 2) and the reformer.

Table 3.5 Steady-state tubular packed-bed catalytic reactor model.

Fluid Phase

Mass balance

$$-u_s\frac{\partial C_{i,b}}{\partial z}+\varepsilon D_{er}\left[\frac{\partial^2 C_{i,b}}{\partial r^2}+\frac{1}{r}\frac{\partial C_{i,b}}{\partial r}\right]+k_m a_v\left(C_{i,s}^S-C_{i,b}\right)=0 \qquad (3.10)$$

Energy balance

$$-u_s\left(\rho c_p\right)\frac{\partial T_b}{\partial z}+\lambda_{er}\left[\frac{\partial^2 T_b}{\partial r^2}+\frac{1}{r}\frac{\partial T_b}{\partial r}\right]+k_h a_v\left(T_s^S-T_b\right)=0 \qquad (3.11)$$

Boundary conditions

$$r=0,\ z\geq 0:\quad \left.\frac{\partial C_{i,b}}{\partial r}\right|_{r=0}=0,\quad \left.\frac{\partial T_b}{\partial r}\right|_{r=0}=0 \qquad (3.12)$$

$$r=r_R,\ z\geq 0:\quad \left.\frac{\partial C_{i,b}}{\partial r}\right|_{r=r_R}=0, \qquad (3.13)$$

$$-\lambda_{er}\left.\frac{\partial T_b}{\partial r}\right|_{r=r_R}=\alpha_R\left(T_b|_{r=r_R}-T_f\right)+\frac{\sigma\left(T_b^4|_{r=r_R}-T_{ss}^4\right)}{\frac{1}{\epsilon_1}+\frac{A_R}{A_f}\left(\frac{1}{\epsilon_2}-1\right)} \qquad (3.14)$$

$$z=0,\ r\geq 0:\quad C_{i,b}=C_i^0,\quad T_b=T^0 \qquad (3.15)$$

Catalyst Particle

Mass balance

$$\frac{1}{r_p^2}\frac{\partial}{\partial r_p}\left[r_p^2 D_e\frac{\partial C_{i,s}}{\partial r_p}\right]+\rho_S\sum_j \nu_{ij}R_j=0 \qquad (3.16)$$

Energy balance

$$\rho_B\sum_j \eta_j(-\Delta H)_j R_j^S-k_h a_v\left(T_s^S-T_b\right)=0,\quad \eta_j=\frac{1}{R_j^S V_p}\int_{V_p}R_j dV_p \qquad (3.17)$$

Boundary conditions

$$r_p=0,\ r\geq 0,\ z\geq 0:\quad \left.\frac{\partial C_{i,s}}{\partial r_p}\right|_{r_p=0}=0 \qquad (3.18)$$

$$r_p=d_p/2,\ r\geq 0,\ z\geq 0:\quad -D_e\left.\frac{\partial C_{i,s}}{\partial r_p}\right|_{r_p=d_p/2}=k_m\left(C_{i,s}^S-C_{i,b}\right) \qquad (3.19)$$

Equation (3.17) gives the energy balance to the fluid-catalyst particle interface. The influence of the reaction occurring inside the catalyst particle is accounted for through the use of the effectiveness factor presented. The determination of this factor requires the solution of equations (3.16-3.19), that give both the concentration profiles inside a particle and the catalyst surface temperature for each radial and axial coordinate throughout the reformer. The catalyst particle is assumed to have spherical geometry. Once again, the boundary conditions (3.18) and (3.19) establish the symmetry around the catalyst particle centre and the mass transfer between the solid and fluid phases. As can be seen, the solid phase is not modelled separately from the fluid phase, taking into account the heat transfer through the catalytic bed, but instead the concept of effective heat conduction (discussed in Section 3.3.4) that lumps the two phases together is used. This kind of models can also be referred to as pseudo-heterogeneous models.

From Table 3.5 it can be seen that the derived model has six parameters that determine the behaviour of the system. These are the mass and heat transfer coefficients for the film surrounding the reformer particles, k_m and k_h, the effective diffusivity and thermal conductivity in the radial direction of the fixed-bed, D_{er} and λ_{er}, the overall heat transfer coefficient, α_R, and the effective diffusivity in the catalyst particle, D_e. All these parameters as well as the fluid phase properties are considered constant throughout the reactor. These were calculated from well-known correlations and estimation methods. Detailed information on the correlations used and assumptions made can be found in Appendix B.1.

All the input parameters, such as initial temperature and composition, system dimensions and properties, and model parameters for both the steam reformer and the solid oxide fuel cell are presented in the next chapter, together with the main simulation results obtained. The values of the physical properties are presented in Appendix B.2.

Notation

$A(K_i)$	pre-exponential factor of the adsorption constant, K_i
$A(k_j)$	pre-exponential factor of the rate coefficient, k_j
A_f	fuel channel outer surface area $[2\pi r_f L]$, m^2
A_R	reformer outer surface area $[2\pi r_R L]$, m^2

a_v	external particle surface area per unit reformer volume $[6/d_p(1-\varepsilon)]$, m^{-1}
C_i	molar concentration of component i, mol/m^3
c_p	fluid phase heat capacity, kJ/kgK
D_e	effective diffusivity in the catalyst particle, m^2/s
D_{ea}	effective diffusivity in the axial direction, m^2/s
D_{er}	effective diffusivity in the radial direction, m^2/s
d_p	catalyst particle diameter, m
D_R	reactor diameter, m
E_j	activation energy of reaction j, kJ/mol
k_h	heat transfer coefficient - film surrounding the reformer particles, kJ/m^2sK
k_m	mass transfer coefficient - film surrounding the reformer particles, m/s
K_1, K_3	equilibrium constant of reactions I and III, bar^2
K_2	equilibrium constant of reaction II
K_{CH_4}	adsorption constant for CH_4, bar^{-1}
K_{CO}	adsorption constant for CO, bar^{-1}
K_{H_2}	adsorption constants for H_2, bar^{-1}
k_j	rate constant of reaction j
L	system length, m
P	pressure
p_i	partial pressure of component i, bar
Pe_{ah}	axial heat Peclet number $[d_p \varepsilon u_i \varrho c_p / \lambda_{ea}]$
Pe_{am}	axial mass Peclet number $[d_p u_i / D_{ea}]$
Pe_{rh}	radial heat Peclet number $[d_p \varepsilon u_i \varrho c_p / \lambda_{er}]$
Pe_{rm}	radial mass Peclet number $[d_p u_i / D_{er}]$
Pr	Prandtl number
r	radial coordinate in the reformer, m
R_j	rate of reaction j in the reformer, $mol/kg_{cat}s$
r_p	radial position in the spherical reformer particles, m
r_R, r_f	reactor and fuel channel outer radius, m
$\Re$	gas constant, kJ/molK
Re	Reynolds number
Sc	Schmidt number
T	temperature, K
u_s	superficial velocity in the reformer, m/s
u_i	interstitial velocity in the reformer, m/s
V_p	catalyst particle volume, m^3
z	system axial coordinate, m

Greek letters

α_R	overall heat transfer coefficient, kJ/m^{2}sK
$(-\Delta H)_j$	heat of reaction j in the reformer, kJ/mol
$(-\Delta H)_i$	enthalpy change of adsorption, kJ/mol
$\in_1, \in_2$	emissivity
ε	void fraction of the packing
ε_p	catalyst porosity
η	reformer catalyst particle effectiveness factor
λ	fluid phase thermal conductivity, kJ/msK
λ_{ea}	effective thermal conductivity in the axial direction, kJ/msK
λ_{er}	effective thermal conductivity in the radial direction, kJ/msK
ρ	fluid phase density, kg/m^3
ρ_B	catalyst bulk density $[\rho_S(1-\varepsilon)]$, kg$_{cat}$/m^3
ρ_S	catalyst density, kg$_{cat}$/m^3
σ	Stefan-Boltzmann constant, W/m^{2}K^4
ν_{ij}	stoichiometric coefficient of component i in reforming reaction j

Superscripts

0	feed conditions
S	catalyst particle surface

Subscripts

b	bulk phase in the reformer
f	fuel channel
i	component
j	reaction
p, s	catalyst particle
R	reformer
ss	solid structure

Chapter 4

Internal Methane Steam Reforming Solid Oxide Fuel Cell – Results

Summary

In this fourth chapter, the solid oxide fuel cell and fixed-bed steam reforming tubular reactor models developed in the previous two chapters are finally coupled and used to simulate temperature, composition, and relevant electrochemical variables along the reformer tube and fuel cell. Such coupling can create, depending on the operating conditions, either an indirect or a combined indirect and direct internal reforming solid oxide fuel cell. Both these configurations of internal reforming are here studied. A base case is first defined and analysed and only then the response to changes in some of the parameters is investigated.

Outline

4.1 Introduction

The first chapter of this thesis introduced the subject of solid oxide fuel cells and internal steam reforming and explained the relevance of thermally coupling these two concepts to achieve a more efficient and simpler to design system. The main challenge associated with an indirect internal reforming fuel cell configuration was then indicated as being the mismatch between the thermal load associated with the steam reforming rate at typical SOFC temperatures and the local amount of heat available from the fuel cell reactions, which is expected to lead to significant local cooling even if extinction of the reforming reactions is avoided. Chapters 2 and 3 were related to the development of the SOFC and fixed-bed steam reforming tubular reactor models, respectively. In this fourth chapter, the steady-state simulation results obtained as a consequence of coupling these two models are used as the means to demonstrate the described local cooling effects as well as the solutions proposed for the operation of such a system. Such coupling can create, depending on the operating conditions, either an indirect internal reforming solid oxide fuel cell (IIR SOFC) or a combined indirect and direct internal reforming SOFC (IIR-DIR SOFC) if some methane flows through from the reformer to the fuel cell anode (methane slippage). Section 4.2 presents the results related to an indirect internal reforming SOFC (assuming no methane slippage) and Section 4.3 the results related to a combined indirect and direct internal reforming SOFC.

4.1.1 Solution Method for the Developed Models

As seen in the previous two chapters, the steady-state SOFC model is one-dimensional in the axial direction (see Section 2.4, Chapter 2) while the steady-state fixed-bed reactor model is three-dimensional in the axial and radial reactor directions, and in the radial catalyst particle co-ordinate (see Section 3.4, Chapter 3). The resulting system of equations is then a two-point boundary-value problem composed by a complex set of first and second-order ordinary differential, second-order partial differential, and non-linear algebraic equations with thermal coupling along the system length.

To avoid convergence problems during the solution of the above-described model, the normal procedure of turning models into their dimensionless form was

adopted, although the resultant dimensionless equations are not presented here. For that purpose, all dimensionless variables were defined relative to the conditions at the inlet of the fixed-bed reformer. The same has been done for all the models and simulation results presented in this thesis.

For the solution of the resultant problem, the equations just described were simultaneously solved making use of the gPROMS modelling environment (general process modelling system, from Process Systems Enterprise Ltd.). The orthogonal collocation on finite elements spatial discretisation integration method was employed for each dimension. The order of the interpolation polynomials and number of elements used for the integration method were a compromise between the accuracy of results (minimisation of numerical problems) and capacity of the machine in use. Third-order collocation polynomials on 14, 2, and 4 elements, for the axial direction (this axial direction is common to both the reformer and the SOFC), radial reactor direction, and radial catalyst particle co-ordinate, respectively, was found to give a converged solution (in all simulations here presented) in which mass and energy balance errors associated with numerical integration did not exceed 1% (Table 4.2 in Section 4.2.1 illustrates the system energy balances). Any non-smoothness on the several profiles (particularly the temperature profiles) presented is just a consequence of the number of elements used.

Although only the final simulation results of the coupled reformer-SOFC model are here presented and discussed, the two models were first developed and tested separately and only then coupled together (each one of the models was initially tested using typical temperature profiles to simulate the presence of the other one). However, the IIR-SOFC system here studied is such that there is stream reversal of flow (reformer exit stream is the inlet stream to the SOFC fuel channel), thermal coupling between the reformer and the SOFC along the system length, and where steep temperature gradients can occur at the reformer entrance. All these factors lead to a complex mathematical problem of difficult initialisation. To initialise such problem it was necessary to create intermediate solutions that were then fed to the programme as initial estimates of all the variables. This was done in a similar procedure as the one of starting-up a process, by increasingly allowing for the chemical reactions to occur and for heat to be transferred between the two-coupled systems, and until the final problem solution was encountered.

4.2 Indirect Internal Reforming SOFC

The aim of this section is to present the simulation results of the developed indirect internal reforming solid oxide fuel cell model. The model is here used to simulate temperature, composition and relevant electrochemical variables along the reformer tube and fuel cell as well as their response to changes in some of the parameters. A base case is first defined and fully analysed and only then the change in some of the parameter values is studied. The purpose of studying these changes is twofold: (i) seek an improved set of operating conditions and (ii) check the system sensitivity to operating conditions and parameters. Many simulations for several combinations of the various operating conditions have been performed throughout the period of this work, although, for simplicity, only the results for a selected set of conditions (and respective changes), corresponding to the base case defined in the next section, are here presented.

4.2.1 Base Case

For this base case, the system length is taken to be 400 mm, the fuel and air inlet temperatures are both 1173 K, and the total operating pressure is 1 bar*. The reformer fuel feed molar composition is 23.5% CH_4, 47% H_2O, 2.2% CO, 6% H_2, and 21.3% CO_2 (steam to carbon ratio equal to 2). Such composition is calculated assuming a pre-mixed feed between pure methane and the recycled fuel channel exit gases, although recycling is not accounted for in the model. As mentioned before, when modelling fuel cells, in addition to all geometry and property data and inlet temperatures and compositions, it is usual to specify the average current density (or total current) being drawn by the fuel cell, the fuel utilisation factor, and the air ratio. These three parameters are given quantities from which the molar flux of fuel and air are then determined, as shown by equations (2.35-2.36), Section 2.4.3, Chapter 2. The current density considered is 3000 Am^{-2}, with a fuel utilisation of 75%, and an air ratio of 10

* For the fixed-bed reactor tube and for the base case conditions, the pressure drop is estimated to be 0.8 bar (Froment and Bischoff, 1990). This shows that in the future, and if modelling an equivalent fixed-bed reactor with such small catalyst particles, pressure drop should be taken into account. However, in the present study, the operating pressure considered, was assumed as an average value that applies throughout the system; a reasonable assumption, given all the uncertainties associated with the remaining estimates.

(this air ratio value was chosen such that the maximum fuel cell temperature does not exceed 1273 K); these values imply a molar flux of fuel of 1.77×10^{-4} mols^{-1} and a molar flux of air of 2.97×10^{-3} mols^{-1}. These are all typical values of solid oxide fuel cells operation (Achenbach, 1994; Ferguson et al., 1996). Note that, for convenience, these base conditions will also be used in Chapters 5 and 6. The remaining system dimensions and values assigned to the model parameters (either for the SOFC or for the fixed-bed reformer) are presented in Table 4.1. The notation is the same presented at the end of Chapters 2 and 3.

Table 4.1 Assigned model parameter values.

Parameter	Value	Parameter	Value
r_R	2.26×10^{-3} m	r_f	3.19×10^{-3} m
r_{ss}	4.09×10^{-3} m	r_a	4.67×10^{-3} m
d_p	0.4×10^{-3} m		
D_e	3.61×10^{-6} m^{2}s^{-1}	α_R	0.1 kJm^{-2}s^{-1}K^{-1}
D_{er}	1.19×10^{-4} m^{2}s^{-1}	λ_{er}	5.44×10^{-4} kJm^{-1}s^{-1}K^{-1}
k_m	1.69 ms^{-1}	k_h	0.574 kJm^{-2}s^{-1}K^{-1}
ρ_S *	2335.2 kg$_{cat}$m^{-3}	ε *	0.4
$h_a = h_f$	0.1 kJm^{-2}s^{-1}K^{-1}	$\epsilon_1=\epsilon_2$ **	0.9
R_{OHM}	3×10^{-5} Ωm^2	λ_{ss}	2×10^{-3} kJm^{-1}s^{-1}K^{-1}
k_{A,H_2}	2.13×10^{8} Am^{-2}	m	0.25
$k_{A,CO}$	2.98×10^{8} Am^{-2}	E_A	110 kJmol^{-1}
k_C	1.49×10^{10} Am^{-2}	E_C	160 kJmol^{-1}

* Xu and Froment (1989a, 1989b).** Bessette II et al. (1995) and Haynes and Wepfer (2001).

The values of the model parameters, such as mass and heat transfer coefficients, diffusivities and thermal conductivities, together with all the physical properties which they depend on, were determined (for the inlet conditions) in Appendices B.1 and B.2. These are all assumed to be average values, which apply throughout the system (a reasonable assumption, given the uncertainty associated with these estimates). The ohmic resistance and solid structure thermal conductivity values, are typical of a SOFC electrolyte at 1000 °C (Iwata et al., 2000; Larminie and Dicks, 2000; Bessette II et al., 1995; Minh and Takahashi, 1995; Ahmed et al., 1991). Table 4.1 also presents the kinetic parameters (Achenbach, 1994) for the activation overpotentials presented in Section 2.4.3, Chapter 2. From the models developed in Chapters 2 and 3, the only variables

missing are the enthalpy of reaction of both the reforming and electrochemical reactions as well as the Gibbs free energy required, for instance, for the calculation of the open-circuit potential (see Chapter 2). Such thermodynamic properties were calculated assuming ideal gas and by integration (according to the specific method rules) of the heat capacity of each component in the correspondent gas mixture. The heat capacity was, in turn, calculated using the method of Joback (Reid et al., 1988). All these were incorporated in the developed programme and allowed to vary with temperature.

Finally, a 'reduced activity' catalyst is used in the reformer. Specifically, an IIR catalyst relative activity is defined as the ratio between the activity of the catalyst in use and that of a conventional Ni catalyst (Xu and Froment, 1989a) at typical feed conditions (temperature, pressure, and composition). A reduced relative activity implies the use of either a conventional nickel catalyst with only a certain fraction of Ni content accessible or an inherently less active catalyst. For this base case a relative activity of 0.2% is considered. As will be seen, this level of activity reduction is required to avoid almost instantaneous conversion of methane at the reformer entrance. The simulation results obtained are now presented and discussed.

Figures 4.1 and 4.2 show some of the characteristic results for the just defined base case. The component mole fraction profiles in both the reformer and the SOFC fuel channel are presented, for an easier interpretation, in two separate figures, Figures 4.1a and 4.1b. It can be seen that, due to the very fast reforming reaction at such high temperatures, the methane is practically all consumed in the first one third of the reformer. Therefore, in this region, the hydrogen and carbon monoxide mole fractions increase rapidly while methane, water, and carbon dioxide decrease. After this point, there is no more methane to be reformed and the reverse shift reaction leads to a slight mole fraction decrease in H_2 and CO_2 and increase in CO and H_2O. The effect of the reformer fuel inlet composition on these profiles is analysed in Section 4.2.6. At the outlet of the reformer, the fuel stream molar composition is 44.9% H_2, 24.6% CO, 23.1% H_2O, and 7.4% CO_2. This stream flows back into the SOFC where the H_2 and CO are now gradually converted, by means of the electrochemical reactions, to H_2O and CO_2 (note that the flow of fuel in the SOFC fuel channel is counter-flow to both the fuel stream in the reformer and the air stream in the SOFC air channel). At the outlet of

the fuel channel, the fuel stream molar composition is 14.7% H_2, 7.3% CO, 53.3% H_2O, and 24.7% CO_2. The reason why the exit anode gas is still rich in both hydrogen and carbon monoxide is related to the chosen fuel utilisation value. As referred to above, for these base case simulations, the fuel utilisation is taken as 75%. This means that only 75% of the inlet fuel (in this case, 75% of the inlet methane) is taking part in the production of electricity. As discussed in Chapter 2, Section 2.2.4.1, high fuel utilisation values can represent a problem in fuel cell operation, since the hydrogen concentration and, consequently, the open-circuit potential and operating potential decrease with increasing fuel utilisation. This is why fuel utilisation values lower than 100% are normally used, and a fraction of the unconverted fuel is recycled.

As mentioned earlier, these simulation results are for a catalyst with a relative activity of 0.2%. The results show that, if a catalyst with a higher amount of nickel had been used, almost instantaneous methane conversion would have been observed. However, it is worth noting that, as the original catalyst is a highly active one with a high nickel content (Xu and Froment, 1989a, 1989b), the dilution is still within the envelope of commercially available steam reforming catalysts.

Figures 4.1c and 4.1d present the temperature profiles for the reformer (both at the centre and at the wall), the fuel channel, the solid structure, and the air channel. It can be seen that, although the steam reforming reaction is strongly endothermic, there is enough heat on the fuel cell side to enable such reaction. For a better understanding of the heat transfer phenomena within this coupled system, Table 4.2 illustrates the global energy balance to the system, as well as the partial energy balances to the reformer and fuel cell. For this purpose, and for each one of the three sub-systems, the enthalpy of the inlet and outlet streams, together with the heat consumed and/or produced due to the various reactions, the SOFC power output, and the heat transferred between the two systems, are presented. This is done first in more detail for the global system and then in a more compact manner for the reformer and SOFC alone. To determine the enthalpy of each stream, a reference temperature of 298 K and mean ideal gas heat capacity values between 298 K and the stream temperature were assumed for each component. For consistency, the enthalpy change of both the reforming and electrochemical reactions was determined based on the same reference temperature.

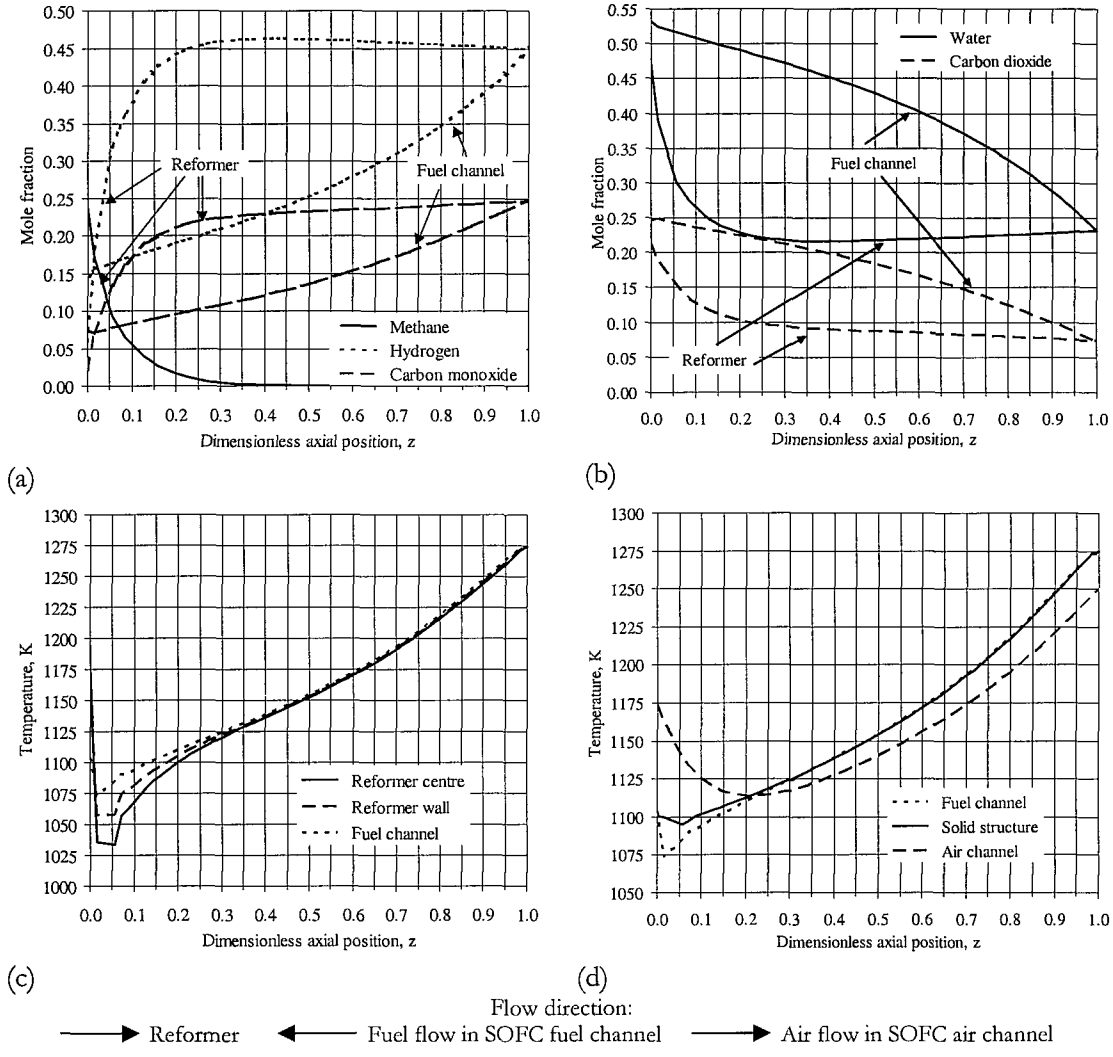

Figure 4.1 Reformer and fuel channel mole fraction profiles (a-b) and reformer and solid oxide fuel cell temperature profiles (c-d) for the base case.

From Table 4.2, the total heat produced in the fuel cell can be calculated as the difference between the enthalpy change due to the electrochemical reactions ("Reaction enthalpy change" in Table 4.2) and the fuel cell power output. This production of heat is, as shown previously (see Section 2.2.3, Chapter 2), due to entropy changes of the electrochemical reactions, resistance to current flow, and polarisation losses. For these conditions, and from the data in Table 4.2, the total heat required by the steam reforming reactions can be determined and represents 58% of that total heat produced in the cell. The remaining heat is responsible for the temperature increase of the fuel and air streams, as can be easily worked out from Table 4.2.

Under these base case conditions, and as defined in Chapter 2, the terminal voltage obtained is 0.644 V and the fuel efficiency, which reflects the inefficiency in terms of energy utilisation in the cell, 46.5%. One last consideration in terms of energy efficiency of this particular system is related to the requirement for cell cooling. As mentioned in Chapters 1 and 2, the cell cooling is usually achieved by flowing excess air through the cathode (Koh et al., 2000; Achenbach, 1994), which is why an air ratio value of 10 was here considered. However, one of the advantages of an IR-SOFC configuration is that this requirement for excess air is normally significantly reduced. For example, and for these conditions, if part of the total heat produced in the cell was not consumed by the steam reforming reactions, the air stream flowrate would have to be increased by a factor of around 2.5 in order to remove all the excess heat produced and guarantee that the total temperature increase across the cell would not exceed 100 K. If, however, the air flowrate was not altered, the outlet temperature of the air stream would be 100 K higher than the value observed in Figure 4.1d.

Table 4.2 Energy balances to the IIR-SOFC system (base case).

Global energy balance (W)			
	Inlet	Outlet	
Reformer	6.902		
SOFC fuel channel		8.203	
SOFC air channel	82.102	87.904	
	89.004	96.107	
Reaction enthalpy change*	22.374		
Power output		15.499	
Total	111.378	111.606	Error: 0.20%
Reformer energy balance (W)			
	Inlet	Outlet	
Reformer	6.902	8.595	
Reaction enthalpy change*		9.331	
Heat transferred from SOFC	10.981		
Total	17.883	17.926	Error: 0.24%
SOFC energy balance (W)			
	Inlet	Outlet	
SOFC	90.697	96.107	
Reaction enthalpy change*	31.705		
Power output		15.499	
Heat transferred to reformer		10.981	
Total	122.402	122.587	Error: 0.15%

* The reaction enthalpy change is added to the enthalpy of the inlet or outlet streams if it is an overall exothermic or endothermic process, respectively.

The simulations demonstrate the local cooling associated with the indirect internal reforming: the reformer temperature decreases rapidly by 140 K from its inlet value in the first 5% of the system length (see Figure 4.1c). This cooling effect is attributed to the specific reaction conditions, under which the inherent kinetics of the reforming reactions are extremely rapid and orders of magnitude higher than the corresponding fuel cell electrochemical reactions. In fact, for these conditions, and even though a diluted catalyst is being used, the indirect internal reforming reaction rate is about 170 times higher than the fuel cell electrochemical reactions. Such local cooling effects are not compatible with the SOFC ceramic materials and, thus, need to be eliminated. To eliminate such effect it is required to reduce the local reforming reaction rate and the corresponding local energy flux demand. However, the steam reforming catalyst still needs to provide sufficient activity for the lifetime of the stack so that the rate of the reforming reaction is matched to the rate of the electrochemical reactions (despite the high H_2O/CH_4 ratio of 2, some coking of the nickel catalyst will still occur over a long period of operation). On this basis, application of an appropriate reforming catalyst activity is essential to ensure that the temperature variations are kept to a minimum, to reduce thermal stresses and thereby contribute towards a long stack life. All this is discussed in the following sections and in the two next chapters.

As mentioned earlier, radiative heat transfer is also accounted for in the model. It has a particularly high influence on the temperature dip of 140 K observed in Figure 4.1c, as it accounts for 79% of the total heat transferred between the fuel cell and the reformer (also presented in Table 4.2). If the additional heat transfer by radiation were not accounted for, this dip would be as high as 204 K; this emphasises the fact that heat transfer by radiation needs to be considered when modelling systems operating at such high temperatures. Figure 4.1c also illustrates the temperature profiles within the reformer itself indicating both radial (between the centre of the reformer and the wall) and axial temperature gradients. From this figure, one could be led to assume that the inclusion of radial dispersion terms in the fixed-bed reactor model was an unnecessary assumption, as the maximum temperature difference between the reformer centre and the wall is 24 K. However, it should be noted that the reformer radius is only 2.26 mm, which results in a significant radial temperature gradient of 10.6 Kmm^{-1}. In addition, if

such radial dispersion terms were not taken into account in the fixed-bed reactor model, the temperature minimum value would probably have been overestimated.

Finally, from Figure 4.1d it can be noticed that the air stream leaves the system at the high temperature of 1250 K. This does not necessarily represent an operational drawback in terms of energy waste. The high-quality heat produced by SOFCs usually provides many opportunities for thermal integration, being potentially suited for industrial cogeneration applications (Minh and Takahashi, 1995).

The relevant electrochemical variables for the SOFC are presented in Figure 4.2. Figure 4.2a presents the open-circuit potential for standard temperature and pressure and pure reactants (for convenience, this is referred to as "standard potential"), the open-circuit potential (OCP), and the terminal potential or voltage. For the relation between these three different potentials, see Section 2.4.3, Chapter 2. Figures 4.2b and 4.2c present the anode and cathode overpotentials in terms of voltage and resistance, respectively. Finally, Figure 4.2d presents the different current densities, i.e., the total current density drawn from the cell and the partial current densities that result from the hydrogen and carbon monoxide oxidation reactions.

All the above figures are directly related to the cell component mole fraction and temperature profiles in Figure 4.1. As discussed in Chapter 2, the standard potential decreases with increasing temperature and the OCP, governed by the Nernst equation (equation (2.25) in Chapter 2), drops with the partial pressure of hydrogen as this is used up and replaced by steam. On the other hand, the current density is related to both the OCP and the SOFC temperature. Higher OCP values imply a higher difference between this and the terminal potential and, consequently, higher current density. Higher temperatures lead to lower overpotentials and, consequently, higher current density. It is noted from Figure 4.2d that the current density produced by carbon monoxide oxidation is higher than that produced by hydrogen oxidation. The ratio of these two current densities is equal to the inverse ratio of the respective polarisation resistances in Figure 4.2c. The purpose of showing the behaviour of the electrochemical variables in Figure 4.2 is to demonstrate that, the steep temperature gradients observed in Figure 4.1 are also very important in terms of the overall performance of the cell. As can be seen, the temperature decrease at the system entrance is responsible for high overpotentials in that region, and thus, for an overall less efficient operation.

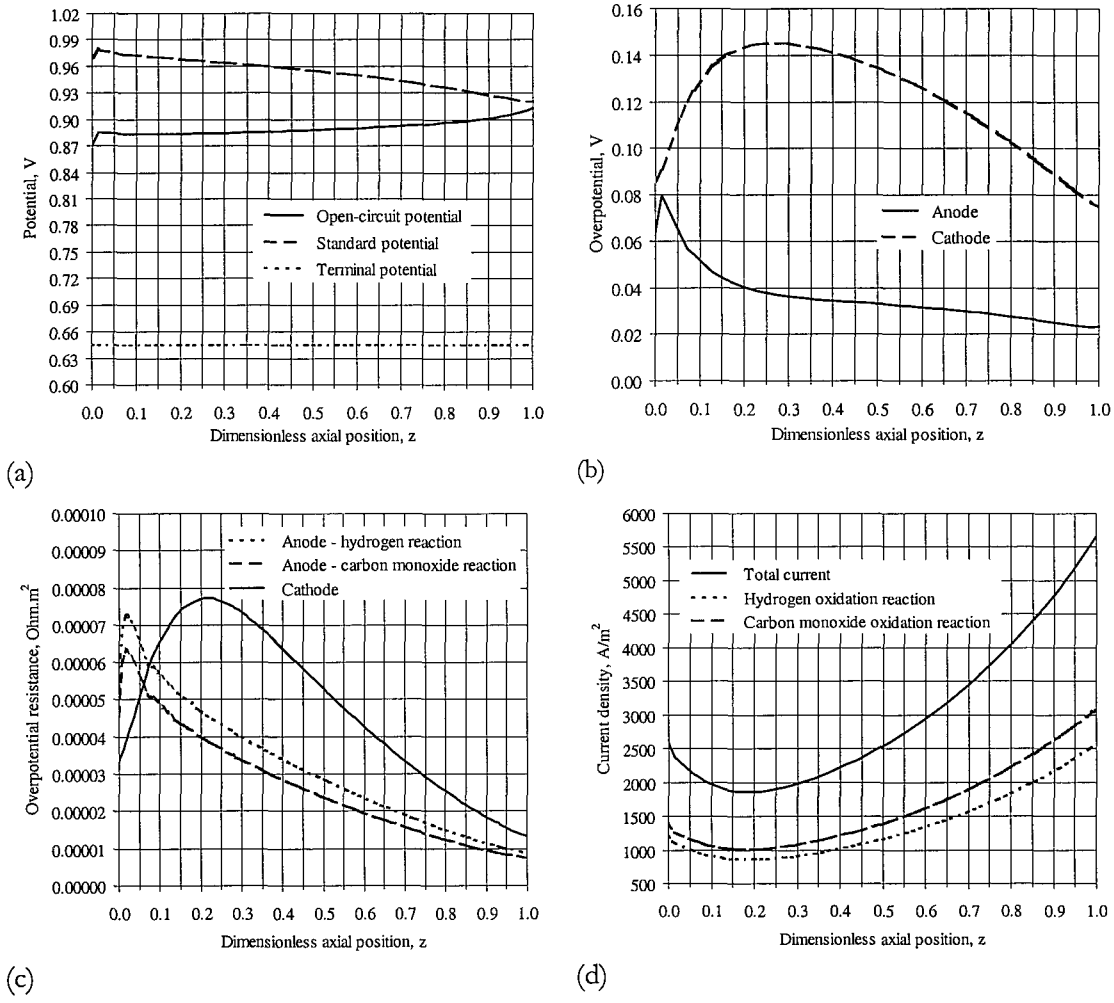

Figure 4.2 Potential (a), overpotential (b-c), and current density (d) profiles for the base case.

4.2.2 Effect of Different Catalyst Activities

As mentioned above, the observed local cooling is caused by the fast reforming reactions. To eliminate such effect it is then necessary to slow down the rate of such reactions (and the corresponding local energy flux demand). This could be achieved using catalysts with a much lower metal surface area, partially poisoned catalysts or catalysts sintered at high temperature. However, these methods are unlikely to guarantee long catalyst life. The first two methods lead to high loss of catalyst activity whenever deactivation occurs (either via coke deposition or sulphur poisoning), while in the last one, sintering can easily lead to complete pore blockage and hence, unacceptable

reduced overall rate of reaction (Ahmed et al., 1989). In Chapter 5 will be shown that the use of catalysts with non-uniform distribution of active metal within the inert support and a diffusive barrier placed near the outer surface of the catalyst is an effective way of achieving such rate reduction. One other possible solution for this problem is the use of oxide-based catalysts. Such catalysts have a much lower activity when compared with conventional Ni steam reforming catalysts and are highly resistant to carbon deposition (Ramírez-Cabrera et al., 2000a). Figure 4.3 illustrates the effect of using catalysts with activities that cover a range from metal to oxide-based catalysts.

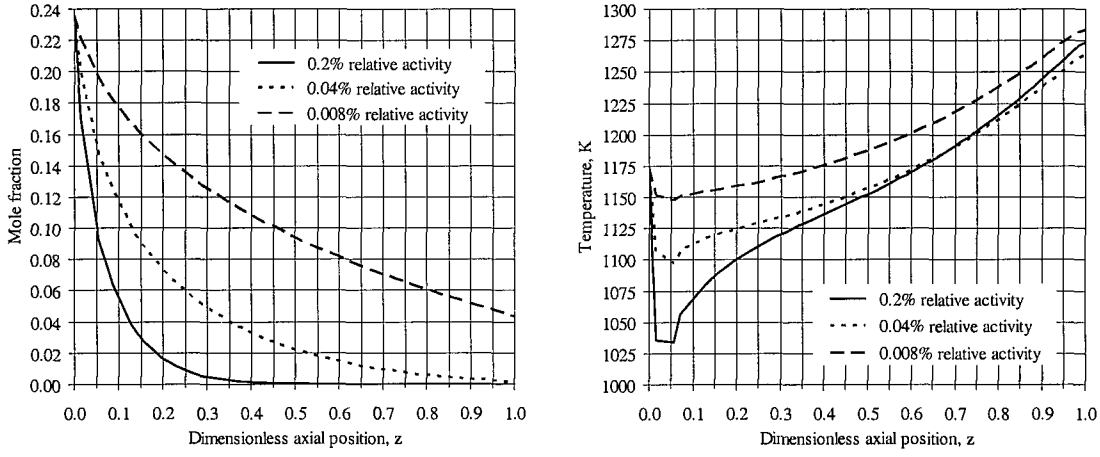

(a) (b)

Figure 4.3 Reformer CH_4 mole fraction (a) and temperature profiles (b) for different catalyst relative activities.

Figures 4.3a and 4.3b present the reformer mole fraction and temperature profiles, respectively, which result from using catalysts containing different relative activities: 0.2% (base case), 0.04%, and 0.008%. The simulations show that reducing the catalyst activity definitely smoothes the temperature profile at the entrance of the reformer. However, it can also be seen that for the lowest relative activity not all the methane is converted in the reformer and flows through to the SOFC anode. This phenomenon is referred to as methane slippage to the SOFC anode. As the methane concentration at the SOFC fuel channel was expected to be low in most cases, the current model neglects reforming on the anode. This places a lower limit on the catalyst content allowed. Therefore, anode reforming should be included when there is a significant carry-over of methane from the reformer. This is studied in Section 4.3.

4.2.3 Effect of Fuel Inlet Temperature

One alternative to reduce the reforming reaction rate at the reformer entrance could be reducing the fuel inlet temperature. Figure 4.4 shows the reformer temperature profiles for fuel inlet temperature values of 1023, 1098, and 1173 K (base case). Reducing the fuel inlet temperature while maintaining the air inlet one reduces the local cooling associated with the IIR, as the decrease in temperature from its inlet value at the reformer entrance becomes less pronounced (region z ~ 0.05 in Figure 4.4). However, another problem is posed as these lower fuel inlet temperature values lead to a large overall temperature increase along the cell tube that could require an increased air ratio to reduce it. Besides, lower inlet temperatures are associated with higher overpotentials that cause a decrease in the fuel cell potential and efficiency values, respectively, to 0.633 V and 45.7% for an inlet temperature of 1023 K and to 0.639 V and 46.1% for 1098 K. Thus, there is no obvious advantage in decreasing the fuel inlet temperature.

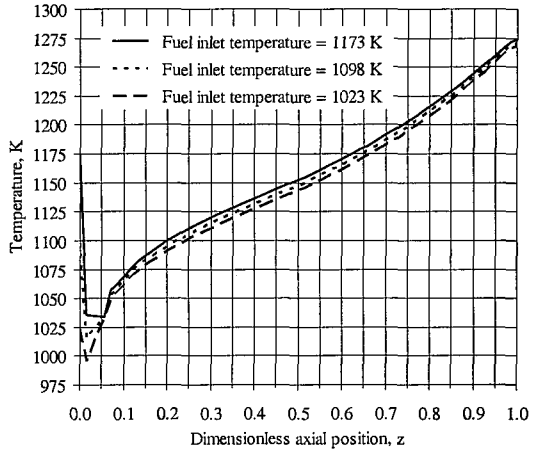

Figure 4.4 Reformer temperature profiles for different fuel inlet temperatures.

4.2.4 Effect of Current Density

The system sensitivity towards changes in the operating conditions is now examined. Figure 4.5 presents the reformer temperature profiles for average current density values of 2000, 3000 (base case), and 4000 Am^{-2}. An increase in the current density generates higher ohmic resistance and overpotentials, leading to lower terminal voltages and

efficiencies (51.8% for a current density of 2000 Am^{-2} against 41.8% for 4000 Am^{-2} - as compared to the base case value of 46.5%). To a less efficient operation is generally associated a higher amount of heat produced in the cell and, consequently, higher temperatures. As can be seen in Figure 4.5, as the current density increases, the outlet temperature increases significantly. It should be noted that these simulations are all for an air ratio value of 10 (base case). Generally, if the current density is to be increased, a higher air ratio value is required to remove that excess heat produced in the cell. The best operation is then a compromise between the power output increase resulting from a higher current density and the loss in power associated with a considerable increase in the air stream flowrate, as well as many other factors. As for the temperature dip at the reformer entrance, there is no significant difference between the three current density values considered. No significant differences are observed in the mole fraction profiles.

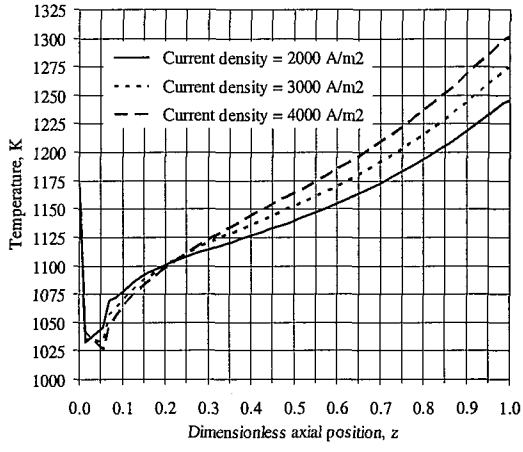

Figure 4.5 Reformer temperature profiles for different average current densities.

4.2.5 Effect of Operating Pressure

Figure 4.6 presents the reformer methane mole fraction and temperature profiles for operating pressure values of 1 (base case), 5, and 10 bar (note that an increase in the operating pressure does not imply a change of the inlet flowrates but only of the velocity of each stream). From Figure 4.6 it can be seen that as the pressure increases the methane consumption rate decreases, reducing the local cooling effect at the reformer entrance. Two different effects contribute to this. On one hand, the reaction

rate decreases with increasing pressure. In fact, such an effect could have been a priori predicted by observing the kinetic expressions used for the reforming reaction rate (Table 3.2 in Chapter 3). If these are divided into the terms corresponding to the forward and to the backward reactions, it can be easily worked out that with an increase in the operating pressure, the first term decreases and the second one increases. This is if only the hydrogen partial pressure term (to the power of 2.5 or to 3.5) in the denominator is taken into account. However, the term DEN^{-2}, decreases with increasing pressure, further contributing to a reaction rate decrease. On the other hand, if the pressure increases, higher open-circuit potential and lower overpotentials are obtained (Section 2.4.3, Chapter 2). This leads to a higher terminal potential and power output, and to system efficiencies of 53.1% for an operating pressure of 5 bar and of 55.5% for 10 bar (as compared to the base case value of 46.5%). As a consequence of this more efficient operation, the overall temperature of the system decreases, further decreasing the reforming reaction rate. Hence, in this particular case, the observed decrease in the methane rate consumption in Figure 4.6a, is in part due to the kinetic expressions in use. If different expressions were used, a different behaviour would be expected. An example of this is seen in Section 4.3.8, where instead of Ni catalysts, IIR oxide-based catalysts are considered.

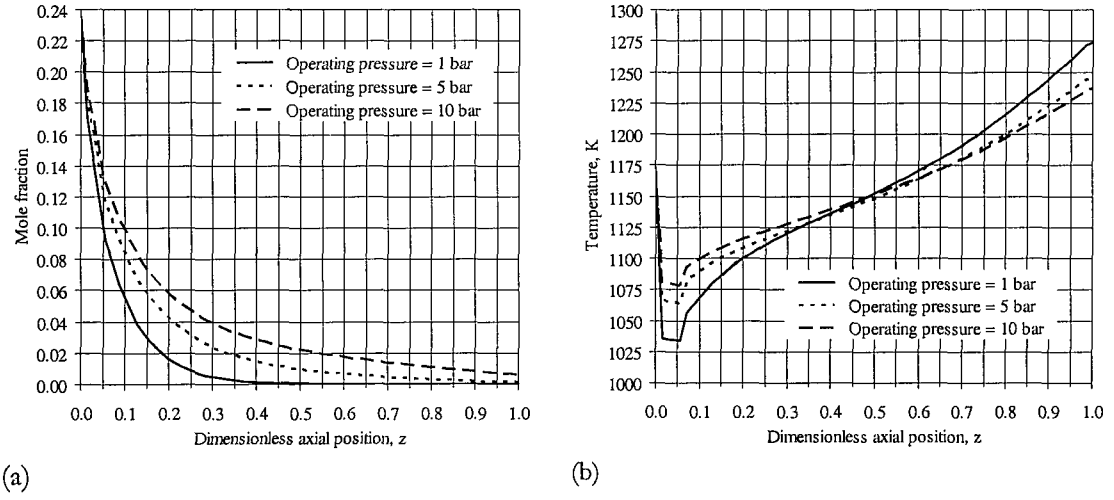

(a) (b)

Figure 4.6 Reformer methane mole fraction (a) and temperature profiles (b) for different operating pressures.

Finally, these results demonstrate that increasing the operating pressure is an effective way of reducing both the temperature dip caused by the reforming reactions

and the overall temperature increase across the cell (Iwata et al., 2000). However, it should be noted that, as the CH_4 consumption rate decreases with increasing pressure, some methane slippage to the SOFC anode may occur, and thus, as discussed in Section 4.2.2, a combined direct and indirect internal reforming SOFC needs to be studied.

4.2.6 Effect of Reformer Inlet Composition

Under the base case conditions, the reformer fuel feed composition was 23.5% CH_4, 47% H_2O, 2.2% CO, 6% H_2, and 21.3% CO_2. For this reformer inlet composition, it was reported in Section 4.2.1: that at the entrance of the reformer, and until all the methane is completely reformed, the hydrogen and carbon monoxide mole fractions increase rapidly while methane, water, and carbon dioxide decrease; and that after that point the reverse shift reaction leads to a slight mole fraction decrease in H_2 and CO_2 and increase in CO and H_2O. However, for this base case, the fuel feed was rich in CO_2, which could have influenced the above reported behaviour of the mole fraction profiles within the reformer, particularly the direction of the shift reaction. The purpose of this section is then to examine the influence of using a different feed composition (much lower in CO_2). Figure 4.7 presents the simulation results obtained when using a reformer fuel feed molar composition of 30% CH_4, 60% H_2O, 3.3% CO, 3.3% H_2, and 3.4% CO_2. Note that the steam to carbon ratio is kept equal to 2 as was done for the base case conditions.

Figures 4.7a and 4.7b present the mole fraction profiles in both the reformer and the SOFC fuel channel. As observed in Figures 4.1a and 4.1b, due to the very fast reforming reaction at such high temperatures, the methane is practically all consumed in the first one third of the reformer. After this point, the same decrease in the concentration of H_2 and CO_2 and increase in CO and H_2O due to the reverse shift reaction is observed, although less pronounced than under the base case conditions. At the outlet of the reformer, the fuel stream content is now 59.5% in H_2, 19.6% in CO, 17.5% in H_2O, and 3.4% in CO_2. Figure 4.7c presents the corresponding reformer, fuel channel, and air channel temperature profiles. These temperature profiles are similar to the ones presented in Figures 4.1c and 4.1d, the only difference being the location and value of the temperature minimum at the entrance of the reformer. As the partial

pressure of methane in the fuel feed is higher, the reaction rate is higher than for the base case, and thus, the local cooling effect is slightly more pronounced and occurs closer to the reformer entrance. Under these feed conditions, the terminal voltage obtained is 0.659 V and the fuel efficiency 47.6%.

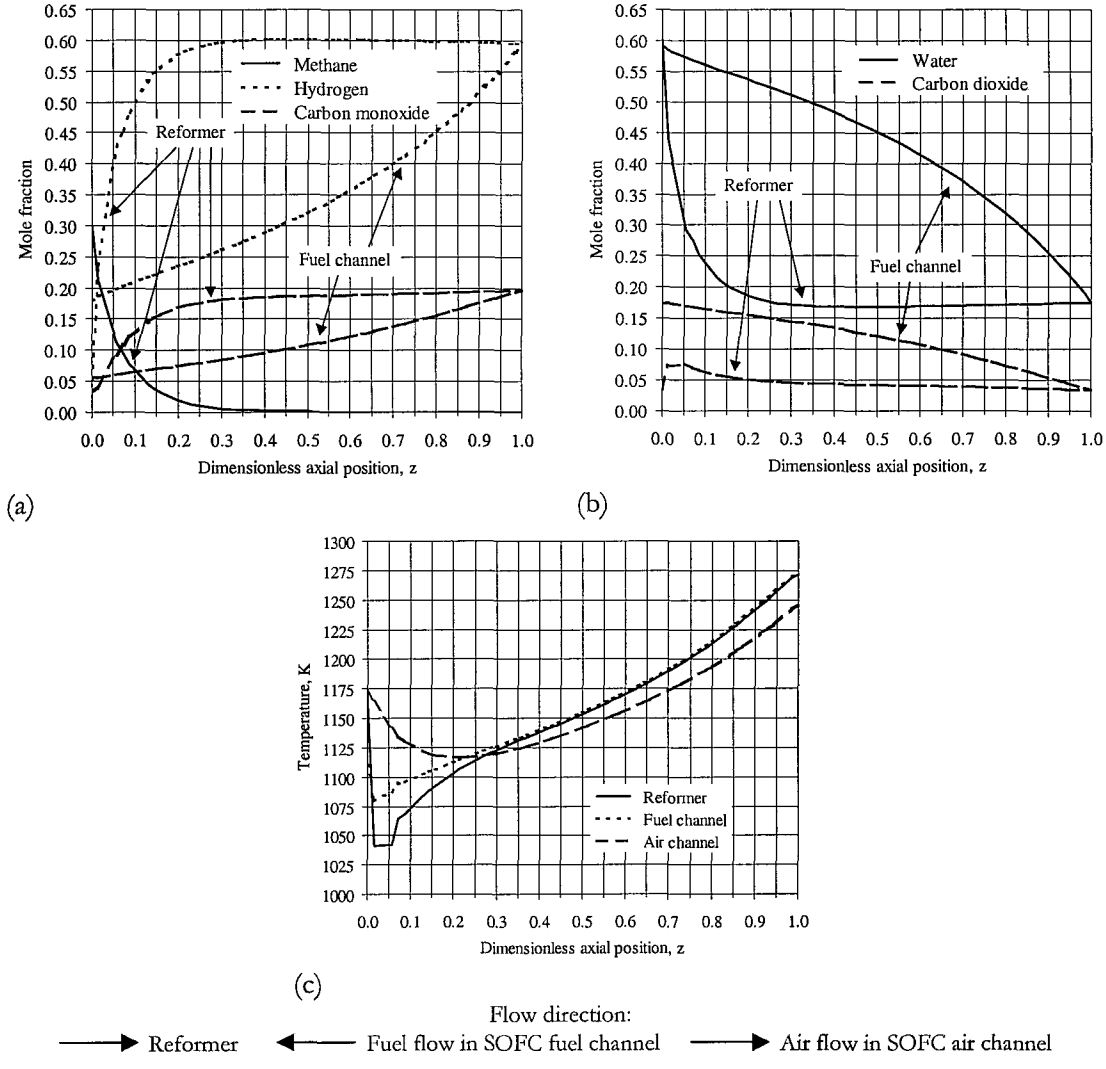

Figure 4.7 Reformer and fuel channel mole fraction profiles (a-b) and reformer, fuel channel, and air channel temperature profiles (c) for a different reformer inlet composition.

4.2.7 Counter-Flow & Co-Flow Operation

The air flow through the cell first supplies heat to the reforming reactions and then removes the excess heat produced in the cell (see Figure 4.1d). By increasing or

decreasing either the flowrate or the inlet temperature of this stream, it is possible to control to some extent the heat removal from the system and, consequently, the temperature at the air channel outlet/fuel channel inlet, $z \sim 1$. So far it has been considered that the air flow is counter-flow to the fuel flow in the SOFC fuel channel, a counter-flow configuration. However, the system behaviour should also be analysed for a co-flow configuration. For this purpose, the air channel mass and energy balances and corresponding boundary conditions (equations (2.21) and (2.23) in Chapter 2) have been altered. The same operating conditions as the ones used for the base case described in Section 4.2.1 have been considered.

Figures 4.8 and 4.9 show some of the characteristic results for this co-flow configuration. The component mole fraction profiles in both the reformer and the SOFC fuel channel are presented, for an easier interpretation, in two separate figures, Figures 4.8a and 4.8b. These are very similar to the ones presented in Figures 4.1a and 4.1b. Since the temperature close to the reformer entrance is higher than in the counter-flow case, the methane is practically all consumed in the first one fifth of the reformer instead of the first one third previously observed. The composition of the fuel stream at the outlet of the reformer and at the outlet of the SOFC channel is analogous to the reported in Section 4.2.1.

Figures 4.8c and 4.8d present the temperature profiles within the reformer and fuel cell for this co-flow case. Comparing Figures 4.8c and 4.8d to Figures 4.1c and 4.1d, it can be seen that, while in the counter-flow configuration the temperature increases along the air flow direction by heat accumulation with the maximum temperature at the outlet, in the co-flow configuration the temperature profile has a peak near the outlet of the fuel and air channels, $z \sim 0$. Moreover, the temperature increase in the case of a co-flow configuration is larger than in the counter-flow case, since the air and fuel streams in the former configuration contain the generated heat without convecting it to the outside. As a result of this the mean cell temperature is higher, leading to lower overpotentials (see Figure 4.9b) and a higher efficiency. For this co-flow configuration, the terminal voltage is 0.706 V and the cell efficiency 50.9%.

In a previous study, Achenbach (1994) considered that the more efficient system is found for a counter-flow configuration. However, the system studied by Achenbach is one of a direct internal reforming SOFC for which, in a counter-flow configuration, the air has the highest temperature at the location where the heat for the reforming reactions is required. In the IIR-SOFC system studied here, this only happens for a co-flow configuration. So, comparing both modes of operation, the co-flow may be the more efficient. However, one can also realise from Figures 4.8c and 4.8d that the large temperature decrease observed close to the reformer entrance (247 K) is not desirable for a ceramic system.

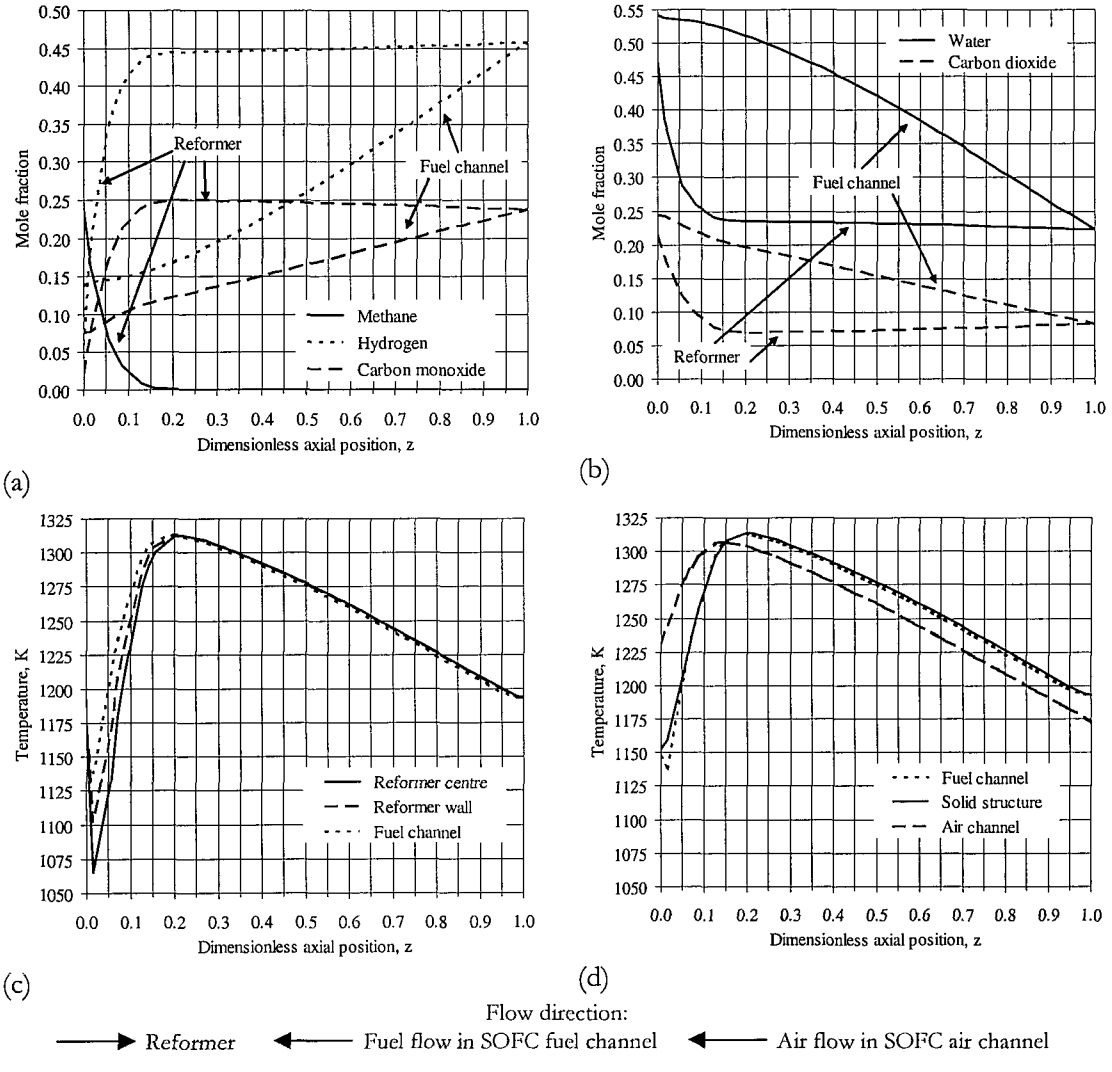

Figure 4.8 Reformer and fuel channel mole fraction profiles (a-b) and reformer and solid oxide fuel cell temperature profiles (c-d) for a co-flow configuration.

Similarly to Figure 4.2, the relevant electrochemical variables for this co-flow SOFC configuration are presented in Figure 4.9. Figure 4.9a presents the open-circuit potential for standard temperature and pressure and pure reactants ("standard potential"), the open-circuit potential (OCP), and the terminal potential. Figures 4.9b and 4.9c present the anode and cathode overpotentials in terms of voltage and resistance, respectively. Finally, Figure 4.9d presents the different current densities, i.e., the total current density drawn from the cell and the partial current densities that result from the hydrogen and carbon monoxide oxidation reactions.

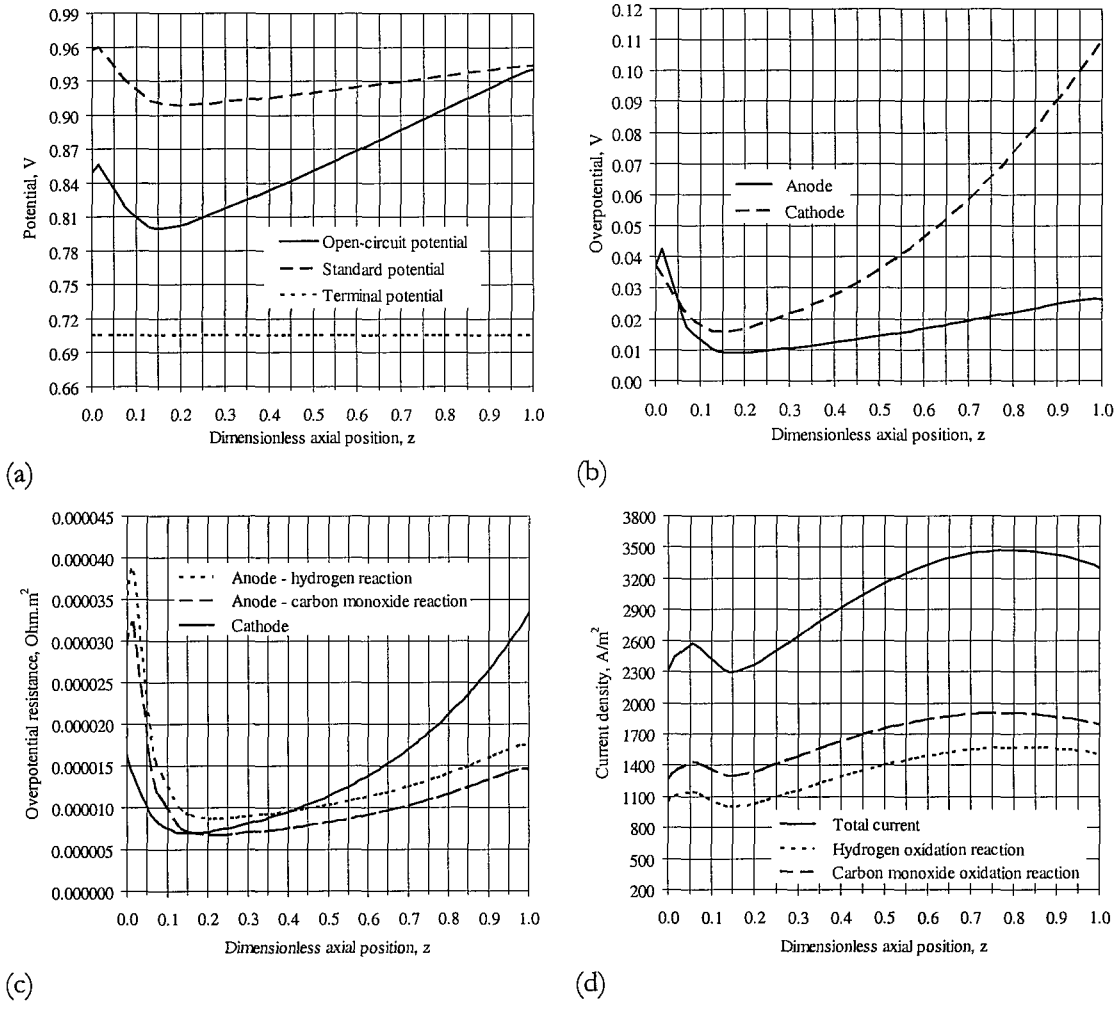

Figure 4.9 Potential (a), overpotential (b-c), and current density (d) profiles for a co-flow configuration.

As mentioned in Section 4.2.1, these figures are directly related to the cell component mole fractions and temperatures profiles, in this case, the ones presented in

Figure 4.8. However, Figure 4.8 has shown that only the temperature profiles changed significantly in relation to the counter-flow configuration analysed in Section 4.2.1, and thus, only these are responsible for the major differences observed between Figures 4.2 and 4.9. The standard potential decreases with increasing temperature and thus decreases in the air flow direction (different in Figures 4.2 and 4.9). The OCP also decreases in the air flow direction. This decrease is now more significant due to the double effect of a decreasing standard potential and a decreasing hydrogen partial pressure. On the other hand, higher temperatures lead to lower overpotentials (Figures 4.9b and 4.9c) and, consequently, a higher terminal potential. As for the current density profiles, these are now more uniform throughout the length of the system. In Figure 4.2d, it was observed that the current density at the fuel channel entrance ($z \sim 1$) was much higher than at the outlet. This was due to the combined effect of having the highest temperature and hydrogen partial pressure at that location. However, these two effects now occur at opposite ends of the system, leading to the profiles in Figure 4.9d.

4.3 Combined Direct & Indirect Internal Reforming SOFC

The above simulations have demonstrated that, for an annular design of an IIR SOFC, the use of conventional reforming Ni catalysts leads to full methane consumption and undesirable local cooling close to the fixed-bed reformer entrance. The use of oxide-based catalysts, or catalysts within their activity range, was one of the suggestions to smooth those temperature profiles. However, oxides and other, less active, reforming catalysts were shown not to fully convert all the methane, although successfully alleviating the local temperature minimum. Consideration is given now to additional methane reforming on the SOFC anode, creating a combined DIR and IIR SOFC model. This is important whenever such lower activity catalysts are applied and some unconverted methane flows through to the fuel cell.

As discussed in Chapter 1, DIR in a SOFC requires an anode material that possesses good catalytic properties both for steam reforming and effective generation of power (Lee et al., 1990). It has been shown that Ni cermet anodes can provide sufficient activity for steam reforming without the need for any additional catalyst (Dicks, 1998;

Clarke et al., 1997). The aim of this third section is to simulate the behaviour of this coupled reactor and to note the effect on important factors such as steepness of the temperature gradients or overall performance of the fuel cell. For that purpose, the kinetics of direct internal reforming in SOFCs needs to be first analysed.

4.3.1 Kinetics of Direct Internal Reforming in SOFCs

Although conventional methane steam reforming has been widely studied and there are several publications dealing with its kinetics and catalytic aspects (Rostrup-Nielsen, 1984; Xu and Froment, 1989a, 1989b; Twigg, 1996), there is only a small amount of data available for the kinetics of reforming in SOFC anodes. Table 4.3 presents some of the rate equations so far published for Ni cermet anodes. Lee et al. (1990) studied the methane conversion with different Ni/ZrO_2 anode materials. For 60 vol.% Ni cermets, they found an activation energy of 98 kJ/mol. Achenbach and Riensche (1994) and Belyaev et al. (1995) both showed that the steam reforming reaction rate was first order in methane and zero order in water, for a 80 wt.% ZrO_2 and 20 wt.% Ni cermet and for a mixed Ni-(5 wt.%)ZrO_2-(2 wt.%)CeO_2 anode, respectively. Dicks et al. (2000) studied the CH_4 reforming rate given by a thin electrolyte-supported Ni-YSZ anode using a tubular plug flow differential reactor. Ahmed and Foger (2000) investigated Ni-YSZ and Ni-YSZ modified (addition of a basic compound) anodes. They found that the reaction order in methane increased from 0.85 for the Ni–YSZ anode to 1.4 for the modified anode, the order in steam changed from -0.35 to -0.8, and the activation energy from 95 kJ/mol to 210 kJ/mol. Other kinetic expressions and a review in advances of DIR catalysts advances can be found in Nakagawa et al. (2001), Bebelis et al. (2000), Dicks (1998), and Clarke et al. (1997).

For the simulation of the combined DIR and IIR SOFC system, the equations developed in Chapter 2 describing the mass and energy balances in the fuel channel (Tables 2.2 and 2.3) have been modified accordingly. The first order kinetic expression derived by Achenbach and Riensche (1994) and presented in Table 4.3, with an activation energy of 82 kJ/mol and a pre-exponential constant of 4274 mol/(sm^2bar),

has been adopted. Such kinetic expression is considered to be typical of DIR-SOFCs performance.

Table 4.3 Rate equations for methane reforming on SOFC anodes.

Kinetic equation	Reference
$R_{CH_4} = k_0 p_{CH_4} p_{H_2O}^{-1.25} \exp\left(-\frac{E_a}{\Re T}\right)$	Lee et al., 1990
$R_{CH_4} = k_0 p_{CH_4} \exp\left(-\frac{E_a}{\Re T}\right)$	Achenbach and Riensche, 1994 Belyaev et al., 1995
$R_{CH_4} = \frac{k_0 p_{CH_4}}{\left(1 + k_H p_{H_2}^{0.5} + k_S p_{H_2O}/p_{H_2}\right)^n} \exp\left(-\frac{E_a}{\Re T}\right)$	Dicks et al., 2000
$R_{CH_4} = k_0 p_{CH_4}^{\alpha} p_{H_2O}^{\beta} \exp\left(-\frac{E_a}{\Re T}\right)$	Ahmed and Foger, 2000

4.3.2 Base Case

For this combined DIR and IIR SOFC system a base case also needs to be defined. The conditions are the same as the ones presented in Section 4.2.1 above, except that, for convenience, an IIR relative activity of 0.008% is now considered, leading to a significant methane slippage to the SOFC. Similarly to Figures 4.1 and 4.2, Figures 4.10 and 4.11 show some characteristic results for this DIR-IIR SOFC base case conditions.

The component mole fraction profiles in both the reformer and the SOFC fuel channel are presented, for an easier interpretation, in two separate figures, Figures 4.10a and 4.10b. It can be seen that, in the reformer, and as the steam reforming reaction proceeds, the hydrogen and carbon monoxide mole fractions increase, while methane, water, and carbon dioxide decrease. The final reformer methane conversion is 74% and, at the outlet of the reformer, the fuel stream content is 4.5% in CH_4, 37.5% in H_2, 20.3% in CO, 27.6% in H_2O, and 10.1% in CO_2. This stream then flows back into the SOFC where the remaining methane is finally all converted. As a consequence of this anode steam reforming reaction, the H_2 and CO mole fractions in the fuel channel first increase, and then continuously decrease as these are gradually converted, by means of the electrochemical reactions, to H_2O and CO_2 (note that the flow of fuel in the SOFC fuel channel is counter-flow to both the fuel stream in the reformer and the air stream

in the SOFC air channel). At the outlet of the fuel channel, the fuel stream content is 13.7% in H_2, 7.9% in CO, 54.3% in H_2O, and 24.1% in CO_2.

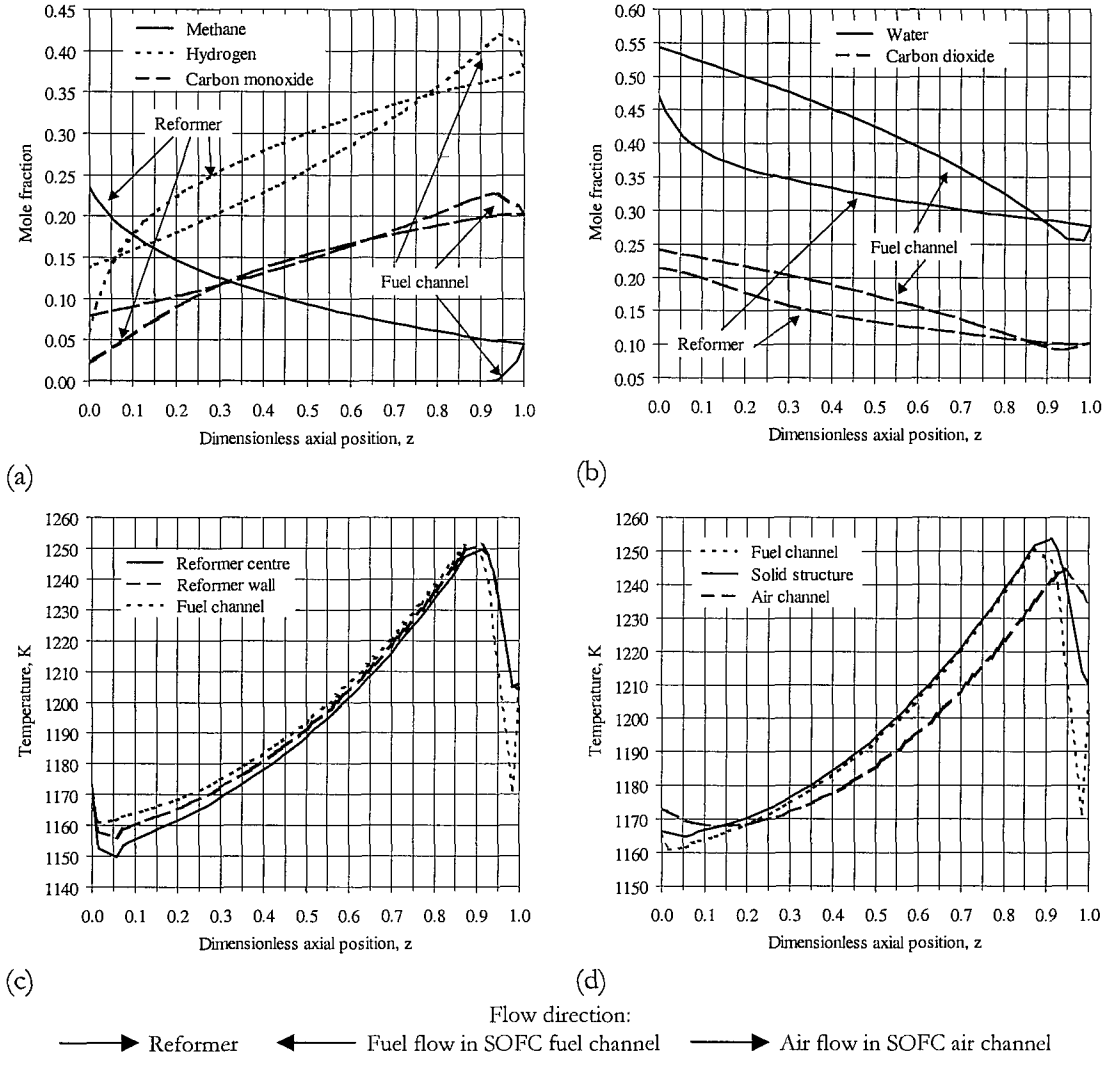

Figure 4.10 Reformer and fuel channel mole fraction profiles (a-b) and reformer and solid oxide fuel cell temperature profiles (c-d) for the DIR-IIR SOFC base case.

Figures 4.10c and 4.10d present the corresponding temperature profiles for the reformer (both at the centre and at the wall), the fuel channel, the solid structure, and the air channel. Table 4.4 illustrates the global energy balance to this DIR-IIR SOFC coupled system, as well as the ones to the reformer and fuel cell alone. The conditions under which the enthalpy of the various streams and the enthalpy change of the reforming and electrochemical reactions were determined were described in Section 4.2.1. For these base case conditions, and from the data in Table 4.4, the total heat

required by the steam reforming reactions (both in the reformer and in the SOFC fuel channel) represents 60% of the total heat produced in the cell. Comparing Tables 4.2 and 4.4, it can be noticed that both the reaction enthalpy changes in the reformer and in SOFC are much lower for the combined DIR-IIR SOFC system. In the reformer, not all the methane is fully converted, and thus, less heat is required by the reforming reactions. On the SOFC, the remaining methane is reformed, and thus, the total reaction enthalpy change is lower (as the negative heat of reaction of the reforming reactions cancels the positive heat of reaction of the electrochemical reactions). One other point to note in Table 4.4 is the heat transferred between the two systems, either by conduction or radiation. As part of the heat needed for the steam reforming reactions is now required in the SOFC instead of in the reformer, less heat needs to be transferred. Under these base case conditions, the terminal voltage is 0.688 V and the efficiency 49.6%.

In terms of temperature profiles, it is clear that, with a lower activity catalyst, the steep temperature gradients once observed in the internal reformer at $z \sim 0$ have been eliminated. However, due to the fast kinetics of the endothermic reforming reaction in the SOFC (DIR), there are now steep temperature gradients in the fuel channel, air channel, and reformer at $z \sim 1$. It should be noted that, at the fuel channel inlet, the ratio between the rate of the reforming reaction and the rate of the electrochemical reactions is approximately 13. This ratio clearly shows that the rates of the two reactions are not comparable, thus generating the described temperature gradients across the fuel cell. This can be compared to the case in which a more active catalyst is used in the reformer (Figure 4.1c) and steep temperature gradients occur at the entrance of the reformer instead ($z \sim 0$). Figure 4.10b then demonstrates that if the total inlet methane is to be converted when using a less active IIR catalyst, all that is achieved is a shift of the steep temperature gradients from the entrance of the reformer ($z \sim 0$) to the entrance of the SOFC fuel channel ($z \sim 1$). It will be shown in Sections 4.3.3 and 4.3.4 below that, in order to eliminate these local gradients, it is not sufficient to modify the reformer catalyst activity alone. In Chapter 6, the alternative solution of non-uniformly distributing the catalyst within the axial direction of the reformer is also analysed.

The relevant electrochemical variables for this DIR-IIR SOFC system are presented in Figure 4.11. Figure 4.11a presents the open-circuit potential for standard temperature and pressure and pure reactants, the open-circuit potential, and the terminal potential. Figures 4.11b and 4.11c show the anode and cathode overpotentials in terms of voltage and resistance, respectively, and Figure 4.11d the different current densities, i.e., the total current density drawn from the cell and the partial current densities that result from the hydrogen and carbon monoxide oxidation reactions.

All the above figures are directly related to the cell component mole fractions and temperatures profiles in Figure 4.10, as discussed in Section 4.2.1. The main differences, between these profiles and the ones presented in Figure 4.2, are at the fuel channel entrance ($z \sim 1$), as both the temperature and component mole fraction profiles vary significantly in this region. Also, as the overall temperature of the system is higher, the overpotentials are lower and the terminal voltage is higher.

Table 4.4 Energy balances to the combined DIR-IIR SOFC system (base case).

Global energy balance (W)			
	Inlet	Outlet	
Reformer	6.902		
SOFC fuel channel		8.829	
SOFC air channel	82.102	86.453	
	89.004	95.282	
Reaction enthalpy change*	22.617		
Power output		16.537	
Total	111.621	111.819	Error: 0.18%
Reformer energy balance (W)			
	Inlet	Outlet	
Reformer	6.902	7.821	
Reaction enthalpy change*		6.908	
Heat transferred from SOFC	7.739		
Total	14.641	14.729	Error: 0.60%
SOFC energy balance (W)			
	Inlet	Outlet	
SOFC	89.923	95.282	
Reaction enthalpy change*	29.525		
Power output		16.537	
Heat transferred to reformer		7.739	
Total	119.448	119.558	Error: 0.09%

* The reaction enthalpy change is added to the enthalpy of the inlet or outlet streams if it is an overall exothermic or endothermic process, respectively.

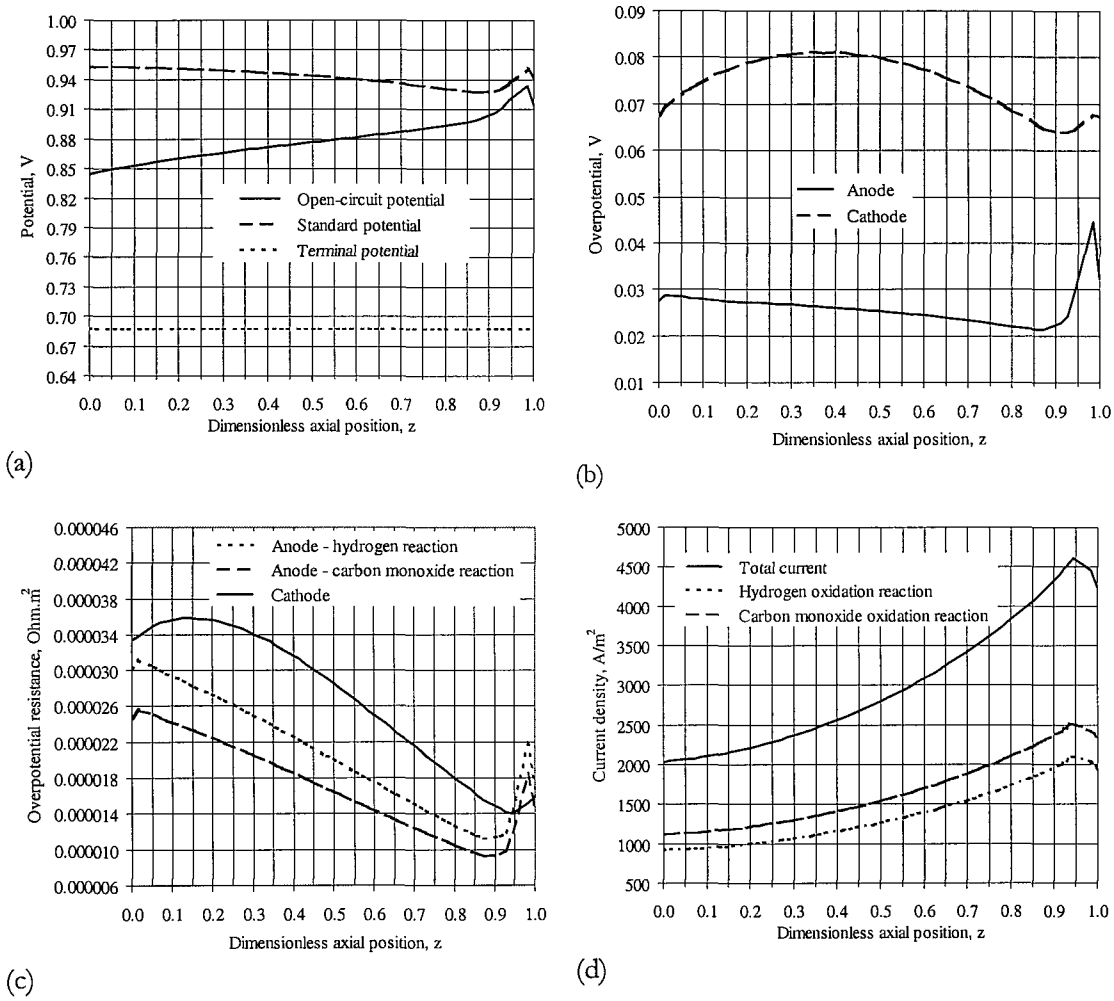

Figure 4.11 Potential (a), overpotential (b-c), and current density (d) profiles for the DIR-IIR SOFC base case.

4.3.3 Effect of Different IIR Catalyst Activities

Figure 4.12 illustrates the effect of using different IIR catalyst activities. Figure 4.12a presents the CH_4 reformer and fuel channel mole fraction profiles and Figures 4.12b, 4.12c, and 4.12d the reformer, fuel channel, and air channel temperature profiles, which result from using catalysts containing IIR relative activities of 0.04%, 0.008% (base case), and 0.002%. As expected, Figure 4.12a shows that the amount of non-converted methane in the reformer increases as the catalyst relative activity decreases. Also clear is the fact that, when there is methane carry-over to the anode, the catalyst activity on the anode side is such that all the methane is converted in the first 10% of the system length

(z ~ 1). As a result of this and of the high endothermicity of the steam reforming reaction, the temperature drops seriously at z ~1. The fuel channel temperature drop, for instance, can be as high as 165 K for the lowest relative activity case (see Figure 4.12d).

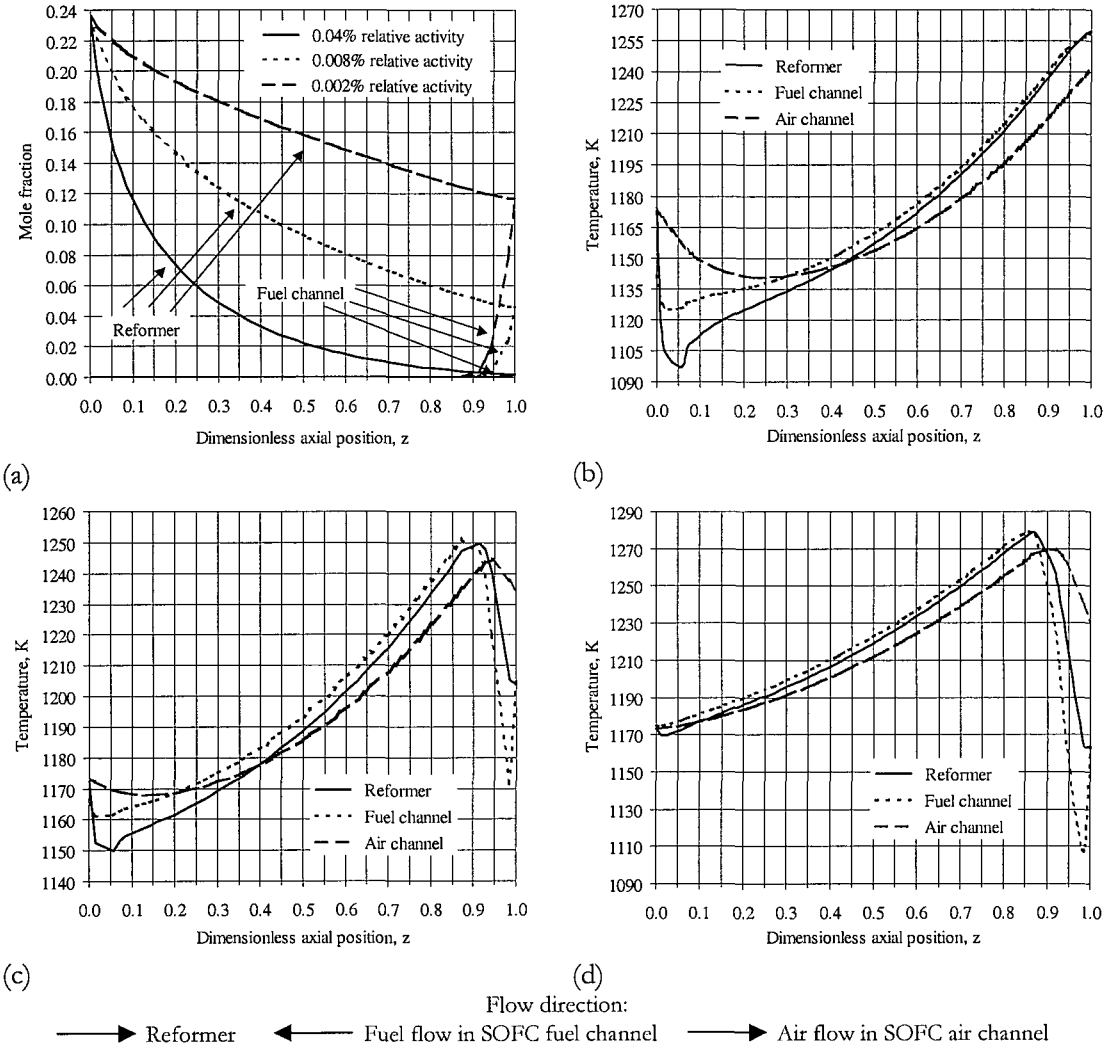

Figure 4.12 Reformer and fuel channel CH_4 mole fraction profiles (a) and reformer, fuel channel, and air channel temperature profiles for IIR catalyst relative activities of 0.04% (b), 0.008% (c), and 0.002% (d).

As for the electrochemical variables, as the IIR catalyst relative activity decreases, the overall system temperature increases and so do the voltage and system efficiency. This temperature increase has two main causes. On one hand, less heat is leaving the system, as the air outlet temperature is lower. It is worth noting that the air stream flowrate is about 10 times higher than the fuel flowrate, and so, even a small

decrease in the air outlet temperature implies a considerable increase in the overall system temperature. On the other hand, and as referred to in the previous section, less heat needs to be transferred, either by convection or radiation, from the cell to the reformer, since most of the heat necessary to sustain the endothermic reforming reaction is supplied locally by the exothermic electrochemical reactions, and so, the total net heat released in the cell is higher.

4.3.4 Effect of Different DIR Catalyst Activities

As mentioned before, one way to improve the system performance would be to decrease the rate of the anode steam reforming reaction. Sunde and Hendriksen (1997) found that the ratio between the two reaction rates could be controlled, within certain limits and without significant power loss, by optimising the electrode thickness. Hendriksen (1997) found that a reduction of the reforming reaction rate by a factor of 10 was the ideal situation for their system. The effect of reducing the DIR reaction rate by such a factor is now analysed. Dicks (1998) reported the same large temperature drop at the fuel inlet for a DIR-SOFC. Suggestions to minimise this effect were to apply anode recycle, admit the fuel in stages along the cell (applied by Westinghouse), or design the anode material with a lower steam reforming activity. It is worth noting that the combination of IIR with DIR implies a lower methane concentration at the anode entrance and a better temperature distribution than if only DIR was applied.

In order to investigate possible ways of eliminating the large temperature gradients, simulations were carried out in which the anode catalyst activity is reduced by a factor of 10 for IIR relative activities of 0.008% and 0.002%, respectively. Figure 4.13 presents the reformer and fuel channel mole fraction profiles and the reformer, fuel channel, and air channel temperature profiles for these two cases.

In Figures 4.13b and 4.13d it can be seen that the temperature profiles at the entrance of the SOFC fuel channel ($z \sim 1$) are smoothed out by the decrease in the DIR catalyst activity. The high temperature drop once observed in Figure 4.12 in the first 10% of the fuel channel is now almost eliminated. With such DIR catalyst activity reduction, simulations indicated that the reforming reaction proceeds until around 50%

(see Figures 4.13a and 4.13c) of the system length instead of the previously observed 10% shown in Figure 4.12a.

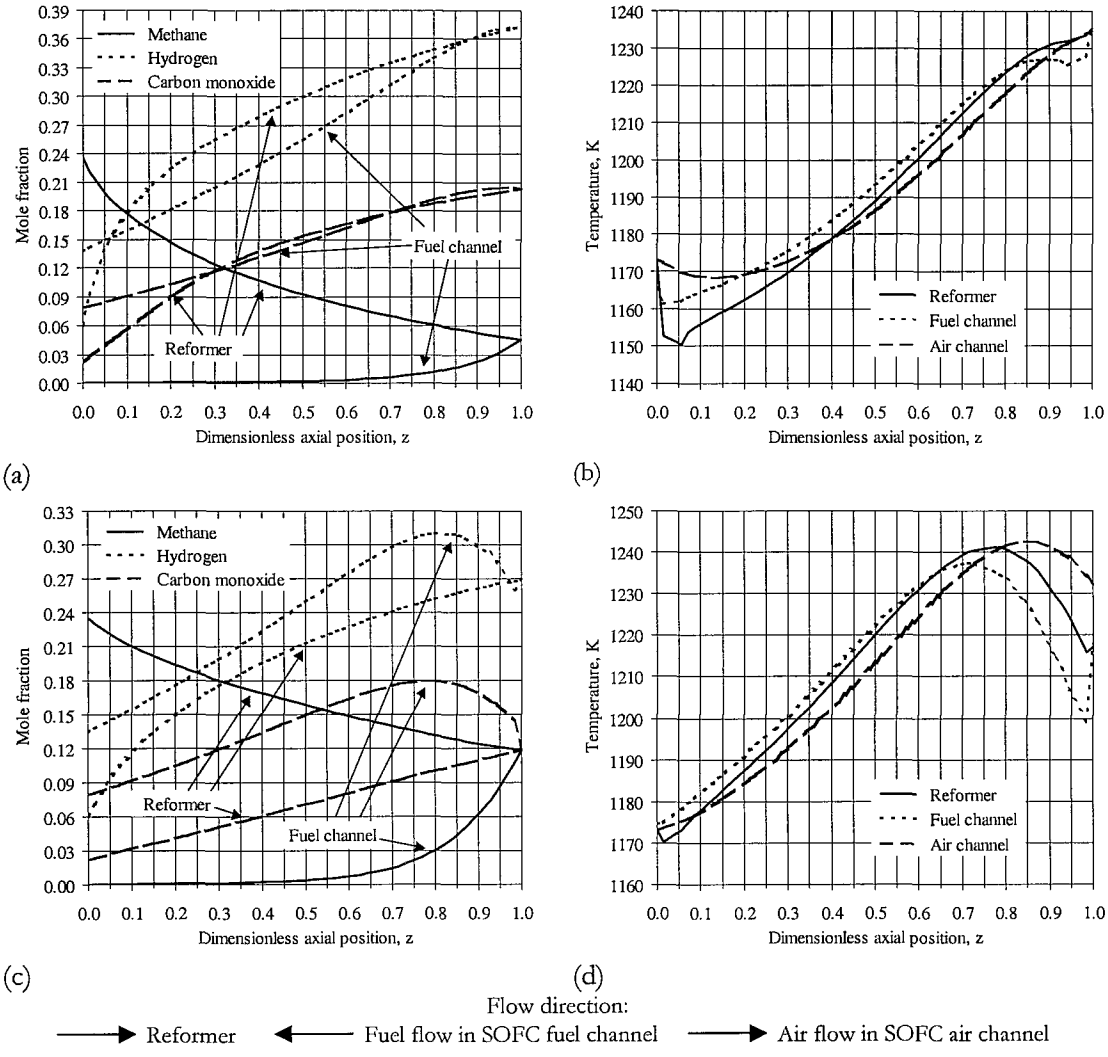

Figure 4.13 Reformer and fuel channel mole fraction profiles and reformer, fuel channel, and air channel temperature profiles for IIR catalyst relative activities of 0.008% (a-b) and 0.002% (c-d) and a slower DIR kinetics.

4.3.5 Effect of Current Density

Figure 4.14 presents the reformer temperature profiles for average current density values of 2000, 3000 (base case), and 4000 Am^{-2}. Figure 4.14a is for the base case values of both IIR and DIR catalyst activity and Figure 4.14b for the case where the anode catalyst activity is reduced by a factor of 10. In both cases, an increase in the current

density, leads to lower terminal voltages, lower efficiencies (53.7% for a current density of 2000 Am^{-2} and 45.8% for 4000 Am^{-2} - as compared to the base case value of 49.6%), and a consequent increase in the overall system temperature. As seen from Figure 4.14a, this temperature increase leads to even higher temperature gradients at the fuel channel entrance ($z \sim 1$), making the system even less likely for operation if full DIR catalyst activity is used.

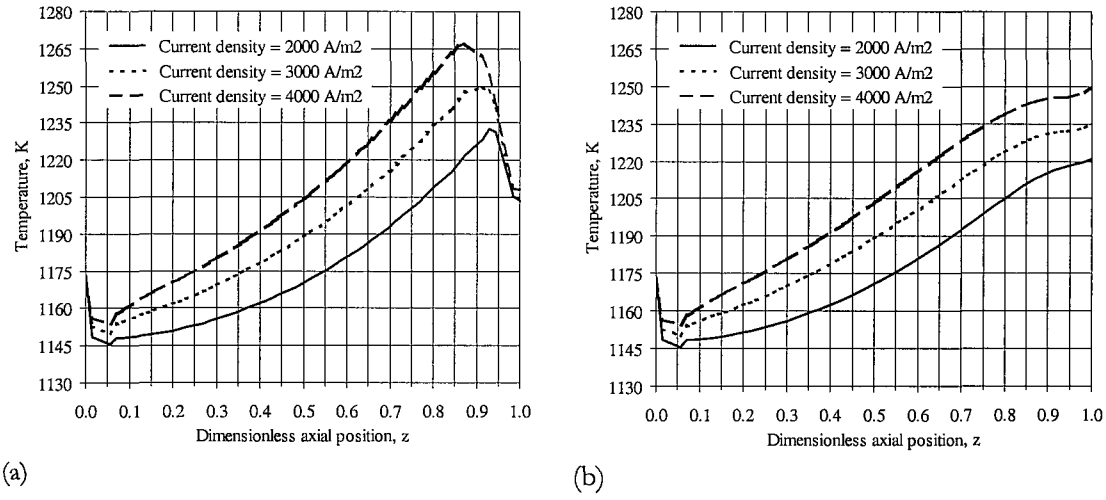

Figure 4.14 Reformer temperature profiles for different average current densities for the base case (a) and for a slower DIR kinetics (b).

Under such conditions, the lower current density case appears to be the most favourable, although the power output would be significantly lower (11.9 W for a current density of 2000 Am^{-2} and 20.4 W for 4000 Am^{-2}). Figure 4.14b shows that the temperature profiles at the SOFC fuel channel entrance ($z \sim 1$) are smoothed out by a decrease in the DIR catalyst activity, proving the system feasibility.

4.3.6 Effect of Operating Pressure

Figure 4.15 presents the reformer methane mole fraction and temperature profiles for pressure values of 1 (base case), 5, and 10 bar, with the base case values of both IIR and DIR catalyst activity. From Figure 4.15a it can be seen that as the pressure increases the methane rate consumption in the reformer decreases and more methane proceeds to the SOFC. On the SOFC side, the methane is all consumed within the first 10% of the

channel length, independently of the pressure considered. However, since the amount of methane flowing into the SOFC anode increases with pressure, the cooling effect at the cell entrance ($z \sim 1$), due to the fast kinetics of the endothermic DIR, is more pronounced for higher pressures. These results are obviously sensitive to the kinetic expressions used. For instance, the DIR kinetic expression derived by Achenbach and Riensche (1994) is first order in CH_4, and so, an increase in pressure implies a proportional increase in the reaction rate. It is this effect combined with the higher amount of non-converted methane at the SOFC fuel channel entrance that leads to the steep temperature gradients observed in Figure 4.15b. However, if different kinetic expressions are considered, this may no longer be true.

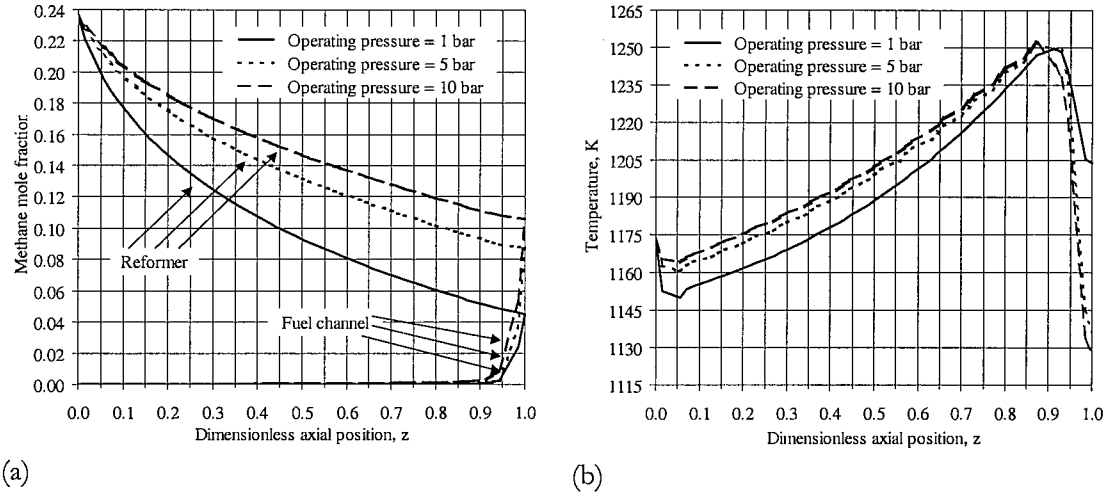

Figure 4.15 Reformer and fuel channel methane mole fraction profiles (a) and reformer temperature profiles (b) for different operating pressures.

From Table 4.3, it can be seen that there is considerable disagreement on the influence of H_2O partial pressures on the reaction rate, although there is consensus that the order in CH_4 is close to one. For instance, the DIR kinetic expressions by Achenbach and Riensche (1994) and Lee et al. (1990) differ in regard to the influence of H_2O. Figure 4.16 presents the same profiles as in Figure 4.15 but using the DIR kinetic expression by Lee et al. (1990) instead of the one by Achenbach and Riensche (1994). The kinetic expression by Lee et al. (1990) is first order in CH_4 but –1.25 order in H_2O, and thus, in contrast, the overall reaction rate decreases with an increase in pressure. Therefore, and as demonstrated in Figure 4.16, an increase in pressure leads to a lower DIR reaction rate, even if the amount of CH_4 at the fuel channel is higher, and the DIR

proceeds now until 15% of the channel length. As a consequence, the relative decrease in temperature from one pressure value to another is not as pronounced as in Figure 4.15. Among the kinetic expressions in Table 4.3, only the one presented by Lee et al. (1990) decreases with pressure.

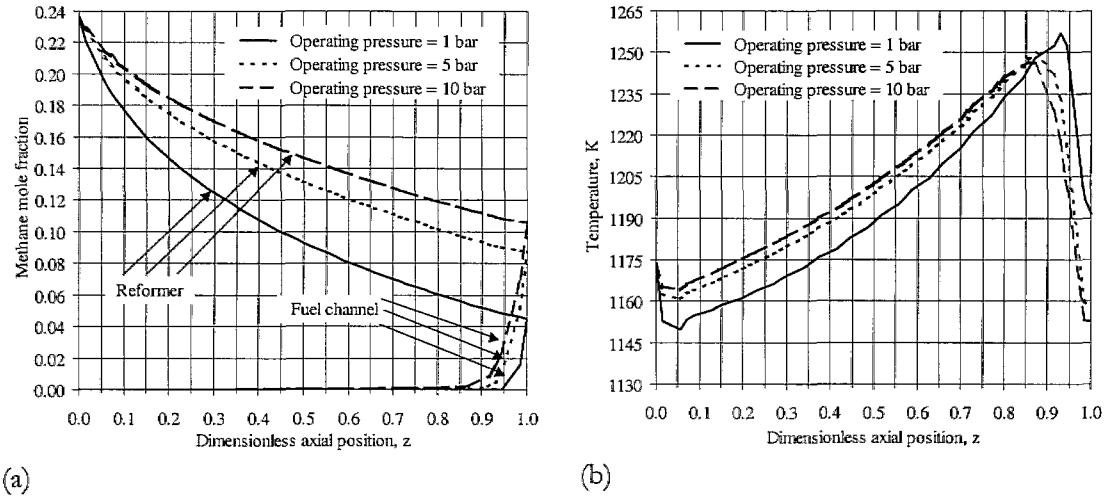

(a) (b)

Figure 4.16 Reformer and fuel channel methane mole fraction profiles (a) and reformer temperature profiles (b) for different pressures using the DIR kinetics from Lee et al. (1990).

In terms of fuel cell performance, if the pressure increases, higher voltages and electric power, and efficiencies of 55.1% for an operating pressure of 5 bar and of 57.1% for 10 bar (as compared to the base case value of 49.6%) are obtained for the simulation results presented in Figures 4.15 and 4.16.

4.3.7 Counter-Flow & Co-Flow Operation

As has been done in Section 4.2.7, the system behaviour is here also analysed for a co-flow configuration, for which the same operating conditions as the ones used in the base case are considered. Figure 4.17a presents the reformer, fuel channel, and air channel temperature profiles for the co-flow case. Comparing Figure 4.17a to Figures 4.10c and 4.10d it can be seen that while in the counter-flow configuration the temperature increases along the air flow direction by heat accumulation, reaching a maximum temperature close to the air stream outlet, in the co-flow configuration the lower temperatures occur close to the air channel entrance ($z \sim 1$). This is due to the

combined cooling effect of the cold air feed and the endothermic DIR. The mean cell temperature is similar in both cases, although it is higher for the co-flow configuration. This is due to a lower air stream outlet temperature and consequent lower heat convection to the outside.

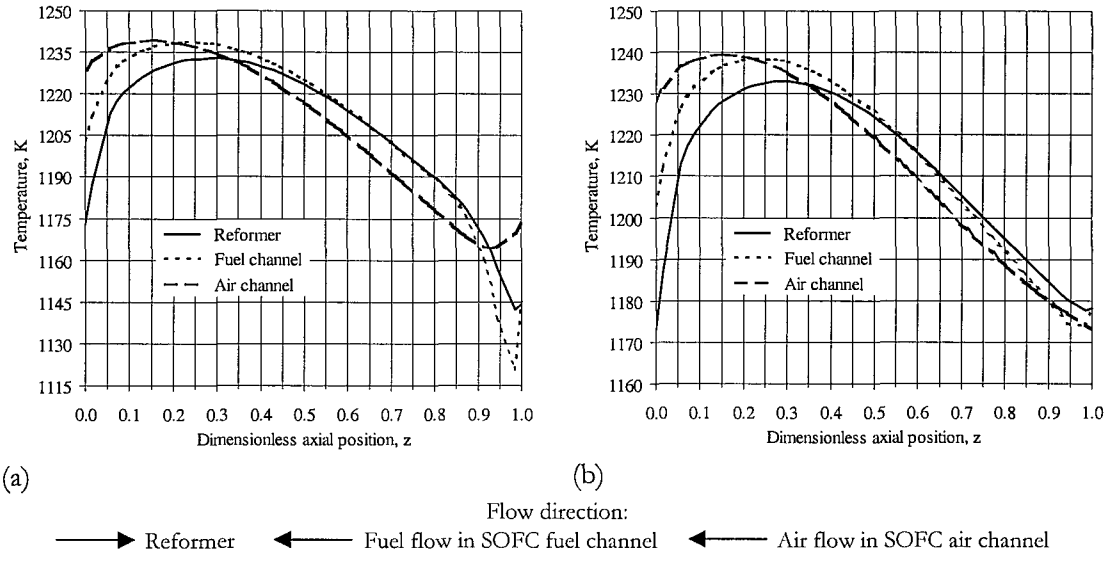

Figure 4.17 Reformer, fuel channel, and air channel temperature profiles for a co-flow configuration: base case (a) and slower DIR kinetics (b).

For this co-flow configuration, the terminal voltage is 0.693 V and the efficiency 50.0%. The mole fraction profiles in both the reformer and SOFC fuel channel are similar to the ones in Figures 4.10a and 4.10b. Figure 4.17b presents the same temperature profiles for an IIR catalyst relative activity of 0.008%, for a slower DIR kinetics, and for a co-flow configuration. Compared to Figure 4.17a, the temperature profile at z ~ 1 is smoothed out by decreasing the DIR activity.

4.3.8 Indirect Internal Reforming Oxide-Based Catalysts

The steady-state simulation of an indirect internal reforming solid oxide fuel cell has demonstrated that the use of typical metal-based (e.g. Ni) steam reforming catalysts leads to full methane consumption and undesirable local cooling in the first one third of the reformer. Use of less active reforming catalysts, in the range of oxide-based catalysts, leads to incomplete methane conversion in the reformer and subsequent

reforming on the SOFC anode. On the SOFC fuel channel, and due to the fast kinetics of the endothermic reforming reaction, that methane is all converted and the temperature drops considerably in the first 10% of the channel length. Reduction of the anode catalyst activity by a factor of 10, which reduces the DIR reaction rate, has shown to smooth the temperature profiles at the SOFC fuel channel entrance.

All the above simulations, were obtained by introducing the concept of an IIR catalyst relative activity, defined as the ratio between the activity of the catalyst in use and that of a conventional Ni catalyst (Xu and Froment, 1989a). Such reduced relative activity was required to avoid almost instantaneous conversion of methane at the reformer entrance and implied the use of either a conventional nickel catalyst with only a certain fraction of Ni content accessible or an inherently less active catalyst, such as the case of oxide-based catalysts.

However, recently, kinetics for steam reforming over oxide-based catalysts have been determined (Laosiripojana, 2003; Ramírez-Cabrera et al., 2000b, 2002a, 2002b; Aguiar et al., 2002c). The oxide catalysts studied were based on two classes: doped cerias and perovskites. Ceria is often a component of some SOFC anodes and is well known for its redox properties, as a catalyst for partial oxidation of methane to synthesis gas, and for the ability to resist carbon deposition and catalyse carbon combustion. On the other hand, the mixed ionic/electronic conduction of $La_{1-x}Sr_xFeO_{3-\delta}$ makes these materials attractive for hydrocarbon oxidation. $La_{0.7}Ca_{0.3}CrO_{3-x}$ has also been studied. All the oxide catalysts studied have shown significant activity for methane steam reforming. The perovskites were intrinsically more active, although Gd-CeO_2 was the most active on a weight basis. The cerias showed fractional apparent reaction orders in methane, negative reaction orders in hydrogen, and approximately zero reaction order in steam (in contrast to metal cermets at SOFC temperatures, where hydrogen has a positive effect and steam a weak negative effect). Activation energies for steam reforming were in the range of 120 to 160 $kJmol^{-1}$, similar to those for the reaction of dry methane (Laosiripojana, 2003; Aguiar et al., 2002c). In this last section, and to finish with the simulations of the combined direct and indirect internal reforming SOFC system, the results obtained using the kinetic data for Gd-CeO_2 at 900 °C are presented. For that purpose, the Gd-CeO_2 experimental data was fitted (Laosiripojana, 2003) to a kinetic

equation of the form $r = k_1 p_{CH_4}^{0.6} / \left(1 + k_2 p_{H_2}^{0.5}\right)^*$. Figures 4.18 and 4.19 present the simulation results obtained.

Figure 4.18 presents the results for the same base case conditions as the ones in Section 4.2.1 and Figure 4.19 for the same conditions except that the operating pressure is of 5 bar.

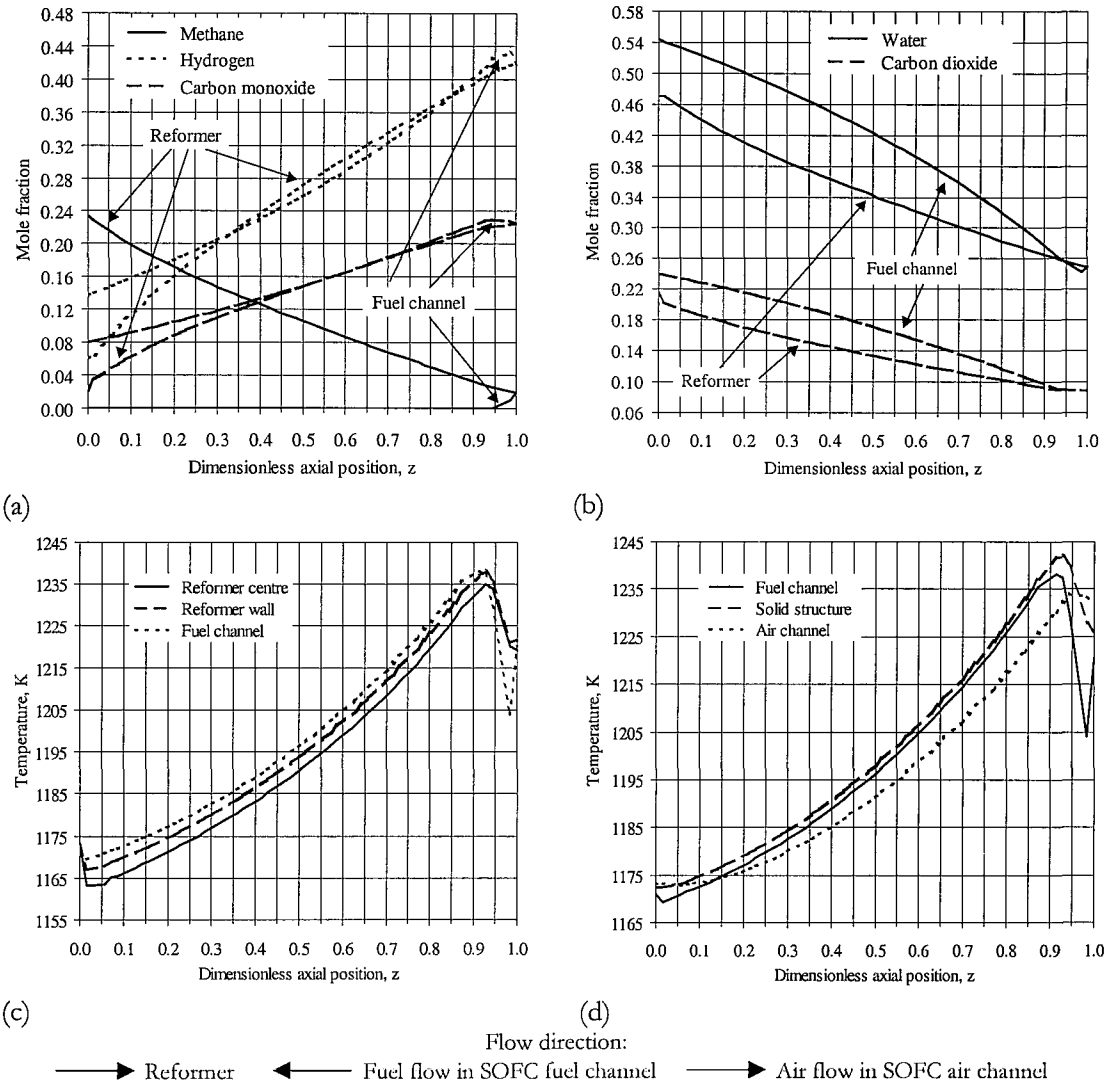

Figure 4.18 Reformer and fuel channel mole fraction profiles (a-b) and reformer and solid oxide fuel cell temperature profiles (c-d) for the DIR-IIR SOFC base case conditions but using the kinetic data of Gd-CeO_2 for the IIR catalyst.

* The rate constant k_1 has a pre-exponential factor of 33.9×10^3 kmol/(bar$^{0.6}$kg$_{cat}$h) and an activation energy value of 117 kJ/mol. The adsorption constant k_2 has a pre-exponential factor of 1.52×10^{-7} bar$^{-0.5}$ and an enthalpy change of adsorption of -180 kJ/mol (Laosiripojana, 2003).

It can be seen that, with such catalysts the methane is no longer practically all consumed in the first one third of the reformer, as shown in Figure 4.1, but is now gradually consumed throughout the reformer. At the outlet of the reformer, the CH_4 conversion is 88% and the fuel stream molar composition is then 2% CH_4, 41.9% H_2, 22.4% CO, 24.9% H_2O, and 8.8% CO_2. Therefore, some methane slippage still occurs. This stream flows back into the SOFC where the methane is finally fully converted and the H_2 and CO are gradually converted, by means of the electrochemical reactions, to H_2O and CO_2. At the outlet of the fuel channel, the fuel stream molar composition is 13.6% H_2, 8% CO, 54.4% H_2O, and 24% CO_2.

As for the temperature profiles, a relatively smooth temperature profile is achieved at the entrance of the reformer compared to the steep temperature profiles in Figure 4.1. However, a local cooling effect, caused by the high rate of direct methane reforming on the anode, is predicted at the entrance of the SOFC fuel channel entrance. Nevertheless, and compared to the results presented above, the use of oxides is shown to have a promising application in IIR-SOFCs. Note that all these are still preliminary results, as the developed oxides still require further optimisation in terms of composition and surface area. As mentioned above, the aim of obtaining an IIR-SOFC system with smoother temperature profiles is not only important to avoid thermal stresses in the ceramic materials, but also in improving the overall performance of the cell. For example, for the results presented in Figure 4.18, the terminal voltage obtained is 0.690 V and the fuel cell efficiency 49.8% (as compared to the base case values of 0.644 V and 46.5%), which indicate a more efficient operation.

In Section 4.2.5, it was observed that as the pressure increases the methane consumption rate decreases. This was true for the steam reforming kinetics then in use but is no longer true for the Gd-CeO_2 kinetic expression now in study. As can be seen from Figures 4.18 and 4.19, no such effect is observed. In fact, in this case, the pressure has no real effect in the methane conversion in the internal reformer, as two opposite effects occur. On one hand, the reaction rate increases with increasing pressure as can easily be worked out from the form of the kinetic expression in use. But, on the other hand, the system temperature at 5 bar is lower, which leads to a lower reaction rate. As already mentioned in Section 4.2.5, if the pressure increases, higher open-circuit potential and lower overpotentials are obtained. This leads to a higher terminal potential

and power output, and to a fuel cell efficiency equal to 54.9%. This is why the overall system temperature is lower.

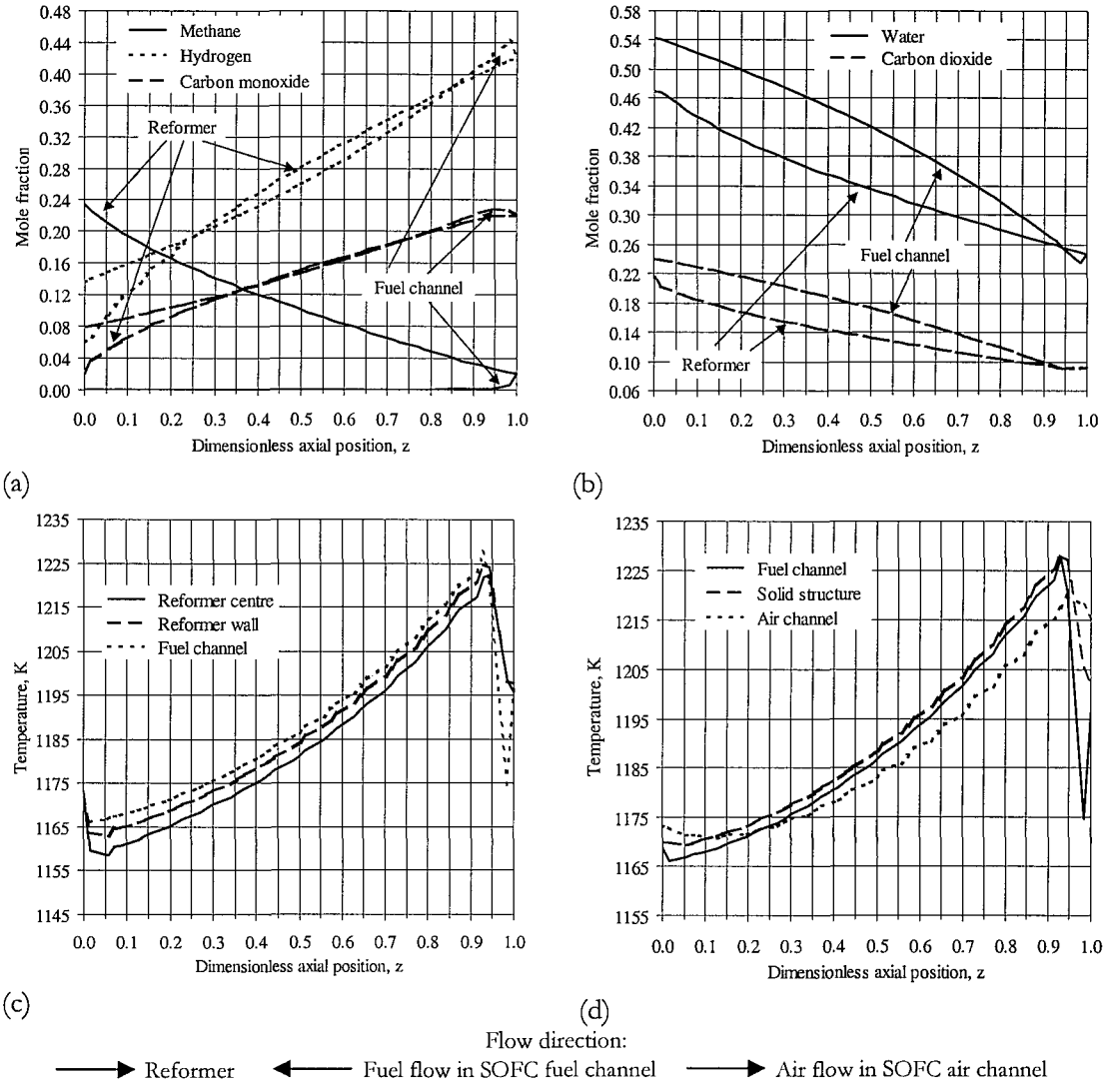

Figure 4.19 Reformer and fuel channel mole fraction profiles (a-b) and reformer and solid oxide fuel cell temperature profiles (c-d) for the DIR-IIR SOFC base case conditions but using the kinetic data of Gd-CeO_2 for the IIR catalyst and for a pressure of 5 bar.

Finally, one should note that the results presented in this chapter are in accordance with the ones reported in the literature, either in terms of the general SOFC performance or in terms of the terminal voltages and composition and temperature profiles presented. Some of these have already been referred to in Chapter 2, Section 2.3. For instance, Bessette II et al. (1995) has also shown that, for the case of a tubular DIR-SOFC, all the methane gets fully converted in the first 10 cm of the cell length

with a considerable thermal sink associated with the endothermic DIR. Fellows (1998), Meusinger et al. (1998), Achenbach and Riensche (1994), Dicks (1998), and Clarke et al. (1997) all agree with these results and have reported that in DIR cells, all the methane is usually completely reformed within a small distance from the anode entrance leading to a local sub-cooling in that area. Nagata et al. (2001) concluded, for the case of a tubular IIR-SOFC, that by setting either an appropriate uniform or graded catalyst density, a moderate or flatter temperature distribution in the cell stack and a higher temperature of the exhaust gas was obtained.

Publications based on the work presented in this chapter include Aguiar et al. (2002a, 2002b, 2002c, 2002d).

In the next chapter, Chapter 5, another alternative method of reducing the steam reforming reaction rate is discussed.

Chapter 5

Catalysts with Non-Uniform Activity & Diffusivity Distributions for Use in IR-SOFCs

Summary

In the previous chapter, it has been shown that the use of typical metal-based reforming catalysts in an IIR-SOFC system leads to full methane consumption and undesirable local cooling at the reformer entrance. This local cooling is caused by a local thermal mismatch between the two systems as the reforming reactions are extremely rapid and orders of magnitude higher than the fuel cell ones. To eliminate such local cooling it has been considered necessary to slow down the rate of such reactions. In Chapter 4, it has been shown that the use of oxide-based catalysts or catalysts within their activity range can lead to smoother temperature profiles. In this fifth chapter, two other possible solutions of reducing the rate of the reforming reactions are investigated: the use of catalysts with non-uniform distribution of active metal within the inert support and the use of a diffusion barrier placed near the outer surface of the catalyst. Optimal catalyst activity and effective diffusivity distributions, that guarantee the catalyst performance despite any catalyst deactivation, are first determined for a single catalyst pellet and are subsequently implemented in the previously developed DIR-IIR SOFC model.

Outline

5.1 Introduction

In the previous chapter, the solid oxide fuel cell and fixed-bed steam reforming reactor models developed in Chapters 2 and 3, respectively, were coupled and used to simulate temperature, composition, and relevant electrochemical variables along the reformer tube and fuel cell. The simulation results demonstrated that the use of typical metal-based steam reforming catalysts leads to full methane consumption and undesirable local cooling in the first one third of the reformer. The occurrence of this local cooling is due to the fact that the inherent kinetics of the reforming reactions, under these reaction conditions, are extremely rapid and orders of magnitude higher than the fuel cell electrochemical reactions, leading to a local thermal mismatch between the two systems. Thus, to eliminate such local cooling effect it has been considered necessary to slow down the rate of such reactions (and the corresponding local energy flux demand). As discussed before, this reduction of the steam reforming reaction rate could be achieved using catalysts with a much lower metal surface area, partially poisoned catalysts, or catalysts sintered at high temperature. However, these methods are unlikely to guarantee long catalyst life. The first two methods lead to high loss of catalyst activity whenever deactivation occurs, while in the last one, sintering can easily lead to complete pore blockage and hence, unacceptable reduced overall rate of reaction (Ahmed et al., 1989). Therefore, such catalysts are not appropriate for the IIR-SOFC system under study, as the required thermal coupling between the inner reformer and the outer solid oxide fuel cell would be compromised if deactivation occurred. One possible solution for this problem could be the use of oxide-based catalysts. Such catalysts have a much lower activity when compared with conventional Ni steam reforming catalysts and are highly resistant to carbon deposition (Ramírez-Cabrera et al., 2000a). In Chapter 4, it was shown that the use of oxide-based catalysts or catalysts within their activity range leads to smoother temperature profiles but can sometimes result in some methane slippage to the SOFC fuel channel. In addition, it has also been shown that such methane slippage can lead to significant temperature gradients at the entrance of the SOFC fuel channel. In this fifth chapter, two other possible solutions of reducing the rate of the reforming reactions are investigated: the use of conventional nickel catalysts but with non-uniform distribution of active metal within the inert support or the use of

a diffusion barrier placed near the outer surface of the catalyst. The combination of these two methods is expected to retain a low, but approximately constant total reaction rate as and when catalyst deactivation occurs. Moreover, diffusional limitations will tend to lead to a local equilibrium being approached at the active sites of the catalyst, thereby further reducing the overall rate of reaction. The described methods suggest the determination of both an activity and an effective diffusivity distribution. Different distributions representing such effects need to be considered. Figure 5.1 is a schematic representation of a spherical catalyst pellet with such distributions.

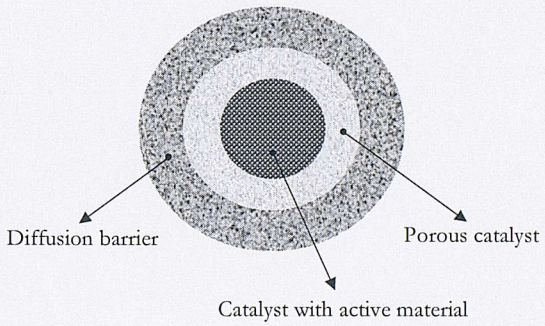

Figure 5.1 Representation of possible distributions of active material and effective pore sizes in a spherical catalyst pellet.

The aim of this chapter is then (i) to demonstrate that such distributions of activity and effective diffusivity can indeed lead to a lower activity which remains relatively constant despite deactivation and (ii) to determine appropriate distributions of active catalyst and effective pore sizes, which best match the rates of the reforming and electrochemical reactions despite any subsequent catalyst deactivation. This is first performed, in Section 5.3, for a single reforming catalyst pellet. In Section 5.4, the obtained distributions are implemented, without further optimisation, in the previously developed DIR-IIR SOFC model, to demonstrate that such distributions do allow for a better thermal coupling of a reformer with a SOFC system. The results have been presented in general for a typical reforming catalyst pellet under typical reforming operating conditions (Xu and Froment, 1989b) and not specifically for the dimensions of the system presently under study. Hence, the subject of this chapter should be seen as a possible or suggested method for reducing the rate of the reforming reactions in a IIR-SOFC system and as an alternative to using, for example, inherently less active oxide

catalysts. The simulations presented in the previous chapter, where the concept of relative catalyst activity was introduced, have assumed one of these approaches.

The possibility of improving catalyst performance by suitably distributing the active element within the inert support has already been studied, both theoretically and experimentally, as can be seen in the following section.

5.2 Optimal Catalyst Pellet Activity Distributions

In most applications, the catalyst is deposited on a high surface area support in the form of a pellet. The reactants diffuse from the bulk fluid, through the porous network of the support, and react at the active catalytic sites. The products so formed diffuse through that same porous network back to the bulk fluid. Transport resistances within the support alter the concentration of the chemical species at the catalyst sites and lead to concentration and temperature gradients within the catalyst. As a consequence, the reactions occur at different rates, depending on the position of the catalyst site within the porous support. For this reason, the question naturally arises as to how should this catalytic material be distributed within the support to optimise the catalyst performance (Morbidelli et al., 2001).

Intrapellet activity gradients were traditionally thought to be detrimental to catalyst performance. However, the effects of deliberate nonuniform distribution of catalytic material within the support on the performance of a catalyst pellet started receiving attention in the late 1960's. Both experimental and theoretical studies demonstrated that nonuniformly distributed catalysts can offer superior conversion, selectivity, durability, and thermal sensitivity characteristics over those wherein the activity is uniform. The performance indexes that influence the definition of an optimal catalyst distribution include effectiveness, selectivity, yield, and deactivation rate. The key parameters which affect the choice of the optimal catalyst profile are kinetic behaviour of the reactions, the transport effects present, and the production cost of the catalyst. Many investigators have optimised catalyst performance based on one or more of the above criteria. The obtained profile was typically optimal within the class considered, but no proof could be produced that it was also the optimal among any arbitrary distribution. Such proof was first given by Morbidelli et al. (1982), who

demonstrated analytically, that under the constraint of a fixed total amount of active material, the optimal catalyst distribution is an appropriately chosen Dirac-delta function; that is, all the active catalyst should be deposited at a specific radial position within the pellet, this position being dependent upon the physical parameters of the pellet (shape, size, reactant diffusivity), mass transfer coefficient between the bulk fluid and the pellet external surface, reactant concentration in the bulk fluid surrounding the pellet, and kinetic parameters of the reaction. It was also shown that this catalyst distribution remains optimal, even for the most general case of an arbitrary number of reactions, following arbitrary kinetics, occurring in a nonisothermal pellet, with finite external heat and mass transfer resistances (Wu et al., 1990; Chemburkar et al., 1987; Vayenas and Pavlou, 1987; Morbidelli et al., 1985; Morbidelli and Varma, 1982). Subsequently, it was noted that a Dirac-type distribution implies that the local pellet loading does not have an upper bound and that the catalyst dispersion remains constant. However, when the loading is bounded, as is the case in practice, and there is no loss in catalyst dispersion with increase loading, the optimum distribution was shown to be a step-distribution (Baratti et al., 1993). If the dispersion does not remain constant, and there are large catalyst crystallites with increased loading, it was shown that the optimal distribution is no longer a step but a more disperse distribution. Morbidelli et al. (1982) examined the more realistic case in which the catalyst is distributed in a step manner centred on the optimal Dirac-delta function location. These authors demonstrated that the maximum value of the effectiveness factor is not much affected compared with the optimal one, as long as the thickness of the active layer is less than 5% of the pellet characteristic dimension. A comprehensive review of optimal catalyst distribution in pellets prior to 1993 has been presented by Gavriilidis et al. (1993). Baratti et al. (1997) did further work in this field and concluded that, for the same problem as before, an optimal multi-step distribution is also possible, depending the number and location of the steps upon the specific problem under study.

Becker and Wei (1977) approached the problem by numerically analysing the effects of different catalyst distributions. They compared the effectiveness factors for four catalysts: active ingredient deposited in an interior layer, in a middle layer, in an exterior layer, and uniformly in the entire support. These authors showed that, for bimolecular Langmuir kinetics under isothermal conditions, when a kinetic controlled

regime is present, the best distribution is the inner one, while for a diffusion-controlled regime, the best distribution is the outer one. For the intermediate regime, the middle distribution is the one having the highest effectiveness factor.

Considerable amount of theoretical research has been conducted in the area of optimal catalyst distributions as compared to experimental research. Early work was mostly related to automotive exhaust catalysts. Experimental research conducted so far demonstrated a good qualitative, and in certain cases, quantitative agreement with the theory (Lee and Varma, 1988; Gavriilidis et al., 1993).

The optimisation problem presented was also extended to fixed-bed reactors. For such a reactor, fluid phase reactant concentrations and temperature vary with position, and hence, optimisation and modelling problems become much more complex. For this reason, fewer reactor studies have appeared in the literature compared with those for single pellets. One of the earliest works in this area was the modelling of CO oxidation in monolith reactors for automobile converters (Becker and Wei, 1977). The optimisation of an isothermal fixed-bed reactor, where a bimolecular Langmuir-Hinshelwood reaction occurs, was performed analytically by Morbidelli et al. (1986a, 1986b). It was shown that the optimal activity distribution, which maximises the outlet reactor conversion for a fixed amount of catalyst, is again a Dirac-delta distribution placed at a location inside the pellet that depends upon the position along the reactor axis. Since this was difficult to apply in practice, the sub-optimal case where all pellets have the same Dirac-delta distribution was also considered. Significant improvements were observed when comparing the performance of this latter reactor with one packed with uniformly active or externally coated catalyst particles. However, the performance of this sub-optimal reactor was still inferior to that of the rigorous optimal reactor (Morbidelli et al., 1986a, 1986b). Furthermore, an alternative sub-optimal distribution where the fixed-bed is divided in multiple zones, where in each zone the catalyst location is the same but different from the other zones, was also investigated (Lee et al., 1987; Lee and Varma, 1988). Hence, these results demonstrated that, the optimisation of the outlet conversion of a reactor is determined by the local optimisation of each pellet. However, Wu (1994) applied the same optimal catalyst activity distribution theory to the yield or selectivity optimisation of a fixed-bed reactor for isothermal parallel

reacting systems and found that the local optimisation of each pellet did not necessarily give rise to the maximum outlet yield or selectivity.

An important area where optimal catalyst pellet activity distributions can be used to improve process performance involves reacting systems whose activity changes with time (Gavriilidis et al., 1993; Corbett and Luss, 1974), such as systems undergoing deactivation and processes where small amounts of undesired components are removed from a stream. For such systems only the initial catalyst distribution can be controlled, while the performance index is integrated over the desired catalyst lifetime. This topic has been addressed both theoretically and experimentally. Both non-selective and selective poisoning mechanisms of deactivation have been considered (Gavriilidis et al., 1993). For the case of selective poisoning, and considering that the rate of deactivation depends linearly on the local active catalyst concentration, it has been shown that the optimal distribution, which is assumed to be bounded between zero and a maximum value (that corresponds to the saturation of the support), is a step-type distribution (Brunovská et al., 1990). In the ideal case, where these bounds are neglected, this step-distribution becomes a Dirac-delta distribution. To optimise such deactivating systems, profit per time, taking into account the price of the product and the cost of catalyst replacement or regeneration, has been considered as the objective function. Selective poisoning in a fixed-bed catalytic reactor has been analysed by Markos et al. (1990), who optimised the catalyst pellet distribution, assumed as a Dirac-delta distribution, in a multiple zone reactor, for first-, second-, and consecutive first-order reactions. In this case, the objective function considered accounted for the catalyst and raw materials cost as well as for the production of valuable products. Markos et al. (1990) showed that the desired catalyst lifetime plays an important role. In general, for shorter catalyst lifetimes, locations closer to the external surface show superior performance, while operating time greatly increases if the activity location moves into the pellet interior. An interesting topic within the subject of distribution of catalyst in pellets is composite catalysts (Gavriilidis et al., 1993). These consist of small particles of the active catalyst embedded in a support. The support has much larger pores and therefore the diffusion coefficient is much larger than in the active catalyst. This represents the main advantage of composite catalysts, since the reactants have a much easier access to the active catalyst

particles than in the case where the entire pellet consists of the active catalyst alone. The advantages of these catalytic systems in the presence of deactivation were studied by Varghese and Wolf (in Gavriilidis et al., 1993). These authors reported that the complete plugging of the larger support pores is significantly delayed relative to the case of a pellet that contains the active catalyst alone, leading to a longer catalyst life and a better utilisation of the active catalyst at the centre of the pellet.

More information on optimal distribution of catalyst in single pellets, reactors, or membrane reactors, as well as on preparation of pellets with nonuniform distribution of catalyst, can be found in a recently published review by Morbidelli et al. (2001).

Note that in all the references just reported, the initial purpose of determining optimal catalyst pellet activity distributions was to improve the performance of the catalyst or reactor in study. However, in this work, optimal distributions, of both activity and effective diffusivity, are determined with the final goal of reducing the reaction rate subject to the condition that the catalyst performance is guaranteed to be approximately constant even when deactivation occurs. For this purpose, two of the results mentioned above are important. Becker and Wei (1977) reported that, when a diffusion-controlled regime is present, the best distribution to optimise the performance of a catalyst is to have the active ingredient deposited in an exterior layer. The opposite effect is expected to achieve a reduced reaction rate. In addition, Markos et al. (1990) reported that catalyst lifetime increases if the active metal is placed in the pellet interior. One last point, composite catalysts have been used to improve diffusion through the pores of the support into the active sites (Gavriilidis et al., 1993). As discussed in Section 5.4.2, composite materials are here used with the opposite objective.

5.3 Catalyst Particle Model

This section is concerned with the reforming catalyst particle model. The steady-state model of a spherical catalyst particle is presented in Table 5.1. As the steam reforming reaction was known to be highly endothermic, temperature gradients were expected and, therefore, both mass and thermal balances were considered initially (in opposition to

what was later done in the development of the reformer model in Chapter 3). The model boundary conditions at the catalyst surface account for the existence of external mass and temperature gradients.

Table 5.1 also presents the total (integrated) reaction rate, r_{total}, defined as the ratio between two overall rates of reaction. The first is the reaction rate when pore diffusion and/or activity profiles are considered and the second one is the reaction rate for a uniform distribution of active material and no pore diffusion limitations. This definition of total reaction rate is convenient since it accounts for the changes in the reaction rate within the pellet due both to transport resistances, which lead to concentration and temperature gradients, as well as to changes due to the non-uniform distribution of active element within the pellet. A unity value of r_{total} indicates that intraphase diffusion is not a significant limitation and that the active metal is uniformly distributed in the pellet, whereas lower values of r_{total} indicate that only some catalyst percentage is being used in an effective manner, because of diffusional limitations and/or because the pellet has a distributed activity profile.

Table 5.1 Steady-state single catalyst particle model.

Mass balance	$\frac{1}{r_p^2}\frac{\partial}{\partial r_p}\left[r_p^2 D_e(r_p)\frac{\partial C_{i,s}}{\partial r_p}\right]+\rho_S\alpha(t)a(r_p)\nu_i R=0$	(5.1)
Energy balance	$\frac{1}{r_p^2}\frac{\partial}{\partial r_p}\left[r_p^2\lambda_e\frac{\partial T_s}{\partial r_p}\right]+\rho_S\alpha(t)a(r_p)(-\Delta H)R=0$	(5.2)
Boundary conditions	$\left.\frac{\partial C_{i,s}}{\partial r_p}\right\|_{r_p=0}=0,\quad \left.\frac{\partial T_s}{\partial r_p}\right\|_{r_p=0}=0$	
	$D_e(R_p)\left.\frac{\partial C_{i,s}}{\partial r_p}\right\|_{r_p=R_p}=-k_m\left(C_{i,s}^S-C_{i,b}\right)$	(5.3)
	$\lambda_e\left.\frac{\partial T_s}{\partial r_p}\right\|_{r_p=R_p}=-k_h\left(T_s^S-T_b\right)$	
Total reaction rate	$r_{total}=\frac{\frac{1}{V_p}\int_{V_p}\alpha(t)a(r_p)R\,dV_p}{R_b}=\frac{3}{R_p^3}\frac{\int_{r_p}\alpha(t)a(r_p)Rr_p^2dr_p}{R_b}$	(5.4)

The functions $a(r_p)$ and $D_e(r_p)$ in equations (5.1), (5.2), and (5.4) stand for the catalyst particle relative activity and effective diffusivity distributions that will be determined. $a(r_p)$ is defined as the ratio between the activity of the catalyst in use and that of a conventional Ni catalyst – $a(r_p)$ equal to unity indicates that full catalyst activity is in use and $a(r_p)$ equal to zero indicates that no active material is present. In order to reduce the size of the optimisation problem, it is assumed that the profiles can be described in terms of three parameters; depending upon their values, these can approximate uniform, step-change, or s-shaped type profiles at various positions within the pellet. A minimum allowed value was defined for the effective diffusivity profile in order to minimise the risk of total pore blockage. Thus, on the outer diffusive barrier this coefficient could be as low as 10% of its normal value. Detailed information on the profiles assumed can be found in Appendix C.1. $\alpha(t)$ represents the activity dependence with time, assuming that the catalyst deactivates uniformly within the pore structure; this can be shown to be the worst-case scenario.

To avoid convergence problems during the solution of the above model as well as of the optimisation problem defined next, the normal procedure of turning models into their dimensionless form was adopted, although not presented here. For that purpose, all dimensionless variables were defined relatively to the bulk conditions.

5.3.1 Optimisation Problem

The optimisation problem being solved is then the one of reducing the rate of the reforming reaction, while maintaining the catalyst performance in face of possible deactivation. As mentioned before, this is done by determining the optimal activity and effective diffusivity catalyst profiles so that the catalyst total reaction rate remains approximately the same even when deactivation occurs.

In order to fully define such optimisation problem it is necessary to define the objective function to be minimised as well as the constraints to impose. An objective function that was found to represent the behaviour just described is the ratio between two total reaction rates, the one of a fresh catalyst and the one of a partially deactivated catalyst (in the present work a catalyst with 50% deactivation was considered). To represent such catalysts, use is made of the function $\alpha(t)$ in Table 5.1. This equals one

for a fresh catalyst and 0.5 for a catalyst with 50% deactivation. As for the constraints, these consist of the model of the system in study, in this case the catalyst particle model in Table 5.1, of the functions representing the activity and effective diffusivity distributions considered, and of a limitation on the minimum value allowed for the total reaction rate. In the case of a single catalyst particle this constraint implies only that the total reaction rate is not allowed to be lower than or equal to zero. However, when solving such optimisation problem with the final goal of thermal matching the reforming and electrochemical reactions in an IIR-SOFC system, this constraint would be represented by the minimum reaction rate required to, for example, guarantee that the reformer temperature would not be lower than a certain specified value. The optimisation problem just described can be stated as

$$\min_{a(r_p), D_e(r_p)} \quad \frac{r_{total}\big|_{fresh\ catalyst}}{r_{total}\big|_{deact.\ catalyst}} \tag{5.5}$$

s.t. $r_{total} >$ minimum value (5.6)

Catalyst particle model in Table 5.1 (5.7)

Activity and effective diffusivity distributions considered (5.8)

The above system of ordinary and algebraic equations is also solved using the gPROMS modelling environment (general process modelling system, from Process Systems Enterprise Ltd.) with the orthogonal collocation on finite elements method. Third order polynomials and one hundred finite elements have been used. The optimisation problem is solved using gOPT (general dynamic optimisation tool, also from Process Systems Enterprise Ltd.).

5.3.2 Catalyst Particle Data

For the kinetics of the reaction, the intrinsic rate equations for the steam reforming of methane, derived by Xu and Froment (1989a) and presented in Chapter 3, are also considered here. As a reminder, these authors considered that the process in study was

described by three reactions (see Section 3.2) although only the steam reforming reaction, $CH_4 + H_2O \leftrightarrow 3H_2 + CO$, is here considered. The catalyst particle data, including dimensions and bulk conditions, were derived assuming a typical catalyst particle within a typical steam reformer reactor as presented in Xu and Froment (1989b). Thus, a particle radius of 2 mm (thickness of the active layer by Xu and Froment (1989b)), a total operating pressure of 24 bar, a temperature of 900 K, and a bulk phase molar composition of 20% CH_4, 61% H_2O, 6% CO, and 13% H_2 is here considered. The remaining model parameters were estimated based on the correlations in Appendix B.1 (same correlations used for the determination of the parameters of the reformer model developed in Chapter3) and are presented in Table 5.2.

Table 5.2 Data for the single reforming catalyst pellet model.

$\overline{D_e}$	1.37×10^{-6}	m^2s^{-1}	λ_e*	1.17×10^{-3}	$kJs^{-1}m^{-1}K^{-1}$
k_h	2.37	$kJs^{-1}m^{-2}K^{-1}$	k_m	0.159	ms^{-1}

*Votruba et al. (1972).

5.4 Catalyst Particle Optimisation Results

The results of the optimisation study have shown that for a single spherical pellet, an "egg-yolk" type distribution of active catalyst coupled with a diffusion barrier placed in the outer regions of the pellet, mathematically represented by close to step-wise distributions, lead to optimum performance in which the total rate of reaction remains virtually constant despite any catalyst deactivation. The optimal distributions obtained are such that the active material is placed in the particle centre until $r_p/R_p = 0.425$ (r_p/R_p is the dimensionless catalyst particle radial coordinate) and the diffusion barrier is placed in the outer region from $r_p/R_p = 0.599$. Figure 5.2 presents the described optimal distributions (presented in dimensionless form – see Appendix C.1). Figure 5.3 presents the methane and hydrogen mole fraction, the dimensionless local reaction rate, and the total reaction rate profiles (for fresh and deactivated catalyst) for a typical steam reforming catalyst particle, i.e., a catalyst particle with uniform profiles, and for a catalyst particle using the above optimal catalyst activity and effective diffusivity distributions. Note that the total reaction rate as defined by equation (5.4) in Table 5.1 represents the local reaction rate integrated over the entire pellet. In Figure 5.3 this total reaction rate is

represented as a function of the catalyst radial coordinate and, therefore, each point represents the integrated reaction rate value from the centre of the particle until that point.

From Figure 5.3(d) and comparing the total reaction rate values at the catalyst surface for a typical catalyst pellet (6.68×10^{-2}) and for a catalyst particle where the optimal activity and effective diffusivity profiles are imposed (5.19×10^{-4}), a significant reduction is observed. Furthermore, while for the first case the total reaction rate decreases considerably as deactivation occurs (~25% decrease), this does not happen when the optimal activity and effective diffusivity distributions are applied (~3% decrease). Such values do not imply that it is the local reaction rate that remains approximately constant, but only the overall performance of the particle. In fact, from Figure 5.3(c), it can be seen a shift in the reaction front from the surface of the catalyst to the boundary of active material placed near the centre of the catalyst. In addition, although the decrease of the total reaction rate at the surface of the particle between a fresh catalyst pellet and a deactivated one is only ~3%, for the maximum local reaction rate value an increase of ~2% is actually observed.

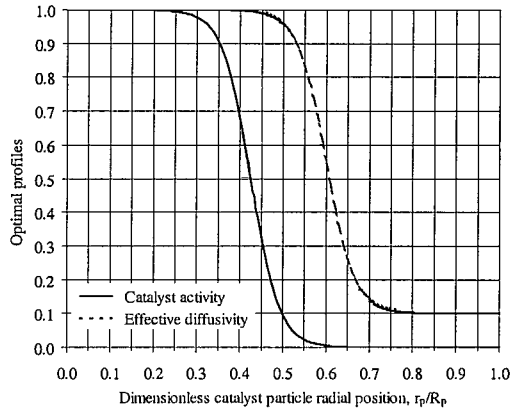

Figure 5.2 Determined optimal catalyst activity and dimensionless effective diffusivity distributions.

Figure 5.3 also presents the methane and hydrogen mole fraction profiles. For the case where the optimal distributions are imposed, the shape of the mole fraction profiles at the outer region of the pellet (where the diffusion barrier is placed) indicates an increased mass transfer limitation and a consequent slower diffusion of the reactants

into the centre and of the products to the surface of the catalyst. As a consequence of these diffusion limitations, the methane mole fraction reaching the active material, placed only at the centre of the catalyst, is lower than for the uniform distribution case, leading to the desired decrease in the reaction rate. Examination of the catalyst particle temperature profiles showed that external temperature gradients are generally higher than internal temperature gradients, although, for these reaction conditions, both can be considered negligible. The same is true for the case where optimal distributions are imposed.

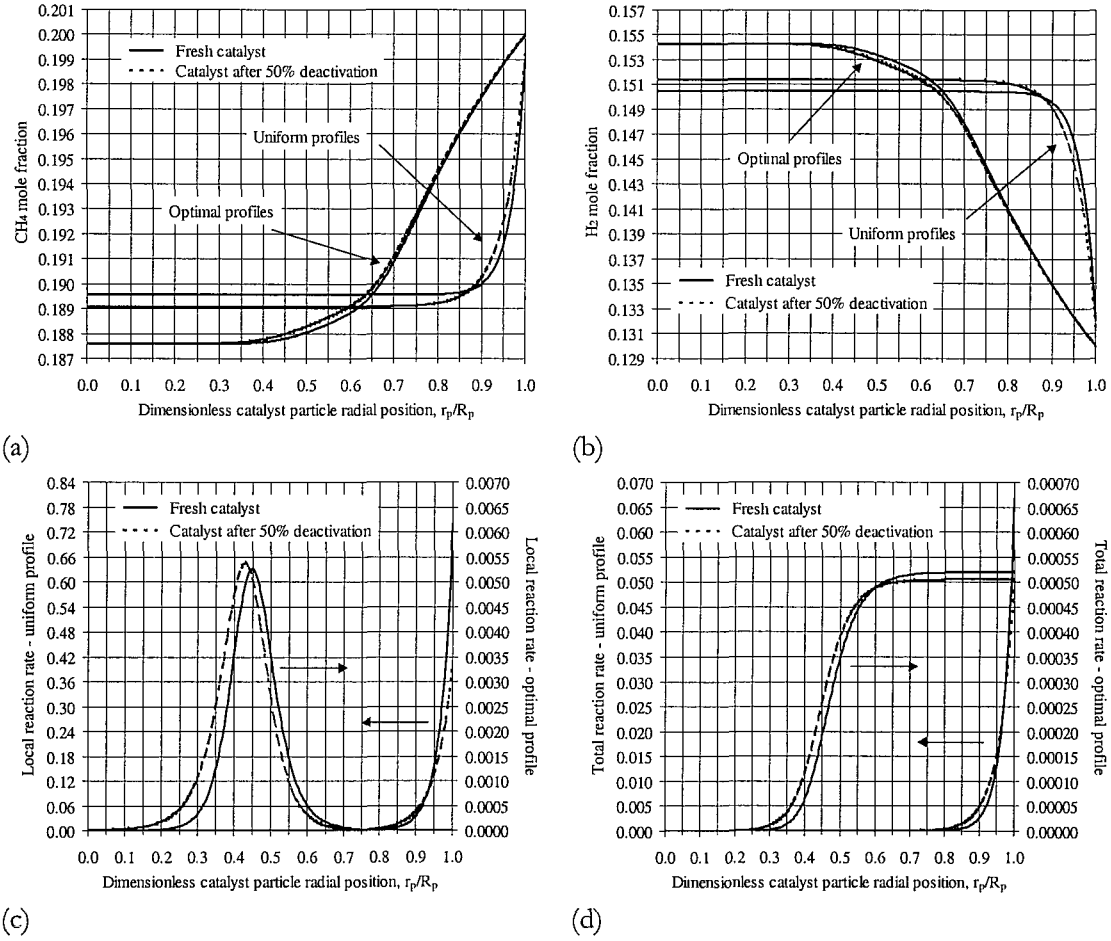

Figure 5.3 Typical performance of a steam reforming catalyst pellet with and without an imposed close to step-wise activity profile ($0 \leq r_p/R_p \leq 0.425$) and an imposed diffusion barrier ($0.599 \leq r_p/R_p \leq 1$) before and after 50% deactivation: (a) methane mole fraction profile; (b) hydrogen mole fraction profile; (c) dimensionless local reaction rate; (d) total (integrated) reaction rate.

The results have also shown that the optimum is relatively flat, indicating that the performance is not overly sensitive to the exact location of the barrier and the

distribution of active sites. This can be an advantage from the design point of view (since the activity-non activity barrier is not so strictly defined) or a way of controlling the overall reaction rate value since this changes with the location of the optimum. Furthermore, the presence of an activity profile appears to be much more important than that of a diffusivity profile, but the presence of both is useful. Figures 5.4 and 5.5 can confirm this last statement. Figures 5.4 and 5.5 present the methane and hydrogen mole fraction, the dimensionless local reaction rate, and the total reaction rate profiles (for fresh and deactivated catalyst) for a typical steam reforming catalyst particle, i.e., a catalyst particle with uniform profiles, and for two other catalyst particles: one where only the optimal catalyst activity distribution is imposed (Figure 5.4) and one where only the a optimal effective diffusivity distribution is imposed (Figure 5.5).

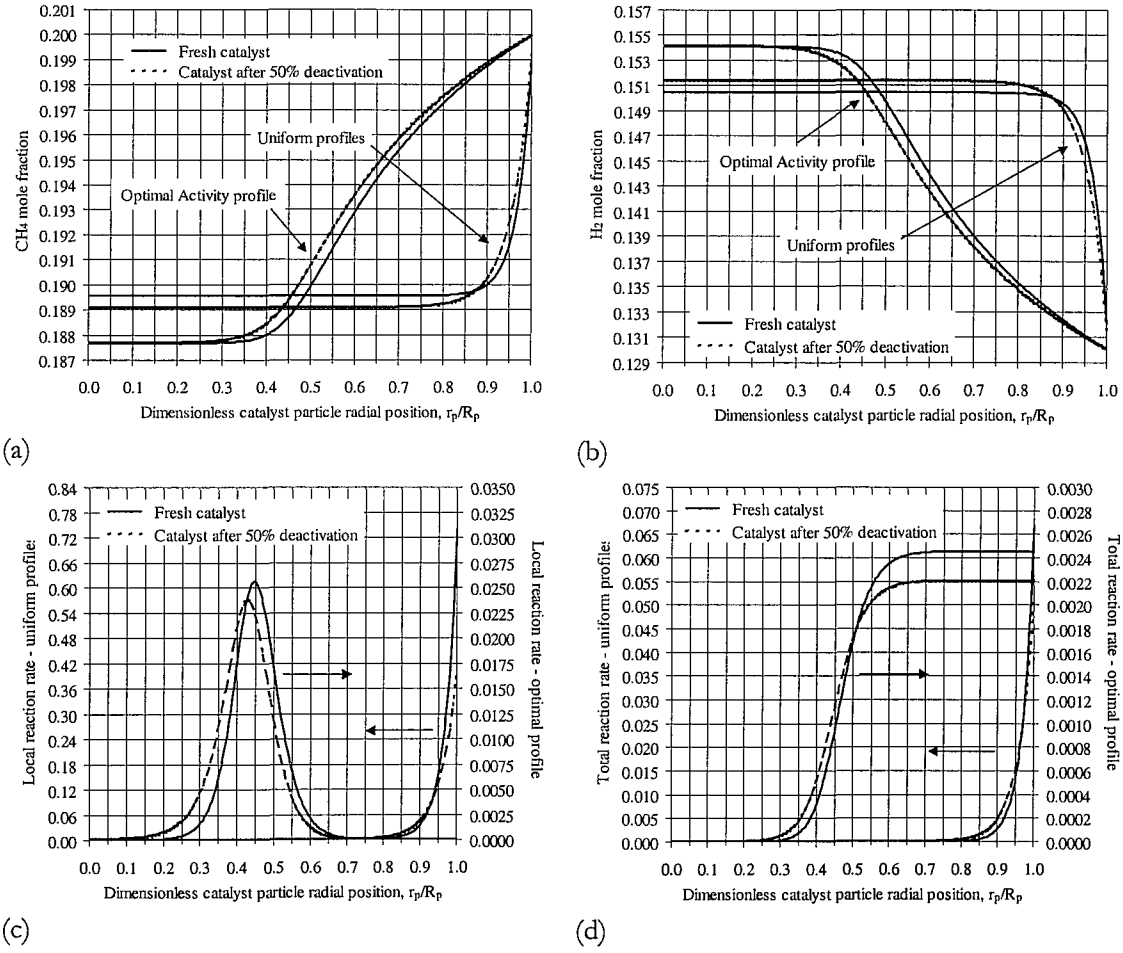

Figure 5.4 Typical performance of a steam reforming catalyst pellet with and without an imposed close to step-wise activity profile ($0 \leq r_p/R_p \leq 0.425$) before and after 50% deactivation: (a) methane mole fraction profile; (b) hydrogen mole fraction profile; (c) dimensionless local reaction rate; (d) total (integrated) reaction rate.

From Figure 5.4 and comparing the total reaction rate values at the catalyst surface for a typical catalyst pellet ($6.68x10^{-2}$) and for a catalyst particle where only the optimal activity profile is imposed ($2.46x10^{-3}$), a significant reduction is observed. Furthermore, while for the case where both optimal distributions were imposed the total reaction rate only decreased by ~3% when deactivation occurred, in this case the total reaction rate decrease is now of ~10%. From Figure 5.5 and comparing again the total reaction rate values at the catalyst surface for a typical catalyst pellet and for a catalyst particle where only the effective diffusivity profile is imposed ($2.60x10^{-2}$), no significant reduction is observed and for this case the reduction in the total reaction rate when deactivation occurs is of ~27%.

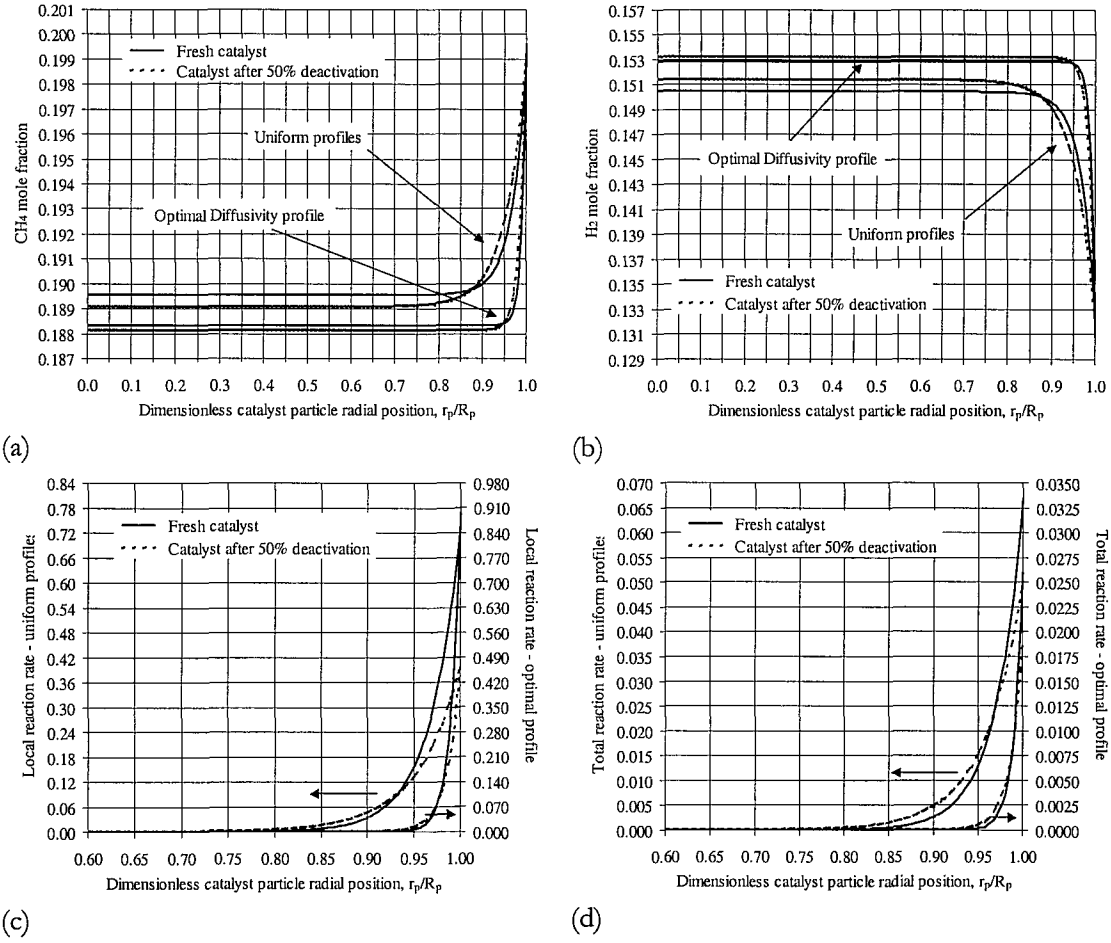

Figure 5.5 Typical performance of a steam reforming catalyst pellet with and without an imposed diffusion barrier ($0.599 \leq r_p/R_p \leq 1$) before and after 50% deactivation: (a) methane mole fraction profile; (b) hydrogen mole fraction profile; (c) dimensionless local reaction rate; (d) total (integrated) reaction rate.

The results also suggest that there are many profile combinations that lead to a near-optimum or desired value of the objective function. The chosen profile combination depends then on the main objective, i.e., on how much the rate of the steam reforming reaction needs to be reduced (constraint (5.6) in optimisation problem). Once this information is known, the optimisation problem can be modified to ensure that the total reaction rate is greater than a certain specified value, that can, for example, allow for the desired heat integration of the IIR-SOFC system.

5.4.1 Effect of a Simpler First Order Kinetic Expression

The calculation of optimal activity and effective diffusivity distributions were also performed considering simpler first order kinetics in relation to methane and carbon monoxide. Such kinetic expression was obtained by modifying the previously used steam reforming kinetics by Xu and Froment (1989a). The optimisation results when using this simpler kinetic expression have also shown that for a spherical pellet, an "egg-yolk" type distribution of active catalyst coupled with a diffusion barrier placed in the outer regions of the pellet, lead to optimum performance in which the total rate of reaction remains virtually constant despite any catalyst deactivation. The optimal distributions obtained are now such that the active material is placed in the particle centre until $r_p/R_p = 0.476$ and the diffusion barrier is placed in the outer region from $r_p/R_p = 0.581$. Figure 5.6 presents the described optimal distributions.

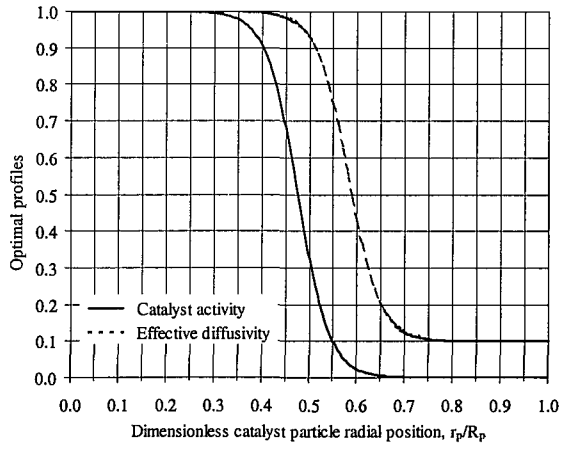

Figure 5.6 Determined optimal catalyst activity and dimensionless effective diffusivity distributions when using a simpler first order kinetic expression.

Figure 5.7 presents the methane and hydrogen mole fraction, the dimensionless local reaction rate, and the total reaction rate profiles (for fresh and deactivated catalyst) for a typical steam reforming catalyst particle, i.e., a catalyst particle with uniform profiles, and for a catalyst particle using the determined optimal catalyst activity and effective diffusivity distributions.

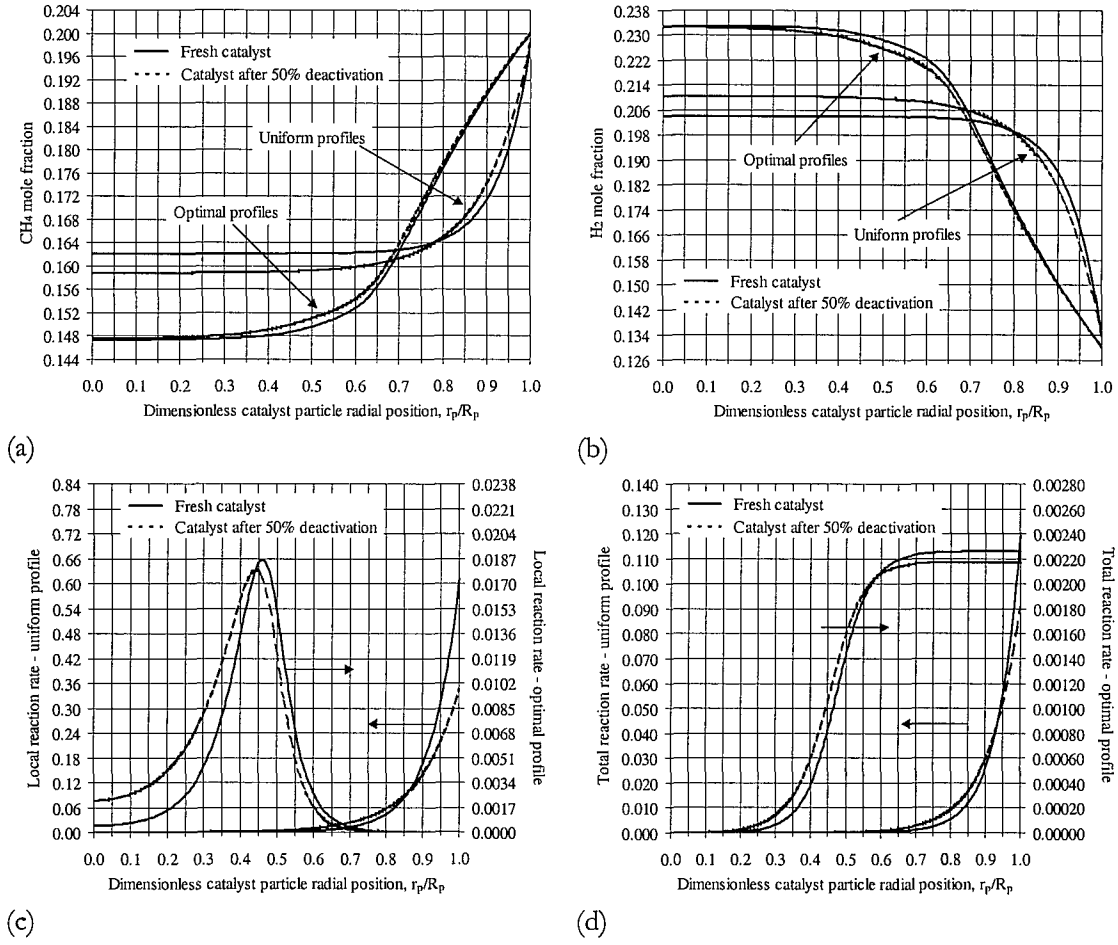

Figure 5.7 Typical performance of a steam reforming catalyst pellet with and without an imposed close to step-wise activity profile ($0 \leq r_p/R_p \leq 0.476$) and an imposed diffusion barrier ($0.581 \leq r_p/R_p \leq 1$) before and after 50% deactivation for a simpler first order kinetic expression: (a) methane mole fraction profile; (b) hydrogen mole fraction profile; (c) dimensionless local reaction rate; (d) total (integrated) reaction rate.

Although the profiles presented are not quantitatively equivalent to the ones in Figure 5.3, the relative behaviour between the case where the optimal distributions are imposed and the case where uniform distributions are applied, is the same.

From Figure 5.7(d), for instance, and comparing the total reaction rate values at the catalyst surface for a typical catalyst pellet ($1.19x10^{-1}$) and for a catalyst particle where the optimal activity and effective diffusivity profiles are imposed ($2.26x10^{-3}$), a significant reduction is observed. Furthermore, while for the first case the total reaction rate decreases considerably as deactivation occurs (~23% decrease), this does not happen when the optimal activity and effective diffusivity distributions are applied (~4% decrease).

The behaviour of the catalyst particle has been shown to be qualitatively equivalent for both kinetic expressions considered. Thus, the effect of reducing the reaction rate by imposing activity and effective diffusivity distributions is not simply a feature of a certain catalyst particle or kinetics, although the exact location of those distributions is. All this is in accordance with the reported by Morbidelli et al. (1982), who stated that the specific radial position within the pellet where the optimal activity distribution is placed is dependent upon the physical parameters of the pellet, the mass transfer coefficient between the bulk fluid and the pellet external surface, the reactant concentration in the bulk fluid surrounding the pellet, and the kinetic parameters of the reaction.

5.4.2 Pellets with Diffusion Barriers: Practical Considerations

As mentioned in Section 5.3, a minimum allowed value has been defined for the effective diffusivity distribution in order to minimise the risk of total pore blockage. For the results presented above, it has been considered that, on the outer diffusive barrier, this coefficient could be as low as 10% of its normal value. In practice, the implication of such a reduction in the catalyst effective diffusivity value is that the pore radius and porosity of the imposed diffusion barrier must satisfy that value*. Or, alternatively, the minimum allowed value imposed, when determining mathematically the optimal catalyst distributions, must satisfy the specific properties of the barrier being produced. In terms

* For example, reducing the effective diffusivity to 10% of its normal value implies, for the conditions here studied, that the pore size must be either reduced by a factor of around 15, if no porosity changes are taken into account, or by a factor of around 6, if the porosity of the outer diffusion barrier is assumed to be 0.3. This would imply the fabrication of a mesoporous material.

of the optimisation problem, for example, the lower the minimum allowed value is, the lower are both the objective function and the total reaction rate values. All this indicates that, to correctly determine the optimal catalyst distributions, that satisfy the specific research objective, collaboration between experimental and computational work is required.

Therefore, parallel to the work presented in this thesis, some experimental work has also been carried out in the fabrication of pellets with diffusion barriers (Cabello-Sánchez et al., 2003; Laosiripojana, 2003; Aguiar et al., 2001a). So far, preliminary results related to the fabrication of those barriers are very promising. It has been found that the use of high calcination temperatures promotes sintering of the diffusion barrier material, which decreases its porosity and, consequently, the rate of methane reforming reactions. Some information on the fabrication methods of pellets with diffusion barriers can be found in Appendix C.2.

5.5 Internal Reforming SOFC & Optimal Distributions

The aim of this section is to show that the overall effect of using such non-uniform distributed catalysts is equivalent to the effect of using inherently less-active oxide catalysts. Simulation results obtained when imposing activity and effective diffusivity distributions to the reforming catalysts in the combined direct and indirect internal reforming solid oxide fuel cell model developed in previous chapters are presented. For that purpose, the activity and effective diffusivity distributions presented in Figure 5.2 are applied to the base case system conditions defined in Chapter 4, Section 4.2.1, where a relative catalyst activity of 0.2% was then considered. Only the component mole fractions and temperature profiles are here presented as all the system variables and their response to changes in some of the parameters have already been fully studied in Chapter 4. Figures 5.8c and 5.8d illustrate the profiles obtained. For convenience, Figures 5.8a and 5.8b present the same profiles when typical reforming catalysts, i.e. reforming catalysts with uniform distributions, are considered (these results have already been presented in Section 4.2.1, Figure 4.1).

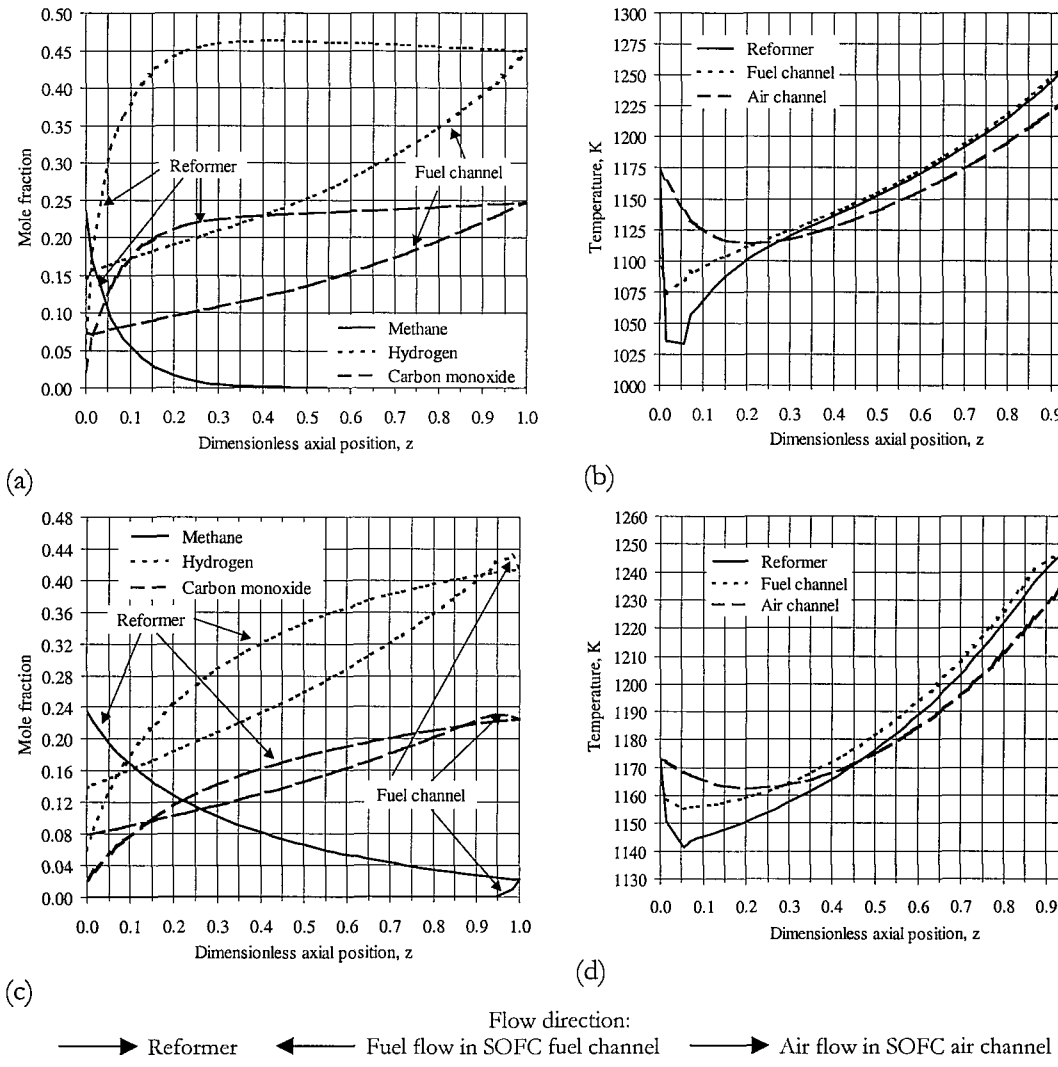

Figure 5.8 Reformer and fuel channel methane, hydrogen, and carbon monoxide mole fraction profiles and reformer, SOFC fuel channel, and SOFC air channel temperature profiles: for the base case conditions presented in Section 4.2.1, Chapter 4 (a-b) and for the case where activity and effective diffusivity distributions are imposed to the reforming catalysts (c-d).

Figures 5.8a and 5.8c present the methane, hydrogen, and carbon monoxide mole fraction profiles in both the reformer and the SOFC fuel channel. It can be seen from Figure 5.8c that, due to the successful reduction in the reforming reaction rate, the methane is no longer all consumed in the first one third of the reformer, but is now gradually converted along the reformer, achieving a final conversion of 87%. At the outlet of the reformer, the fuel stream molar composition is now 2.1% CH_4, 41.5% H_2, 22.4% CO, 25.2% H_2O, and 8.8% CO_2. As previously observed in Sections 4.3 and 4.4, some methane slippage occurs to the SOFC fuel channel.

Figures 5.8b and 5.8d present the corresponding reformer, SOCF fuel channel, and SOFC air channel temperature profiles. As can be seen, the purpose of smoothing the temperature profiles at the entrance of the reformer has been accomplished by imposing the above determined optimal distributions. As for the methane that flows through to the SOFC fuel channel, this is, in accordance to the reported in Section 4.3, all consumed in the first 10% of the fuel channel length, leading to thermal gradients in this region. However, these temperature gradients are not as pronounced as the ones reported before, showing the feasibility of using catalysts with non-uniform distribution of the active metal and a diffusion barrier placed on the outer surface, to thermally couple the two systems. For reference, under these conditions, the terminal voltage is 0.681 V and the efficiency 49.1%, as compared to a voltage of 0.644 V and an efficiency of 46.5% obtained for the base case conditions in Chapter 4.

Figures 5.9 and 5.10 present the same profiles as in Figures 5.8c and 5.8d but for the case where activity and effective diffusivity distributions are imposed on a reformer catalyst with the full activity reported by Xu and Froment (1989a) and for the case where this same catalyst is 50% deactivated, respectively. The purpose of showing such mole fraction and temperature profiles is to demonstrate that with the option of using such catalysts, the original conventional Ni catalysts can now be used, and that the system performance under such catalyst conditions is equivalent to the case where a relative uniform catalyst activity of 0.2% was assumed, as shown in Figures 5.8a and 5.8b. A consequence of this is, however, that steep temperature gradients at the entrance of the reformer are still present, and the original aim of this research is not fulfilled.

From Figure 5.10 it can be seen that even after 50% catalyst deactivation, the system performance is still approximately the same, and so the aim of reducing the reforming reaction rate even when deactivation occurs is successfully accomplished. The same would not be true for the case where an initial relative catalyst activity of 0.2% was assumed. The reason for this is that the optimal distributions determined were for a full active catalyst particle with a radius of 2 mm, where the effectiveness factor (that is equivalent, for uniform catalyst distributions, to the total reaction rate defined in Table 5.1) was 6.68×10^{-2} (see Section 5.4). This value is in accordance with the effectiveness factors reported by Xu and Froment (1989a). In order to guarantee that the catalyst

performance is not significantly affected by deactivation, such conditions should apply, for which the reaction is said to be diffusion limited. However, for a less active catalyst as is the case where a relative activity of 0.2% was considered, this is no longer true, as the reaction is now much slower and diffusion is no longer the limiting step. In such case, the effectiveness factor is generally close to unity (for the conditions in Figures 5.8a and 5.8b, the effectiveness factor is around 0.9). Under such conditions, any change in the catalyst activity due to deactivation has a proportional effect on the reaction rate. Therefore, even though the results presented in Figure 5.8c and 5.8d might have seemed promising, with deactivation the local thermal mismatch between the heat required by the reforming reactions and the heat released by the fuel cell would probably lead to the already well-known undesired temperature gradients.

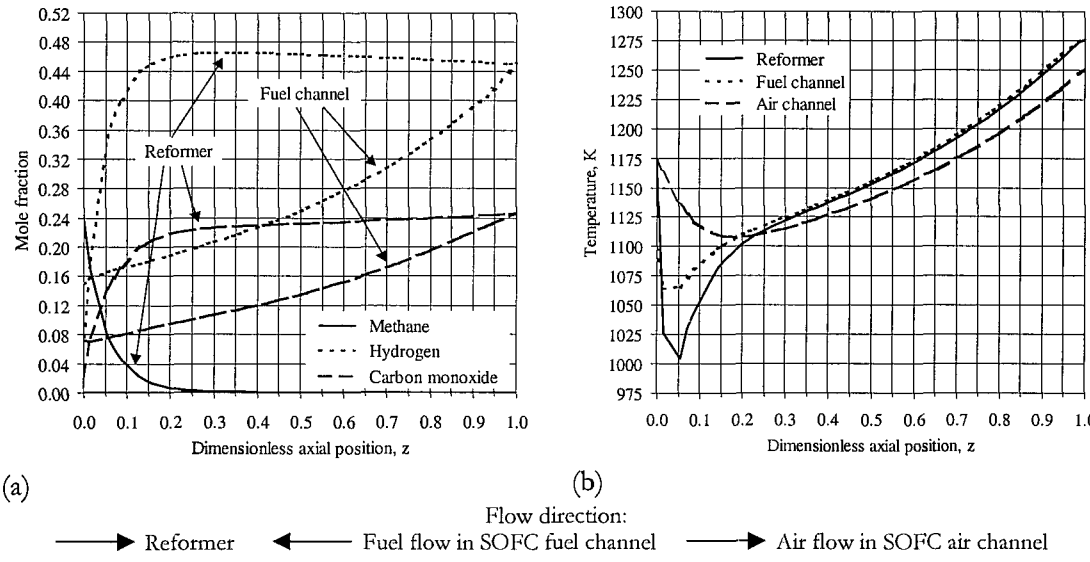

Figure 5.9 Reformer and fuel channel methane, hydrogen, and carbon monoxide mole fraction profiles (a) and reformer, SOFC fuel channel, and SOFC air channel temperature profiles (b) for the case where activity and effective diffusivity distributions are imposed on the fully active reformer catalyst reported by Xu and Froment (1989a).

One suggestion at this point would be the use of a non-uniform catalyst distribution throughout the reformer fixed-bed, which could be achieved by mixing fully active catalyst pellets (fabricated according to the optimal distributions then determined) together with pellets of inert. This way, those catalysts would be diffusion limited and, hence, both a reduced reaction rate and an approximately constant performance with deactivation would be guaranteed.

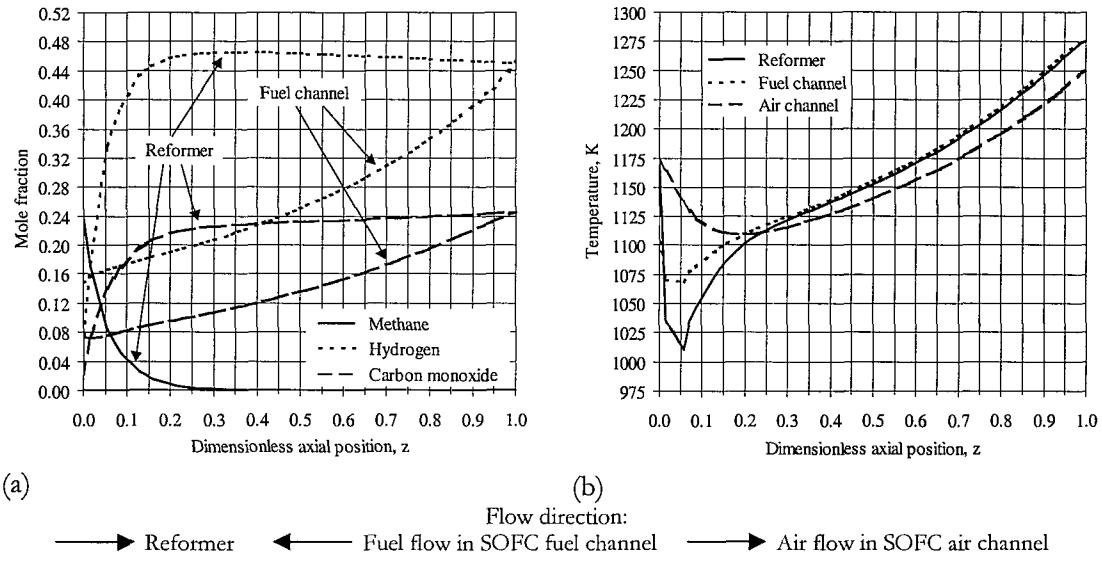

Figure 5.10 Reformer and fuel channel methane, hydrogen, and carbon monoxide mole fraction profiles (a) and reformer, SOFC fuel channel, and SOFC air channel temperature profiles (b) for the case where activity and effective diffusivity distributions are imposed considering the fully active reformer catalyst reported by Xu and Froment (1989a) but with 50% deactivation.

5.5.1 Other Considerations

In an ideal situation, such optimal distributions should be determined for each catalyst particle in the reformer fixed-bed, as bulk phase composition and temperature vary with position along the reactor. However, this would demand the solution of an excessively complex mathematical problem, which would be likewise difficult to apply in practice. As discussed in Section 5.2, possible sub-optimal cases would be either to consider that all catalyst pellets have the same activity and effective diffusivity distributions, as done above, or that the fixed-bed is divided in multiple zones, where in each zone the catalyst distributions are the same but different from the other zones. This last option could also be applied to the case of distributing Ni and oxide-based catalysts unevenly in the reactor bed. In such a case, the least active catalyst would, for example, be placed in the first part of the reformer, to avoid the steep temperature gradients observed in Figure 5.8b, and the more active one would be placed in the second part, to guarantee that no methane slippage to the SOFC fuel channel would occur. In Chapter 6, this last option is analysed, for the case of a coated-wall indirect internal reforming solid oxide fuel cell, by non-uniformly distributing the catalyst along the axis of the reformer.

All these are suggestions for the operation of this specific system and can all be implemented and tested. This corroborates the importance of mathematical modelling, providing information that can be useful when optimising. However, at this stage, and as referred to before, collaboration with the parallel experimental work currently under progress (see Appendix C.2), to encounter the best solution in terms of catalyst properties and operating conditions, is considered essential. All this should be seen as future work in SOFCs development.

Publications based on the work presented in this chapter include Aguiar et al. (2001a, 2001b, 2001c).

In the next chapter, one other reforming reactor configuration is studied – a coated-wall reactor. It is expected that, due to the smaller amount of catalyst present in such a configuration, as this is now deposited in the wall of the reactor instead of in a packed-bed, a reduction of the reforming reactions is also achieved.

Notation

$a(r_p)$	catalyst activity distribution as a function of r_p
C_i	molar concentration of component i, mol/m^3
$\overline{D_e}$	nominal effective diffusivity coefficient, m^2/s
$D_e(r_p)$	effective diffusivity distribution as a function of r_p, m^2/s
k_h	heat transfer coefficient for the film surrounding the particle, $kJ/(m^2sK)$
k_m	mass transfer coefficient for the film surrounding the particle, m/s
r_p	catalyst particle radial position, m
r_{total}	total (integrated) reaction rate
R_p	catalyst particle radius, m
R	steam reforming reaction rate, $mol/kg_{cat}s$
t	time
T	temperature, K
V_p	catalyst particle volume, m^3

Greek letters

$\alpha(t)$	activity dependence with time
$(-\Delta H)$	heat of reaction, kJ/mol

λ_e	effective thermal conductivity, kJ/(msK)
ν_i	stoichiometric coefficient of component i
ϱ_S	catalyst density, kg_{cat}/m^3

Superscripts

S	catalyst particle surface

Subscripts

b	bulk
i	component
s	catalyst particle

Chapter 6

Use of a Coated-Wall Reformer in IR-SOFCs

Summary

In the previous two chapters, it has been shown that, in an IIR-SOFC system with a fixed-bed internal reformer: the use of typical metal-based reforming catalysts leads to full methane consumption but undesirable local cooling at the reformer entrance; and the use of oxide-based catalysts, catalysts within their activity range, or catalysts with non-uniform distribution of active metal within the inert support and a diffusion barrier placed near the outer surface can lead to smoother temperature profiles. In this sixth chapter, a different (more realistic) configuration is studied where the reformer is not a packed-bed reactor but a coated-wall reactor and where the amount of catalyst available for the indirect internal reforming is thus lower. For that purpose, a coated-wall steam reforming reactor model, composed of mass and energy balances to the solid and gas phases, is developed. Firstly, steady-state simulation is performed to evaluate the effect of using different reformer configurations on the overall performance of a fuel cell. Secondly, the dynamic response of such system to load changes is presented.

Outline

6.1 Introduction

In the previous two chapters, the solid oxide fuel cell and fixed-bed steam reforming reactor models developed in Chapters 2 and 3, respectively, were coupled and used to simulate temperature, composition, and relevant electrochemical variables along the reformer tube and fuel cell. The simulation results demonstrated that the use of typical metal-based steam reforming catalysts leads to full methane consumption and undesirable local cooling in the first one third of the reformer. As demonstrated in Chapter 4, the occurrence of this local cooling is due to the fact that, under these conditions, the inherent kinetics of the reforming reactions are extremely rapid and orders of magnitude higher than the fuel cell electrochemical ones, leading to a local thermal mismatch between the two systems. To eliminate such local cooling effect it was then found necessary to slow down the rate of such reforming reactions. Studied solutions to this problem included the use of oxide-based catalysts, or catalysts within their activity range, and, alternatively, the use of conventional nickel catalysts but with non-uniform distribution of active metal within the inert support and/or a diffusion barrier placed near the outer surface. In Chapters 4 and 5, it has been shown that both these methods can lead to smoother temperature profiles but can sometimes result in some methane slippage to the SOFC fuel channel. In addition, it has also been shown that such methane slippage can lead to significant temperature gradients at the entrance of the SOFC fuel channel, which can be eliminated by an appropriate reduction of the anode cermet reforming activity.

This sixth chapter presents a different IIR-SOFC configuration, where the reforming catalyst is no longer pellets in a packed-bed but is instead coated on the walls of the reformer (the remaining system geometry is the same presented in the previous chapters). This configuration is from now on referred to as a coated-wall indirect internal reforming SOFC. As the amount of catalyst available for the indirect internal reforming in the described configuration is lower, a reduction of the reforming reaction rate is expected. In such a case, a broader catalyst activity range is expected and metal-based catalysts might be able to be used (possibly with a diffusion barrier as discussed above), if such is proved to be the best option.

This chapter has two main aims. The first aim is to develop the model for the inner steam reforming coated-wall reactor and to demonstrate that such coated-wall indirect internal reforming SOFC configuration is a good alternative, which can also avoid the steep temperature gradients described in previous chapters. Such a coated-wall reformer would typically be a narrow channel with a catalytic washcoat placed at the walls and can, therefore, be treated as monolithic type reactor. Thus, this chapter first starts with a brief literature review in modelling of monolithic reactors. Based on the issues discussed in Section 6.2, Section 6.3 presents the coated-wall reformer model developed. In Section 6.4, the simulation results of this coated-wall indirect internal reforming SOFC are presented and the effect of some parameters illustrated and discussed. The second aim of this chapter is to briefly study the dynamics of such an IIR-SOFC system, as can be seen in Section 6.5. For that purpose, the dynamic form of the model (which is also presented in Section 6.3) is coupled with the dynamic form of the solid oxide fuel cell model (the steady-state version was presented in Chapter 2). This coupled dynamic model is here used to simulate the response of the cell under step load changes.

6.2 Monolithic Type Reactors

Monolithic structures or monolithic reactors are relatively new in comparison with other more traditional fixed-bed or fluidised-bed heterogeneous reactors. In the past twenty-five years, considerable work has been done in the analysis of such reactors, whose main applications include automotive exhaust gas emissions control, as an afterburning reactor for the combustion of hydrocarbons and CO, catalytic combustion, and selective catalytic reduction, the most widely used catalytic NO_x removal technology (Santos et al., 1998; Hayes and Kolaczkowski, 1994). A monolith reactor resembles a honeycomb structure consisting of hundreds of individual parallel passageways of the order of one mm inside dimension and a variety of cross sectional shapes. The wall (substrate) may be either ceramic or metal and can be either coated with a high surface area washcoat (e.g. alumina), of 10 to 50 μm, that contains the dispersed catalyst, or may itself contain the catalyst as an integral part of its structure (Kolaczkowski, 1999; Leung et al., 1996). Such a monolith support structure combines a relatively high surface-to-volume ratio

with a low pressure drop and is thus favoured when compared with a packed-bed reactor (Kolaczkowski, 1995). In a monolith type combustor, for example, as the fuel and air flow down the channels, the reactants (e.g. methane and oxygen) are transported to the catalyst surface, where they diffuse through the porous structure to react on the catalyst active sites. The reaction products, on the other hand, diffuse through that same porous structure back to the gas phase that continues flowing down the channels. Simultaneously, and due to the high exothermicity of the combustion reactions, the temperature of the catalyst layer increases. This energy is transferred by convection to the gas phase and its temperature increases in the axial direction. Heat conduction through the walls and radiation between the walls are other two heat transfer processes in the axial direction (Kolaczkowski, 1999).

6.2.1 Modelling of Monolithic Reactors

As done in Chapter 3 for the development of the fixed-bed reactor model, issues concerning modelling of catalytic monolithic reactors are now briefly discussed. Modelling of monolith reactors has been widely studied and published. In automobile exhaust gas applications, typical monolithic reactors operate in the laminar flow region and have a negligible pressure drop. The hydrodynamic entrance region is usually a small fraction of the overall reactor length and fully developed flow can be assumed in the major part of the reactor (Hayes and Kolaczkowski, 1994; Hayes et al., 1992). Modelling of the heat and mass transfer processes in these reactors combined with heterogeneous and/or homogeneous reactions can be realised through distributed or lumped parameter models. In the literature, the most common modelling procedure involves splitting the computational domain into several parts and modelling each part separately. Normally, the domain is split into the gas and solid phases, and each one of these phases can then be modelled as a one-dimensional (Kirchner and Eigenberger, 1996, 1997; Nakhjavan et al., 1995; Groppi et al., 1995a; Sinkule and Hlavacek, 1978; Heck et al., 1976) or a multi-dimensional (Wanker et al., 2000; Jahn et al., 1997; Leung et al., 1996; Groppi et al., 1995a, 1995b; Hayes and Kolaczkowski, 1999, 1994; Young and Finlayson, 1976a, 1976b; Lee and Aris, 1977; Heck et al., 1976) system. One-

dimensional models are normally preferred to two-dimensional ones as the latter models are generally more difficult to solve and require more computational time.

For the gas phase, a one-dimensional model considers only variations along the axial direction of the reactor, relying on average radial concentrations and temperatures, while a two-dimensional model considers gas-phase mass and heat variations both in the axial and radial directions. In a one-dimensional model, discontinuities at the wall are accounted for by introducing heat and mass transfer coefficients, and thus, good correlations to determine their values are normally required. In a two-dimensional model, however, it is possible to correctly impose a flux boundary condition, and heat and mass transfer coefficient correlations are not needed (Hayes et al., 1992). In fact, such heat and mass transfer coefficients, in the form of the dimensionless Nusselt (Nu) and Sherwood (Sh) numbers are generally computed from the radial temperature and concentration gradients obtained from two-dimensional models (Wanker et al., 2000; Leung et al., 1996; Hayes and Kolaczkowski, 1994; Heck et al., 1976). However, and as will be seen later in this section, there is still controversy over the correct value of these dimensionless numbers in a monolith channel under reacting conditions. Different gas phase models based on different assumptions, depending on the purpose for which they are used, can be developed. Some models consider constant physicochemical properties of the gas phase (Sinkule and Hlavacek, 1978; Lee and Aris, 1977; Young and Finlayson, 1976a; Heck et al., 1976) while others consider that these vary with temperature and/or composition along the reactor (Groppi et al., 1995b). Some models consider mass and heat axial dispersion (Hayes and Kolaczkowski, 1994) while others consider that these can be neglected (Groppi et al., 1995a; Young and Finlayson, 1976a). One other issue is related to the velocity profile assumed. In a laminar flow catalytic tubular reactor, with gaseous reactants and an exothermic reaction, there is a radial velocity profile, with the velocity at the centreline being twice the average velocity. Because of this, there is a potential for the development of radial concentration and temperature gradients. The magnitude of these radial gradients depends on the relative rates between mass and heat transfer and chemical reaction (Hayes and Kolaczkowski, 1999). Groppi et al. (1995b) concluded that, under the conditions studied, enhancement of gas-solid heat transfer due to hydrodynamic development was minor in relation to other phenomena, and thus,

continuity equations used to determine actual velocity profiles could be avoided by assuming an invariant radial parabolic shape profile of axial velocity. Other authors do consider fully developed laminar velocity profiles that vary with both radial and axial positions in two-dimensional models (Hayes and Kolaczkowski, 1994). For transient simulation, a quasi-static approximation is commonly made relying on the fact that the thermal capacity of a solid is much larger than the one of a gas and, thus, the solid dominates the transient behaviour of the system (Young and Finlayson, 1976a; Heck et al., 1976).

As for the solid phase, various approaches have also been followed. Some references state that, since the catalytic layers are very thin when compared to the monolith walls, it can be assumed that the reactions are actually taking place on the wall-gas interface and so there is no need to take the solid phase mass balance into account (Young and Finlayson, 1976a). As for the heat balance, some references do not account for the radial heat effects occurring in the solid phase (which consists of the washcoat and support), but solve a simple heat balance equation in the axial direction. Thus, radial heat conduction in the solid phase is a priori neglected and the washcoat assumed to be isothermal at each point along the reactor (Wanker et al., 2000; Hayes and Kolaczkowski, 1994). Other models derived consider axial heat dispersion (Hayes and Kolaczkowski, 1994; Sinkule and Hlavacek, 1978) or heat transfer by radiation (Hayes and Kolaczkowski, 1994; Sinkule and Hlavacek, 1978; Lee and Aris, 1977). In automobile exhaust gas applications, radiation is believed to be relevant in the light-off vicinity where large temperature gradients occur. The effect of wall conduction was studied by Heck et al. (1976), Young and Finlayson (1976a), and by Lee and Aris (1977), who also addressed the effect of radiation, showing that radiative heat transfer can be accounted for by properly increasing the wall heat conduction coefficient. Leung et al. (1996), Groppi et al. (1995a, 1995b), Hayes and Kolaczkowski (1994), and Hayes et al. (1992) all developed two-dimensional models considering axial conduction, radiation, and catalytic reaction at the wall. Groppi et al. (1995a, 1995b) concluded that the contributions of wall conduction and radiation could be reasonably neglected in the simulation of ceramic monoliths, allowing for saving of computational time. Hayes et al. (1992) concluded that the axial conduction (in the solid) has a bigger effect than radiation.

One issue widely discussed within the literature concerning monolithic reactors is the diffusion process. This can involve interphase diffusion from the gas-phase to the coated-wall (discussed next) and intraphase diffusion within the coating. In applications involving catalyst pellets, it is generally recognised that diffusion within the porous structure of the catalyst may restrict the rate of reaction. In a washcoat, for example, if the catalytic reaction rate constant is very large, then the concentration may be very low at the support-washcoat wall compared to the bulk concentration value. In such a case, the reaction is said to be mass transfer controlled. When the kinetic rate constant is small, the concentration at the wall is not very different from the average bulk concentration, and the reaction is said to be kinetically controlled. Since reaction rate constants are exponentially dependent on temperature, in automobile exhaust gas applications it is generally believed that the reaction is kinetically controlled in one region of the reactor and mass transfer controlled in the other region. The transition from kinetic to mass control is frequently referred to as the light-off point, with which a sharp increase in temperature is normally associated (Hayes and Kolaczkowski, 1994). To describe this mass transfer limitation, an effectiveness factor (already discussed in Chapters 3 and 5) is often used. Neglecting diffusion resistances can lead to serious overestimation of the performance of a reactor. Several researchers on monolith reactors have assumed that the washcoat layer is so thin that diffusional resistances are not important, and used an effectiveness factor of unity (Lee and Aris, 1977; Heck et al., 1976). However, as shown in a number of studies (Santos et al., 1998; Leung et al., 1996; Kolaczkowski and Serbetcioglu, 1996; Nakhjavan et al., 1995; Hayes and Kolaczkowski, 1994; Zygourakis and Aris, 1983), diffusion limitations may become significant at temperatures as low as 800 K, depending on the type of fuel and catalyst/washcoat properties. Kolaczkowski (1999) stated that, "not recognising that diffusion limitations exist in the catalyst layer may lead to false conclusions being drawn about the activity of a certain catalyst and higher rates of reaction may be achieved by simply decreasing the thickness of the catalyst layer in combination with an increase in the geometric surface area per unit volume of the monolith". When modelling monolith reactors, the effect of pore diffusion can be included in the mass and energy balances via the boundary conditions set at the gas/washcoat interphase. This is generally addressed by including the above referred effectiveness factor in the rate expression for the heterogeneous

reaction. As in the case of catalyst pellets, the simplest case to consider here is the one of a rectangular slab porous catalyst, for which the diffusion/reaction problem in the washcoat can be solved analytically, assuming isothermal conditions, infinite geometry, first-order irreversible chemical reaction, no flux across the centre of the slab, and steady-state conditions (Wanker et al., 2000; Groppi et al., 1995a).

Finally, another important topic widely discussed in the literature concerning modelling of monolithic type reactors is interphase mass and heat transfer. There have been a number of investigations, both numerical and experimental (Bennett et al., 1991) on this subject. Numerous correlations for the calculation of the Nusselt (Nu) and Sherwood (Sh) dimensionless numbers have been suggested and discussed. Such correlations can be for laminar or developing flow and for square, circular, and triangular ducts. However, there is still controversy over the correct value of these numbers in a monolith channel. The calculation of these numbers is normally based on the assumption of either a constant wall temperature or a constant wall heat flux and most of the correlations available are for non-reacting conditions. One other point to note is that most of the referred correlations predict average values for the entire reactor length and not a local value as would be desired (Hayes and Kolaczkowski, 1999). The CO oxidation on a monolithic reactor, for example, is generally characterised by a jump in the Nu and Sh values when sudden light-off occurs, which is preceded and followed by two asymptotic Nu and Sh values. Several numerical investigations (Lee and Aris, 1977; Heck et al., 1976; Young and Finlayson, 1976a) predicted Nu and Sh numbers in the range of 3.0 to 4.5 for the fully developed region, under steady-state conditions, and for an adiabatic cylindrical system. For other geometries, such as square or triangular ducts, the value may be lower but is generally of the same order of magnitude. Hayes et al. (1992) determined, for the catalytic oxidation of propane in a monolith reactor, a Nu number value of 4.6. This is in accordance with the work by Hayes and Kolaczkowski (1994, 1999) who stated that, for reacting systems, the asymptotic Nu and Sh values should not be expected to be the same as for the non-reacting constant wall temperature and flux cases, as neither of those boundary conditions apply, but of the same order of magnitude. Hayes and Kolaczkowski (1994) stated that this is especially true when the reaction proceeds fairly slowly or is mass transfer limited, for which case the wall

temperature may be almost constant. Although most of the work published on this subject is for catalytic oxidation, Sundaram and Froment (1980) formulated a two-dimensional model of a homogeneous tubular reactor, with constant wall temperature and an endothermic reaction, and proposed correlations which gave higher Nu number values but again of the same order of magnitude as for laminar flow in ducts (Hayes and Kolaczkowski, 1994). Also widely discussed are the values of these Nu and Sh numbers under transient conditions. In such a case, if the transition is sharp, the Sh and Nu values generally exhibit discontinuities. However, there are still no correlations available (to use in one-dimensional models) that describe the value of these numbers under transient conditions (Hayes et al., 1992).

6.3 Coated-Wall Reforming Reactor Model

This section is concerned with a model of a coated-wall steam reforming reactor. The developed model is presented in Table 6.1. In this case, dynamics (time dependent behaviour) have been included in the formulation, although the system steady-state (SS) behaviour is first considered (time derivatives set equal to zero in Table 6.1). As described above, here the integration domain has been split into the gas phase and the solid phase, and each one of these phases has been modelled separately. For the gas phase, given the small radial dimension and contrary to what has been done in Chapter 3, one-dimensional mass and energy balances (that assume a mean velocity value) are considered*. As seen in the previous section and through equations (6.1-6.2) and (6.5-6.6), in a one-dimensional gas phase model, discontinuities at the coated-wall are accounted for by introducing heat and mass transfer coefficients. As for the solid phase balances, and as mentioned in Section 6.2.1, it is usual to consider that the catalytic layer is so thin, that it can be assumed both that the reactions take place in the interface gas-solid and that the washcoat is isothermal at each point along the reactor. Here, the solid phase is indeed considered isothermal in the radial direction and, thus, only the energy balance to the gas/coating interface (6.5) is necessary. This takes into account the heat

* Given the high aspect ratio and Peclet number values ($L/D = 88.5$ and $Pe = uL/D \cong 800$, where u is the velocity and D the diffusivity coefficient), it was found reasonable to neglect both axial dispersion and Taylor dispersion effects.

transfer between the gas and solid phases as well as the overall heat transfer from the gas stream flowing through the SOFC fuel channel to the reformer (as the reformer and SOFC models need to be coupled – see previous chapters) and the heat transfer by radiation between the SOFC solid structure (see Chapter 2) and the reformer. However, for the mass balance, and to take intraphase mass diffusion into account, mass radial gradients are considered, leading to the coated-wall or coating mass balance (6.4) in Table 6.1. No mass axial convection or dispersion are assumed. The boundary condition (6.6) quantifies the mass transfer between the two phases and the boundary condition (6.7) indicates that there is no reactant transport across the reformer wall.

Table 6.1 Dynamic coated-wall reactor model.

	Gas Phase	
Mass balance	$\frac{\partial C_{i,b}}{\partial t} = -u\frac{\partial C_{i,b}}{\partial z} + k_m \frac{A_c}{V_b}(C_{i,c}^S - C_{i,b}) = 0 \text{ at SS}$	(6.1)
Energy balance	$(\rho c_p)\frac{\partial T_b}{\partial t} = -u(\rho c_p)\frac{\partial T_b}{\partial z} + k_h \frac{A_c}{V_b}(T_c^S - T_b) = 0 \text{ at SS}$	(6.2)
Initial conditions	Initial steady-state	
Boundary conditions	$z = 0: \quad C_{i,b} = C_i^0, \quad T_b = T^0$	(6.3)
	Coating	
Mass balance	$\varepsilon_c \frac{\partial C_{i,c}}{\partial t} = \frac{1}{r}\frac{\partial}{\partial r}\left[D_e r \frac{\partial C_{i,c}}{\partial r}\right] + \rho_c \sum_j \nu_{ij} R_j = 0 \text{ at SS}$	(6.4)
Energy balance	$\rho_c c_{p_c}\frac{\partial T_c}{\partial t} = k_h \frac{A_c}{V_c}(T_b - T_c) + \rho_c \sum_j \eta_j (-\Delta H)_j R_j^S + + \alpha_R \frac{A_R}{V_c}(T_f - T_c) + \frac{A_R}{V_c}\frac{\sigma(T_{ss}^4 - T_c^4)}{\frac{1}{\epsilon_1} + \frac{A_R}{A_f}\left(\frac{1}{\epsilon_2} - 1\right)} = 0 \text{ at SS}$	(6.5)
Effectiveness factor	$\eta_j = \frac{1}{R_j^S V_c}\int_{V_c} R_j dV_c$	
Initial conditions	Initial steady-state	
Boundary conditions	$r = r_{coating}, \; z \geq 0: \quad D_e \left.\frac{\partial C_{i,c}}{\partial r}\right\|_{r=r_{coating}} = k_m(C_{i,c}^S - C_{i,b})$	(6.6)
	$r = r_R, \; z \geq 0: \quad \left.\frac{\partial C_{i,c}}{\partial r}\right\|_{r=r_R} = 0$	(6.7)

The influence of pore diffusion in the reaction occurring in the coated-wall is accounted for through the use of the effectiveness factor, η_j, presented in Table 6.1. The determination of this factor requires the solution of equations (6.4-6.7), that give both the radial concentration profiles and the temperature of the coated-wall. As for the initial conditions for the dynamic model, and as only disturbances to the system will be studied, these are considered as the initial steady-state solution to which a disturbance is then imposed (no attempt is made here to deal with start-up). As done in Chapter 3, the chemical species considered are CH_4, H_2O, CO, H_2, and CO_2. The mass and energy balances are derived assuming constant velocity, density, and heat capacity. Tests have been made to check whether constant velocity and density were sensible assumptions to take. Differences encountered were found negligible.

From Table 6.1 it can be seen that the derived model has four parameters that determine the behaviour of the system. These are the mass and heat transfer coefficients for the film between the gas phase and the coated-wall, k_m and k_h, the overall heat transfer coefficient between the coating and the SOFC fuel channel, α_R, and the effective diffusivity in the solid coating, D_e. The mass and heat transfer coefficients are calculated, based on the presented in Section 6.2.1, assuming Nu and Sh numbers equal to 3.75, as the predicted values for these numbers are in the range 3.0-4.5 for the fully developed region and steady-state conditions. As for the overall heat transfer (which includes all the appropriate thermal resistances in series between the coated-wall and the external surface of the reformer wall) and effective diffusivity coefficients, and although it is recognised that the flow conditions in the two systems are different, it is assumed, as a first approximation, that these have the same values as the ones calculated for the fixed-bed reactor model. This is also done since the coating is assumed to have, in the absence of specific property data, the same properties (catalyst density and porosity) as the catalyst particles in that model. As mentioned above and similar to what has been done for the fixed-bed reformer model, all the fluid phase properties are considered constant throughout the reactor (the calculation methods used to determine their values are presented in Appendix B.1). These are all assumed to be average values, which apply throughout the system (a reasonable assumption, given the uncertainty associated with these estimates). All the input parameters are presented in the next section together with the simulation results obtained.

6.4 Internal Reforming SOFC & Coated-Wall Reformer

The aim of this section is to present the simulation results of the developed coated-wall internal reforming solid oxide fuel cell model. As done in Chapter 4, the model is here used to simulate temperature, composition, and relevant electrochemical variables along the reformer tube and fuel cell as well as their response to changes in some of the parameters. Many simulations for several combinations of operating conditions have been performed throughout the period of this work, although, for simplicity, only the results for a selected set of conditions, corresponding to the base case defined in the next section (and possible variations from it), are presented. As in the previous chapters, to avoid convergence problems during the solution of this model, the normal procedure of turning models into their dimensionless form was adopted, although the resultant dimensionless equations are not presented, and the gPROMS modelling environment was used. Issues related to the solution of such a coupled model were discussed in Chapter 4.

6.4.1 Base Case

The base case conditions here considered are the same as in Chapter 4. Briefly, for this base case, the system length is taken to be 400 mm, the fuel and air inlet temperatures are both 1173 K, and the total operating pressure is of 1 bar. The reformer fuel feed molar composition is 23.5% CH_4, 47% H_2O, 2.2% CO, 6% H_2, and 21.3% CO_2. The current density considered is 3000 Am^{-2}, with a fuel utilisation of 75%, and an air ratio of 10; these values imply a molar flux of fuel of 1.77 x 10^{-4} $mols^{-1}$ and a molar flux of air of 2.97 x 10^{-3} $mols^{-1}$. The coated-wall model parameters (and the properties assumed for the catalyst coating) are presented in Table 6.2. The catalyst coating thickness value, for these base case conditions, was chosen based on the typical washcoat thickness range of 10-50 μm indicated in Section 6.2. The remaining system dimensions and solid oxide fuel cell parameters have the same values presented in Chapter 4. Finally, a 'reduced activity' catalyst is also used for the base case conditions of this coated-wall internal reforming SOFC. As mentioned before, this IIR catalyst relative activity is defined as the ratio between the activity of the catalyst in use and that of a conventional Ni catalyst

(Xu and Froment, 1989a). Such a reduced relative activity implies the use of either a conventional nickel catalyst with only a certain fraction of Ni content accessible or an inherently less active catalyst. For these base case conditions, a relative activity of 0.2% is considered. Note that, as referred to in Chapter 4, this dilution is still within the range of activities of conventional catalysts. The simulation results obtained are now presented and discussed. In this chapter, only temperature and mole fraction profiles are presented, as the behaviour of the relevant electrochemical variables has already been fully examined in Chapter 4.

Table 6.2 Assigned model parameter values.

Parameter	Value	Parameter	Value
D_e	3.61×10^{-6} m^2s^{-1}	α_R	0.1 $kJm^{-2}s^{-1}K^{-1}$
k_m	0.404 ms^{-1}	k_h	0.108 $kJm^{-2}s^{-1}K^{-1}$
ρ_c *	2335.2 $kg_{cat}m^{-3}$	ε_c *	0.528
c_{p_c} **	1.2 $kJkg^{-1}K^{-1}$	$\delta_{coating}$ ***	50 μm
r_R	2.26×10^{-3} m	$r_{coating}$ ***	2.21×10^{-3} m

* Xu and Froment (1989a, 1989b). ** Twigg (1996). *** Base case value only.

Figure 6.1 shows some of the characteristic results for the defined base case. The component mole fraction profiles in both the reformer and the SOFC fuel channel are presented in Figure 6.1a. It can be seen that, due to the lower amount of catalyst present in this coated-wall reformer (the geometric dilution from a packed-bed to a 50 μm thick coating is approximately 20), the methane is now gradually converted along the reforming reactor with a final conversion of 86.5% (not an equilibrium conversion). Note that the IIR catalyst relative activity used in this base case is the same used for the base case conditions in Section 4.2.1, for which the methane was practically all consumed in the first one third of the reformer. The general behaviour of the reformer and fuel channel mole fraction profiles is the same observed in previous chapters. At the reformer outlet, the fuel stream molar composition is 2.3% CH_4, 41.3% H_2, 22.3% CO, 25.3% H_2O, and 8.8% CO_2 and at the outlet of the fuel channel is 13.9% H_2, 7.8% CO, 54.2% H_2O, and 24.1% CO_2. Figure 6.1b presents the methane and hydrogen mole fraction profiles in the reformer: at the gas phase, at the inner coating surface, and close to the reformer wall. These profiles demonstrate that, at the reformer entrance, some pore diffusion limitation is present even in a 50 μm thick catalyst coating. In fact, in this

region, the reforming reaction effectiveness factor is around 0.8. If a thicker catalyst coating had been used, a lower effectiveness factor would have been expected.

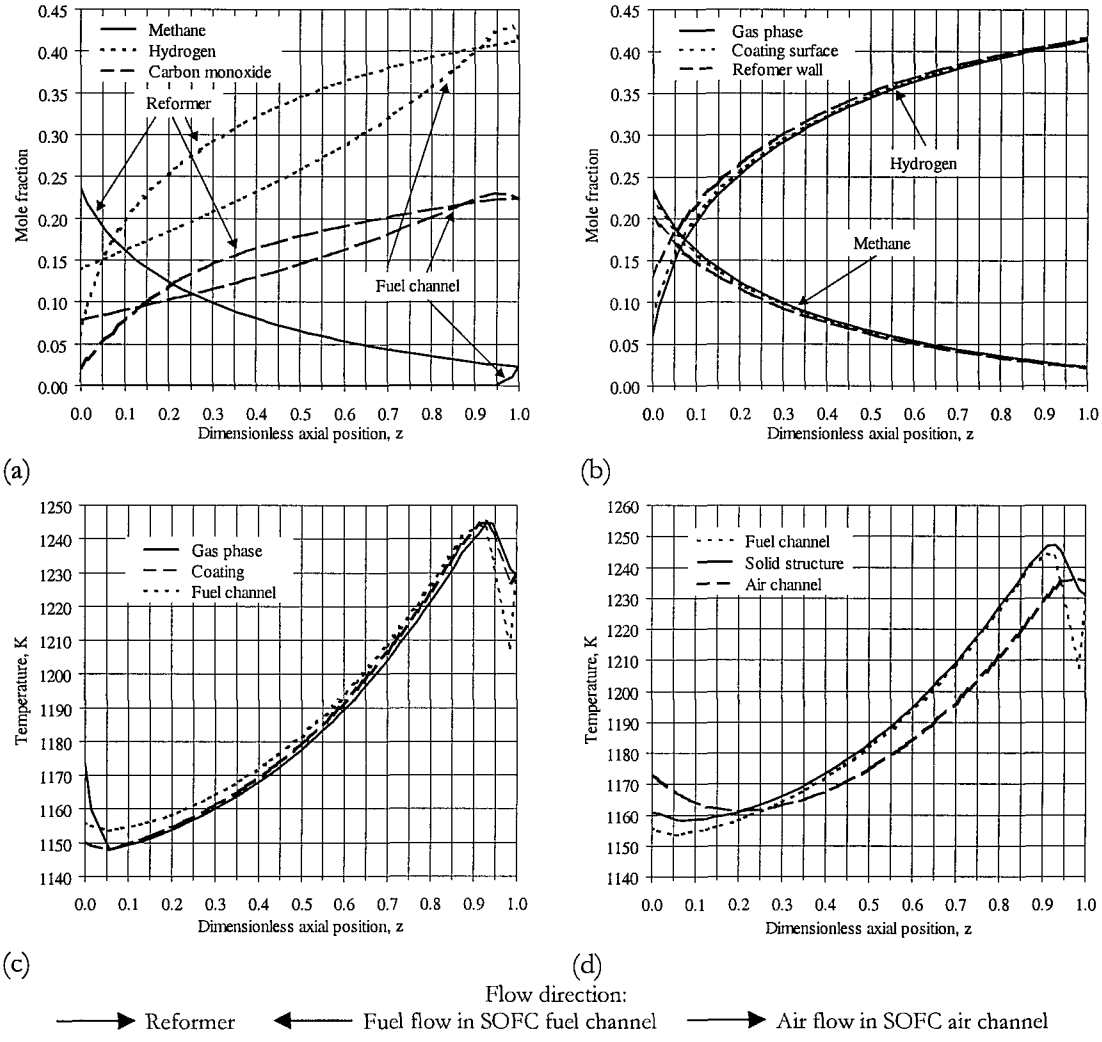

Figure 6.1 Reformer and fuel channel mole fraction profiles (a-b) and reformer and solid oxide fuel cell temperature profiles (c-d) for the base case.

Figures 6.1c and 6.1d present the temperature profiles for the reformer, gas phase and coating, the fuel channel, the solid structure, and the air channel. The simulations demonstrate that the steep temperature gradients previously observed at the entrance of the reformer (see Section 4.2.1), and associated with the indirect internal reforming, are no longer present. Such cooling effect was then attributed to the specific reaction conditions, under which the inherent kinetics of the reforming reactions were extremely rapid and orders of magnitude higher than the fuel cell reactions. In fact, for the packed-bed reactor base case conditions, the indirect internal reforming reaction rate

was about 170 times higher than the fuel cell electrochemical reactions. That number has now been reduced by a factor of approximately 20, proving the feasibility of a coated-wall configuration in reducing the reforming reaction rate.

Also from Figure 6.1c, it can be seen that, as the endothermic steam reforming reactions occur only in the solid phase, close to the entrance of the reformer the coating temperature is lower than the gas phase temperature. However, after a certain point, the heat transfer from the SOFC to the reformer exceeds the heat required by the reforming reactions and the coating temperature becomes higher than the gas phase temperature. At the entrance of the SOFC fuel channel, and as lower methane slippage occurs, only a maximum temperature drop of around 40 K is now observed. In order to reduce this temperature drop, a higher amount of IIR catalyst or a less active DIR catalyst would have been required. Finally, it should be noted that these results are similar to the ones presented in Section 4.3 when lower IIR activity catalysts were used. Under these base case conditions, the voltage obtained is 0.680 V and the fuel efficiency 49.1%, as compared to the values of 0.644 and 46.5% indicated in Section 4.2.1. As already seen in Section 4.3.2, these values demonstrate that moderately reducing the indirect internal reforming reaction rate is not only an effective solution in order to smooth the temperature profiles but also in order to increase the overall efficiency of the system, as part of the heat needed for the endothermic steam reforming reactions is now required in the SOFC instead of in the reformer.

Finally, these results seem to demonstrate that the coated-wall indirect internal reforming SOFC configuration here proposed is a feasible solution for the operation of a SOFC, as a considerable reduction of the IIR reaction rate can be achieved. However, it should also be noted that, the lower amount of IIR catalyst available in this coated-wall configuration, raises again the potential problem of catalyst deactivation. Hence, new catalytic materials for application in such a configuration are required. A possible solution is the use of precious metal catalysts which, although more active than nickel catalysts, are more resistant to carbon deposition and, thus, their dilution with inert material should not be detrimental for a long-term SOFC operation.

6.4.2 Effect of Different IIR Catalyst Thicknesses & Activities

As mentioned earlier, the above simulation results are for a catalyst with a relative activity of 0.2%. In the case of the coated-wall reformer configuration here studied, and although such was not possible for the packed-bed reformer configuration, the fully active Ni catalysts studied by Xu and Froment (1989a), which imply a relative activity of 100%, can now be used. However, for such a catalyst, even a 2 μm thick catalyst coating (the geometric dilution from a packed-bed to a 2 μm thick coating is approximately 550) can prove to be too active, leading to fast full CH_4 conversion and large temperature gradients close to the entrance of the reformer (as can be observed from Figure 6.2).

One other point worth discussing is that different coating thicknesses can also be used. Figure 6.3 presents the reformer mole fraction and temperature profiles, which result from using catalysts with different thicknesses: 50 μm (base case), 100 μm, and 200 μm. As expected, an increase in the coating thickness leads to an increase in the final methane conversion in the reformer and, thus, to less methane slippage to the SOFC fuel channel. However, once again, the local cooling effect at the entrance of the reformer increases. In order to find the desired SOFC operation, the best combination between catalyst thickness and activity needs to be determined.

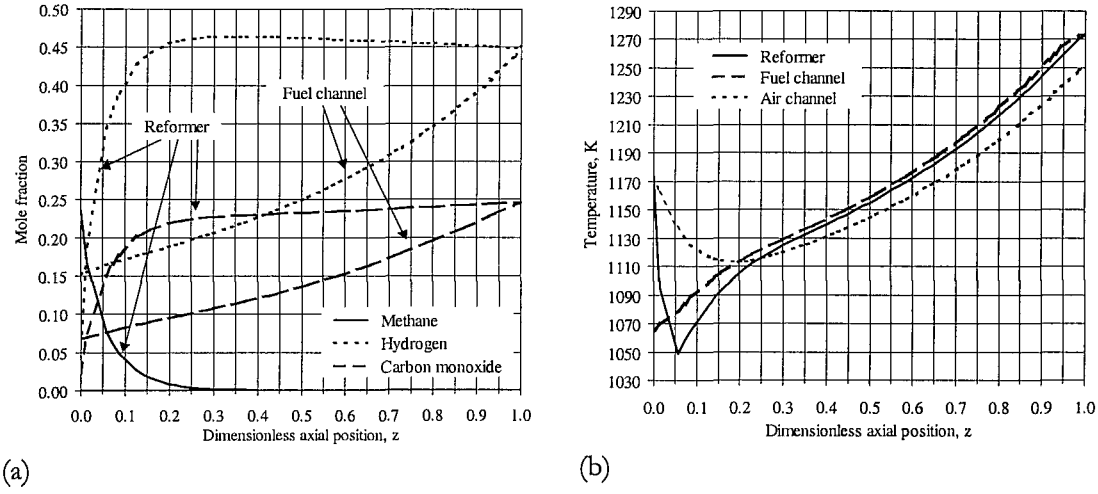

(a) (b)

Figure 6.2 Reformer and fuel channel mole fraction profiles (a) and reformer, fuel channel, and air channel temperature profiles (b) for a 2 μm thick catalyst coating and a fully active Ni catalyst (Xu and Froment, 1989a).

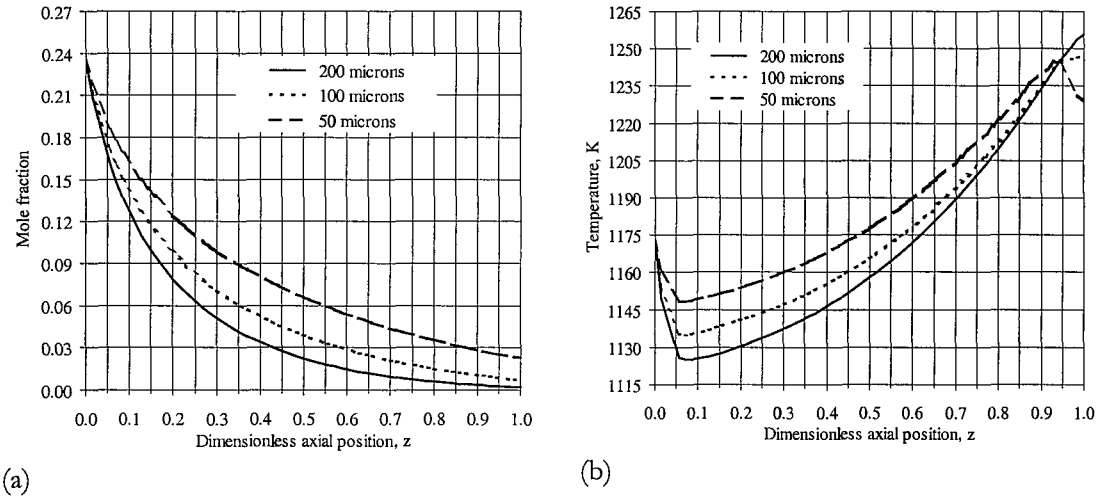

Figure 6.3 Reformer CH_4 mole fraction (a) and temperature profiles (b) for different catalyst coating thicknesses and a 0.2% catalyst relative activity.

Note that one of the solutions proposed in Chapter 4 to reduce the reforming reaction rate while having high resistance to deactivation, was the use of inherently less active catalysts, such as oxide-based catalysts. However, from the results presented in Section 4.3.8, it is clear that the combination of the oxide catalysts for which data is available with a coated-wall reformer configuration would lead to a very low methane conversion at the reformer exit and, ultimately, extremely large temperature gradients at the entrance of the SOFC fuel channel. Thus, oxide-based catalysts can be an effective solution for a packed-bed reformer configuration but, without further development, are not yet appropriate for the configuration here proposed.

6.4.3 Effect of IIR Catalyst Non-Uniform Distribution

Many other solutions or suggestions can be made at this stage. In Chapter 5, the use of catalysts with non-uniform distribution of active metal within the pellet combined with a mass transfer barrier placed on the outer surface demonstrated to be effective in reducing the reforming reaction rate while guaranteeing the catalyst performance in face of possible deactivation. Such an approach could also be successfully applied for the case of this coated-wall configuration. In fact, this is in accordance with the reported by Leung et al. (1996) and Dalla Betta et al. (1993), who, by applying a thin layer of inactive washcoat on top of the active catalyst layer, showed that the diffusion resistance of a washcoat material may be used advantageously in controlling sharp temperature

gradients at the inlet of a combustion reactor. Leung et al. (1996) stated that this can reduce the rate of reaction markedly and also avoid possible catalyst deactivation. The determination of the correct thickness of such a mass transfer barrier to the system under study here would require further work. For example, for the case of a combustion reactor, Dalla Betta et al. (1993) reported that such a barrier should have approximately the same thickness as the washcoat applied, while Leung et al. (1996) showed that a layer of only 4 μm in thickness (10% of the washcoat thickness) can have a significant effect in reducing the reaction rate.

One other possible method, also referred to in Chapter 5, could be to distribute the IIR catalyst non-uniformly along the axial distance of the reforming reactor. Figure 6.4 presents the mole fraction and temperature profiles obtained for a 50 μm thick catalyst coating, with a linear axial relative activity profile (the profile used is such that the relative activity varies from 0.01% at the reformer entrance to 1.5% at the reformer exit). This profile was determined (based on the knowledge acquired throughout the course of this work) to guarantee that the methane was gradually but fully converted in the reactor, as easily verified in Figure 6.4a.

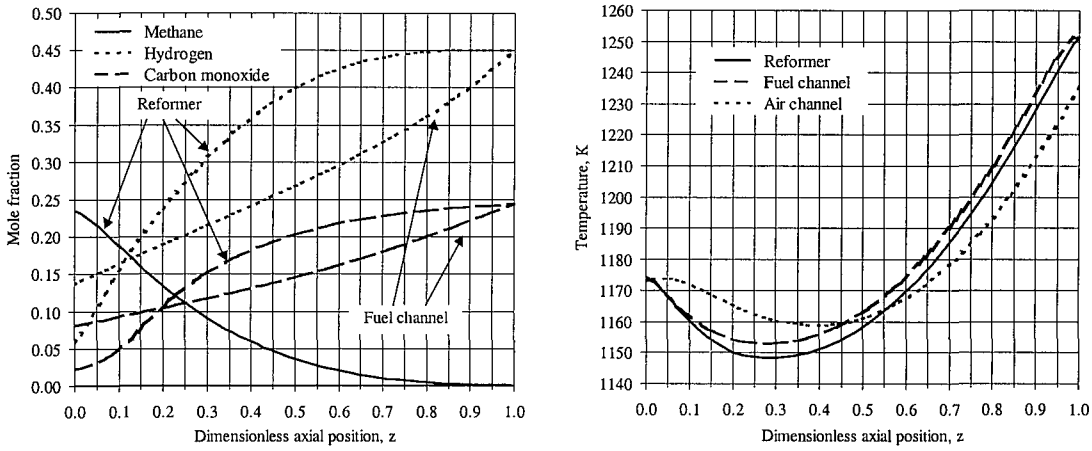

(a) (b)

Figure 6.4 Reformer and fuel channel mole fraction profiles (a) and reformer, fuel channel, and air channel temperature profiles (b) for a 50 μm thick catalyst coating with non-uniform axial distribution.

From Figure 6.4b it can be seen that, with such a profiled relative activity, the temperature first decreases very smoothly and by only 25 K from its inlet value and then starts gradually increasing until the top end of the system. Note that, although this

approach has not been included in the results presented in Chapter 4, this would also be feasible for application with a fixed-bed reforming reactor, where the net effect on the mole fraction and temperature profiles would be the same. Other axial activity profiles (linear or non-linear) combined with different catalyst coating thicknesses could also have been used. The simple case, where different catalysts or catalysts with different relative activities are placed in separate sections of the reactor (equivalent to imposing an activity step change type function in the catalyst bed), could also be considered.

6.5 Dynamic Simulation of an Internal Reforming SOFC

As mentioned above, the dynamic response of the coated-wall internal reforming SOFC to load changes is also investigated in this chapter. Load changes are a frequent transient process during SOFC operation and, thus, knowledge of the system behaviour as well as of its response time after such disturbances is required. Dynamic simulation can be seen as a first step towards the control of such processes when disturbances or changing load requirements occur, and at start-up or shutdown. In this section, current density step changes are simulated and the overall system response analysed. The dynamic model of the coated-wall reforming reactor has been presented in Section 6.3. The dynamic version of the steady-state solid oxide fuel cell model presented in Chapter 2 (Tables 2.2 and 2.3) has also been developed, although this is not presented here.

Figures 6.5 and 6.6 present the transient voltage, mole fraction, and temperature profiles for the case where a current density step change from 3500 to 4000 A/m^2 is imposed to the system. With the exception of the current density value (and all the input parameters that depend on it), the base case operating conditions and parameters presented in Section 6.4.1 have also been considered here. From the fuel utilisation factor expression (2.35), Table 2.5 in Chapter 2, it can be easily seen that, if a positive current density step change is applied, while keeping the fuel feed flow rate constant, an increase in the fuel utilisation factor from the initial to the final steady-sate is expected. However, to guarantee that the cell is able to sustain such a high fuel utilisation value, several approaches can be followed. The simplest two are: to apply a simultaneous positive step change in the fuel feed rate or to supply the cell in advance with the required fuel feed flow rate. For the simulation results presented in Figures 6.5 and 6.6,

the equivalent to the latter approach was assumed. Thus, during simulation, the inlet fuel and air flow rates were a priori determined based on the final current density value of 4000 A/m^2 and only then the current density step change was applied. Note that this does not imply that such an approach is considered a suitable control policy. Under such conditions, the fuel utilisation increases from 65.6 to 75% and the fuel efficiency from 41.5 to 45.2%.

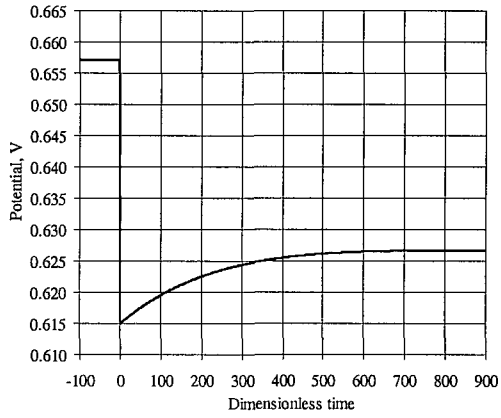

Figure 6.5 Transient cell potential variation after a current density step-change from 3500 A/m^2 to 4000 A/m^2.

As can be seen from Figure 6.5, after a positive current density step change, the intermediate period between the disturbance imposed and the new steady-state, is characterised by an undershooting of the cell voltage. In order to understand the reason why this voltage undershooting occurs, some of the knowledge acquired in Chapter 4 is required: with lower temperature values, higher overpotentials and, consequently, lower voltage values are associated (the opposite is also true) and with higher current density values, higher cell temperatures, due to the higher amount of waste heat produced, are expected. Thus, as immediately after the positive step change in the current density, the cell temperature is still low and related to the initial current density value, the cell voltage is lower than the new steady-state value. Figure 6.6 illustrates the temperature increase just described. As can be seen, at Time = 50 (dimensionless time = 50 corresponds to 18 seconds), the temperature is still low and close to the corresponding temperature of the initial current density value of 3500 A/m^2. With time, the system temperature increases and with it the cell voltage, which is closely related to the system temperature. Other simulations have shown that the magnitude of the voltage undershoot is directly

related to the magnitude of the current density step change applied. The results reported here show the same general response and trends published by Achenbach (1994, 1995) for a planar SOFC and by Hall and Colclaser (1999) for a tubular SOFC.

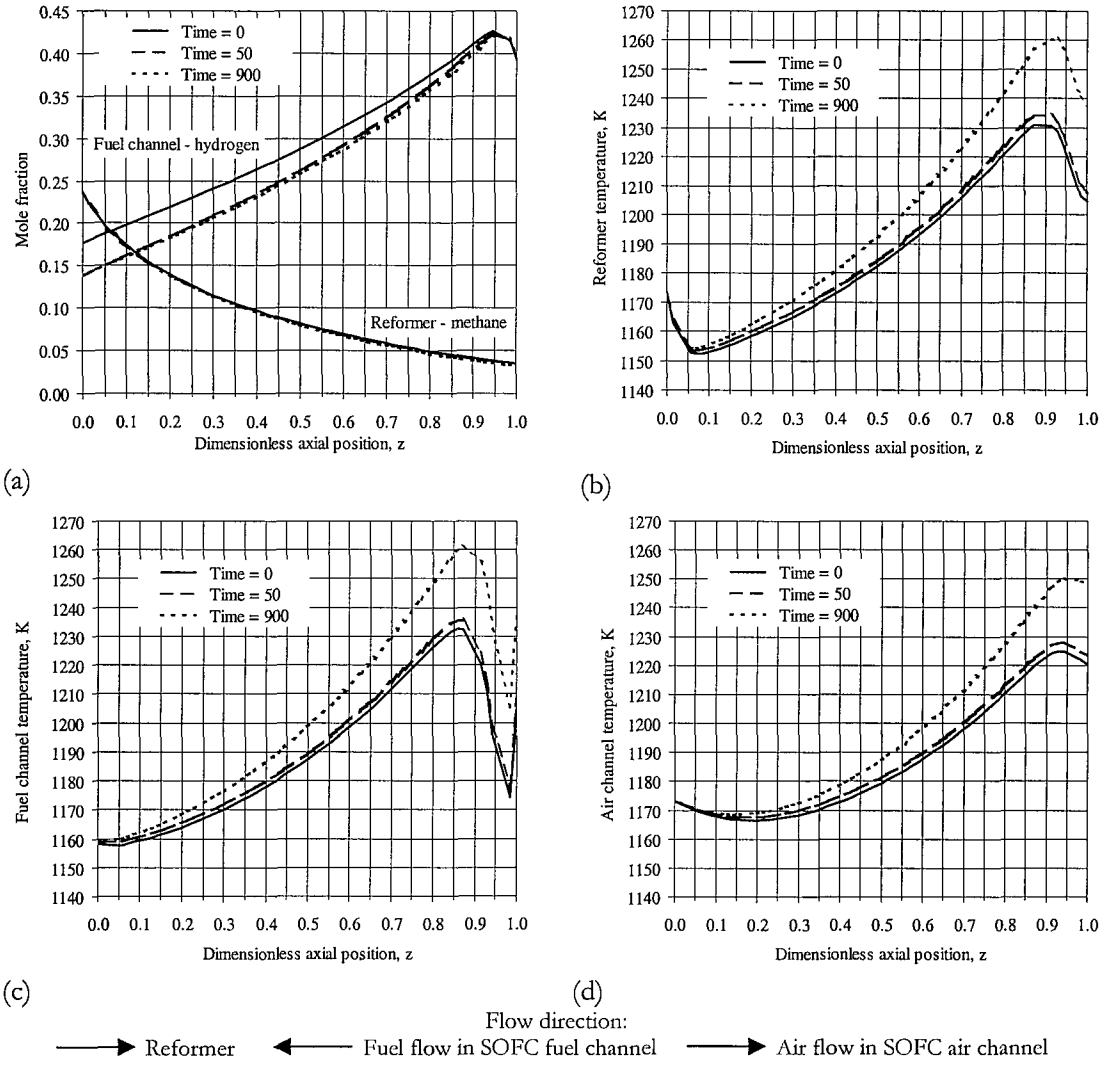

Figure 6.6 Transient CH_4 reformer and H_2 fuel channel mole fraction profiles (a) and reformer, fuel channel, and air channel temperature profiles (b-d) after a current density step-change from 3500 A/m² to 4000 A/m² (Time = dimensionless time).

Figure 6.6 also illustrates that the composition and temperature profiles have a different response time when subject to load changes. From Figure 6.6a, for instance, it can be seen that, as the fuel inlet flowrate is still the same, the CH_4 conversion has only a slight increase; any changes observed are due to the increase in the temperature of the reformer. However, in terms of the fuel channel mole fraction profiles, it can be seen that the change in the H_2 mole fraction profile is immediate, showing that more H_2 is

converted for the new higher current density value. As seen in the previous chapters, H_2 and CO conversion in the SOFC fuel channel is directly proportional to the current density being drawn from the cell and, thus, any changes in this are immediately reflected in the fuel channel composition profiles. However, it should be noted that some of the effects just described are a consequence of the assumptions made during the model development. For instance, for the fuel cell reactions, kinetic control was assumed hence, the immediate response of the fuel channel H_2 mole fraction profiles. In addition, as mentioned in Chapter 4 (Section 4.2.1), the reformer feed inlet composition was determined by assuming a certain ratio of anode gas recycle. However, if anode gas recycle had been accounted for in the model, the dynamic response of the system would be different from the one described above, as, for instance, oscillations in the reformer feed composition would be expected. These and other factors should then be accounted for if a more detailed dynamic analysis of the system is required.

One conclusion that can be drawn from the results above is that, for control purposes, an appropriate change of the inlet gas flow rates should be linked with a load change. For instance, for the current density step change just illustrated, and since the overall cell temperature increases, an obvious control action would be to increase the inlet air flow rate to remove the excess heat produced in the cell. A more appropriate control strategy would have to come from more detailed studies of the system dynamics.

Finally, and as an example of what would happen if a negative current density step change occurred, Figures 6.7 and 6.8 present the same profiles as in Figures 6.5 and 6.6 but for the case where the current density changes from 3000 to 2500 A/m^2.

From Figure 6.7 it can be seen that, after a negative current density step change, the intermediate period between the disturbance imposed and the new steady-state is characterised by an overshooting of the cell voltage, the hydrogen conversion decreases almost immediately, and the overall cell temperature decreases. Under such conditions, a decrease in the fuel utilisation from 75 to 62.5% as well as a decrease in the fuel efficiency from 49.1 to 43.1% are observed.

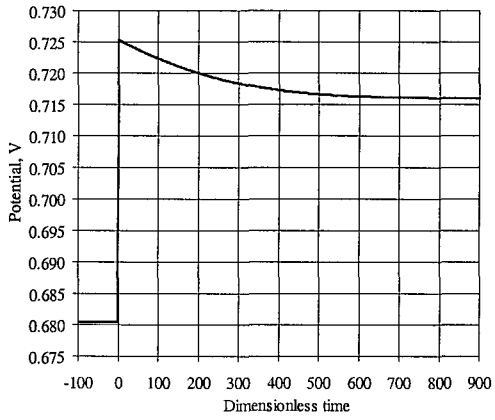

Figure 6.7 Transient cell potential variation after a current density step-change from 3000 A/m² to 2500 A/m².

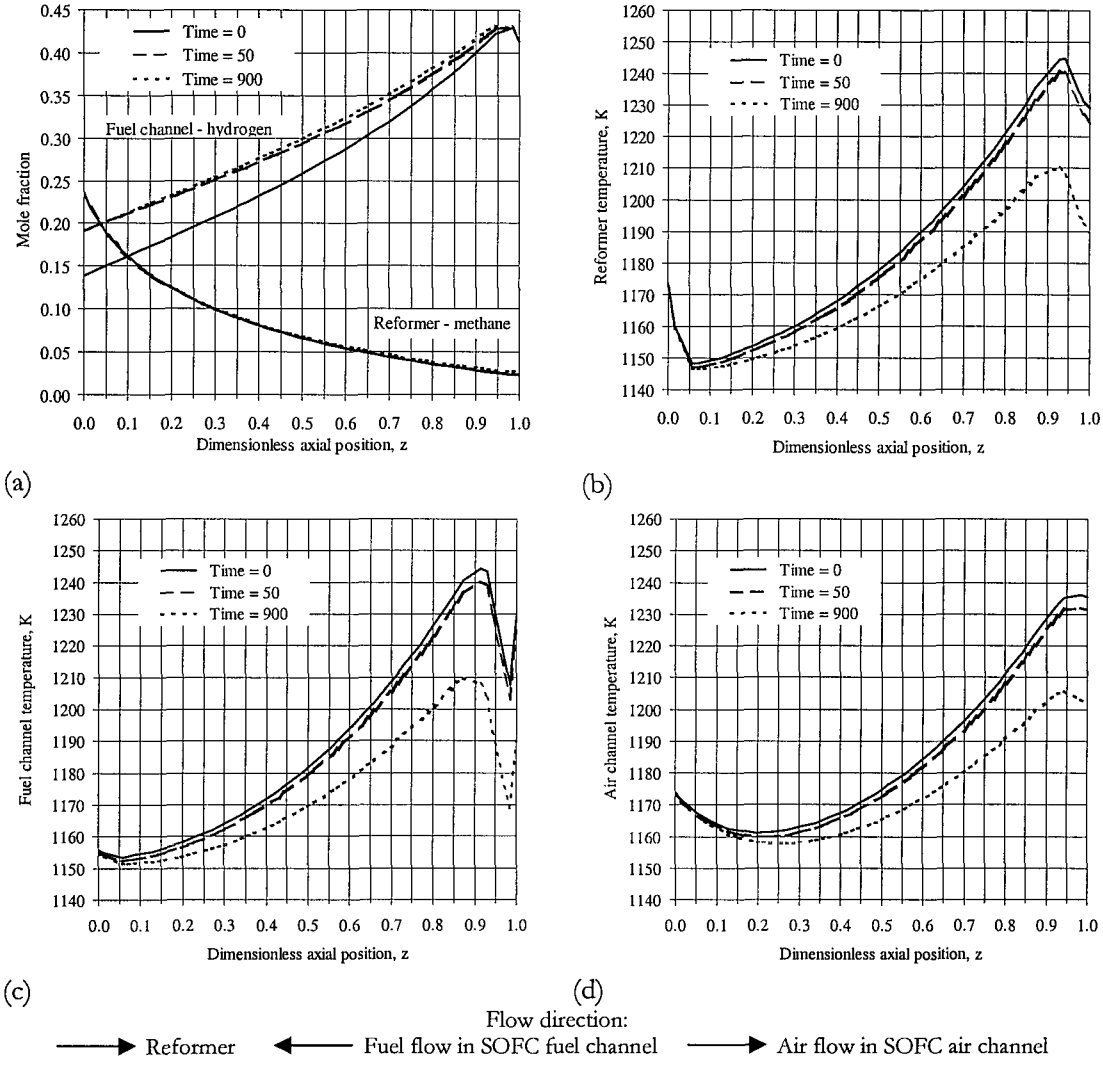

Figure 6.8 Transient CH_4 reformer and H_2 fuel channel mole fraction profiles (a) and reformer, fuel channel, and air channel temperature profiles (b-d) after a current density step-change from 3000 A/m² to 2500 A/m² (Time = dimensionless time).

Notation

A_c	coating inner surface area $[2\pi r_{coating}L]$, m^2
A_f	fuel channel outer surface area $[2\pi r_f L]$, m^2
A_R	reformer outer surface area $[2\pi r_R L]$, m^2
C_i	molar concentration of component i, mol/m^3
c_p	fluid phase heat capacity, kJ/kgK
c_{p_c}	coating heat capacity, kJ/kgK
D_e	effective diffusivity in the coating, m^2/s
k_h	heat transfer coefficient, kJ/m^2sK
k_m	mass transfer coefficient, m/s
L	system length, m
r	radial coordinate in the reformer, m
R_j	rate of reaction j in the reformer, $mol/kg_{cat}s$
$r_{coating}$	coating inner radius, m
r_R , r_f	reactor and fuel channel outer radius, m
Re	Reynolds number
T	temperature, K
t	time, s
u	velocity of the gas phase in the reformer, m/s
V_b	gas phase volume $[\pi r_{coating}^2 L]$, m^3
V_c	coating volume $[\pi(r_R^2 - r_{coating}^2)L]$, m^3
z	system axial coordinate, m

Greek letters

α_R	overall heat transfer coefficient, kJ/m^2sK
$\delta_{coating}$	catalyst coating thickness, μm
$(-\Delta H)_j$	heat of reaction j in the reformer, kJ/mol
$\in_1, \in_2$	emissivity
ε_c	coating porosity
η	reformer catalyst particle effectiveness factor
λ	fluid phase thermal conductivity, kJ/msK
ρ	fluid phase density, kg/m^3
ρ_c	coating density, kg_{cat}/m^3
σ	Stefan-Boltzmann constant, W/m^2K^4
ν_{ij}	stoichiometric coefficient of component i in reforming reaction j

Superscripts

0	feed conditions
S	coating inner surface

Subscripts

b	gas phase
c	coating or coated-wall
f	SOFC fuel channel
i	component
j	reaction
R	reformer
ss	SOFC solid structure

Chapter 7

Summary, Main Conclusions & Suggestions for Future Work

7.1 Summary

In the past few years, thermal coupling of endothermic and exothermic reactions, where the endothermic reaction generally leads to the desired product and the exothermic one serves as the process heat source, have been the subject of several studies and are seen as a promising application for autothermal multifunctional reactors. As with any other developing technology, alternative autothermal reactor designs, based on different heat recovery mechanisms, have been proposed. In the present work, autothermal operation has been applied to a high temperature solid oxide fuel cell with internal methane steam reforming (IR-SOFC). Fuel cells are energy conversion devices that produce electricity as well as heat directly from a gaseous fuel by electrochemical combination of that fuel with an oxidant. Thus, in an IR-SOFC system, the heat necessary to sustain the endothermic reforming reactions, which produce the hydrogen and carbon monoxide required for the fuel cell operation, can be provided by the excess heat generated in the SOFC, which would otherwise be viewed as an inefficiency of the cell. Several possible configurations have also been proposed for this type of systems. The present work investigates an indirect or integrated internal reforming SOFC configuration (IIR-SOFC), where the reformer section is separate but adjacent to the fuel cell anode and in close thermal contact with it and for which the endothermic and exothermic processes need to be thermally coupled. However, it has been demonstrated that such thermal coupling is not easy to achieve because of the mismatch between the thermal load associated with the rate of steam reforming at typical SOFC temperatures and the local

amount of heat available from the SOFC reactions, which leads to undesirable local cooling effects. To reduce this thermal mismatch it was found necessary to slow down the local rate of the reforming reactions. Catalysts with a much lower metal surface area, partially poisoned catalysts, or catalysts sintered at high temperature could be seen as possible approaches. However, in addition to a reduced reforming reaction, it is also important that such IIR catalysts provide sufficient activity for the lifetime of the system and guarantee the thermal match at all times despite potential catalyst deactivation by coke or sulphur. Thus, the above referred approaches were considered infeasible, as the application of an appropriate reforming catalyst activity was considered essential to ensure that temperature gradients were kept to a minimum, to reduce thermal stresses, and to contribute towards a long system life. Mathematical modelling was the medium used to address all these issues. To simulate temperature, composition, and relevant electrochemical variables both in the reformer tube and fuel cell and to analyse possible solutions of eliminating the described local cooling effects, a simultaneous direct and indirect internal reforming solid oxide fuel cell model has been developed. Two different reformer configurations have been studied. The first one, in which most of the work presented in this thesis was based, is a fixed-bed steam reforming reactor, that leads to a fixed-bed IIR-SOFC, and the second one a coated-wall steam reforming reactor, that leads to a more realistic coated-wall IIR-SOFC.

As a first approach, a reduced activity catalyst has been used in the reformer to study the sensitivity of the IIR-SOFC system to catalyst activity changes. Such reduced relative activity, defined as the ratio between the activity of the catalyst in use and that of a conventional nickel catalyst (Xu and Froment, 1989a), was required to avoid almost instantaneous methane conversion at the entrance of the reformer and implied the use of either a conventional nickel catalyst with only a certain fraction of Ni content accessible or an inherently less active catalyst. However, during the course of this work, kinetics for steam reforming over oxide-based catalysts have been determined, and thus, these were also considered. Such catalysts have a much lower activity when compared with conventional nickel steam reforming catalysts and are highly resistant to carbon deposition (Ramírez-Cabrera et al., 2000a). Among other possible approaches, the use of catalysts with non-uniform distribution of active metal within the inert support and the use of a diffusive barrier placed near the outer catalyst surface have been addressed.

7.2 Main Conclusions

Based upon the summary of work presented above, the main conclusions drawn from the various simulations performed are now listed.

7.2.1 Fixed-bed Indirect Internal Reforming SOFC

From the simulations performed with the fixed-bed steam reforming reactor IIR-SOFC configuration the following main conclusions have been drawn.

1. Autothermal operation of a solid oxide fuel cell can be successfully achieved if the hydrogen and carbon monoxide required for its operation are produced internally by methane steam reforming.

   It has been shown that, although the steam reforming reactions are strongly endothermic, there is enough heat on the fuel cell side to enable such reactions, and that, for the operating conditions studied, the total heat required by the steam reforming reactions represents 58% of the total heat produced in the solid oxide fuel cell (heat production in a fuel cell is due to entropy changes of the electrochemical reactions, resistance to current flow, and polarisation losses). The remaining heat is used to provide the temperature increase of the fuel and air streams. It has also been shown that, with such an IR-SOFC configuration, the requirement for cell cooling, which is usually achieved by flowing excess air through the cathode, is significantly reduced, thereby increasing the overall system efficiency.

2. Use of typical metal-based (e.g. Ni) steam reforming catalysts leads to full methane consumption and undesirable local cooling close to the entrance of the reformer.

   Use of a diluted reforming catalyst (even as low as 0.2%) leads to a full methane conversion and rapid decrease in the reformer temperature (of 140 K from its inlet value) in the first one third of the reformer. This cooling effect has been attributed to the specific reaction conditions, under which the indirect internal

reforming reaction rate has been estimated to be about 170 times higher than the fuel cell electrochemical reactions (if an indirect internal reforming catalyst with a higher amount of Ni had been used, almost instantaneous methane conversion would have been observed). To eliminate such local cooling effects it has been considered necessary to slow down the rate of the reforming reactions and the corresponding local energy flux demand.

3. Use of less active reforming catalysts leads to smoother temperature profiles but can sometimes result in incomplete methane reformer conversion and subsequent reforming on the SOFC anode (direct internal reforming).

   Less active catalysts can be either oxide-based catalysts, catalysts within their activity range, or conventional nickel catalysts but with non-uniform distribution of active metal within the inert support and/or a diffusion barrier placed near the outer surface. Oxide-based catalysts have shown to be promising for application in IIR-SOFCs, as these are less prone to deactivation and lead to smoother temperature profiles and reasonably low methane slippage to the fuel cell side. It has been shown that the use of conventional nickel catalysts with non-uniform distribution of active metal within the inert support and a diffusion barrier placed near the outer surface of the catalyst can lead to a low and approximately constant total reaction rate as and when catalyst deactivation occurs, thereby also leading to smother temperature profiles.

4. Reforming on the solid oxide fuel cell anode can result in full methane conversion and large temperature gradients at the entrance of the fuel channel.

   In cases in which there is methane slippage to the fuel cell side, steam reforming also occurs on the SOFC cermet anode. For such cases, it has been shown that all the methane is fully converted in the first 10% of the fuel channel length and that, depending on the amount of methane slippage, large temperature gradients can occur in this region. This cooling effect is again caused by the fast kinetics of the endothermic direct internal reforming reaction. However, reduction of the anode catalyst reforming activity by a factor of 10 has shown to smooth the

temperature profiles at the SOFC fuel channel entrance. Previous workers have shown that such an anode can still provide the necessary activity for the electrochemical reactions.

5. System analysis to changes in operating conditions and parameters also allows for relevant conclusions to be drawn.

5.1 It has been shown that decreasing the fuel inlet temperature gives a smoother temperature profile at the reformer entrance, but one that leads to undesirable large temperature gradients within the system.

5.2 It has been shown that increasing the current density leads to a lower efficiency and a higher overall temperature rise across the cell and that, if methane slippage to the SOFC fuel channel occurs, an increase in the current density leads to a higher temperature gradient at the fuel channel entrance.

5.3 It has been shown that increasing the operating pressure leads to a higher efficiency, a lower overall temperature rise across the cell, and, for the particular reforming kinetic expressions used, to a lower local cooling effect at the reformer entrance (caused by the reforming reactions). If methane slippage to the SOFC fuel channel occurs, an increase in the operating pressure leads to higher temperature gradients at the fuel channel entrance. It has also been demonstrated that the relation of this local cooling effect (at the entrance of the fuel channel) with pressure depends on the kinetic expression used for the DIR reaction rate.

5.4 It has been shown that a co-flow configuration (co-flow of the air and fuel streams in the fuel cell) is more efficient but leads to steeper temperature gradients near the reformer entrance than a counter-flow one. If methane slippage to the SOFC fuel channel occurs, the efficiency of the two configurations is very similar. In all cases, the counter-flow configuration has shown to be more advantageous.

7.2.2 Coated-Wall Indirect Internal Reforming SOFC

From the simulations performed with the coated-wall steam reforming reactor IIR-SOFC configuration the following main conclusions have been drawn.

1. The use of a coated-wall steam reforming reactor has shown to have the same overall behaviour as the fixed-bed reactor.

   Although infeasible for the fixed-bed reformer configuration, fully active Ni catalysts can be used in combination with a coated-wall reactor, as the amount of catalyst available for the IIR is lower. However, it has been shown that even a 2 μm thick catalyst coating is too active, leading to full methane conversion and large temperature gradients close to the entrance of the reformer. In addition, the lower amount of IIR catalyst available in this coated-wall IIR-SOFC configuration, raises the potential problem of catalyst deactivation. Precious metal catalysts may mitigate these deactivation effects.

2. For a coated-wall IIR-SOFC configuration, catalyst coating thickness and catalyst activity can be combined to achieve a certain desired operation.

   A less active reforming catalyst but of greater thickness can lead to a gradual methane conversion in the reformer and smoother temperature gradients. Depending on the activity and thickness of the catalyst, methane slippage to the SOFC fuel channel may also occur. The best combination between catalyst coating thickness and activity needs to be determined.

3. Use of a non-uniformly distributed IIR catalyst along the axial distance of the reforming reactor can lead to a smoother temperature profile along the reactor.

   The axial IIR catalyst profile was determined with the purpose of guaranteeing that the methane was gradually but fully converted in the reactor. Special cases under this subject can be to place different catalysts in different sections of the

reformer according to the specific purpose. The same results would be obtained for the fixed-bed internal reforming reactor SOFC configuration.

4. Use of oxide-based catalysts may not be appropriate for application with a coated-wall indirect internal reforming SOFC.

   Based on the results obtained for the fixed-bed IIR-SOFC, it appears that an oxide-based catalyst coated-wall reformer would lead to a very low final methane conversion in the reformer and, ultimately, extremely large temperature gradients at the entrance of the SOFC fuel channel. Note that these results are only valid for oxide catalysts for which data is available and that these still require further optimisation in terms of composition and surface area.

5. The dynamic response of the coated-wall internal reforming SOFC to load changes has also been investigated, leading to the following conclusions.

   5.1 After a positive current density step change, the intermediate period between the disturbance imposed and the new steady-state is characterised by an undershooting of the cell voltage, the hydrogen conversion increases almost immediately, and the overall cell temperature increases.

   5.2 After a negative current density step change, the intermediate period between the disturbance imposed and the new steady-state is characterised by an overshooting of the cell voltage, the hydrogen conversion decreases almost immediately, and the overall cell temperature decreases.

7.2.3 Further Discussion

All the conclusions above summarised are for the set of operating conditions analysed. Although several other operating conditions or combination of operating conditions and parameters could have been analysed, these were chosen as typical of SOFC operation and with the final purpose of illustrating the problems associated with IIR-SOFCs. The work here presented should then be seen as a first step (as several

simplifying assumptions were made) towards the development of these particular IIR-SOFC systems. The use of more refined correlations or estimation methods for the determination of the various parameters in the model as well as the development of a more detailed model describing more rigorously the different phenomena occurring in such a system could also be seen as being of major importance at this stage. However, prior acquisition of experimental data, which can allow for the model validation and refinement, is essential. Therefore, validation of the present model should be part of the near future work. In addition, it should be noted that the results here presented are all for a single channel within a SOFC module. In the future, and for a better understanding of the behaviour of these complex systems, full SOFC modules and stacks also need to be modelled and tested.

From the points stated in the previous section, a few further notes of discussion should be added. Although most of the results presented are for an assumed reduced catalyst activity, these are intended to provide information on the activity of the catalysts required for an effective internal reforming SOFC operation with little or no local cooling. In relation to the use and application of oxide-based catalysts, it should be noted that the kinetic expressions here used are still preliminary results, as the developed oxides still require further optimisation in terms of composition and surface area. Thus, and even though the oxides for which data is available were shown not appropriate for application on the coated-wall IIR-SOFC configuration, their application for a fixed-bed reformer is believed to be perfectly feasible. Further research into new and more appropriate oxides, as well as into their kinetic information is thus required. As an alternative, the use of a non-uniform catalyst distribution throughout the catalyst bed has also been suggested and shown to be an effective approach to fully and gradually convert all the methane in the reformer channel. However, in order to optimise such an activity profile, more detailed information on the catalysts to be used is also required. As for the use of non-uniform distribution of active metal within a pellet or simply the use of a mass transfer barrier placed on the pellet outer surface (for the fixed-bed reformer configuration) or on the coating surface (for the coated-wall reformer one), this still requires further work both experimentally, on the fabrication of those mass transfer barrier materials, and through modelling, to determine the most appropriate barrier

properties. Within this subject, consideration of appropriate deactivation mechanisms is also found necessary. If all these approaches prove that some extent of methane slippage to the SOFC fuel channel still occurs, then further study is required in the development of new anode materials that, again, can assure a reduced DIR reaction rate, resistance to carbon deposition, but similar electrochemical performance. Mathematical modelling is again an important tool in determining the desired DIR catalyst activity or, alternatively, in determining the performance of the SOFC system when using specific produced catalysts.

Finally, although a coated-wall reformer as been proposed as a more realistic option, catalyst deactivation is, as mentioned before, a problem within such a system. Hence, new catalytic materials for application in such a configuration are also required. These could include, for instance, precious metals, which, although more active than nickel catalysts, are more resistant to carbon deposition and, thus, their dilution with inert material should not be detrimental for a long-term SOFC operation.

7.3 Suggestions for Future Work

Although the full aim of this project has been accomplished, several research fronts can still be followed in the development of an IIR-SOFC technology. In addition to all the issues already discussed in Section 7.2.3, a few other suggestions for future work are now listed.

1. Consideration of other configurations, such as a planar geometry instead of the tubular one here analysed. Such a study should provide information on which configuration is the most appropriate, although it is believed that both should lead to similar operation and/or similar problems as the ones described in this thesis.

2. Dynamic analysis of the system, with special attention to stability issues, multiplicity of steady-states, and simulation of the system under start-up, shutdown, variable power, and disturbances on any of the operating conditions. These are directly linked with the control of the process when such disturbances or changing load

requirements occur, and thus, control issues should also be addressed. The effect of anode gas recycle in the dynamic behaviour of the system is also important. Anode gas recycle has been one of the methods suggested by Dicks (1998) to minimise the large temperature drop effect at the fuel inlet for a DIR-SOFC.

3. Study of the possibility of introducing some oxygen together with steam as the inlet to the reformer. This should allow for the exothermic partial oxidation of methane to occur together with the steam reforming reaction (requiring again the appropriate combination of an exothermic with an endothermic reaction), thus alleviating the local cooling at the entrance of the reformer.

4. Model validation based on experimental data obtained from an indirect internal reforming SOFC system.

References

Achenbach, E. (1994). Three-dimensional and time-dependent simulation of a planar solid oxide fuel cell stack. Journal of Power Sources, 49, 333-348.

Achenbach, E., & Riensche, E. (1994). Methane/steam reforming kinetics for solid oxide fuel cells. Journal of Power Sources, 52, 283-288.

Achenbach, E. (1995). Response of a solid oxide fuel cell to load change. Journal of Power Sources, 57, 105-109.

Acres, G.J.K., Frost, J.C., Hards, G.A., Potter, R.J., Ralph, T.R., Thompsett, D., Burstein, G.T., & Hutchings, G.J. (1997). Electrocatalysts for fuel cells. Catalysis Today, 38, 393-400.

Acres, G.J.K. (2001). Recent advances in fuel cell technology and its applications. Journal of Power Sources, 100, 60-66.

Aguiar, P., Lapeña-Rey, N., Chadwick, D., & Kershenbaum, L. (2001a). Improving catalyst structures and reactor configurations for autothermal reaction systems: application to solid oxide fuel cells. Chemical Engineering Science, 56, 651-658.

Aguiar, P., Ramírez-Cabrera, E., Lapeña-Rey, N., Atkinson, A., Kershenbaum, L.S., & Chadwick, D. (2001b). Indirect Internal Steam Reforming of Methane in Solid Oxide Fuel Cells. Studies of Surface Science and Catalysis (Eds.: Iglesia, E., Spivey, J.J., Fleisch, T.H.), 136, 501-506.

Aguiar, P., Ramírez-Cabrera, E., Atkinson, A., Kershenbaum, L.S., & Chadwick, D. (2001c). Catalyst Configurations for Indirect Internal Steam Reforming in SOFCs. Proceedings of the Seventh International Symposium on Solid Oxide Fuel Cells, Tsukuba, Japan (Eds.: Yokokawa, H., Singhal, S.C.), 2001-16, 703-711.

Aguiar, P., Chadwick, D., Kershenbaum, L. (2002a). Modelling of an indirect internal reforming solid oxide fuel cell. Chemical Engineering Science, 57, 1665-1677.

Aguiar, P., Chadwick, D., & Kershenbaum, L. (2002b). Effect of Anode Reforming Kinetics on Combined Integrated and Direct Internal Reforming. Proceedings of the Fifth European Solid Oxide Fuel Cell Forum, Lucerne, Switzerland (Ed.: Huijsmans, J.), 1, 515-522.

Aguiar, P., Ramírez-Cabrera, E., Laosiripojana, N., Atkinson, A., Kershenbaum, L.S., & Chadwick, D. (2002c). Oxide Catalysts in Indirect Internal Steam Reforming of

Methane in SOFC. Proceedings of the Fourth International Tokyo Conference on Advanced Catalytic Science and Technology, Tokyo, Japan.

Aguiar, P., Chadwick, D., & Kershenbaum, L. (2002d). Effect of Methane Slippage on an Indirect Internal Reforming Solid Oxide Fuel Cell. To be published.

Ahmed, S., McPheeters, C., & Kumar, R. (1991). Thermal-Hydraulic Model of a Monolithic Solid Oxide Fuel Cell. Journal Electrochemical Society, 138, 2712-2718.

Ahmed, K., Kershenbaum, L., & Chadwick, D. (1989). Sintering effects in a nickel-alumina catalyst. Chemical Engineering Science, 44, 999-1000.

Ahmed, K., & Foger, K. (2000). Kinetics of internal steam reforming of methane on Ni/YSZ-based anodes for solid oxide fuel cells. Catalysis Today, 63, 479-487.

Ahmed, K., & Foger, K. (2001). Approach to equilibrium of the water-gas shift reaction on a Ni/zirconia anode under solid oxide fuel-cell conditions. Journal of Power Sources, 103, 150-153.

Avci, A.K., Trimm, D.L., & Ilsen Önsan, Z. (2001). Heterogeneous reactor modeling for simulation of catalytic oxidation and steam reforming of methane. Chemical Engineering Science, 56, 641-649.

Badwal, S.P.S., & Foger, K. (1996). Solid Oxide Electrolyte Fuel Cell Review. Ceramics International, 22, 257-265.

Baratti, R., Wu, H., Morbidelli, M., & Varma, A. (1993). Optimal Catalyst Activity Profiles in Pellets. X. The Role of Catalyst Loading. Chemical Engineering Science, 48, 1869-1881.

Baratti, R., Feckova, V., Morbidelli, M., & Varma, A. (1997). Optimal Catalyst Activity Profiles in Pellets. 11. The Case of Multiple-Step Distributions. Industrial Engineering Chemistry Research, 36, 3416-3420.

Bebelis, S., Zeritis, A., Tiropani, C., & Neophytides, S.G. (2000). Intrinsic Kinetics of the Internal Steam Reforming of CH_4 over a Ni-YSZ-Cermet Catalyst-Electrode. Industrial Engineering Chemistry Research, 39, 4920-4927.

Becker, E.R., & Wei, J. (1977). Nonuniform Distribution of Catalysts on Supports. I. Bimolecular Langmuir Reactions. Journal of Catalysis, 46, 365-371.

Belyaev, V.D., Politova, T.I., Mar'ina, O.A., & Sobyanin, V.A. (1995). Internal steam reforming of methane over Ni-based electrode in solid oxide fuel cells. Applied Catalysis A: General, 133, 47-57.

Bennett, C.J., Kolaczkowski, S.T., & Thomas, W.J. (1991). Determination of Heterogeneous Reaction Kinetics and Reaction Rates Under Mass Transfer Controlled Conditions for a Monolith Reactor. Trans IChemE, 69B(11), 209-220.

Bessette II, N.F., Wepfer, W.J., & Winnick, J. (1995). A Mathematical Model of a Solid Oxide Fuel Cell. Journal Electrochemical Society, 142, 3792-3800.

Bird, R.B., Stewart, W.E., & Lightfoot, E.N. (1960). Transport Phenomena. John Wiley.

Blanks, R.F., Wittrig, T.S., & Peterson, D.A. (1990). Bidirectional adiabatic synthesis gas generator. Chemical Engineering Science, 45, 2407-2413.

Brunovska, A., Morbidelli, M., & Brunovsky, P. (1990). Optimal Catalyst Pellet Activity Distributions for Deactivating Systems. Chemical Engineering Science, 45, 917-925.

Cabello-Sánchez, F.J., Laosiripojana, N., Atkinson, A., Chadwick, D. (2003). Zirconia approaches to coated barriers for methane steam reforming catalysts. To be published.

Cacciola, G., Antonucci, V., & Freni, S. (2001). Technology up date and new strategies on fuel cells. Journal of Power Sources, 100, 67-79.

Campanari, S. (2001). Thermodynamic model and parametric analysis of a tubular SOFC module. Journal of Power Sources, 92, 26-34.

Carrette, L., Friedrich, K.A., Stimming, U. (2000). Fuel Cells: Principles, Types, Fuels, and Applications. ChemPhysChem, 1, 162-193.

Cavallaro, S., & Freni, S. (1998). Syngas and electricity production by an integrated autothermal reforming/molten carbonate fuel cell system. Journal of Power Sources, 76, 190-196.

Cavallaro, S., Mondello, N., & Freni, S. (2001). Hydrogen produced from ethanol for internal reforming molten carbonate fuel cell. Journal of Power Sources, 102, 198-204.

Chemburkar, R.M., Morbidelli, M., & Varma, A. (1987). Optimal Catalyst Activity Profiles in Pellets. VII. The Case of Arbitrary Reaction Kinetics with Finite External Heat and Mass Transport Resistances. Chemical Engineering Science, 42, 2621-2632.

Clarke, S.H., Dicks, A.L., Pointon, K., Smith, T.A., & Swann, A. (1997). Catalytic aspects of the steam reforming of hydrocarbons in internal reforming fuel cells. Catalysis Today, 38, 411-423.

Corbett, Jr., W.E., & Luss, D. (1974). The Influence of Non-Uniform Catalytic Activity on the Performance of a Single Spherical Pellet. Chemical Engineering Science, 29, 1473-1483.

Costamagna, P., Arato, E., Antonucci, P.L., & Antonucci, V. (1996). Partial Oxidation of CH_4 in Solid Oxide Fuel Cells: Simulation Model of the Electrochemical Reactor and Experimental Validation. Chemical Engineering Science, 51, 3013-3018.

Debenedetti, P.G., & Vayenas, C.G. (1983). Steady-State Analysis of High Temperature Fuel Cells. Chemical Engineering Science, 38, 1817-1829.

Dalla Betta, R.A., Ezawa, N., Tsurumi, K., Schlatter, J.C., Nickolas, S.G. (1993). Two stage process for combusting fuel mixtures. U.S. Patent No. US005183401.

De Groote, A.M., & Froment, G.F. (1996). Simulation of the catalytic partial oxidation of methane to synthesis gas. Applied Catalysis A: General, 138, 245-264.

De Wasch, A.P., & Froment, G.F. (1972). Heat transfer in packed beds. Chemical Engineering Science, 27, 567-576.

De Wasch, A.P., & Froment, G.F. (1971). A two dimensional heterogeneous model for fixed bed catalytic reactors. Chemical Engineering Science, 26, 629-634.

Dicks, A.L. (1996). Hydrogen generation from natural gas for the fuel cell systems of tomorrow. Journal of Power Sources, 61, 113-124.

Dicks, A.L. (1998). Advances in catalysts for internal reforming in high temperature fuel cells. Journal of Power Sources, 71, 111-122.

Dicks, A.L., Pointon, K.D., & Siddle, A. (2000). Intrinsic reaction kinetics of methane steam reforming on a nickel/zirconia anode. Journal of Power Sources, 86, 523-530.

Ding, Y., & Alpay, E. (2000). Adsorption-enhanced steam-methane reforming. Chemical Engineering Science, 55, 3929-3940.

Fellows, R. (1998). A novel configuration for direct internal reforming stacks. Journal of Power Sources, 71, 281-287.

Ferguson, J.R., Fiard, J.M., & Herbin, R. (1996). Three-dimensional numerical simulation for various geometries of solid oxide fuel cells. Journal of Power Sources, 58, 109-122.

Finnerty, C.M., Coe, N.J., Cunningham, R.H., & Ormerod, R.M. (1998). Carbon formation on and deactivation of nickel-based/zirconia anodes in solid oxide fuel cells running on methane. Catalysis Today, 46, 137-145.

Finnerty, C., Tompsett, G.A., Kendall, K., & Ormerod, R.M. (2000). SOFC system with integrated catalytic fuel processing. Journal of Power Sources, 86, 459-463.

Frauhammer, J., Eigenberger, G., Hippel, L.v., & Arntz, D. (1999). A new reactor concept for endothermic high-temperature reactions. Chemical Engineering Science, 54, 3661-3670.

Froment, G.F., & Bischoff, K.B. (1990). Chemical Reactor Analysis and Design (2nd ed.). John Wiley.

Gardner, F.J., Day, M.J., Brandon, N.P., Pashley, M.N., & Cassidy, M. (2000). SOFC technology development at Rolls-Royce. Journal of Power Sources, 86, 122-129.

Gavriilidis, A., Varma, A., & Morbidelli, M. (1993). Optimal Distribution of Catalyst in Pellets. Catalysis Reviews & Science Engineering, 35, 399-456.

Grevskott, S., Rusten, T., Hillestad, M., Edwin, E., & Olsvik, O. (2001). Modelling and simulation of a steam reforming tube with furnace. Chemical Engineering Science, 56, 597-603.

Groppi, G., Belloli, A., Tronconi, E., & Forzatti, P. (1995a). Analysis of Multidimensional Models of Monolith Catalysts for Hybrid Combustors. AIChE Journal, 41, 2250-2260.

Groppi, G., Belloli, A., Tronconi, E., & Forzatti, P. (1995b). A Comparison of Lumped and Distributed Models of Monolith Catalytic Combustors. Chemical Engineering Science, 50, 2705-2715.

Gunn, D.J. (1987). Axial and Radial Dispersion in Fixed Beds. Chemical Engineering Science, 42, 363-373.

Guo, X., Hidajat, K., & Ching, C. (1999). Simulation of a solid oxide fuel cell for oxidative coupling of methane. Catalysis Today, 50, 109-116.

Guo, X., Hidajat, K., & Ching, C. (1997). Oxidative Coupling of Methane in a Solid Oxide Membrane Reactor. Industrial Engineering Chemistry Research, 36, 3576-3582.

Hall, D.J., & Colclaser, R.G. (1999). Transient Modeling and Simulation of a Tubular Solid Oxide Fuel Cell. IEEE Transactions on Energy Conversion, 14, 749-753.

Hayes, R.E., Kolaczkowski, S.T., & Thomas, W.J. (1992). Finite-Element Model for a Catalytic Monolith Reactor. Computers chemical Engineering, 16, 645-657.

Hayes, R.E., & Kolaczkowski, S.T. (1994). Mass and Heat Transfer Effects in Catalytic Monolith Reactors. Chemical Engineering Science, 49, 3587-3599.

Hayes, R.E., & Kolaczkowski, S.T. (1999). A study of Nusselt and Sherwood numbers in a monolith reactor. Catalysis Today, 47, 295-303.

Haynes C., & Wepfer, W.J. (2001). Characterizing heat transfer within a commercial-grade tubular solid oxide fuel cell for enhanced thermal management. International Journal of Hydrogen Energy, 26, 369-379.

Haynes C., & Wepfer, W.J. (2000). `Design for power' of a commercial grade tubular solid oxide fuel cell. Energy Conversion & Management, 41, 1123-1139.

He, W. (1998). Dynamic model for molten carbonate fuel-cell power-generation systems. Energy Conversion Management, 39, 775-783.

He, W., & Chen, Q. (1998). Three-dimensional simulation of a molten carbonate fuel cell stack under transient conditions. Journal of Power Sources, 73, 182-192.

He, W., & Chen, Q. (1995). Three-dimensional simulation of a molten carbonate fuel cell stack using computational fluid dynamics technique. Journal of Power Sources, 55, 25-32.

Heck, R.H., Wei, J., & Katzer, J.R. (1976). Mathematical Modeling of Monolithic Catalysts. AIChE Journal, 22, 477-484.

Hendriksen, P.V. (1997). Model Studies of Internal Steam Reforming in SOFC Stacks. Proceedings of the 5th International Symposium on Solid Oxide Fuel Cells (Eds.: Stimming, U., Singhal, S., Tagawa, H., Lehnert, W.; The Electrochemical Society), 97-18, 1319-1328.

Hirano, A., Suzuki, M., & Ippommatsu, M. (1992). Evaluation of a New Solid Oxide Fuel Cell System by Non-isothermal Modeling. Journal Electrochemical Society, 139, 2744-2751.

Incropera, F.P., & De Witt, D.P. (1990). Fundamentals of heat and mass transfer (3rd ed.). Singapore: Wiley.

Ishihara, T., Yamada, T., Akbay, T., & Takita, Y. (1999). Partial oxidation of methane over fuel cell type reactor for simultaneous generation of synthesis gas and electric power. Chemical Engineering Science, 54, 1535-1540.

Iwata, M., Hikosaka, T., Morita, M., Iwanari, T., Ito, K., Onda, K., Esaki, Y., Sakaki, Y., & Nagata, S. (2000). Performance analysis of planar-type unit SOFC considering current and temperature distributions. Solid State Ionics, 132, 297-308.

Jahn, R., Snita, D., Kubicek, M., & Marek, M. (1997). 3-D modeling of monolith reactors. Catalysis Today, 38, 39–46.

Joon, K. (1996). Critical issues and future prospects for molten carbonate fuel cells. Journal of Power Sources, 61, 129-133.

Joon, K. (1998). Fuel cells – a 21st century power system. Journal of Power Sources, 71, 12-18.

Kirchner, T., & Eigenberger, G. (1997). On the dynamic behavior of automotive catalysts. Catalysis Today, 38, 3-12.

Kirchner, T., & Eigenberger, G. (1996). Optimization of the Cold-Start Behaviour of Automotive Catalysts using an Electrically Heated Pre-Catalyst. Chemical Engineering Science, 51, 2409-2418.

Koh, J., Kang, B.S., & Lim, H.C. (2000). Effect of various stack parameters on temperature rise in molten carbonate fuel cell stack operation. Journal of Power Sources, 91, 161-171.

Kolaczkowski, S.T. (1995). Catalytic Stationary Gas Turbine Combustors: A Review of the Challenges Faced to Clear the Next Set of Hurdles. Trans IChemE, 73A, 168-190.

Kolaczkowski, S.T., & Serbetcioglu, S. (1996). Development of combustion catalysts for monolith reactors: a consideration of transport limitations. Applied Catalysis A: General, 138, 199-214.

Kolaczkowski, S.T. (1999). Modelling catalytic combustion in monolith reactors – challenges faced. Catalysis Today, 47, 209-218.

Kolios, G., & Eigenberger, G. (1999). Styrene synthesis in a reverse-flow reactor. Chemical Engineering Science, 54, 2637-2646.

Kolios, G., Frauhammer, J., & Eigenberger, G. (2000). Autothermal fixed-bed reactor concepts. Chemical Engineering Science, 55, 5945-5967.

Kordesch, K., & Simader, G. (1996). Fuel Cells and Their Applications. New York: VCH.

Kulkarni, M.S., & Dudukovic, M.P. (1996). A Bidirectional Fixed-Bed Reactor for Coupling of Exothermic and Endothermic Reactions. AIChE Journal, 42, 2897-2910.

Kunii, D., & Smith, J.M. (1960). Heat Transfer Characteristics of Porous Rocks. AIChE Journal, 6, 71-78.

Kvamsdal, H.M., Svendsen, H.F., Hertzberg, T., & Olsvik, O. (1999). Dynamic simulation and optimization of a catalytic steam reformer. Chemical Engineering Science, 54, 2697-2706.

Laosiripojana, N. (2003). Reaction Engineering of Indirect Internal Steam Reforming of Methane for Application in Solid Oxide Fuel Cells. Ph.D Thesis, University of London, England.

Larminie, J., & Dicks, A. (2000). Fuel Cell Systems Explained. New York: Wiley.

Lee, H.H. (1985). Heterogeneous reactor design. London: Butterworth.

Lee, C.K., Morbidelli, M., & Varma, A. (1987a). Optimal Catalyst Activity Profiles in Pellets. 6. Optimization of the Isothermal Fixed-Bed Reactor with Multiple Zones. Industrial Engineering Chemistry Research, 26, 167-170.

Lee, C.K., & Varma, A. (1988). An Isothermal Fixed-Bed Reactor with Nonuniformly Active Catalysts: Experiments and Theory. Chemical Engineering Science, 43, 1995-2000.

Lee, A.L., Zabransky, R.F., & Huber, W.J. (1990). Internal Reforming Development for Solid Oxide Fuel Cells. Industrial Engineering Chemistry Research, 29, 766-773.

Lee, S., & Aris, R. (1977). On the Effects of Radiative Heat Transfer in Monoliths. Chemical Engineering Science, 32, 827-837.

Leung, D., Hayes, R.E., & Kolaczkowski, S.T. (1996). Diffusion Limitation Effects in the Washcoat of a Catalytic Monolith Reactor. The Canadian Journal of Chemical Engineering, 74, 94-103.

Levent, M., Budak, G., & Karabulut, A. (1998). Estimation of concentration and temperature profiles for methane-steam reforming reaction in a porous catalyst. Fuel processing technology, 55, 251-263.

Maggio, G., Freni, S., & Cavallaro, S. (1998). Light alcohols/methane fuelled molten carbonate fuel cells: a comparative study. Journal of Power Sources, 74, 17-23.

Markos, J., Brunovska, A., & Letkova, Z. (1990). Optimal Catalyst Pellet Activity Distributions – Fixed-Bed Reactor with Catalyst Deactivation. Computers chemical Engineering, 14, 1317-1322.

Martinez, O.M., Pereira Duarte, S.I., & Lemcoff, N.O. (1985). Modeling of Fixed Bed Catalytic Reactors. Computers chemical Engineering, 9, 535-545.

Matros, Y.S., & Bunimovich, G.A. (1996). Reverse-Flow Operation in Fixed Bed Catalytic Reactors. Catalysis Review & Science Engineering, 38, 1-68.

Meusinger, J., Riensche, E., & Stimming, U. (1998). Reforming of natural gas in solid oxide fuel cell systems. Journal of Power Sources, 71, 315-320.

Minh, N.Q., & Takahashi, T. (1995). Science and Technology of Ceramic Fuel Cells. Elsevier, Amsterdam.

Morbidelli, M., Gavriilidis, A., & Varma, A. (2001). Catalyst Design: Optimal Distribution of Catalyst in Pellets, Reactors, and Membranes. Cambridge University Press.

Morbidelli, M., Servida, A., & Varma, A. (1986a). Optimal Catalyst Activity Profiles in Pellets. 4. Analytical Evaluation of the Isothermal Fixed-Bed Reactor. Industrial Engineering Chemistry Research, 25, 307-313.

Morbidelli, M., Servida, A., Carra, S., & Varma, A. (1986b). Optimal Catalyst Activity Profiles in Pellets. 5. Optimization of the Isothermal Fixed-Bed Reactor. Industrial Engineering Chemistry Research, 25, 313-321.

Morbidelli, M., Servida, A., Carra, S., & Varma, A. (1985). Optimal Catalyst Activity Profiles in Pellets. 3. The Nonisothermal Case with Negligible External Transport Limitations. Industrial Engineering Chemistry Fundamental, 24, 116-119.

Morbidelli, M., Servida, A., & Varma, A. (1982). Optimal Catalyst Activity Profiles in Pellets. 1. The Case of Negligible External Mass Transfer Resistance. Industrial Engineering Chemistry Research, 21, 278-284.

Morbidelli, M., & Varma, A. (1982). Optimal Catalyst Activity Profiles in Pellets. 2. The Influence of External Mass Transfer Resistance. Industrial Engineering Chemistry Research, 21, 284-289.

Mori, T., Higashiyama, K., Yoshioka, S., Kobayashi, T., & Itoh, S. (1989). Steam Reforming Reaction of Methane in Internally-Reformed Molten Carbonate Fuel Cell. Journal Electrochemical Society, 136, 2230-2234.

Nagata, S., Momma, A., Kato, T., & Kasuga, Y. (2001). Numerical analysis of output characteristics of tubular SOFC with internal reformer. Journal of Power Sources, 101, 60-71.

Nakagawa, N., Sagara, H., & Kato, K. (2001). Catalytic activity of Ni¯YSZ¯CeO_2 anode for the steam reforming of methane in a direct internal-reforming solid oxide fuel cell. Journal of Power Sources, 92, 88-94.

Nakhjavan, A., Bjornbom, P., Zwinkels, M.F.M., & Jaras, S.G. (1995). Numerical Analysis of the Transient Performance of High-Temperature Monolith Catalytic

Combustors: Effect of Catalyst Porosity. Chemical Engineering Science, 50, 2255-2262.

Neophytides, S.G. (1999). The reversed flow operation of a crossflow solid oxide fuel cell monolith. Chemical Engineering Science, 54, 4603-4613.

Neophytides, S.G., & Tripakis, A. (1996). The Transient Operation of a Solid Oxide Fuel Cell Monolith Under Forced Periodic Reversal of the Flow. The Canadian Journal of Chemical Engineering, 74, 719-728.

Nieken, U., Kolios, G., & Eigenberger, G. (1995). Limiting Cases and Approximate Solutions for Fixed-Bed Reactors with Periodic Flow Reversal. AIChE Journal, 41, 1915-1925.

Odendaal, W., Gobie, W., & Carberry, J.J. (1987). Thermal parameter sensitivity in the simulation of the non-isothermal, non-adiabatic fixed-bed catalytic reactor - the two-dimensional heterogeneous model. Chemical Engineering Communications, 58, 37-62.

Palsson, J., Selimovic, A., & Sjunnesson, L. (2000). Combined solid oxide fuel cell and gas turbine systems for efficient power and heat generation. Journal of Power Sources, 86, 442-448.

Park, S., Gorte, R.J., & Vohs, J.M. (2000). Applications of heterogeneous catalysis in the direct oxidation of hydrocarbons in a solid-oxide fuel cell. Applied Catalysis A: General, 200, 55-61.

Park, H., Lee, Y., Kim, M., Chung, G., Nam, S., Hong, S., Lim, T., & Lim, H. (2002). Studies of the effects of the reformer in an internal-reforming molten carbonate fuel cell by mathematical modeling. Journal of Power Sources, 104, 140-147.

Pedernera, M., Borio, D.O., & Porras, J.A. (1997). Steady-State Multiplicity in Cocurrently Cooled Autothermal Reactors. AIChE Journal, 43, 127-134.

Quinta Ferreira, R.M., Almeida-Costa, C.A., & Rodrigues, A.E. (1996). Effect of Intraparticle Convection on the Transient Behavior of Fixed-Bed Reactors: Finite Differences and Collocation Methods for Solving Unidimensional Models. Computers chemical Engineering Science, 20, 1201-1225.

Quinta Ferreira, R.M., Costa, A.C., & Rodrigues, A.E. (1992a). Dynamic Behavior of Fixed-Bed Reactors with "Large-Pore" Catalysts: A Bidimensional Heterogeneous Diffusion/Convection Model. Computers chemical Engineering Science, 16, 721-751.

Quinta Ferreira, R.M., Marques, M.M., Babo, M.F., & Rodrigues, A.E. (1992b). Modelling of the Methane Steam Reforming Reactor with Large-Pore Catalysts. Chemical Engineering Science, 47, 2909-2914.

Ramírez-Cabrera, E., Atkinson, A., & Chadwick, D. (2000a). The influence of point defects on the resistance of ceria to carbon deposition in hydrocarbon catalysis. Solid State Ionics, 136-137, 825-831.

Ramírez-Cabrera, E., Atkinson, A., & Chadwick, D. (2000b). Partial Oxidation and Steam Reforming of Methane over Ce0.9Gd0.1O2-x. Proceedings of the Fourth European Solid Oxide Fuel Cell Forum, Lucerne, Switzerland (Ed.: McEvoy, A.J.), 1, 49-58.

Ramírez-Cabrera, E., Atkinson, A., Rudkin, R., & Chadwick, D. (2002a). Partial Oxidation and Steam Reforming of Methane over La1-xSrxCr1-yFeyO3-δ Mixed Conductor. Proceedings of the Fifth European Solid Oxide Fuel Cell Forum, Lucerne, Switzerland (Ed.: Huijsmans, J.), 1, 546-553.

Ramírez-Cabrera, E., Atkinson, A. & Chadwick, D. (2002b). Reactivity of Ceria, Gd- and Nb-Doped Ceria to Methane. Applied Catalysis B: Environmental, 36, 93-206.

Rase, H.F. (1990). Fixed-bed reactor design and diagnostics: gas-phase reactions. London: Butterworth.

Reid, R.C., Prausnitz, J.M., & Poling, B.E. (1988). The Properties of Gases & Liquids. 4th ed., McGraw Hill, New York.

Rostrup-Nielsen, J. (1984). Catalytic Steam Reforming. Catalysis: Science and Technology, Volume 5, 1-117, Springer-Verlag, Berlin.

Rostrup-Nielsen, J., & Christiansen, L.J. (1995). Internal steam reforming in fuel cells and alkali poisoning. Applied Catalysis A: General, 126, 381-390.

Rodrigues, A.E., & Quinta Ferreira, R.M. (1990). Effect of Intraparticle Convection on the Steady-State Behavior of Fixed-Bed Catalytic Reactors. Chemical Engineering Science, 45, 2653-2660.

Salinger, A.G., & Eigenberger, G. (1996a). The Direct Calculation of Periodic States of the Reverse Flow Reactor - I. Methodology and Propane Combustion Results. Chemical Engineering Science, 51, 4903-4913.

Salinger, A.G., & Eigenberger, G. (1996b). The Direct Calculation of Periodic States of the Reverse Flow Reactor - II. Multiplicity and Instability. Chemical Engineering Science, 51, 4915-4922.

Santos, A., Bahamonde, A., Schmid, M., Avila, P., & García-Ochoa, F. (1998). Mass transfer influences on the design of selective catalytic reduction (SCR) monolithic reactors. Chemical Engineering and Processing, 37, 117–124.

Shinoki, T., Matsumura, M., Sasaki, A. (1995). Development of an Internal Reforming Molten Carbonate Fuel Cell Stack. IEEE Transactions on Energy Conversion, 10, 722-729.

Sinkule, J., & Hlavacek, V. (1978). Heat and Mass Transfer in Monolithic Honeycomb Catalysts – III: Radiation Model. Chemical Engineering Science, 33, 839-845.

Smith, J.M. (1981). Chemical Engineering Kinetics. 3rd ed., McGraw Hill, Singapore.

Snyder, Jon D., & Subramaniam, B. (1994). A Novel Reverse Flow Strategy for Ethylbenzene Dehydrogenation in a Packed-Bed Reactor. Chemical Engineering Science, 49(24B), 5585-5601.

Sundaram, K.M., & Froment, G.F. (1980). Two Dimensional Model for the Simulation of Tubular Reactors for Thermal Cracking. Chemical Engineering Science, 35, 364-371.

Sunde, S., & Hendriksen, P.V. (1997). A Mathematical Model for Internal Reforming at Composite Anodes for Solid Oxide Fuel Cells. Proceedings of the 5th International Symposium on Solid Oxide Fuel Cells (Eds.: Stimming, U., Singhal, S., Tagawa, H., Lehnert, W.; The Electrochemical Society), 97-18, 1329-1338.

Tagawa, T., Moe, K.K., Ito, M., & Goto, S. (1999). Fuel Cell Type Reactor for Chemicals-Energy Co-generation. Chemical Engineering Science, 54, 1553-1557.

Tsiakaras, P., & Demin, A. (2001). Thermodynamic analysis of a solid oxide fuel cell system fuelled by ethanol. Journal of Power Sources, 102, 210-217.

Twigg, M.V. (1996). Catalyst Handbook. 2nd ed., Manson Publishing.

Vayenas, C.G., Debenedetti, P.G., Yentekakis, I., & Hegedus, L.L. (1985). Cross-Flow, Solid-State Electrochemical Reactors: A Steady-State Analysis. Industrial Engineering Chemistry Research, 24, 316-324.

Vayenas, C.G., & Pavlou, S. (1987). Optimal Catalyst Activity Distribution and Generalized Effectiveness Factors in Pellets: Single Reactions with Arbitrary Kinetics. Chemical Engineering Science, 42, 2633-2645.

Votruba, J., Hlavacek, V., & Marek, M. (1972). Packed bed axial thermal conductivity. Chemical Engineering Science, 27, 1845-1851.

Xu, J., & Froment, G.F. (1989a). Methane Steam Reforming, Methanation and Water-Gas Shift: I. Intrinsic Kinetics. AIChE Journal, 35, 88-96.

Xu, J., & Froment, G.F. (1989b). Methane Steam Reforming, Methanation and Water-Gas Shift: II. Diffusional Limitations and Reactor Simulation. AIChE Journal, 35, 97-103.

Wanker, R., Raupenstrauch, H., & Staudinger, G. (2000). A fully distributed model for the simulation of a catalytic combustor. Chemical Engineering Science, 55, 4709-4718.

Wu, H. (1994). Application of Optimal Catalyst Activity Distribution Theory. AIChE Journal, 40, 2060-2064.

Wu, H., Brunovska, A., Morbidelli, M., & Varma, A. (1990). Optimal Catalyst Activity Profiles in Pellets. VIII. General Nonisothermal Reacting Systems with Arbitrary Kinetics. Chemical Engineering Science, 45, 1855-1862.

Zygourakis, K., & Aris, R. (1983). Multiple Oxidation Reactions and Diffusion in the Catalytic Layer of Monolith Reactors. Chemical Engineering Science, 38, 733-744.

Yagi, S., & Kunii, D. (1960). Studies on Heat Transfer Near Wall Surface in Packed Beds. AIChE Journal, 6, 97-104.

Yagi, S., & Kunii, D. (1957). Studies on Effective Thermal Conductivities in Packed Beds. AIChE Journal, 3, 373-381.

Yamamoto, O. (2000). Solid oxide fuel cells: fundamental aspects and prospects. Electrochimica Acta, 45, 2423-2435.

Yoshiba, F., Ono, N., Izaki, Y., Watanabe, T., & Abe, T. (1998). Numerical analyses of the internal conditions of a molten carbonate fuel cell stack: comparison of stack performances for various gas flow types. Journal of Power Sources, 71, 328-336.

Young, L.C., & Finlayson, B.A. (1976a). Mathematical Models of the Monolith Catalytic Converter: Part I. Development of Model and Application of Orthogonal Collocation. AIChE Journal, 22, 331-343.

Young, L.C., & Finlayson, B.A. (1976b). Mathematical Models of the Monolith Catalytic Converter: Part II. Application to Automobile Exhaust. AIChE Journal, 22, 343-353.

Appendix A

Appendices Related to Chapter 2

A.1 Butler-Volmer Equation & Activation Overpotentials

The aim of this appendix is to provide detailed information on the Butler-Volmer equation for activation overpotentials and on the common approximations for low and high overpotentials.

The anode and cathode activation overpotential expressions used in the solid oxide fuel cell model derived in Chapter 2 were the following (equations (2.29-2.31) in Table 2.4):

$$\frac{1}{R_{A,H_2}} = \frac{2F}{\Re T_f} K_{A,H_2} \left(\frac{p_{H_2,f}}{p^0} \right)^m \exp\left(-\frac{E_A}{\Re T_f} \right) \tag{A.1}$$

$$\frac{1}{R_{A,CO}} = \frac{2F}{\Re T_f} K_{A,CO} \left(\frac{p_{CO,f}}{p^0} \right)^m \exp\left(-\frac{E_A}{\Re T_f} \right) \tag{A.2}$$

$$\frac{1}{R_C} = \frac{4F}{\Re T_a} K_C \left(\frac{p_{O_2,a}}{p^0} \right)^m \exp\left(-\frac{E_C}{\Re T_a} \right). \tag{A.3}$$

These expressions are such that the overpotentials are written in terms of electrical resistances and are based on the work of Achenbach (1994). As is shown next, equations (A.1-A.3) are simplified equations based on the Butler-Volmer equation for activation overpotentials and on the assumption that those overpotentials are small. The data utilised for the calculation of these overpotentials are mean values from the cited literature (Achenbach, 1994).

The Butler-Volmer equation relates the current density of an electrochemical reaction to the activation overpotential and is given by:

$$j = j_0\left[\exp\left(\frac{\alpha nF}{\Re T}\eta\right) - \exp\left(-\frac{(1-\alpha)nF}{\Re T}\eta\right)\right]. \tag{A.4}$$

where j_0 is the exchange current density and α the transfer factor or coefficient. The exchange current density can be determined experimentally and is the current when the forward and reverse electrode reaction rates are equal, i.e., at the equilibrium potential. This is a characteristic of each particular system and operating conditions. High exchange current densities imply a high electrochemical reaction rate and, thus, a good fuel cell performance is expected (Minh and Takahashi, 1995). The transfer coefficient is considered as the fraction of the change in the polarisation that leads to a change in the reaction rate constant.

When these overpotentials are small, the following simplification is generally valid:

$$\exp\left(\frac{\alpha nF}{\Re T}\eta\right) - \exp\left(-\frac{(1-\alpha)nF}{\Re T}\eta\right) = \left(1+\frac{\alpha nF}{\Re T}\eta\right) - \left(1-\frac{(1-\alpha)nF}{\Re T}\eta\right) = \frac{nF}{\Re T}\eta.$$

And thus,

$$j = j_0\frac{nF}{\Re T}\eta \Leftrightarrow \eta = \frac{j}{j_0}\frac{\Re T}{nF}. \tag{A.5}$$

As the activation overpotentials given by equations (A.1-A.3) are expressed in terms of an electrical resistance, $R_{polarisation}$, the same needs to be done here. Hence,

$$\eta = jR_{polarisation} \Rightarrow R_{polarisation} = \frac{1}{j_0}\frac{\Re T}{nF} \Leftrightarrow \frac{1}{R_{polarisation}} = j_0\frac{nF}{\Re T}. \tag{A.6}$$

Taking equation (A.3) as an example, the following relation for the cathode overpotential exchange current density is obtained:

$$j_{0,C} = \frac{1}{R_C}\frac{RT_a}{4F} = K_C\left(\frac{p_{O_2,a}}{p^0}\right)^m \exp\left(-\frac{E_C}{\Re T_a}\right). \tag{A.7}$$

By replacing this into equation (A.6), the cathode overpotential expression, in terms of an overpotential and not of a resistance as in equation (A.3), is finally obtained:

$$\eta_C = \frac{j}{K_C\left(\frac{p_{O_2,a}}{p^0}\right)^m \exp\left(-\frac{E_C}{\Re T_a}\right)} \frac{\Re T_a}{4F}. \tag{A.8}$$

Equation (A.8) should be a valid expression for η_C provided it is small. Similar expressions can be obtained for the anode exchange current densities, j_{0,A,H_2} and $j_{0,A,CO}$, and for the anode overpotentials, η_{A,H_2} and $\eta_{A,CO}$. Once these exchange current densities are known, either the complete Butler-Volmer equation or the simplification used for higher overpotentials can be derived. The complete Butler-Volmer should be used when η is of intermediate value. However, for higher overpotentials than these, the second term on the right hand side of equation (A.4) can generally be neglected and the following relation is obtained.

$$j = j_0\left[\exp\left(\frac{\alpha nF}{\Re T}\eta\right)\right] \Leftrightarrow \eta = \frac{\Re T}{\alpha nF}\ln\left(\frac{j}{j_0}\right) \tag{A.9}$$

By replacing $j_{0,C}$ into the above equation, η_C for high activation overpotentials can be obtained, the same happening with η_{A,H_2} and $\eta_{A,CO}$. Therefore, and based on the approximations described, three expressions for the activation overpotentials can be derived. For low overpotentials, η_C is expressed by equation (A.8). For intermediate overpotentials, η_C is expressed, as a non-explicit equation, by equation (A.10). And for high overpotentials, η_C is expressed by equation (A.11).

$$j = K_C\left(\frac{p_{O_2,a}}{p^0}\right)^m \exp\left(-\frac{E_C}{\Re T_a}\right)\left[\exp\left(\frac{\alpha 4F}{\Re T_a}\eta_C\right) - \exp\left(-\frac{(1-\alpha)4F}{\Re T_a}\eta_C\right)\right]. \tag{A.10}$$

$$\eta_C = \frac{\Re T_a}{\alpha 4F}\ln\left(\frac{j}{K_C\left(\frac{p_{O_2,a}}{p^0}\right)^m \exp\left(-\frac{E_C}{\Re T_a}\right)}\right). \tag{A.11}$$

Figure A.1 compares the activation overpotentials predicted by equations (A.8), (A.10), and (A.11) as a function of current density (these were computed assuming

temperature and gas composition values, similar to the ones obtained mid-way through the system length, under the base case conditions defined in Chapter 4, Section 4.2.1 – T = 1150°C; $y_{H_2} = 0.25$; $y_{CO} = 0.14$; and $y_{O_2} = 0.21$).

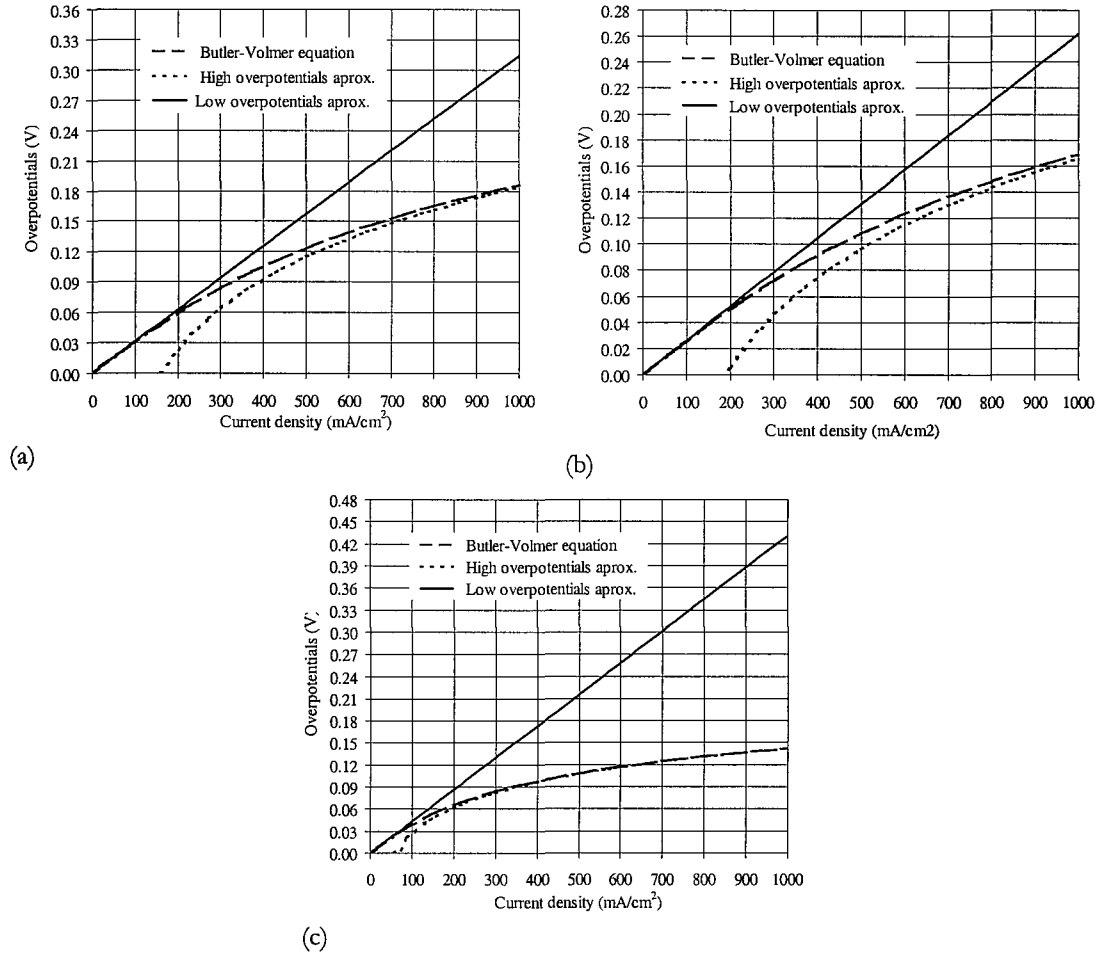

Figure A.1 Comparison between the activation overpotentials predicted by the Butler-Volmer equation and its simplifications for high and low overpotentials: (a) hydrogen oxidation reaction; (b) carbon monoxide oxidation reaction; and (c) oxygen reduction reaction.

As can be seen, for low overpotentials the expression (A.8) and (A.10) present similar predictions and for high overpotentials the same happens with equations (A.10) and (A.11). As for the implications that these might have on the simulations performed, it can also be seen from Figure A.1 that, for the conditions here considered, the maximum error between the approximation for low overpotentials used and the overpotential given by the Butler-Volmer equation is of 0.02 V. This value is for a current density of 400 mA/cm^2, the maximum current density value simulated in this

thesis. It should be noted, however, that both a decrease in operating temperature and in gas composition (H_2, CO, and O_2) lead to higher overpotentials. However, as there are uncertainties in the parameters of equations (A.1-A.3), it has been decided to use the overpotential expressions as reported. For more accurate predictions, research must be carried out to determine more appropriate parameters.

Notation

E_A, E_C	activation energy (equations (A.1-A.3)), kJ/mol
F	Faraday's constant (F = N*e*), C/mol
K_{A,H_2}	pre-exponential factor (equations (A.1)), A/m^2
$K_{A,CO}$	pre-exponential factor (equations (A.2)), A/m^2
K_C	pre-exponential factor (equations (A.3)), A/m^2
j	current density, A/m^2
j_0	exchange current density, A/m^2
m	exponent (equations (A.1-A.3))
n	number of electrons participating in the electrochemical reaction
p^0	standard partial pressure, bar
p_i	partial pressure of component i, bar
R_{A,H_2}	anode overpotential (polarisation resistance) for H_2 oxidation, Ωm^2
$R_{A,CO}$	anode overpotential (polarisation resistance) for CO oxidation, Ωm^2
R_C	cathode overpotential (polarisation resistance), Ωm^2
T	temperature, K
y_i	molar fraction of component i

Greek letters

α	transfer factor or coefficient
η_{A,H_2}	anode overpotential for H_2 oxidation, V
$\eta_{A,CO}$	anode overpotential for CO oxidation, V
η_C	cathode overpotential, V

Subscripts

a	air channel
A	anode
C	cathode
f	fuel channel
i	component

Appendix B

Appendices Related to Chapter 3

B.1 Model Parameters & Correlations Used

The aim of this appendix is to provide detailed information on the correlations used and assumptions made during the calculation of the parameters and fluid phase physical properties required by the fixed-bed reformer model developed in Chapter 3. Tables B.1 and B.2 summarise the used correlations and estimation methods.

As referred to in Chapter 3, the derived model has six parameters that determine the behaviour of the system. These are the mass and heat transfer coefficients for the film surrounding the reformer particles, k_m and k_h, the effective diffusivity and thermal conductivity in the radial direction of the fixed-bed, D_{er} and λ_{er}, the overall heat transfer coefficient, α_R, and the effective diffusivity in the catalyst particle, D_e.

The calculation of the mass and heat transfer coefficients between the fluid and the particles of a packed bed, k_m and k_h, is often done by correlating dimensionless groups that characterise the flow conditions. It is common to correlate experimental data in terms of the j_D and j_H factors, or indirectly the Schmidt, Sc, Prandtl, Pr, and Reynolds, Re, numbers. The correlations adopted here are shown in Table B.1.

The advancement on non-isothermal fixed-bed reactors modelling stressed the need for an improved understanding of the effective diffusivity and effective thermal conductivity coefficient values, either in the axial or in the radial directions. Here only radial dispersion is considered and so only the radial effective diffusivity and effective thermal conductivity coefficients need to be calculated. The correlation adopted for the calculation of the convective heat transfer coefficient, α_R, is also presented here.

Table B.1 Correlations used for the calculation of the model parameters.

k_m [1]	$j_D = \frac{\varrho k_m}{G} Sc^{2/3}$, $Sc = \frac{\mu}{\varrho D_{im}}$
	$j_D = \frac{0.458}{\varepsilon} Re^{-0.407}$ $(\text{for } Re > 10)$, $Re = \frac{d_p G}{\mu}$
k_h [1]	$j_H = \frac{k_h}{c_p G} Pr^{2/3}$, $Pr = \frac{c_p \mu}{\lambda}$, $j_H \approx j_D$
D_{er} [2,3]	$Pe_{rm}(d_p) = \frac{d_p u_i}{D_{er}} \approx 8-10$
	$\lambda_{er} = \lambda_{er}^0 + \lambda_{er}^t$
λ_{er} [3,4]	$\frac{\lambda_{er}^0}{\lambda} = \left(1-\sqrt{1-\varepsilon}\right)\left(1+\varepsilon\frac{\alpha_{rs} d_p}{\lambda}\right) + \frac{2\sqrt{1-\varepsilon}}{1+\left(\frac{\alpha_{rs} d_p}{\lambda} - B\right)\frac{\lambda}{\lambda_s}}\Theta$
	$\Theta = \frac{\left[1+\left(\frac{\alpha_{rs} d_p}{\lambda}-1\right)\frac{\lambda}{\lambda_s}\right]B}{\left[1+\left(\frac{\alpha_{rs} d_p}{\lambda}-B\right)\frac{\lambda}{\lambda_s}\right]^2} \ln\frac{1+\frac{\alpha_{rs} d_p}{\lambda_s}}{B\frac{\lambda}{\lambda_s}} - \frac{B-1}{1+\left(\frac{\alpha_{rs} d_p}{\lambda}-B\right)\frac{\lambda}{\lambda_s}} +$
	$+\frac{B+1}{2B}\left(\frac{\alpha_{rs} d_p}{\lambda}-B\right)$
	$\alpha_{rs} = 0.227 x 10^{-3} \frac{p}{2-p}\left(\frac{T}{100}\right)^3$, $p = 0.8$, $B = 1.25[(1-\varepsilon)/\varepsilon]^{10/9}$ for spheres
	$\lambda_{er}^t = \varepsilon\rho c_p D_{er} \Rightarrow \frac{\lambda_{er}^t}{\lambda} = \psi\, Pr\, Re$, where $\psi = 0.14\left[1+46\left(\frac{d_p}{2r_R}\right)^2\right]^{-1}$
α_R [4]	$\alpha_R = \alpha_R^0 + 0.01152\frac{2r_R}{d_p} Re$, $\alpha_R^0 = 0.0987\,kJ/(m^2 sK)$
	$D_{e,i} = \frac{\varepsilon_p}{\tau} D_i \approx \varepsilon_p^2 D_i$
$D_{e,i}$ [3]	$\frac{1}{D_i} = \frac{1}{D_{im}} + \frac{1}{D_{K,i}} = \frac{\sum_{j\neq i}\frac{1}{D_{ij}}\left(y_{mol,j} - y_{mol,i}\frac{\nu_j}{\nu_i}\right)}{1 - y_{mol,i}\sum_j(\nu_j/\nu_i)} + \frac{4}{3} r_{pore}\left(\frac{2}{\pi}\frac{\Re x 10^3 T}{M_i}\right)^{0.5}$

[1] Smith (1981); [2] Gunn (1987); [3] Froment and Bischoff (1990); [4] De Wasch and Froment (1972).

Gunn (1987) presented accurate correlations to calculate the radial effective diffusivity coefficient, D_{er}. However, for practical purposes, the radial mass Peclet

number, Pe_{rm}, based on the particle diameter can be considered to lie between 8 and 10 (Froment and Bischoff, 1990). In this work it is assumed $Pe_{rm}(d_p) = 9$.

Several authors (Yagi and Kunii, 1957, 1960; Kunii and Smith, 1960) have set up models for calculating the λ_{er} and α_R coefficients introduced in Section 3.3.3, Chapter 3. In these models the flux by effective conduction is considered to consist of two contributions, the first static, λ_{er}^0, and the second dynamic, λ_{er}^t. The static contribution is composed by the transport through the fluid in the voids, either by conduction or radiation between neighbour voids, and by the transport in which the solid phase is involved. This last transport is due to the conduction through the contact surface between particles, the conduction in the stagnating film in the vicinity of the contact surface, the radiation from particle to particle, and the conduction through the particles. Zehner and Schlunder derived the formula for the static contribution of the effective conduction in Table B.1 (Froment and Bischoff, 1990). α_{rs} is the radiation coefficient for the solid and p the emissivity of the solid. The dynamic contribution arises exclusively from the transport in the fluid and corresponds to the mixing that is described by the effective diffusion in the radial direction, D_{er}. When the analogy between mass and heat transfer is complete, the relations in Table B.1 are obtained. The data for the convective heat transfer coefficient near the wall, α_R, are very scattered. De Wasch and Froment (1972) published data that are believed to have the high degree of precision required for the accurate prediction of severe situations in reactors. Table B.1 presents the correlation for air for α_R, where α_R^0 is a static contribution dependent on the type and size of the catalyst.

The effective diffusivity coefficient in a catalyst particle, D_e, is related to the molecular diffusivity, D_i, by the relation in Table B.1. This relation is meant to account for the complicated pore structure inside a catalyst pellet, where the diffusion path length along the pores is greater than the measurable pellet thickness. This is due to the tortuous nature of the pores and to the pore constrictions. The molecular diffusivity is then corrected by a tortuosity factor, τ, and by the catalyst porosity, ε_p, originating the effective diffusivity. The definition of the tortuosity factor includes both the effects of altered diffusion path length as well as changing cross-sectional area in constrictions. As the tortuosity factor value is difficult to obtain, it is often to approximate its value, based

on the random pore model, to $1/\varepsilon_p$, as is done in Table B.1 (Froment and Bischoff, 1990). As for the molecular diffusivity, it is the result of fluid-fluid intermolecular collisions as considered by the kinetic theory of gases, and is often known as the bulk diffusivity, D_{im}. However, when the pore size gets so small that its dimensions are less than the mean path of the fluid, fluid-fluid collisions are no longer the dominant ones. Instead, fluid-wall collisions are important, and the mode of diffusive transport is altered. This can occur for gases at less than atmospheric pressure in typical pellets. The Knudsen diffusivity, $D_{K,i}$, arises then from the kinetic theory of gases. It is a function of the pore radius, r_{pore}, and varies with $T^{0.5}$, but is independent of pressure (Froment and Bischoff, 1990). When both types of diffusion, bulk and Knudsen, are important, both contribute to the molecular diffusion, as seen in Table B.1. Back to the bulk diffusion, and as the system under study is a multicomponent one, a rigorous treatment compared to the one of a binary mixture is needed. A mean effective binary diffusivity for a given component i diffusing through a mixture, D_{im}, is normally calculated. This coefficient depends on the usual binary diffusivities (calculated in Table B.2), on the mixture composition, and on the stoichiometry of the reaction. The relation in Table B.1 for the calculation of D_{im} results from a simplification of the Stefan-Maxwell equation based on the kinetic theory for ideal gases (Froment and Bischoff, 1990).

The calculation of the model parameters requires some physical properties of the fluid phase to be estimated. These are: fluid viscosity, binary diffusivities of the components in the mixture, fluid density, fluid heat capacity, and fluid thermal conductivity. Table B.2 presents the estimation methods used to calculate these properties.

Most of the gas viscosity estimation techniques are based on the Chapman-Enskog theory. The Chapman-Enskog equation for the estimation of the viscosity of a given component i, μ_i, is presented in Table B.2. To use this relation, the collision diameter, σ_i, and the collision integral, $\Omega_{\mu,i}$, must be obtained. $\Omega_{\mu,i}$ is obtained as a complex function of the dimensionless temperature kT/e_i, where k is the Boltzmann's constant and e_i the minimum energy of the potential energy of interaction between two molecules separated by a certain distance. The intermolecular potential function most used, although widely criticised, is the Lennard-Jones potential. With this potential, an

empirical equation for the collision integral has been determined. The symbols A_μ, ..., F_μ in Table B.2 stand for the constant values in that empirical equation. Finally, the collision diameter and the ratio e_i/k are obtained from the Lennard-Jones potentials table (Reid et al., 1988). For the calculation of the mixture viscosity, μ, the relation presented in Table B.2 is used. This relation results from the extension of the Chapman-Enskog theory for multicomponent gas mixtures at low density (Bird et al., 1960).

The diffusion coefficients for binary gas systems are calculated using the theory for low to moderate pressures. The Chapman-Enskog theory is applied, resulting in the relation in Table B.2 for the calculation of binary diffusion coefficients between components i and j. Here, σ_{ij} denotes the mean collision diameter of components i and j, and $\Omega_{D,ij}$ denotes the collision integral for the diffusion coefficient calculation. This integral is given by an empirical function of the dimensionless temperature kT/e_{ij}, where e_{ij} is the mean minimum energy of components i and j. The symbols A_D, ..., G_D in the $\Omega_{D,ij}$ relation stand for constant values. The mixture rules for the calculation of the mean collision diameter, minimum energy, and molecular weight are also illustrated. The collision diameter and the ratio e_i/k for each component are the same used for the above viscosity calculation and are obtained from the Lennard-Jones potentials table (Reid et al., 1988).

The heat capacity of the fluid phase, c_p, is calculated assuming ideal gas behaviour. For the heat capacity of the pure components, $c_{p,i}$, third order polynomials in the temperature are used. The rule to determine the mean heat capacity of the mixture is indicated.

The fluid phase thermal conductivity coefficient is calculated using the theory for gas mixtures at low density. For the thermal conductivity coefficient of the pure components, λ_i, a semi-empirical method for polyatomic gases developed by Eucken is used. For the calculation of the mixture thermal conductivity, λ, a similar relation to the one used for the viscosity is applied and presented in Table B.2. The dimensionless number $\varphi_{i,j}$ is the same for both the viscosity and thermal conductivity coefficients (Bird et al., 1960).

Table B.2 Correlations used for the calculation of the system properties.

μ [1,2]	$\mu = \sum_i \frac{y_{mol,i}\mu_i}{\sum_j y_{mol,j}\varphi_{i,j}}$, $\varphi_{i,j} = \frac{1}{\sqrt{8}}\left(1+\frac{M_i}{M_j}\right)^{-0.5}\left[1+\left(\frac{\mu_i}{\mu_j}\right)^{0.5}\left(\frac{M_j}{M_i}\right)^{0.25}\right]^2$ $\mu_i = 26.69 \times 10^{-7} \frac{\sqrt{M_i x 10^3 T}}{\sigma_i^2 \Omega_{\mu,i}}$ $\Omega_{\mu,i} = A_\mu\left(\frac{kT}{e_i}\right)^{-B_\mu} + C_\mu Exp\left[-D_\mu\left(\frac{kT}{e_i}\right)\right] + E_\mu Exp\left[-F_\mu\left(\frac{kT}{e_i}\right)\right]$ for $0.3 < \frac{kT}{e_i} < 100$
$D_{i,j}$ [1]	$D_{i,j} = \frac{0.00266 \times 10^{-4} T^{1.5}}{P\left(M_{ij} x 10^3\right)^{0.5} \sigma_{ij}^2 \Omega_{D,ij}}$ $\Omega_{D,ij} = A_D\left(\frac{kT}{e_{ij}}\right)^{-B_D} + C_D Exp\left[-D_D\left(\frac{kT}{e_{ij}}\right)\right] + E_D Exp\left[-F_D\left(\frac{kT}{e_{ij}}\right)\right] + G_D Exp\left[-H_D\left(\frac{kT}{e_{ij}}\right)\right]$ $M_{ij} = 2\left(\frac{1}{M_i}+\frac{1}{M_j}\right)^{-1}$, $\sigma_{ij} = \frac{\sigma_i + \sigma_j}{2}$, $e_{ij} = \sqrt{e_i e_j}$
ϱ	Ideal gas law: $\varrho = PM / \Re T$
c_p [1]	$c_p = \sum_i y_{mol,i} c_{p,i} / M$, $c_{p,i} = A_i + B_i T + C_i T^2 + D_i T^3$ (kJ/molK)
λ [2]	$\lambda = \sum_i \frac{y_{mol,i}\lambda_i}{\sum_j y_{mol,j}\varphi_{i,j}}$, $\lambda_i = \left(c_{p,i} + \frac{5}{4}\frac{\Re}{M_i}\right)\mu_i$

[1] Reid et al. (1988); [2] Bird et al. (1960).

B.2 Model Parameters & Physical Properties Values

Table B.3 presents the physical properties values obtained, based on the methods above described, for the base case conditions presented in Section 4.2.1, Chapter 4. The values of the model parameters are presented in Chapter 4, Table 4.1.

Table B.3 Physical properties values.

Property	Value	Property	Value
r_{pore} *	80 Å	ε_p *	0.528
λ_S **	1.17 x 10^{-3} $kJm^{-1}s^{-1}K^{-1}$	λ	1.31 x 10^{-4} $kJm^{-1}s^{-1}K^{-1}$
c_p	2.39 $kJkg^{-1}K^{-1}$	ϱ	0.229 kgm^{-3}
μ	4.03 x 10^{-5} $kgm^{-1}s^{-1}$	Re	2.44

* Xu and Froment (1989a, 1989b).** Votruba et al. (1972).

Notation

c_p	fluid phase heat capacity, kJ/kgK
D_e	effective diffusivity in the catalyst particle, m^2/s
D_{er}	effective diffusivity in the radial direction, m^2/s
D_i	molecular diffusivity for component i, m^2/s
$D_{i,j}$	binary diffusivity of the components in the fluid mixture, m^2/s
D_{im}	mean effective binary diffusivity for component i in the fluid mixture, m^2/s
$D_{K,i}$	Knudsen diffusivity for component i, m^2/s
d_p	catalyst particle diameter, m
e	minimum energy in the Lennard-Jones potentials
G	mass flux, $kg/(m^2s)$
j_D, j_H	dimensionless factors in Table B.1
k	Boltzmann's constant
k_h	heat transfer coefficient - film surrounding the reformer particles, kJ/m^2sK
k_m	mass transfer coefficient - film surrounding the reformer particles, m/s
M_i	molecular weight of component i, kg/mol
M	molecular weight of the fluid phase, kg/mol
P	pressure
Pe_{rm}	radial mass Peclet number $[d_p u_i / D_{er}]$
Pr	Prandtl number
r_{pore}	pore catalyst radius, m
r_R	reactor radius, m
$\Re$	gas constant, kJ/molK
Re	Reynolds number
Sc	Schmidt number
T	temperature, K
u_i	interstitial velocity in the reformer, m/s
$y_{mol,i}$	molar fraction of component i

Greek letters

α_R	overall heat transfer coefficient, kJ/m^{2}sK
ε	void fraction of the packing
ε_p	catalyst porosity
λ	fluid phase thermal conductivity, kJ/msK
λ_S	solid phase thermal conductivity, kJ/msK
λ_{er}	effective thermal conductivity in the radial direction, kJ/msK
Ω	collision integral
ϱ	fluid phase density, kg/m^3
σ_i	collision diameter in the Lennard-Jones potentials
μ	fluid phase viscosity, kg/(ms)
τ	tortuosity factor
ν	stoichiometric coefficient of a component in a reaction

Subscripts

i	component
j	reaction
p, s	catalyst particle
R	reformer

Appendix C

Appendices Related to Chapter 5

C.1 Information on the Activity and Effective Diffusivity Distributions Assumed

The aim of this Appendix is to provide detailed information on the activity and effective diffusivity distributions assumed and determined in Chapter 5.

The functions $a(r_p)$ and $D_e(r_p)$ in equations (5.1), (5.2), and (5.4) in Table 5.1 stand for the catalyst particle activity and effective diffusivity distributions determined. These distributions can be described in terms of three parameters, which, depending upon their values, can approximate uniform, step-change, or s-shaped type profiles (the initially considered profiles) at various positions within the pellet. All these can be mathematically represented as a function of the dimensionless catalyst particle radial position, $r = r_p/R_p$, by the following expression:

$$a(r), \phi(r) = \frac{1}{e^{b(r-a)} + 1}(1-c) + c \qquad (C.1)$$

where $a(r)$ stands for the activity distribution, $\phi(r)$ for the dimensionless effective diffusivity distribution (defined as the ratio between the effective diffusivity along the catalyst particle radius and a nominal effective diffusivity coefficient, $\overline{D_e}$), and *a*, *b*, and *c* for the distribution parameters. Depending on the values of *a*, *b*, and *c*, the distributions represented by equation (C.1) can present different shapes. Figure C.1 presents some illustrative distributions.

The parameter *a* denotes the point in the dimensionless catalyst particle radial position where the activity and effective diffusivity distributions have an inflection point and take the value 0.5 (for $c = 0$).

The parameter *b* is related to the steepness of those distributions – the higher the value of *b*, the steeper is the profile. During initial optimisation it was found that higher values of *b* (that correspond to close to step-change distributions) led to optimal distributions. In a second phase of the work, *b* was then set equal to 30 and only the value of *a* was optimised. This was done as very high values of *b* often led to numerical solution problems.

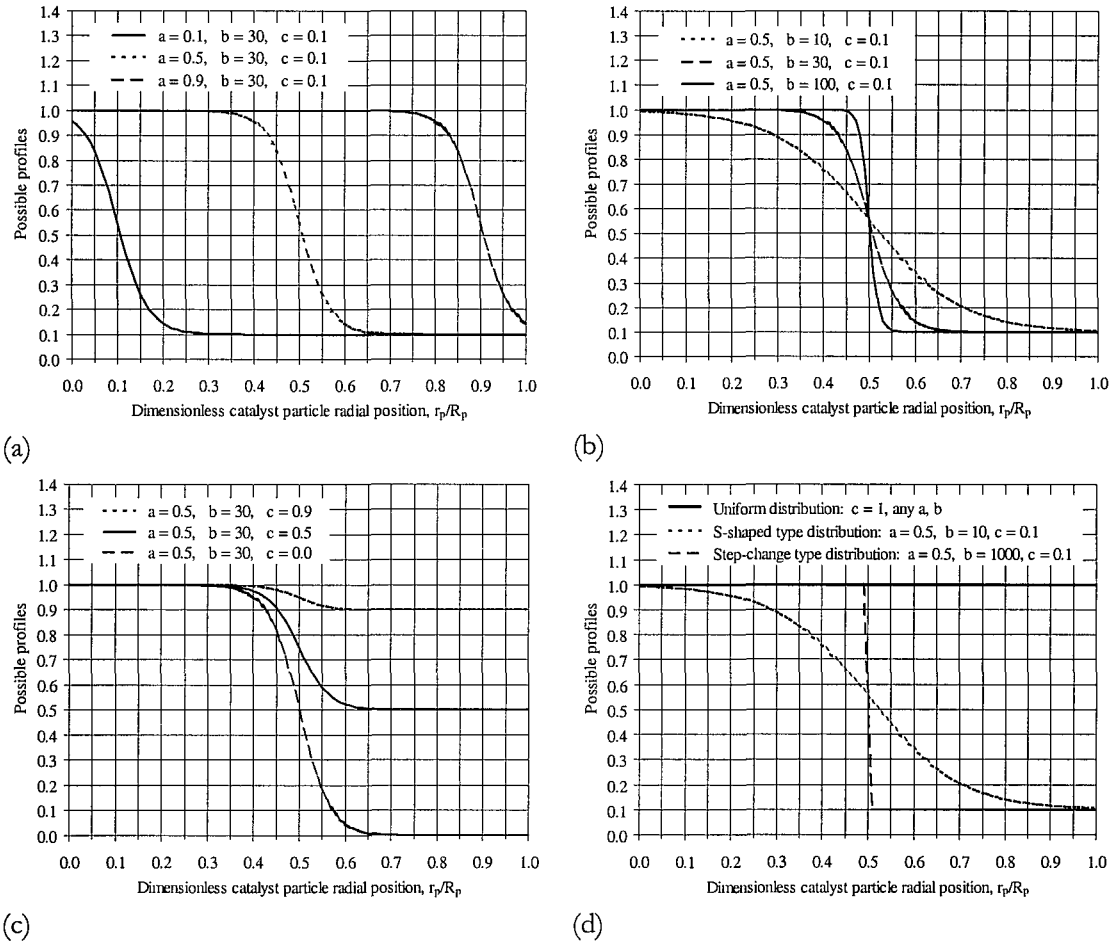

Figure C.1 Behaviour of the distribution (C.1) as a function of the parameters values: (a) different values of *a*; (b) different values of *b*; (c) different values of *c*; (d) equivalent uniform, s-shaped, and step-change type distributions.

The parameter *c* denotes the minimum value allowed for those same functions. In the case of an activity distribution, *c* is always equal to zero, as the minimum value of this function implies a catalyst support with no active material. In the case of a diffusivity distribution, *c* stands for the minimum allowed value for the effective diffusivity, i.e, the effective diffusivity of the mass transfer barrier placed at the outer

surface of the catalyst pellet. Such value is defined in order to minimise the risk of total pore blockage. In Chapter 5, it has been assumed that, on the outer diffusion barrier, the effective diffusivity coefficient could be as low as 10% of its nominal value $\overline{D_e}$.

Figures C.1a, C.1b, and C.1c present the described distributions for various values of the parameters *a*, *b*, and *c*. Near-uniform profiles can be obtained, either when $c = 1$, independently of the values of *a* and *b*, or with $a = 1$. As mentioned above, for large values of *b* such functions resembles step-change profiles, for which *a* determines the point where the step occurs. With moderate values of *a* and *b*, s-shaped equivalent profiles can also be achieved. Figure C.1d presents the equivalent uniform, s-shaped, and step-change distributions that can be obtained.

C.2 Information on the Fabrication of Pellets with Diffusion Barriers

Parallel to the work presented in this thesis, some experimental work has also been carried out in the fabrication of pellets with diffusion barriers (Cabello-Sánchez et al., 2003; Laosiripojana, 2003; Aguiar et al., 2001a). For that purpose, gas-diffusion barriers have been coated on active steam reforming catalysts in order to control and reduce the rate of reaction whilst maintaining the catalyst activity and stability. It has been found that the application of a mass transfer barrier can be done either by partially blocking the pores in a commercial catalyst support, by infiltration with a sol-gel ceramic precursor, or by forming a porous ceramic membrane with much smaller pore size on the support surface. Otherwise, the use of a support with much smaller pore size than commercially available supports (which can be synthesised by sol-gel methods) would be required. The techniques used for the membrane fabrication have been the sol-gel (Aguiar et al., 2001a) and the dip-coating (Cabello-Sánchez et al., 2003; Laosiripojana, 2003) methods, which are widely used in the ceramics field for the production of oxides with a controlled microstructure, shape, density, and porosity.

As mentioned on previous chapters, one of the problems in having steep temperature gradients across the reformer is that these can lead to high mechanical

stresses that result in cracking and fracture of the ceramic catalyst supports. It has been reported that runaway combustion in a multi-staged combustion reactor can be controlled and prevented by adding a diffusion barrier layer on top of the catalyst layer to limit the supply of fuel and/or oxidant to the catalyst. Such diffusion barrier greatly extends the operating range of the catalyst and can be made of a variety of oxides with a low activity for combustion, such as alumina, zirconia or titania (Leung et al., 1996; Dalla Betta et al., 1993). Therefore, the corenite catalysts used in this work are conventional steam reforming catalysts and the barrier of similar materials to the above, which also satisfy the requirement for high resistance to carbon deposition under methane steam reforming conditions. The thickness of the layer that can be applied is limited, as generally layers thicker than a few microns are likely to crack. Hence, the challenge posed is to obtain a pore structure, which does not coarsen or densify at the high operating temperatures in question, although some sintering is always required to give mechanical strength. So far, preliminary results related to the fabrication of diffusion barriers are very promising (Cabello-Sánchez et al., 2003).